The first tissues of plants and animals that encounter environmental pollutants are colonized by microbes. Collectively, these microbes affect the toxicity of environmental pollutants like nanomaterials. Through a combination of zebrafish larvae experiments and computational tehniques, this dissertation unravels and quantifies the effects of interactions between microbes and nanomaterials, and between hosts and microbiota, on nanomaterial toxicity. Ultimately, this can serve as a stepping stone for including microbiota-mediated interactions into mechanistic pathways for nanomaterial safety assessment.

Nanomaterial safety for microbially-colonized hosts

Bregje W. Brinkmann

Nanomaterial safety
for microbially-colonized hosts

microbiota-mediated
physisorption interactions
and particle-specific toxicity

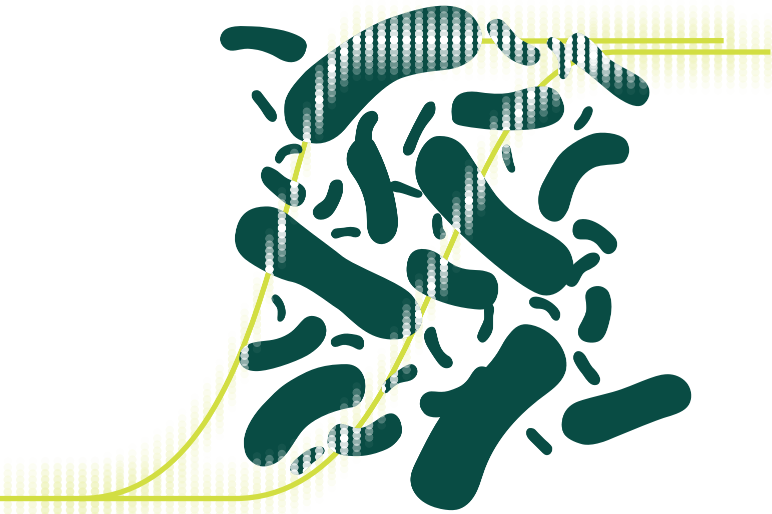

Bregje W. Brinkmann

2022

On the cover:

Graphical representation of microbiota-dependent differences in the sensitivity of hosts to nanomaterials. The sizes of the depicted microbes and the dots of the uncertainty pattern are proportional to the sizes of bacteria and nanoparticles, respectively.

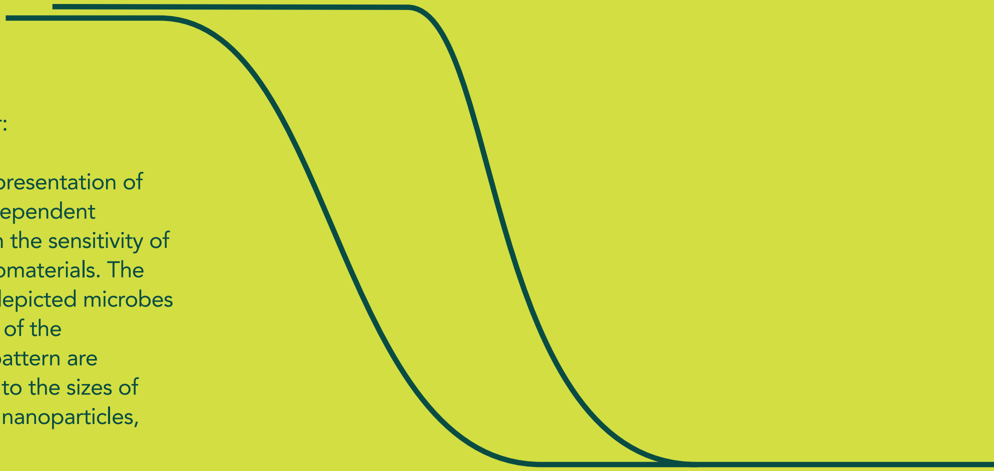

Nanomaterial safety for microbially-colonized hosts

microbiota-mediated physisorption interactions and particle-specific toxicity

Bregje W. Brinkmann

PhD thesis, Leiden University, The Netherlands

The research described in this thesis was conducted at the Institute of Environmental Sciences (CML), Leiden University, the Netherlands.

ISBN 978-90-519-1986-8
Cover Bregje W. Brinkmann
Layout Bregje W. Brinkmann
Printing Ipskamp Printing

Nanomaterial safety for microbially-colonized hosts:
microbiota-mediated physisorption interactions and particle-specific toxicity

Proefschrift

ter verkrijging van
de graad van doctor aan de Universiteit Leiden,
op gezag van rector magnificus prof. dr. ir. H. Bijl,
volgens besluit van het college voor promoties
te verdedigen op donderdag 8 december 2022
klokke 13.45 uur
door

Bregje Willemijn Brinkmann

geboren te Haarlem
in 1993

Promotores:
Prof. dr. ing. M.G. Vijver
Prof. dr. ir. W.J.G.M. Peijnenburg

Promotiecomissie:
Prof. dr. A. Tukker
Prof. dr. ir. P.M. van Bodegom
Prof. dr. H.P. Spaink
Dr. G.J.A. Sevink
Prof. dr. I. Lynch (University of Birmingham)
Dr. L.M. Skjolding (Danmarks Tekniske Universitet)

This work was supported by the project PATROLS of European Union's
Horizon 2020 research and innovation programme under grant number 760813.

Table of contents

PHYSISORPTION INTERACTIONS

PARTICLE-SPECIFIC TOXICITY

Summary

The external tissues of plants and animals are colonized by microbes that collectively form the host-associated microbiota. Antimicrobial substances that reach microbially-colonized tissues, can kill certain members of the microbiota, including members that contribute to host health and development. This forms a concern for nanomaterials that consist of antimicrobial nanoparticles. Many of these particles have been found to disrupt microbiota-dependent biophysiological homeostasis, which raises questions about the safety of antimicrobial nanomaterials for microbially-colonized hosts.

In addition to the effects of nanoparticles on microbiota, microbes can also affect the physicochemical properties of nanoparticles, and can modulate the biophysiological responses of hosts to nanoparticles. The work presented in this thesis investigates this using a combination computational techniques and zebrafish larvae experiments, as introduced in **chapter 1**. This chapter first of all presents an overview of the growing body of work that demonstrates the effects of nanoparticles on host-associated microbiota. Additionally, the chapter describes what chemical transformations of nanoparticles have been found to be mediated by host-associated microbiota. Thereafter, two knowledge gaps are identified, which are investigated in this thesis. Firstly, physisorption interactions between colonizing microbes, their metabolites and nanomaterials are investigated in **chapter 2** and **chapter 3**. Secondly, the influence of colonizing microbes on particle-specific toxicity is quantified, and underlying mechanisms are investigated, in **chapter 4** and **chapter 5**. Combined, these chapters address the research question: '*What mechanisms govern the physisorption-driven and particle-specific effects of colonizing microbiota on nanomaterial toxicity to microbially-colonized hosts?*'

In **chapter 2** we investigate physisorption interactions between ingested nanomaterials and metabolites from enteric microbiota in the gastrointestinal tract. As a starting point for this investigation, we generated a concise overview from the literature of 170 unique enteric microbial metabolites that are produced, modified or regulated by enteric microbiota. Using quantitative structure-activity relationship (QSAR) models we subsequently predicted the adsorption affinity (log k value) of 60 of these metabolites to 13 metal nanomaterials, 5 carbon nanotubes and 1 fullerene. For a case study on four vitamins, a silicon dioxide nanomaterial, and multiwalled carbon nanotube, we moreover performed molecular dynamics (MD) simulations to obtain direct molecular information of these nano-bio interactions. Correlations between QSAR predictions and descriptors from the biological surface adsorption index indicated that hydrophobicity-driven interactions contribute most to the overall

adsorption affinity, while hydrogen-bond interactions and polarity/polarizability-driven interactions differentiate the affinity to metal and carbon nanomaterials. Unconstrained MD simulations provided excellent support for these main interaction types. Additionally, the simulations showed how large and flexible metabolites can gain stability on the nanomaterial surface via conformational changes. Combined, these results provide qualitative and quantitative insight into biologically relevant interactions that could occur between microbial metabolites and ingested nanomaterials in the gastrointestinal tract.

In **chapter 3** we zoom out to study physisorption interactions at the scale of microbes, focusing on the earliest life stages of zebrafish. In this chapter we test the hypothesis that the adsorption of antimicrobial titanium dioxide nanoparticles ($nTiO_2$) onto zebrafish eggs can harm the developing embryo by eradicating early colonizing microbiota. To assess the effectiveness of the eggs' membranes in preventing particle uptake, we first used two-photon microscopy to localize gold nanorods in and on exposed zebrafish eggs. Since no detectable amounts of particles crossed the protective membranes, we continued to explore the effects of adsorbed $nTiO_2$ to microbiota colonizing the zebrafish egg surface. Using particle-induced X-ray emission analysis, we inferred that the TiO_2 could cover 25–45 % of the zebrafish egg surface. Both imaging and culture-based microbial identification techniques revealed that particle adsorption resulted in an overall increase of microbial abundance, despite its antimicrobial effects. Pathogenic *Aeromonas* bacteria tolerated the antimicrobial properties of the nanoparticles. This formed a risk to the larvae that hatched from $nTiO_2$ exposed eggs, which also comprised higher microbial abundance, even without continued exposure to $nTiO_2$. This demonstrates that the adsorption of suspended antimicrobial nanoparticles onto aquatic eggs could facilitate the spatiotemporal dispersal of pathogenic bacteria in aquatic ecosystems.

In the next two chapters, we study the effects of colonizing microbiota on the particle-specific toxicity of nanomaterials. For this purpose, in **chapter 4** we optimize protocols for comparing the acute toxicity of nanomaterials to germ-free and microbially-colonized zebrafish larvae. By combining this methodology with the response addition model, we found that colonizing microbiota protect zebrafish larvae against the particle-specific toxicity of silver nanoparticles (nAg), but do not affect the acute toxicity of zinc oxide nanoparticles (nZnO) to zebrafish larvae. By isolating microbiota from zebrafish larvae at the end of the two day-exposure period, we additionally found that nAg eradicated most of the larvae-associated microbiota, while nZnO did not affect the abundance of larval microbiota significantly. These results show that, at least for certain nanomaterials, it is important to take host-microbe interactions into account when assessing toxic effects of nanoparticles to microbially-colonized hosts.

In **chapter 5** we focus on the specific case of nAg toxicity to zebrafish larvae, to further dissect how members of colonizing microbiota can protect hosts against nanomaterial toxicity. Using an *il1ß*-reporter line, we characterized the accumulation and particle-specific inflammatory effects of nAg in the total body and intestinal tissues of the larvae. This showed that silver gradually accumulated in both the total body and intestinal tissue, yet specifically caused particle-specific inflammation on the skin of larvae. Subsequently, we used three mutant lines to assess if the recognition of microbiota by toll-like receptors (TLRs) contributes to the microbiota-dependent protection against nAg. Both a zebrafish mutant for TLR2, and a mutant for TLR2-adaptor protein TIRAP (Mal) were more sensitive to nAg than their wild type siblings under microbially-colonized conditions. In contrast, both of these mutants were equally sensitive to nAg as their wildtype siblings under germ-free conditions. Irrespective of the presence of microbiota, the sensitivity of a third mutant, for TLR2-adaptor protein MyD88, did not differ from that of its wildtype sibling. Combined, these results suggest that the recognition of microbiota by TLR2 protects zebrafish larvae against nAg toxicity via TIRAP-dependent downstream signaling. More generally, by differentiating between the effects of host-microbiota and microbe-particle interactions, the results of this chapter support the conclusion that host-microbiota interactions affect nanomaterial toxicity to zebrafish larvae.

In **chapter 6** we discuss how the results of this thesis can support microbiota-inclusive nanomaterial safety assessment for humans and the environment. Focusing on microbiota-mediated physisorption interactions, we explain under what circumstances microbial metabolites can particularly be hypothesized to affect exposure scenarios for nanomaterials via biocorona formation. We moreover discuss how test systems can account for the formation of heteroaggregates consisting of microbes and particles, potentially facilitating the dispersal of pathogenic microbes. Thereafter, we discuss implications of the obtained insight into the microbiota-dependent and particle-specific toxicity mechanism for nAg to three common nanosafety testing strategies. Firstly, with regard to the aim to predict chronic exposure outcomes, our results indicate that antimicrobial agents might sensitize hosts to nanomaterials due to the loss of protective microbiota. However, the immunomodulatory effects of other common environmental pollutants could mask this. Secondly, for grouping and read-across approaches, the results of this thesis suggest that enhanced *il1ß* expression could potentially serve as a marker for microbiota-dependent toxicity. If so, this could help predicting microbiota-dependent toxicity outcomes for nanomaterials. Thirdly, concerning cross-species extrapolation, the conservancy of microbiota functioning across hosts, rather than taxonomic microbiota composition, indicates that especially functional measures of

microbiota composition constitute promising targets for cross-host extrapolation. Altogether, I envision that the test approaches, results and insights obtained in this thesis can contribute to the safe and sustainable design of nanomaterials by supporting a transition to microbiota-inclusive nanomaterial safety assessment for humans and the environment.

Samenvatting

De micro-organismen die de externe weefsels van planten en dieren koloniseren, vormen samen de gastheer-geassocieerde microbiota. Antimicrobiële stoffen die in aanraking komen met microbieel-gekoloniseerde weefsels, kunnen bepaalde microben daarvan doden, waaronder de microben die bijdragen aan de gezondheid en ontwikkeling van hun gastheer. Dit vormt een zorg voor nanomaterialen die antimicrobiële nanodeeltjes bevatten. Voor veel van deze deeltjes is aangetoond dat deze de biofysiologische homeostase van gastheren, die afhankelijk is van microbiota, kunnen verstoren. Dit roept vragen op over de veiligheid van antimicrobiële nanomaterialen voor gastheren die door microben zijn gekoloniseerd.

Naast de effecten van nanodeeltjes op microbiota, zijn er effecten van microben op de fysisch-chemische eigenschappen van nanodeeltjes, en de fysiologische respons daarop van de gastheer. Dit proefschrift bundelt werk dat dit onderzoekt middels een combinatie van computermodellen en experimenten met zebravislarven. Dit wordt geïntroduceerd in **hoofdstuk 1**. Dit hoofdstuk presenteert ten eerste een overzicht van het toenemende aantal studies dat effecten aantoont van nanodeeltjes op gastheer-geassocieerde microbiota. Verder beschrijft dit hoofdstuk welke chemische transformaties van nanomaterialen door microben mogelijk worden gemaakt. Daarna worden twee kennishiaten geïntroduceerd die in dit proefschrift worden onderzocht. Ten eerste worden fysisorptie interacties tussen koloniserende microben, hun metabolieten en nanomaterialen onderzocht in **hoofdstuk 2** en **hoofdstuk 3**. Ten tweede wordt de invloed van koloniserende microben op de deeltjes-specifieke toxiciteit van nanomaterialen gekwantificeerd, en worden de daaraan ten grondslag liggende mechanismen onderzocht in **hoofdstuk 4** en **hoofdstuk 5**. Samen behandelen deze hoofdstukken de onderzoeksvraag: '*Welke mechanismen leiden tot de fysisorptie-gedreven en deeltjes-specifieke effecten van microbiota op de toxiciteit van nanomaterialen voor microbieel-gekoloniseerde gastheren?*'

In **hoofdstuk 2** worden fysisorptie interacties onderzocht tussen ingenomen nanomaterialen en metabolieten van enterische microbiota in het maagdarmkanaal. Als startpunt voor dit onderzoek wordt aan de hand van literatuur een overzicht gegenereerd van 170 unieke microbiële metabolieten die door enterische microben worden geproduceerd, aangepast of gereguleerd. Met 'quantitative structure-activity relationship' (QSAR) modellen wordt vervolgens voor 13 metalen nanomaterialen, 5 koolstofnanobuizen en 1 fullereen de adsorptie affiniteit (log *k* waarde) van 60 van deze metabolieten voorspeld. Met moleculair dynamische (MD) simulaties wordt bovendien directe moleculaire informatie verkregen van nano-bio interacties voor een casus van vier vitaminen, een siliciumdioxide nanomateriaal en een meerwandige koolstofnanobuis. De correlaties tussen de QSAR voorspellingen en de ‘biological surface adsorption index’ gaven aan dat door hydrofobiciteit gedreven interacties het meeste bijdragen aan de algehele affiniteit van metabolieten voor nanomaterialen, terwijl waterstofbrug interacties en polariteit/polariseerbaarheid gedreven interacties de affiniteit van metabolieten voor metaal en koolstof nanomaterialen onderscheiden. Vrije MD simulaties ondersteunden deze kern interactie types in grote mate. Daarbij lieten de simulaties zien hoe grote en flexibele metabolieten ander conformaties aan kunnen nemen om stabiliteit te winnen op het oppervlak van nanomaterialen. Samen geven deze resultaten zowel kwalitatief als kwantitatief inzicht in biologisch relevante interacties die in het maagdarmkanaal tussen microbiële metabolieten en ingenomen nanomaterialen kunnen optreden.

Hoofdstuk 3 richt zich op fysisorptie interacties die zich op de grotere schaal van microben voordoen. In dit hoofdstuk wordt veronderstelling getoetst dat de adsorptie van antimicrobiële titaniumdioxide nanodeeltjes (nTiO_2) op zebraviseieren het ontwikkelende embryo kan schaden, door vroeg-koloniserende microbiota te bestrijden. Eerst wordt onderzocht of de membranen die het ei omsluiten de opname van nanodeeltjes tegen kunnen gaan. Daartoe worden goude nanostaafjes in en op blootgestelde zebraviseieren gelokaliseerd door middel van twee-foton microscopie. Hieruit bleek dat de deeltjes de beschermende membranen niet in detecteerbare hoeveelheden passeerden. Vervolgens worden de effecten van geadsorbeerd nTiO_2 op de koloniserende microben op zebraviseieren onderzocht. Dit geadsorbeerd TiO_2 bedekte, bij benadering door middel van ‘particle-induced X-ray emission analysis’, 25-45 % van het oppervlak van zebraviseieren. Zowel op beeld- als op kweek-gebaseerde identificatiemethoden lieten zien dat dit resulteerde in een algehele toename van de hoeveelheid microben, ondanks de antimicrobiële werking van de deeltjes. Ziekteverwekkende *Aeromonas* bacteriën tolereerden de antimicrobiële eigenschappen van de deeltjes. Dit vormde een risico voor de larven die uit de aan nTiO_2 blootgestelde eieren kwamen, aangezien deze ook een grotere hoeveelheid microben bevatten, zelfs zonder voortzetting van de blootstelling aan nTiO_2. Deze resultaten laten zien dat de adsorptie van gesuspendeerde antimicrobiële nanodeeltjes op aquatische eieren de ruimtelijk-temporale verspreiding van ziekteverwekkende bacteriën door aquatische ecosystemen mogelijk kan maken.

In de volgende twee hoofdstukken worden effecten van koloniserende microbiota op de deeltjes-specifieke toxiciteit van nanomaterialen bestudeerd. In **hoodstuk 4** worden hiertoe protocollen geoptimaliseerd, waarmee de acute toxiciteit van nanomaterialen tussen kiemvrije en microbieel-gekoloniseerde zebravislarven vergeleken kan worden. Door deze methodiek met het respons additie model te combineren, bleek dat koloniserende microben zebravislarven tegen de deeltjes-specifieke toxiciteit van zilver nanodeeltjes (nAg) beschermden, maar de toxiciteit van zinkoxide nanodeeltjes (nZnO) niet beïnvloedden. Door aan het eind van de tweedaagse blootstellingsperiode microben van zebravislarven te isoleren, bleek bovendien dat nAg de microbiota van zebravislarven grotendeels bestreed, terwijl nZnO geen significant effect had op de hoeveelheid microben van zebravislarven. Deze resultaten laten zien dat het in ieder geval voor bepaalde nanomaterialen belangrijk is om de interacties tussen een gastheer en haar microbiota mee te nemen in het beoordelen van de toxiciteit van nanodeeltjes voor microbieel-gekoloniseerde gastheren.

In **hoofdstuk 5** wordt, aan de hand van de toxiciteit van nAg voor zebravislarven, verder ontrafeld hoe koloniserende microben de gastheer tegen de toxiciteit van nanomaterialen kunnen beschermen. Met behulp van een transgene *il1ß*-indicatielijn, worden ten eerste de accumulatie en deeltjes-specifieke inflammatoire effecten van nAg gekarakteriseerd in het gehele lichaam en in het darmweefsel van de larven. Dit liet zien dat zilver gelijkmatig ophoopte in zowel het gehele lichaam als in het darmweefsel van larven, hoewel het met name in de huid van larven deeltjes-specifieke ontstekingen veroorzaakte. Vervolgens wordt met behulp van drie mutantlijnen beoordeeld of de herkenning van microbiota door toll-like receptoren (TLRs) bijdraagt aan de microbiota-afhankelijke bescherming tegen nAg. Zowel een zebravismutant voor TLR2, als een mutant voor de TLR2-adaptor TIRAP (Mal), waren gevoeliger voor nAg dan het wildtype in de aanwezigheid van microbiota. Daarentegen waren beide mutanten zonder microbiota even gevoelig voor nAg als het wildtype. Ongeacht de aan- of afwezigheid van microbiota was de gevoeligheid van een derde mutant, voor de TLR2-adaptor MyD88, gelijk aan die van het wildtype. Samen suggereren deze resultaten dat de herkenning van microbiota door TLR2, zebravislarven beschermt tegen de toxiciteit van nAg via TIRAP-afhankelijke signaaltransductie. In algemenere zin ondersteunen deze resultaten, die de effecten van gastheer-microbiota interacties onderscheiden van effecten van microbe-deeltjes interacties, de conclusie dat interacties tussen de gastheer en haar microbiota de toxiciteit van nanomaterialen in zebravislarven beïnvloeden.

In **hoofdstuk 6** bediscussiëren we hoe de resultaten van dit proefschrift bij kunnen dragen aan een microbiota-inclusieve beoordeling van de veiligheid van nanomaterialen. Met betrekking tot de effecten van microbiota op fysisorptie interacties, lichten we toe onder welke omstandigheden microbiële metabolieten met name verondersteld kunnen worden via biocorona vorming de blootstellingsscenario's voor nanomaterialen te beïnvloeden. We bediscussiëren bovendien hoe er in testsystemen rekening gehouden kan worden met de vorming van heteroaggregaten bestaande uit microben en deeltjes. Mogelijk verspreiden deze aggregaten ziekteverwekkende microben. Daarna gaan we in op de implicaties van het verkregen inzicht in de toxiciteit van nAg, waarvan het mechanisme afhangt van microbiota en deeltjes-specifiek is, voor drie gangbare teststrategieën in de nanotoxicologie. Met betrekking tot het doel om chronische effecten te voorspellen, wijzen onze resultaten er ten eerste op dat antimicrobiële stoffen de gastheer gevoeliger kunnen maken voor nanomaterialen door de beschermende microbiota te bestrijden. Echter, andere veelvoorkomende vervuilende stoffen in het milieu kunnen dit maskeren door het immuunsysteem van de gastheer te onderdrukken. Met betrekking tot het groeperen van stoffen en 'read-across' aanpakken, suggereren de resultaten ten tweede dat een toename in *il1ß* expressie mogelijk als marker kan dienen voor het detecteren van microbiota-afhankelijke toxiciteit. Als dat zo is, kan aan de hand daarvan microbiota-afhankelijke toxiciteit worden voorspeld voor nanomaterialen. Met betrekking tot de extrapolatie tussen soorten, geven onze resultaten ten derde aan dat met name het functioneren van microbiota, en niet de taxonomische samenstelling van microbiota, een veelbelovend uitgangspunt vormt voor de extrapolatie van testresultaten tussen verschillende gastheren. Dit volgt uit het behoud van het functioneren van microbiota, in tegenstelling tot de taxonomische samenstelling van microbiota, tussen verschillende gastheren. Al met al heb ik voor ogen dat de testmethoden, resultaten en inzichten die in dit proefschrift zijn verkregen, bij kunnen dragen aan een veilig en duurzaam ontwerp van nanomaterialen, door bij te dragen aan een transitie naar een microbiota-inclusieve beoordeling van de veiligheid van nanomaterialen voor mens en milieu.

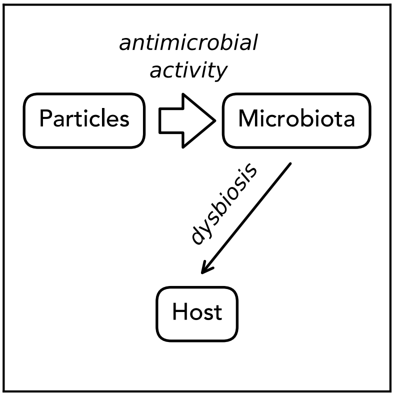
antimicrobial activity
Particles
Microbiota
dysbiosis
Host

CHAPTER 1

General introduction

1.1 Where nano meets micro

Bacteria, archaea, fungi, slime molds and other amoeba, green microalgae, diatoms, oomycetes, dinoflagellates, ciliates, foraminifera, radiolarians, many other protists, bacteriophage and other viruses: a dazzling diversity and abundance of *microorganisms** colonizes the environment. A large part of these microbes occurs ‘free-living’ in soil, water bodies, or air, where they aid, amongst others, in biogeochemical cycling, or the transformation of environmental pollutants (Madigan et al. 2011). Microbes can also colonize the tissue of plant and animal ‘hosts’, forming communities termed *microbiota**. Whilst certain members of colonizing microbiota occasionally cause disease (Jochem and Stecher 2020), many members of host-associated microbiota interact beneficially with the host, supporting biophysiological homeostasis.

Substances that exert antimicrobial activity form one of the main threats to microbially-mediated biophysiological homeostasis. Many of the recently developed antimicrobial products consist of nanoparticles, which are either designed to combat infection or exhibit antimicrobial activity resulting from inherent physicochemical properties (Makabenta et al. 2021). Following the definition recommended by the European Commission (2011), *nanoparticles** are particles that include at least one external dimension that is in between 1 to 100 nm, or alternatively, have a specific surface area exceeding 60 $m^2 \cdot cm^{-3}$. *Nanomaterials,** in turn, are materials consisting for at least 50% of nanoparticles in terms of particle count. Owing to their innovative properties, nanomaterials enable technological advancement across many different sectors. For instance, nanotherapeutics enable the targeted, light-induced activation of cytotoxic agents for cancer treatment, thereby limiting unwanted side effects (Reeßing and Szymanski 2017); nanosensors can act as highly sensitive probes for the detection of environmental pollutants (Willner and Vikesland 2018); nanofertilizers and

---

* Defined on page 30-31.

nanopesticides can facilitate the controlled release of agrochemicals (Hofmann et al. 2020); transparent nano-sized UV-filters are widely applied in sunscreens (Nasir et al. 2011); nanofabrics can dissipate heat in clothing (Iqbal et al. 2022); and as mentioned before, antimicrobial particles are incorporated in healthcare products such as bandages to combat infection.

The use of nanomaterials inevitably results in the release of nanoparticles into the environment. Along their transport through air and (waste)water, potentially attached to soil particles, food or microbes (Westmeier et al. 2018), a part of these nanoparticles will encounter plant or animal tissue. Depending on their exposure route, nanoparticles can reach different external tissues, including the epithelium of skin, leaves, and roots, as well as mucosa of gills, lungs, the mouth, and the gastrointestinal tract. Without any exception, these first-exposed tissues are colonized by microbiota. Hence, it is likely that nanomaterials and microbiota interact at the exposure interface, potentially shaping physiological responses of hosts to nanomaterials. The work presented in this PhD thesis was aimed to unravel via what mechanisms the interactions between hosts, microbiota and nanomaterials affect the safety of nanomaterials to microbially-colonized hosts.

1.2 Nanoscale properties affecting nanomaterial safety

The continued innovation in the field of nano-enabled products and materials offers a valuable opportunity to assess the safety and sustainability of these materials early in the development pipeline. This aligns closely with objectives of the European Union's '*Chemicals Strategy for Sustainability*' (2020), which, as part of the European Green Deal, aims to 'respond more rapidly and effectively to the challenges posed by hazardous chemicals' in the 'transition to chemicals that are safe and sustainable by design' (Doak et al. 2022). Of note, many of the first generation of engineered nanomaterials, including carbon and metal nanoparticles, nanotubes and nanowires, have already entered the market over 15 years ago (Science for Environmental Policy 2017). Currently, newly engineered nanomaterials mainly concern 'smart' nanocomposites and mixtures responding to external stimuli (Mech et al. 2022) and include exotic applications like self-propelled nanorobots (Novotný et al. 2020). Nevertheless, even for first generation nanomaterials, there is still a need for data and insight to be able to mechanistically predict the safety of nanomaterials to animals, humans and the environment, as based on characteristics of the nanoscale. Examples of nanoscale properties that can affect toxicity include the specific morphology (ranging from blunt and spherical shapes, to sharp needle-like shapes), increased reactivity, different or increased mobility, and altered optical, electronic and magnetic properties (quantum effects) of nanomaterials (EFSA Scientific Committee, 2018). Two of such nanoscale properties affecting nanomaterial safety are highlighted in this thesis:

1. *A large surface area that is available for physisorption interactions.*

   A key intrinsic feature of all nanomaterials, is their large surface area resulting from the small size of nanoparticles. Biomolecules that are present in the surrounding of nanomaterials can adsorb onto this surface, forming several either tightly or loosely attached layers termed the *biocorona** (Monopoli et al. 2012; Nasser et al. 2019). The main principles that govern these adsorption interactions, and the potential consequences thereof to nanomaterial safety, are increasingly well understood for proteins that interact with specific targets like receptors (Dawson and Yan 2021). Nevertheless, nanomaterials that are released into the environment, or taken up by a host, are exposed to many other biomolecules. Even in an ideal situation, where the biophysical conditions and biochemical composition of the current and previous surroundings of a nanomaterial have been fully characterized, it is extremely complicated to predict what biomolecules will associate with the nanomaterial surface, for how long, and in what orientation. Yet, this can affect how nanomaterials are recognized by (immune) cells of a host (Walczyk et al. 2010), and can influence the *colloidal stability** of nanomaterials (Gebauer et al. 2012). The latter means that, depending on the chemical composition of the nanomaterial surface, particles will have a different tendency to remain dispersed, or to form agglomerates and aggregates. Considering the consequences of these effects on the immunotoxicity, biodistribution and reactivity of nanomaterials, the uncertainty in the biochemical composition of biocoronae forms one of the main challenges in predicting the effects of nanomaterials mechanistically.

2. *The release of toxic ions from metal nanomaterials in aqueous media.*

   Another challenge in detecting adverse effects for nanomaterials that are specific to the nanoform, is posed by the dissolution of soluble metal and metal oxide nanomaterials in aqueous media. Once dispersed, soluble nanomaterials will release metal ions into the exposure medium. These ions can be toxic at similar or even lower exposure concentrations than the corresponding nanoparticles (Zhai et al. 2016; Yang et al. 2017b; Brun et al. 2018; Sukhanova et al. 2018). Therefore, soluble nanomaterials in aqueous media represent mixtures which can exert toxic effects via their particles, ions, or the combination thereof. In order to determine if the nanoform of a substance contributes to its toxicity, it is necessary to differentiate between the toxicity of

---

* Defined on page 30-31.

> particles (*particle-specific** toxicity) and ions. Due to potential differences in the toxicity mechanisms of particles and ions, the toxicity of their mixture is generally modeled based on the accumulation of responses, rather than based the accumulative particle and ion concentrations (Zhai et al. 2016). Irrespectively, particles and ions often act in concert: ions that are released from particles may exert different toxic effects than ions originating from the corresponding bulk material. A clear example thereof is the 'Troyan horse effect', where nanoparticles first cross a biological barrier that is impermeable to ions, and subsequently release toxic ions from the particle core, or dissociate sorbed molecules from their biocorona, across this biological barrier (EFSA Scientific Committee, 2018).

The work presented in this thesis focuses on gaining mechanistic understanding of the effects of colonizing microbiota on physisorption interactions and particle-specific effects of nanomaterials. These investigations complement previous investigations, which specifically focused on the effects of microbial biotransformations on nanomaterial safety (section 1.3), and the risks of nanomaterial-induced *dysbiosis** (section 1.4). With regard to European nanosafety research, this thesis moreover directly contributes to the project PATROLS (www.patrols-h2020.eu): 'Physiologically-Anchored Tools for Realistic nanomaterial nanOmateriaL Safety testing'. As explained in detail by Doak et al. (2022), this project was aimed at delivering a suite of methods, tools and models that more accurately predict physiological responses to long-term or repeated exposure to low concentrations of nanomaterials. The microbiota-mediated effects that are studied in this thesis, are an example of the physiologically-relevant features and endpoints that were investigated within PATROLS to mimic more realistic exposure scenarios, in order to improve the predictive power of models and test systems.

1.3 Microbiota-mediated biotransformation of nanomaterials

To date, a handful of studies has shown how plant and animal microbiota can chemically transform nanomaterials (Avellan et al. 2018; Yin et al. 2019; Li et al. 2019b; Zheng et al. 2021; Li et al. 2022). As exemplified below, these microbiota-mediated transformations of nanomaterials can have important consequences on the fate and toxicity of nanomaterials.

Focusing on freshwater wetlands, Avellan et al. (2018) showed how microbiota-mediated transformations can affect the dissolution of nanomaterials. Specifically, microbiota associated with the freshwater macrophyte *Egeria densa* facilitated the dissolution of nano gold (nAu) via the formation of hydrogen cyanide. This is remarkable, because the dissolution of nAu is thermodynamically unfavorable under realistic environmental conditions. Thus, microbiota can facilitate the oxidation of otherwise inert metal nanomaterials, changing the bioavailability and toxicity of these materials to biota.

Conversely, microbiota can also aid in the reduction of metal ions, thereby forming metallic nanoparticles. This activity has first been described for bacterial isolates that reduce silver ions (Ag^+) to form nano silver (nAg) (Lin et al. 2014). Interestingly, Yin et al. (2019) later confirmed that members of the human gut microbiota can also exert this activity, demonstrating the relevance of microbially-mediated nAg formation to human health. Because silver is generally considered to be less toxic in its particulate form, this activity may represent a detoxification mechanism against Ag^+.

Alternatively, intestinal microbiota can facilitate sulfidation reactions that transform ions that were shed from nAg into silver sulfide. Li et al. (2019, 2022) inferred this detoxification mechanism for microbiota in the intestines of the water flea *Daphnia magna*. The intestinal microbiota of *D. magna* acquired this protective function, as detected by a higher expression of genes that are involved in sulfate reduction, via changes in the microbiota composition over multiple generations of exposure to nAg. This illustrates how community-level differences in microbiota composition can introduce variability in the exposure dynamics of ingested nanomaterials, affecting the sensitivity of hosts to these materials.

Finally, the work of Zheng et al. (2021) shows how bacterial cell membranes can facilitate the biotransformation of rare-earth metal nanomaterials. Although mineable sources for these metals are uncommon, rare-earth metals are abundant in the Earth crust (Campbell 2014). Moreover, the nanoform of rare earth metals can be applied in many green and high-tech products, including supercapacitors, batteries, sensors and solar cells (Huang and Zhu 2019). Focusing on a representative rare-earth oxide metal nanoparticle, nano lanthanum oxide (nLa_2O_3), Zheng et al. (2021) showed that interactions of nLa_2O_3 with the external membrane of bacteria results in the formation of nano lanthanum phosphate. The reaction disrupted the cell membrane of exposed bacteria via the dephosphorylation of phospholipids. This specifically occurred on the (outer) cell membrane of Gram-negative bacteria, which, as opposed to the cell membrane of Gram-positive bacteria, is not covered by an external peptidoglycan layer. This layer of peptidoglycan can thus protect Gram-positive bacteria against detrimental interactions between nanoparticles and cell membranes. As a consequence, exposure to nLa_2O_3 resulted in a reduced relative abundance of Gram-negative bacteria in bronchoalveolar microbiota of exposed mice. In this way, the microbiota-mediated biotransformation of nanomaterials can contribute to nanomaterials-induced *dysbiosis*,[*] as further described in section 1.4.

---

[*] Defined on page 30-31.

1.4 Nanomaterial-induced dysbiosis

In striking contrast to the limited number of studies reporting effects of microbiota on the chemical biotransformation of nanomaterials (section 1.3), a rapidly increasing number of studies investigated the potential of nanomaterials to induce or cure *dysbiosis*[*] (Fig. 1.1a; Appendix Table S1).

Dysbiosis is a state characterized by an altered abundance of *beneficial microbiota*[*] members, which is often accompanied by increased inter-host variation in microbiota composition (Duperron et al. 2020). It is mostly studied and described for bacterial members of microbiota, whilst other members, like fungi, archaea, protists, microalgae, and viruses, also contribute to host health. Beneficial host-microbiota interactions contribute to the digestion of food and the uptake of nutrients, affect neurobehavioral development, support the defense against pathogens, and prevent oversensitive immune responses. Disturbance of these intricate interactions between hosts and microbiota has been linked to diverse pathologies, including inflammatory bowel disease, obesity, diabetes, kidney disease, cardiovascular disease, autism spectrum disorders and cancer (DeGruttola et al. 2016; Wilkins et al. 2019).

Roughly, the existing research on nanomaterial-induced dysbiosis can be divided into four groups (Fig. 1.1a), which either focus on the safety of nanomaterials to *human and animal health*[*] or *environmental health*[*], including the health of crop species, or focus on the efficacy of fertilizers or nanotherapeutics exerting microbiota-dependent effects. With regard to nanosafety testing, the majority of these investigations focuses on nanoparticles that exhibit antimicrobial activity, like nAg, nano zinc oxide (nZnO) and nano titanium dioxide ($nTiO_2$). These particles, and in particular nAg and $nTiO_2$, are also the most commonly applied particles in industrial consumer products (Eduok and Coulon 2017). Many of the remaining studies focus on nano copper oxide, nano selenium and nano cerium oxide (nanofertilizers), or functionalized carbon, iron and iron oxide nanoparticles (nanosupplements and -therapeutics). Collectively, this body of work demonstrates that nanomaterials can cause shifts in the composition of gut, mouth, lung and rhizosphere microbiota, across a great variety of hosts, including fish, aquatic and terrestrial invertebrates, plants and trees, mice, rats, chicken, pigs, and humans (Fig. 1.1b-d). The exposure routes, exposure duration and exposure concentration applied in these experiments are summarized in Fig. 1.2, and are included in Table S1 of the appendix.

Nanomaterial-induced changes in microbiota composition often coincide with physiological changes in the host. These changes include beneficial effects on host health, such as improved crop growth (Shcherbakova et al. 2017; Dai et al. 2020; Wang et al. 2022), the prevention of diarrhoea among cattle (Xia et al. 2017), and the inhibition of lesions associated with dental caries (Naha et al. 2019; Ostadhossein et al.

2021). However, nanomaterials have also been found to increase the susceptibility of hosts to pathologies that have been related to dysbiosis, such as colitis (Mu et al. 2019) and obesity (Kurtz et al. 2020; Zhu et al. 2021). While these physiological effects might result from changes in microbiota composition, it is often hard to differentiate between the direct effects of nanomaterials on host health, and cascading effects, resulting from nanomaterial-cured or -induced dysbiosis.

Several recent studies addressed the causality between nanoparticle-induced pathologies and changes in microbiota composition using probiotics and fecal microbiota transplants (Li et al. 2019a; Ju et al. 2020; Zhao et al. 2020, 2021). The administration of probiotic *Lactobacillus rhamnosus* GG bacteria, for instance, ameliorated $nTiO_2$-induced intestinal inflammation in juvenile rats (Zhao et al. 2020), and decreased $nTiO_2$-enhanced susceptibility to diet-induced metabolism syndrome in mice (Zhao et al. 2021). Similarly, a probiotic cocktail comprising 11 Lactobacillus strains and 5 Bacteroidetes strains could rescue mice from nano silicon dioxide ($nSiO_2$)-induced lung inflammatory injury (Ju et al. 2020). By contrast, in each of these cases, the inflammatory injury resulting from nanoparticle exposure could also be induced by the administration of fecal microbiota from nanoparticle-exposed individuals.

Likewise, fecal microbiota transplants could reproduce the protective effects of nanomaterials against dysbiosis-related pathologies in two studies on functionalized metal nanoparticles (Deng et al. 2021; Sharma et al. 2022). The first of these studies concerns selenium@albumin complex nanoparticles (nSe@albumin) which offer protection against chemotherapy-associated intestinal mucositis, a common side effect in cancer treatment (Deng et al. 2021). Fecal microbiota transplants from mice exposed to these particles exerted similar protective effects against cisplatin-induced mucositis as nSe@albumin exposure. The second study focused on the protective effect of functionalized gold nanoparticles (nAu), capped with *Cinnamomum verum*-derived bioactives. These particles reduced the susceptibility of mice to high-fat diet induced obesity (Sharma et al. 2022). Similarly, the administration of fecal microbiota obtained from nAu-exposed mice reduced weight gain in healthy mice.

The examples of nanomaterial-induced and -cured pathologies, resulting from nanomaterial-induced changes of microbiota composition, show the importance to consider potential cascading effects due to nanomaterial-induced changes in host-associated microbiota in nanosafety testing.

---

* Defined on page 30-31.

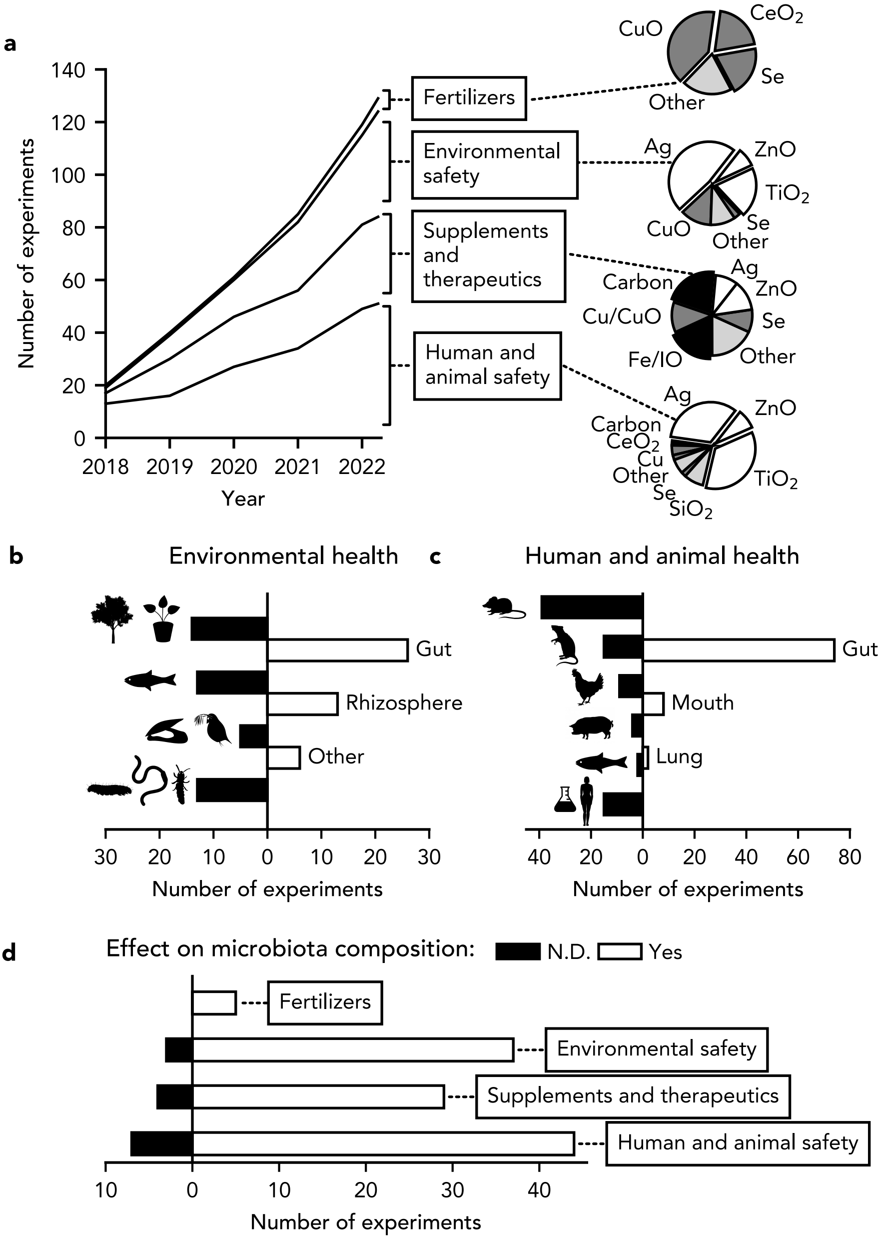

Figure 1.1: *Research investigating the effects of nanomaterials on the composition of host-associated microbiota.* [a] **a**) Accumulative number of studies over time, focused on environmental health ('fertilizers' and 'environmental safety testing') or human and animal health ('supplements and therapeutics' and 'human and animal safety testing'). Pie charts indicate what nanoparticles have been investigated in the concerning studies. Wedge color indicates if particles have mainly ...

[a] Literature was retrieved from the Web of Science Core Collection database, accessed on 27 March 2022 through Leiden University's library, using the search string '(nanomaterial* OR nanoparticle*)' for the title, and the search string '(microbiome OR microbiota)' for the abstract of articles.

… been investigated in relation to nanosafety (white wedges), nanosupplements and -therapeutics (black wedges), nanofertilizers (dark gray wedges) or none of the above (light gray wedges). **b)-c)** Investigated host species (left, black bars) and microbiota type (right, white bars). Host symbols (top-down) depict, for environmental health: plants and trees, fish, aquatic invertebrates (daphnids, flat worms, mussels, and fly larvae) and terrestrial invertebrates (collembolans, earth worms and silk worms); and for human and environmental health: mouse, rat, chicken, pig, fish and human (*in vitro* and model gut systems). **d)** Number of experiments that observed effects (white bars), or no effects (black bars) on microbiota composition. Details of the studies are included in the appendix (Table S1). *Abbreviations*: Ag, silver; CeO_2, cerium dioxide; Cu/CuO, copper/copper oxide; Fe/IO, iron/iron oxide; N.D., not detected; Se, selenium; SiO_2, silicon dioxide; ZnO, zinc oxide.

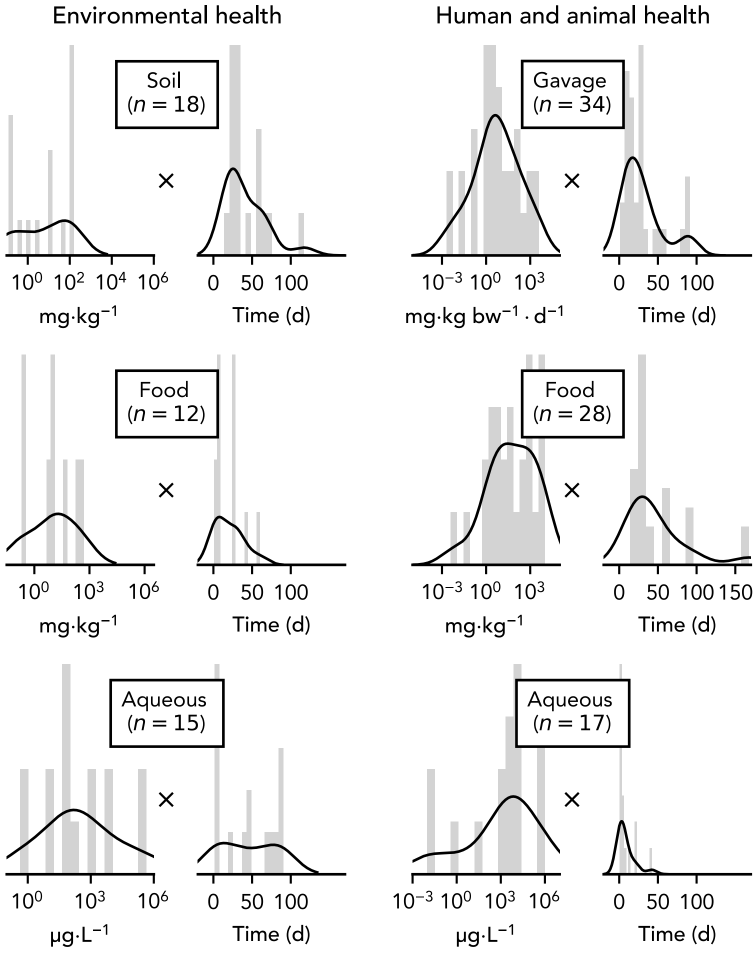

Figure 1.2: *Distribution of the exposure concentration and exposure time applied to investigate potential impacts of nanomaterials on host-associated microbiota.* Density curves and histograms depict distributions for studies concerning environmental health ('nanofertilizers' and 'environmental safety'; left column), and animal and human health ('supplements and therapeutic' and 'human and animal safety'; right column). Rows separate studies applying different exposure routes. Other experimental details are included in Fig. 1.1 and appendix Table S1.

1.5 Research question and aims of this thesis

Given the main focus of microbiota-related nanosafety testing on the chemical biotransformation of nanomaterials (section 1.3) and dysbiosis-related pathologies (section 1.4), the effects of colonizing microbiota on physisorption interactions and the particle-specific toxicity of nanomaterials remain largely unexplored. These topics are investigated in this thesis, by addressing the following research question using a combination of computational methods (section 1.6) and zebrafish larvae experiments (section 1.7):

'What mechanisms govern the physisorption-driven and particle-specific effects of colonizing microbiota on nanomaterial toxicity to microbially-colonized hosts?'

Firstly, **chapter 2** and **chapter 3** of this thesis aim to gain mechanistic understanding of the effects of microbiota-mediated physisorption interactions on nanomaterial safety. To this end, **chapter 2** investigates what metabolites with a microbial origin can be predicted to adsorb onto ingested nanomaterials in the gastrointestinal lumen. In this way, this chapter initiates research on the potential 'microbial fingerprint' of the nanomaterial biocorona. Zooming out to the scale of microbes, **chapter 3** subsequently focuses on the potential of nanoparticles to adsorb onto colonizing microbes. As shown for the physisorption of nanomaterials to pollen, fungal spores (Westmeier et al. 2018) and orally-administered bacteria (Akin et al. 2007; Chen et al. 2021), this can have consequences to the transfer of nanoparticles through ecosystems, and through a host its body.

Secondly, **chapter 4** and **chapter 5** focus on the effects of colonizing microbiota on particle-specific toxicity mechanisms for nanomaterials. To do so, **chapter 4** of this thesis aims to determine if different metal nanomaterials exert particle-specific toxicity in a (partly) microbiota-dependent manner. Subsequently, **chapter 5** aims to unravel if and to what extent signaling pathways for the recognition of microbiota are involved in this particle-specific toxicity.

1.6 Chemoinformatic approaches to study microbiota-mediated physisorption

Computational methods provide a means to study biophysical interactions between microbiota and nanomaterials prior to and in support of more costly laboratory-based experiments. In this thesis, we combine two different chemoinformatic approaches, namely, quantitative structure-activity relationship (QSAR) models and molecular dynamics (MD) simulations. As described below, these techniques differ fundamentally in the way how the chemical properties or biological activity of substances are predicted.

For this reason, these methods can provide complementary insight into the physicochemical properties, biological activity and molecular interactions of substances.

The methodology of QSAR models originates from the work of Corwin Hansch and Toshio Fujita in the early 1960s. They showed how the median toxic concentration of substances can be predicted based on a hydrophobicity term, an electronic term and a steric term (Hansch and Fujita 1964; Gramatica 2008). Each of these explanatory properties can be derived from the chemical structure of the substances. As such, Hansch and Fujita showed that relationships exist between the information that is included in the chemical structure of substances, and their biological activity. Similarly, chemical and physical properties can be predicted based on the chemical structure of substances. In order to derive structure-activity relationships, QSAR models require 'training sets' with substances for which the physical, chemical or biological properties of interest have previously been derived, either experimentally, or using modeling approaches. First, molecular descriptors are computed based on the chemical structure of these substances, using chemoinformatic tools. An overview of available descriptors is given by Grisoni et al. (2018). Next, these descriptors are linked to the physical, chemical or biological property of interest. This can be done using diverse models, ranging from traditional multiple linear regression, to machine learning algorithms like decision trees and artificial neural networks (Gini 2018). Finally, the structure-activity relationships, as given by the models, can be applied to a 'test set', comprising substances that are similar to the training set with respect to the structural features included in the models. Across many different fields, ranging from toxicology to drug discovery, this approach nowadays enables the quantitative prediction of biological, chemical or physical properties of substances based on their chemical structure.

The MD methodology finds its origin in the early 1950s, when Berni Alder and Tom Wainwright had the opportunity to use the spare capacity of a powerful (IBM-704) computer at Lawrence Livermore Laboratories to perform pioneering work on molecular simulations (Battimelli and Ciccotti 2018). In this work, Alder and Wainwright applied physical laws to obtain insight into the motion of hard spheres in a liquid-solid phase transition (Alder and Wainwright 1957). Later on, Martin Karplus and colleagues showed that classical mechanics could also be used to describe the motion of hydrogen atoms in the exchange reaction of H with H_2 (Karplus et al. 1965). This important finding – which contributed to the chemistry Nobel Price in 2013, jointly awarded to Martin Karplus, Michael Levitt and Arieh Warshel – led to the application of physical laws to describe the trajectories of heavier atoms, like carbon, nitrogen and oxygen. Thereby, it created opportunities to obtain molecular information from MD simulations in the study of biological phenomena and in drug design (McCammon et al. 1977; Cheng and Ivanov 2012; Lindahl 2015). Nowadays, the field of

MD simulations includes diverse specializations. We refer the interested reader to in-depth literature on such specializations, enabling, for instance, the simulation of the formation and breakup of chemical bonds (Senftle et al. 2016; Behler 2017), or the simulation at coarser spatial and temporal scales (Barnoud and Monticelli 2015; Vassaux et al. 2020).

1.7 Zebrafish larvae as a model host

Zebrafish larvae are widely adopted as a model organism for research in the fields of developmental biology, ecotoxicology, pharmacology, oncology and immunology. Advantages of zebrafish larvae that are employed within these research areas include their ease of handling, short generation time, high fecundity, *ex vivo* development, transparent eggs and larvae, and many (>70%) human ortholog genes (Howe et al. 2017). Additionally, there are many valuable resources available for zebrafish research, including a rich collection of scientific literature and protocols (https://zfin.org; 'ZFIN Protocol Wiki'), standardized toxicity tests (OECD Test No. 236 'Fish Embryo Acute Toxicity Test'), and transgenic reporter lines and mutants. The ease to derive germ-free zebrafish larvae, available procedures that allow for the (re)colonization of larvae by microbes of interest (Pham et al. 2008), and the possibility to track live microbes *in vivo* using imaging techniques (Stephens et al. 2015; Wiles et al. 2016; Koch et al. 2018), moreover support the use of zebrafish larvae in microbiota research.

Several developmental transitions mark important colonization phases for early life stages of *teleost fish** (Llewellyn et al. 2014) like zebrafish (Fig. 1.3). The first microbes that colonize their tissues, occur on the outer membrane of zebrafish eggs (the *chorion**). Presumably, part of these early colonizers are transferred vertically, that is from parental fish, along the passage of eggs through the oviduct. Additional microbes that colonize the eggs are horizontally acquired from the environment of the eggs. Around two days following external fertilization, zebrafish *larvae** hatch from their eggs. Since it is assumed that chorion microbes cannot pass the chorion membrane, this time of hatching most likely marks the onset of the colonization of larvae. Microbes first colonize the external tissues of larvae, such as skin and gill mucosa. Later on, when larvae open their mouth (~3 days post-fertilization (dpf)) and start feeding independently (~5 dpf), microbes colonize their gastrointestinal tracts (Llewellyn et al. 2014). The core composition of zebrafish microbiota, which varies across development, and is taxonomically distinct, but functionally conserved in comparison to mammalian microbiota, has been studied extensively by Roeselers et al. (2011), Stephens et al. (2016) and Gaulke et al. (2020). Of note, from 6 dpf onwards, the use of zebrafish larvae for animal experimentation is restricted by European legislation (EU Animal Protection

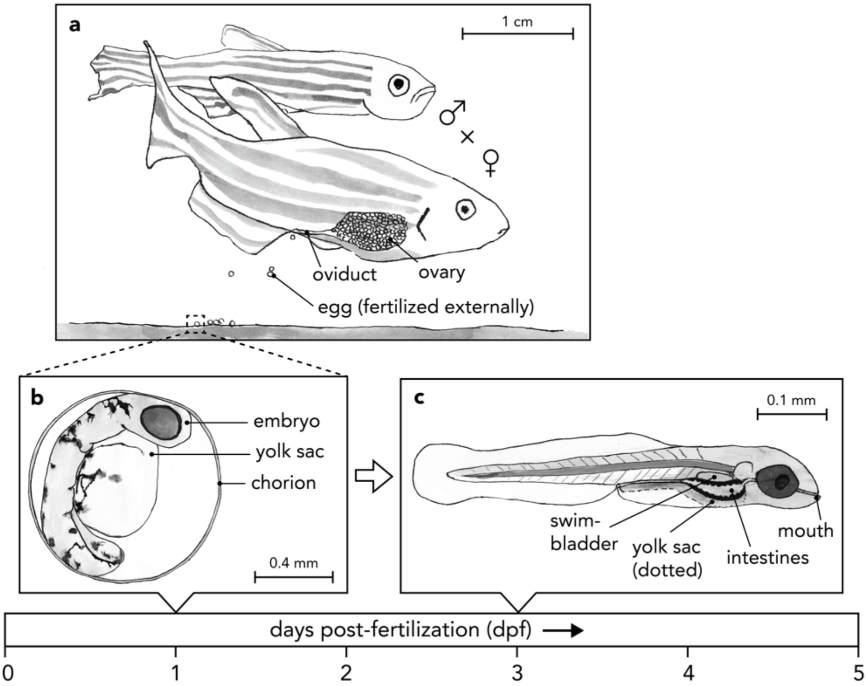

Figure 1.3: *Early zebrafish development with relevant structures for microbial colonization.* **a**) Mating zebrafish females release eggs from their ovaries via the oviduct into the water column. Maternal microbes that stick onto the chorion membrane of released eggs may be transferred to the offspring (vertical colonization). **b**) Following external fertilization, zebrafish embryos develop *ex vivo* inside of the protective chorion of eggs. Microbes from the water column further colonize the chorion (horizontal colonization). It is assumed that microbes cannot pass the chorion membrane. **c**) Around 2 days post-fertilization (dpf), larvae hatch from zebrafish eggs. Microbes from the chorion and water column can colonize the skin and gill tissues of larvae. Once larvae open their mouth at 3 dpf, microbes start to colonize intestinal epithelia. Around 5 dpf, larvae do no longer feed on the yolk sac, and start feeding independently. This facilitates the further development of the intestinal microbiota.

Directive 2010/63/EU), in support of the 3R's aim to Reduce, Refine and Replace animal experimentation. This means that zebrafish larvae are generally studied in the absence of diet-induced variation in microbiota composition.

In addition to the above milestones for microbial colonization, distinct phases in the maturation of the zebrafish immune system can influence the toxicity of nanomaterials. Primitive macrophages and neutrophils are formed in zebrafish embryos during the first day of development, around 15 and 18 hours post-fertilization (hpf), respectively (Herbomel et al. 1999). Neutrophils become mature from 24 to 48 hpf (Bennett et al. 2001; Lietschke et al. 2001). In the meantime, around 26 hpf, the blood circulation starts. Maturation of the adaptive immune system takes considerably longer

---

* Defined on page 30-31.

(up to 4-6 weeks) (Lam et al. 2004), offering the opportunity to study innate immune responses in isolation of the adaptive immune system.

In this thesis, we employ the advantages of zebrafish larvae for (eco)toxicological investigations and microbiota research. **Chapter 3** focuses on zebrafish colonizing microbiota at the earliest stage of colonization, on the chorion membrane. **Chapter 4** and **chapter 5** focus on later stages including early colonization of the intestinal mucosa (3-5 dpf-old larvae). Larvae of this life stage are also used for studying physiological responses to nanoparticles in the presence of a functional innate immune system. In **chapter 3** and **chapter 5**, the transparency of zebrafish embryos and larvae allows for the localization of nanoparticles, microbes and physiological responses in and on embryos and larvae. In **chapter 4**, available protocols for the derivation of germ-free zebrafish larvae are optimized for nanosafety testing, thereby providing a method to detect microbiota-dependent and particle-specific nanomaterial toxicity. Finally, in **chapter 5** this method is applied in combination with several available zebrafish mutant lines, to test the contribution of specific elements of signaling pathways to microbiota-dependent nanomaterial toxicity.

1.8 Outline of this thesis

This thesis consists of six chapters. Each of the four research chapters, following on this general introduction of **chapter 1**, investigates the interactions between hosts, microbiota and nanoparticles from a different viewpoint. The final chapter discusses the implications of the obtained knowledge to human and environmental nanomaterial safety testing, focusing on different actors and common strategies in the field of nanotoxicology.

Chapter 2 investigates the potential of biomolecules that originate from intestinal microbiota to adsorb to different carbon and metal nanomaterials. First, a concise overview of microbial metabolites that are available for these physisorption interactions is generated. Subsequently, the adsorption affinity for these metabolites is predicted statistically, using QSAR models, and computationally, using MD simulations. Finally, key interaction types for these physisorption interactions, derived using both methods, are compared and discussed in relation to the biological functions of the concerning metabolites.

Chapter 3 focuses on adsorption interactions between $nTiO_2$ and microbes that occur on the chorion of zebrafish eggs. The abundance of sorbed particles and microbes on the chorion is examined in relation to the potential of particles to reach internal (embryonic) structures. Different imaging techniques are combined, including two-photon microscopy, confocal microscopy and particle-induced X-ray emission analysis.

The effects of $nTiO_2$ on colonizing microbiota of zebrafish eggs, and potential cascading effects on microbiota of hatched larvae, are assessed in terms of microbiota abundance and functional composition.

Chapter 4 optimizes protocols for the derivation of germ-free zebrafish larvae for nanosafety testing, to test whether nAg and nZnO exert microbiota-dependent, particle-specific toxicity. The response addition model is applied to quantify the particle-specific contributions to toxicity. Additionally, the antimicrobial activity of nAg and nZnO is quantified *in situ*, and nAg-resistant microbes are isolated and identified from exposed larvae.

Chapter 5 combines the germ-free methods of **chapter 4**, in combination with available mutant lines, to explore how components of the Toll-like receptor signaling pathway, involved in the recognition of commensal microbiota, affect nAg toxicity. To gain further mechanistic understanding of these identified effects of colonizing microbiota on nAg toxicity, the accumulation of silver in larvae and in intestinal tissue is quantified over the exposure time, and related pro-inflammatory responses are localized using a transgenic zebrafish line.

Chapter 6 concludes with a general discussion on relevant interactions between particles, colonizing microbiota and hosts in nanosafety testing, as studied in **chapter 2-5**. This final chapter elaborates on the observed influence of colonizing microbiota on particle-specific exposure scenarios, and the microbiota-dependent sensitivity of hosts to nanomaterials. The obtained mechanistic insight is discussed in relation to overarching objectives in the field of (nano)safety testing, including the prediction of chronic effects, the application of read-across, and the use of conserved pathways for cross-species extrapolation. The chapter concludes with recommendations for a transition to rapid and effective microbiota-inclusive nanosafety testing.

Definitions

Beneficial microbiota

A community of microbes that colonizes a specific habitat, including host tissue, with a positive influence on environmental, human or animal health (see below).

Biocorona (plural *biocoronae*)

The collection of biomolecules that forms both tightly and loosely attached layers onto the surface of nanomaterials. Biocoronae can be termed *ecocoronae* when they are formed by biomolecules from the external environment of organisms.

Chorion

Outer protective envelope surrounding the developing embryo in eggs of reptiles, birds, mammals, cephalopods (squids, octopuses, cuttlefish, etc.), pterygotan (i.e. winged or secondarily wingless) insects and teleost fish (see below).

Colloidal stability

The extent to which particles in aqueous media remain dispersed. The higher the colloidal stability of particles, the more these particles will remain dispersed, and the lower the tendency of these particles to form agglomerates and aggregates.

Embryo

The earliest life stage of plants animals, which, in case of oviparous animals, develop inside of the protective envelopes of an egg from the moment of fertilization up to the time of hatching.

Dysbiosis

A state where microbiota do no longer have a positive influence on environmental, human or animal health (see below). In comparison to beneficial microbiota, dysbiosis is characterized by the altered abundance of beneficial microbes and/or by increased variation in microbiota composition between different individuals of the same host.

Environmental health

Within the context of this thesis: the productivity, sustainability and biodiversity of ecosystems and agricultural land, as studied in relation to the intentional or coincidental release of nanofertilizers and other nanomaterials into the environment.

Human and animal health

Within the context of this thesis: the maintenance of biophysical homeostasis and the absence of disease in animals including humans, as studied in relation to the application or coincidental exposure to nanopharmaceuticals, nanosupplements, or other nanomaterials.

Larva (plural *larvae*)

An early life stage of animals prior to metamorphosis into the adult life stage. For oviparous animals, the time of hatching marks the onset of the larval life stage.

Microbial ecotoxicology

According to Ghiglione et al. (2016): ‘a branch of science that studies both

(i) the ecological impacts of chemical (synthetic or natural origin) or biological (toxic species) pollution at the microbial scale and the various functions that they ensure in the ecosystems and

(ii) the role of microbial communities in the ecodynamic of the pollutants (source, transfer, degradation, transformation).’

Microorganism (or shortly, *microbe*)

An organism that is invisible to the naked eye.

Nanomaterial

A material consisting for at least 50% of its particle count out of nanoparticles (see below).

Nanoparticle

Any particle with at least one dimension within the range of 1 to 100 nm, and any particle with a specific-surface area exceeding 60 $m^2 \cdot cm^{-3}$.

Particle-specific

Describing properties, phenomena and effects that result from the presence of particles of a certain material, rather than from the release of ions from this material.

Teleost fish

Evolutionary lineage comprising diverse ray-finned fish, including zebrafish, that can extend their jaw outwards from the mouth owing to their movable premaxilla.

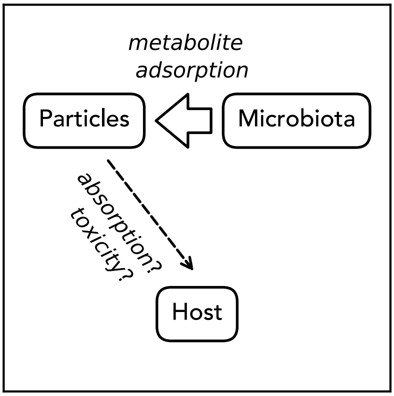
metabolite adsorption
Particles
Microbiota
absorption?
toxicity?
Host

CHAPTER 2

Predicted adsorption affinity for enteric microbial metabolites to metal and carbon nanomaterials

Bregje W. Brinkmann
Ankush Singhal
G.J. Agur Sevink
Lisette Neeft
Martina G. Vijver
Willie J. G. M. Peijnenburg

Published in *Journal of Chemical Information and Modeling*, 62: 3589-3603 (2022).
DOI: 10.1021/acs.jcim.2c00492
Data is available via *Zenodo*. DOI: 10.5281/zenodo.6800734

Abstract

Ingested nanomaterials are exposed to many metabolites that are produced, modified or regulated by members of the enteric microbiota. The adsorption of these metabolites potentially affects the identity, fate and biodistribution of nanomaterials passing the gastrointestinal tract. Here, we explore these interactions using *in silico* methods, focusing on a concise overview of 170 unique enteric microbial metabolites which we compiled from the literature. First, we construct quantitative structure-activity relationship (QSAR) models to predict their adsorption affinity to 13 metal nanomaterials, 5 carbon nanotubes and 1 fullerene. The models could be applied to predict log *k* values for 60 metabolites, and were particularly applicable to 'phenolic, benzoyl and phenyl derivatives', 'tryptophan precursors and metabolites', 'short-chain fatty acids' and 'choline metabolites'. The correlations of these predictions to biological surface adsorption index descriptors, indicated that hydrophobicity-driven interactions contribute most to the overall adsorption affinity, while hydrogen-bond interactions and polarity/polarizability-driven interactions differentiate the affinity to metal and carbon nanomaterials. Next, we use molecular dynamics (MD) simulations to obtain direct molecular information for a selection of vitamins that could not be assessed quantitatively using QSAR models. This showed how large and flexible metabolites can gain stability on the nanomaterial surface via conformational changes. Additionally, unconstrained MD simulations provided excellent support for the main interaction types identified by QSAR analysis. Combined, these results enable assessing the adsorption affinity for many enteric microbial metabolites quantitatively and support the qualitative assessment of an even larger set of complex and biologically relevant microbial metabolites to carbon and metal nanomaterials.

Keywords: Gut microbiota; Nanoparticles; Biomolecular corona; Molecular dynamics simulation; QSAR.

2.1 Introduction

The gastrointestinal tract harbors a dense community of viruses, archaea, bacteria, fungi and protozoa, collectively termed the enteric microbiota. In humans, the enteric microbiota constitute a similar order of magnitude of cells as all host cells combined (Sender et al. 2016). Altogether, these enteric microbiota members have been estimated to comprise nearly a factor 1000 more genes than the host (Tierney et al. 2019). Using this large set of genes, enteric microbes compete and cooperate with one another (Coyte et al. 2019), and interact with the host (Ruan et al. 2020). As part of all of these interactions, enteric microbes produce and excrete, modify and regulate metabolites. Many of these metabolites become available in the intestinal lumen, where they function as antimicrobial agents, signaling molecules and substrates (Krautkramer et al. 2021).

For over a decade, biomolecules have been shown to play a key role in the behavior and toxicity of engineered nanomaterials (ENMs) (Nel et al. 2009; Chen and Riviere 2017). Many biomolecules, and proteins in particular, have been found to associate with the large surface area of ENMs, forming a shell of biomolecules referred to as the 'biomolecular corona' (Monopoli et al. 2012) or 'ecological corona' (Nasser et al. 2019) from a biomedical or ecological perspective, respectively. By changing or masking the surface properties of ENMs, biocoronae can affect the colloidal stability (Gebauer et al. 2012) and identity (Walczyk et al. 2010) of ENMs. The principles that govern the biocorona-mediated recognition of ENMs are increasingly well understood (Dawson and Yan 2021). Nevertheless, environmental metabolites, including many other metabolites than proteins, affect the biodistribution and toxicity of ENMs in a yet unpredictable fashion.

When ENMs are ingested, they will be exposed to the myriad of enteric microbial metabolites that are available in the intestinal lumen. Consequently, they may acquire enteric microbial metabolites in their biocoronae. Several specific interactions between microbial metabolites, the ENM surface, and biological membranes and receptors have already been found to affect the fate and biodistribution of ENMs. In bacterial cultures, for example, bacterial flagellin was found to reduce the colloidal stability of nanosilver, thereby decreasing its antimicrobial activity (Panáček et al. 2018). Furthermore, conjugation of latex nanoparticles with invasin, a bacterial surface protein, has been shown to facilitate the uptake of these particles across the intestinal epithelium of rats (Hussain and Florence 1998). Other research investigating the interactions of microbial metabolites with ENMs mostly focused on complex mixtures of environmentally relevant biomolecules, such as extracellular polymeric substances (Fulaz et al. 2019), or employed the properties of specific microbial biomolecules to develop ENMs that function as biosensors or nanocarriers (Yan et al. 2008; Chen et al. 2014a; Thepphankulngarm et al. 2017). Less specific physisorption processes between enteric microbial metabolites and ENMs, that do not concern specific interaction targets, like receptors, and include other metabolites than proteins, have barely been investigated. Here, we focus on the potential contribution of this understudied set of enteric microbial metabolites to biocorona formation onto ingested ENMs in the intestinal lumen.

In the present study, we construct models and generate data to initiate the assessment of the role of enteric microbial metabolites in biocorona formation onto ingested ENMs. Firstly, we compile a concise overview and categorization of metabolites that are available in the intestinal lumen for biocorona formation. This is based on a literature review. Subsequently, we employ the biological surface adsorption index (BSAI) theory to construct a set of quantitative structure-activity relationship (QSAR) models to predict adsorption affinities for enteric microbial metabolites to various metal and carbon ENMs. In addition to this statistical approach to studying nano-bio interactions at low computational cost, we perform a computationally-demanding free-energy analysis based on molecular dynamics (MD) simulations. For these investigations based on physical modeling, we focus on a selection of vitamins that cannot be assessed using current QSAR models, to obtain direct molecular information on characteristics of nano-bio interactions that need to be considered for these microbial metabolites. Ultimately, this could be used to improve current QSAR models. Additionally, through a combination of QSAR investigations and classical and unconstrained MD simulations, we explore what interaction types are key to the adsorption of enteric microbial metabolites to metal and carbon ENMs. Overall, we anticipate that the results of these investigations support the qualitative and quantitative assessment of biologically relevant adsorption interactions between enteric metabolites and ingested ENMs.

2.2 Results and discussion

2.2.1 Inventory of enteric microbial metabolites

We base this study on a literature search, generating a concise overview of metabolites that are produced or regulated by gastrointestinal microbiota. Ten reviews on intestinal microbial metabolism were selected for this inventory (Ruan et al. 2020; Defaye et al. 2020; Douglas 2020; Fiori et al. 2020; Martin et al. 2020; Sauma and Casaccia 2020; Shah et al. 2020; Silva et al. 2020; Wu et al. 2020; Xing et al. 2020), following the procedure described in the Methods section. This led to a total of 170 unique enteric microbial metabolites. These microbial metabolites were assigned to 13 different functional or structure-based metabolite categories, adopting the categorization conventions from the cited literature. The metabolite categories (with abbreviations specified between brackets) included 'microbe-associated molecular patterns (MAMPs)', 'vitamins', 'short-chain fatty acids (SCFAs)', 'primary bile acids (PBAs)', 'secondary bile acids (SBAs)', 'conjugated bile acids (CBAs)', 'tryptophan precursors and metabolites (Tryptophan)', 'polyamines', 'choline metabolites (Choline)', 'neurotransmitters', 'lipids and lipid precursors (Lipid)', 'phenolic, benzoyl and phenyl derivates (Phenolic)', and 'proteins/enzymes' (Table 2.1). Most of the identified enteric microbial metabolites were categorized as 'phenolic, benzoyl and phenyl derivates' (24 metabolites), followed by 'MAMPs' (23 metabolites) , 'tryptophan precursors and metabolites' (17 metabolites), 'SBAs' (16 metabolites), 'lipids and lipid precursors' (13 metabolites), 'proteins/enzymes' (12 metabolites), 'vitamins' (11 metabolites), 'SCFAs' (8 metabolites), 'CBAs' (7 metabolites), 'neurotransmitters' (6 metabolites), 'choline metabolites' (6 metabolites), 'polyamines' (4 metabolites), and 'PBAs' (2 metabolites). Acetylcholine and 5-hydroxytryptamine were assigned to the categories 'tryptophan precursors and metabolites' and 'neurotransmitters'. The remaining 21 metabolites that had not been assigned to any of these categories, were listed as 'Other'.

Given the large metabolic potential and high intra- and interindividual variation of the enteric metabolome (Tierney et al. 2019), the actual set of available enteric microbial metabolites is likely large and diverse. In order to decide if the selected reviews represent an adequate proportion of this diversity in available enteric microbial metabolites, we determined the percentage of new metabolites that were identified with including increasing numbers of reviews in the inventory (Fig. 2.1). The first three reviews that were included (Defaye et al. 2020; Douglas 2020; Shah et al. 2020), reported 80.5 % (137 metabolites) of the 170 identified microbial metabolites. The next two reviews that were included (Ruan et al. 2020; Xing et al. 2020), contributed 14.1 % (24 metabolites) of the total number of unique metabolites, and the final five reviews (Fiori et al. 2020; Martin et al. 2020; Sauma et al. 2020; Silva et al. 2020; Wu et al. 2020) contributed only 5.3 % (9 metabolites) of the total number of identified metabolites. This saturation in the total number of identified metabolites suggests that sufficient reviews were included in the inventory. Moreover, the metabolites included in the first three reviews represented all of the 13 metabolite categories. This may result from the conserved functional capacity of the enteric metabolome (Tian et al. 2020), and predicts that any metabolite that is not included in the inventory, will likely be functionally and structurally equivalent to the metabolites included in our study. For this reason, we decided that the 170 considered metabolites represented sufficient diversity in enteric microbial metabolites for our further analyses.

Table 2.1: Overview of the enteric microbial metabolites included in this study.

Category	*Metabolites*	*Description*
Microbe-associated molecular patterns	N-formylated peptides, lipoteichoic acid, peptidoglycan, lipopeptides, lipopolysaccharides, glucans, mannans, chitins, capsular polysaccharides, muramyldipeptide	Conserved components of microbial cells that can elicit innate immune responses upon recognition by pattern-recognition receptors.
Vitamins	menaquinone-4, cobalamin, biotin, folate, thiamine, riboflavin, pyridoxine, niacin, pantothenic acid, 5,10-methenyltetrahydropteroylglutamate, mono-/polyglutamylated folate.	B vitamins (B1-3,5,6,8,9,12), vitamin K2 and vitamin H. Organic micronutrients that are essential to the host, but cannot be synthesized by the host.
Short-chain fatty acids	acetic acid, propionic acid, 2-methylpropionic acid, butyric acid, isobutyric acid, hexanoic acid, valeric acid, isovaleric acid, methylbutyric acid	Fatty acids with fewer than six carbon atoms that are produced by gut microbiota in the colon from indigestible fibers, which subsequently can be adsorbed by the host.
Primary bile acids	cholic acid, chenodeoxycholic acid	Cholesterol-derived molecules that are synthesized in the liver, secreted into the duodenum following conjugation with glycine or taurine residues, and resorbed in the ileum.
Secondary bile acids	12-dehydrocholate, 7-ketodeoxycholic acid, 7-dehydrochenodeoxycholate, 3-dehydrocholic acid, 3-dehydrochenodeoxycholic acid, isocholic acid, isochenodeoxycholic acid, lithocholic acid, deoxycholic acid, allolithocholic acid, allodeoxycholic acid, ursocholic acid, ursodeoxycholic acid, hyocholic acid, hyodeoxycholic acid, 7-oxolithocholic acid	Bile acids synthesized from primary-bile acids by gut microbiota in the colon. Functions of bile acids include the elimination of cholesterol, the emulsification of lipophilic vitamins and modulation of immune responses. Bile acids can interact with Farnesoid X receptor and G-protein coupled bile-acid receptor 1.
Conjugated bile acids	taurocholic acid, glycocholic acid, taurohyocholic acid, taurochenodeoxycholic acid, glycochenodeoxycholic acid, glycodeoxycholic acid, taurodeoxycholic acid	Amphiphatic molecules that are derived from primary and secondary bile acids in the liver following conjugation with glycine or taurine residues.
Tryptophan precursors and metabolites	N-acetyltryptophan, indoleacetic acid, indoleacetylglycine, indole, indoxyl sulfate, indole-3-propionic acid, melatonin, melatonin 6-sulfate, 5-hydroxyindole, 5-hydroxytryptamine, indoleacrylic acid, indoleethanol, tryptamine, 3-methylindole, indole-3-carboxylate, acetylcholine	Small indole-based molecules, synthesized from the amino acid tryptophan, acquired through digestion of dietary protein in the small intestines. Many tryptophan metabolites can interact with the aryl hydrocarbon (AhR) receptor, affecting immunity, tissue regeneration and intestinal barrier integrity.
Polyamines	putrescine, cadaverine, spermidine, spermine	Organic polycationic molecules comprising three or more amino groups. Polyamines can interact with negatively charged molecules such as DNA, RNA and proteins.
Choline metabolites	methylamine, dimethylamine, trimethylamine, trimethylamine-N-oxide, dimethylglycine, betaine	Small, water soluble metabolites of choline, some of which are associated with cardiovascular disease and atherosclerosis.
Neurotransmitters	5-hydroxytryptamine, noradrenaline, gamma-aminobutyric acid, dopamine, norepinephrine, acetylcholine, histamine, 5-hydroxytryptamine	Metabolites that can transmit signals from neurons to adjacent target cells by binding synaptic receptors.

Phenolic, benzoyl and phenyl derivatives	benzoate, hippurate, phenylacetate, phenylpropionate, 3-hydroxycinnamate, 2-hydroxyhippurate, 3-hydroxyhippurate, 2-hydroxybenzoate, 3-hydroxybenzoate, 4-hydroxybenzoate, 4-hydroxyphenylacetate, 3-hydroxyphenylpropionate, 4-hydroxyphenylpropionate, 3,4-dihydroxyphenylpropionate, 4-cresol, 4-cresyl sulfate, 4-cresyl glucuronide, phenylacetylglutamine, phenylacetylglycine, phenylpropionylglycine, cinnamoylglycine, 4-ethylphenyl sulfate, phenol, s-equol	Aromatic molecules, not designated to any of the above categories, containing one or multiple phenol, benzoyl or phenyl groups.
Lipids and lipid precursors	sphingomyelin, cholesterol, phosphatidylcholine, phosphoethanolamines, triglycerides, sphingolipids, linoleic acid, caproic acid, endocannabinnoids	Fats and fatty acids, phospholipids and steroids which cannot be designated to any of the above categories.
Proteins/ enzymes	microbial anti-inflammatory molecule, bacteriocins, α-haemolysin, Amuc_1100, serine protease, serpins, lactocepin	Large biomolecules comprising one or multiple polypeptide chains, i.a. functioning as anti-inflammatory agents, toxins, proteases and protease inhibitors.
Other	methanol, ethanol, formate, succinate, lysine, glucose, urea, α-ketoisovalerate, creatine, creatinine, imidazole propionate, hydrogen peroxide, reactive aldehyde, quorum sensing molecules, D-lactate, mycolactone	Molecules that cannot be classified in any of the above metabolite categories.

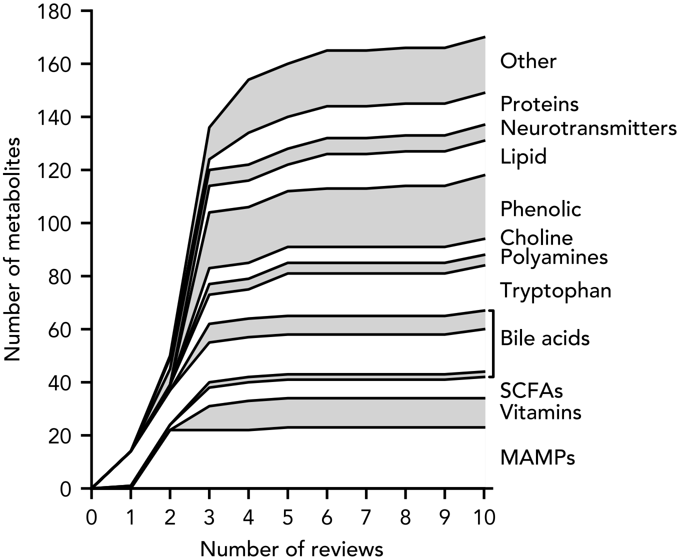

Figure 2.1: *Total number of unique enteric microbial metabolites identified upon including increasing numbers of reviews in the inventory.* Primary bile acids ('gray'), secondary bile acids ('white') and conjugated bile acids ('gray') are stacked (bottom-up).

2.2.2 QSAR models for log k predictions

In the next two parts of our study, we investigate the adsorption affinity of the identified enteric microbial metabolites (Table 2.1) to metal and carbon ENMs using QSAR models and MD simulations. Proteins were excluded from these analyses, because their three-dimensional folding properties require different physical modeling approaches. For the QSAR models, we focus on the 19 ENMs that have been characterized by Chen et al. (2014b), including 13 metal ENMs, 5 carbon nanotubes and 1 fullerene (Table 2.2). The core materials of the metal ENMs include aluminum hydroxide oxide (AlO(OH)), silver (Ag), barium sulfate ($BaSO_4$), silicon dioxide (SiO_2), titanium dioxide (TiO_2), zinc oxide (ZnO), and zirconium(IV)oxide (ZrO_2).

Table 2.2: Overview of the nanomaterials included in the present study. a)

Type	*Name*	*Core material*	*Surface coating*	*Diameter (nm)* b)	*Length (μm)* b)	*SSA (m^2/g)* c)
Metal nano-material	AlOOH	AlO(OH)	None	37	NA	47
	TiO_2_NM105	TiO_2	None	21	NA	51
	ZnO_NM110	ZnO	None	80	NA	12
	SiO_2_Amino	SiO_2	Amino groups	15	NA	200
	SiO_2_Phosphat	SiO_2	Phosphate	15	NA	200
	Ag200_PVP	Ag	Polyvinylpropylene	134	NA	4.5
	$BaSO_4$_NM220	$BaSO_4$	Polymer	32	NA	41
	Ag50_Citrat	Ag	Citrate	20	NA	30
	SiO_2_Naked	SiO_2	None/hydroxyl	15	NA	200
	ZrO_2_Amino	ZrO_2	Amino groups	10	NA	105
	ZrO_2_TODacid	ZrO_2	Trioxadecanoic acid	9	NA	117
	ZrO_2_PEG	ZrO_2	Polyethyleneglycol (PEG600)	9	NA	117
	SiO_2_PEG	SiO_2	Polyethyleneglycol (PEG500)	15	NA	200
Multi-walled carbon nanotube	sMWCNT	Carbon	None	8-15	0.5-2	95
	MWNT_OH	Carbon	Hydroxyl (3.7 % wt -OH)	8-15	~50	95
	MWNT	Carbon	None	8-15	~50	95
	MWNT_COOH_ 20nm	Carbon	Carboxyl (2 % wt -COOH)	10-20	10-30	95
	MWNT_COOH_ 50nm	Carbon	Carboxyl (0.73 % wt -COOH)	30-50	10-20	95
Fullerene	FullrC60	Carbon	None	1	NA	98

a) Reprinted (adapted) with permission from Chen et al. (2014b). Copyright (2014) American Chemical Society; b) Dimensions refer to the primary particle size of nanomaterials. The outer diameter of carbon nanotubes is indicated; c) SSA, specific surface area.

We consecutively apply two QSAR models for each of the ENMs to predict log *k* values. The first model that we apply is the BSAI model established by Xia et al. (2010), which uses Abraham's molecule descriptors [*E,S,A,B,V*] and corresponding nanodescriptors [*r,p,a,b,v*] to predict the adsorption affinity for biomolecules to ENMs following:

$$\log k_i = c + E_i \cdot r + S_i \cdot p + A_i \cdot a + B_i \cdot b + V_i \cdot v, \qquad i = 1, 2, 3, \ldots, n \qquad \text{(eq 2.1)}$$

where c is the adsorption constant; E_i is the excess molar refraction; S_i is the effective solute dipolarity and polarizability; A_i is the effective solute hydrogen-bond acidity; B_i is the effective solute hydrogen-bond basicity; V_i is the McGowan characteristic volume; and n is the number of biomolecules included. The nanodescriptors [*r,p,a,b,v*] weigh the contributions of interactions between biomolecules and the ENM surface resulting from lone-pair electrons ($E_i \cdot r$), polarity/ polarizability ($S_i \cdot p$), hydrogen-bond acidity ($A_i \cdot a$), hydrogen-bond basicity ($B_i \cdot b$), and hydrophobicity ($V_i \cdot v$). We adopted the nanodescriptors derived by Chen et al. (2014b), which have been corrected for the effects of interactions between probe molecules, using Langmuir model extrapolations.

We applied the BSAI model (eq 2.1) to a set of molecules (~2000 molecules) for which the required Abraham's molecule descriptors [*E,S,A,B,V*] have been determined experimentally (Bradley et al. 2014). However, these molecules only include 18 out of the 170 enteric microbial metabolites. Because open-source toolkits for cheminformatics such as Chemistry Development Kit (CDK; http://cdk.github.io/) and RDKit (https://www.rdkit.org) cannot derive Abraham's molecule descriptors from the molecular structure of the metabolites, we used the log *k* predictions from the BSAI model to build a second QSAR model for each of the ENMs. We exclusively used molecular descriptors from CDK as the descriptors for these second QSAR models. As a result, these models could be applied to predict log *k* values based on the molecular structure of enteric microbial metabolites. In the remainder, we refer to the two QSAR models as 'BSAI models' (eq 2.1), and 'CDK models' (Table 2.3, Table S7 and Table S9). Furthermore, we refer to nanodescriptor 'r' as 'r_e', and to nanodescriptor 'p' as 'p_s', to avoid confusion with the Pearson correlation coefficient (r) and statistical p-values, respectively. The subscripts for these nanodescriptors were selected based on their corresponding Abraham molecule's descriptors *E* and *S*.

Since the CDK models only function as a means to apply BSAI models to molecules without known Abraham's molecule descriptors, we omit a detailed discussion of the descriptors that are included in CDK models (Table S2). Nevertheless, it is worth noting that the first descriptor in all models (*ALogP*, *XLogP*, *AMR* and *ATSp1*), explaining most of the variance in log *k* predictions, correlates with the Abraham's molecule descriptor V ($\rho = 0.66$, 0.60, 0.96, and 0.90, respectively, $p<0.001$; Fig. S1). This is consistent with the large contribution of Abraham's molecule descriptor V in BSAI models (Xia et al. 2010), and reflects the importance of interactions between hydrophobic sites of biomolecules and hydrophobic regions on the ENM surface. Xia et al. confirmed this experimentally for MWCNTs, obtaining a significant correlation between the $\log k$ measurements for probe compounds and their $\log K_{o/w}$ values (Xia et al. 2010).

Table 2.3: CDK models for the prediction of the $\log k$ adsorption affinity of metabolites to metal and carbon nanomaterials.

ENM	*Model*	R^2_{train} a)	$R^2_{validate}$ a)	*AD* b)
Ag50_Citrat	$\log k \sim 2.39+ 0.40\cdot \mathit{ALogP} - 0.54\cdot \mathit{Fsp3} + 0.37\cdot \mathit{khs.sOH} - 0.04\cdot \mathit{WTPT.4} - 0.004\cdot \mathit{ATSm1}$	0.82	0.83	0.94
Ag200_PVP	$\log k \sim 2.63 + 0.30\cdot \mathit{ALogP} + 0.32\cdot \mathit{khs.sOH} - 0.01\cdot \mathit{nAtom} - 0.25\cdot \mathit{Fsp3} + 0.22\cdot \mathit{nAcid}$	0.71	0.77	0.93
AlOOH	$\log k \sim 1.79 + 0.49\cdot \mathit{ALogP} + 0.45\cdot \mathit{nHBDon} - 0.57\cdot \mathit{Fsp3} + 0.004\cdot \mathit{ATSm1} - 0.41\cdot \mathit{nBase}$	0.83	0.84	0.93
$BaSO_4$	$\log k \sim 1.73 + 0.30\cdot \mathit{ALogP} + 0.03\cdot \mathit{nAtomP} + 0.23\cdot \mathit{nHBDon} + 0.004\cdot \mathit{ATSm1} + 0.11\cdot \mathit{nSmallRings}$	0.86	0.86	0.92
FullrC60	$\log k \sim 0.15 + 0.79\cdot \mathit{ALogP} - 0.14\cdot \mathit{khs.aasC} + 1.53\cdot \mathit{khs.sssSiH} - 0.0001\cdot \mathit{WPATH} - 0.63\cdot \mathit{khs.aasN}$	0.91	0.90	0.94
sMWCNT	$\log k \sim 1.76 + 0.003\cdot \mathit{ATSp1} + 0.09\cdot \mathit{nAtomP} - 0.39\cdot \mathit{khs.ssssC} + 0.33\cdot \mathit{khs.sBr} - 0.13\cdot \mathit{khs.sOH}$	0.88	0.93	0.93
MWNT_COOH_ 20nm	$\log k \sim -0.81 + 0.12\cdot \mathit{AMR} - 1.18\cdot \mathit{Fsp3} + 0.02\cdot \mathit{ATSm4} + 0.53\cdot \mathit{MDEO.11} + 0.17\cdot \mathit{khs.aaaC}$	0.94	0.97	0.93
MWNT_COOH_ 50nm	$\log k \sim -0.005 + 0.11\cdot \mathit{AMR} - 0.15\cdot \mathit{nRotB} - 0.14\cdot \mathit{C1SP3} + 0.006\cdot \mathit{TopoPSA} + 0.19\cdot \mathit{khs.aaaC}$	0.97	0.98	0.93
MWNT_OH	$\log k \sim -0.35 + 0.005\cdot \mathit{ATSp1} + 0.18\cdot \mathit{nAtomP} - 0.60\cdot \mathit{khs.ssssC} + 0.60\cdot \mathit{khs.sBr} + 0.23\cdot \mathit{nHBDon}$	0.92	0.96	0.94
MWNT	$\log k \sim 1.53 + 0.004\cdot \mathit{ATSp1} - 0.65\cdot \mathit{khs.ssssC} + 0.06\cdot \mathit{nAtomP} + 0.44\cdot \mathit{MDEO.11} - 0.18\cdot \mathit{khs.sOH}$	0.91	0.94	0.94
SiO_2_Amino	$\log k \sim 1.71 + 0.50\cdot \mathit{ALogP} + 0.36\cdot \mathit{nHBDon} - 0.41\cdot \mathit{nBase} + 0.31\cdot \mathit{nAcid} - 0.90\cdot \mathit{khs.sssSiH}$	0.85	0.87	0.93
SiO_2_Naked	$\log k \sim 2.40 + 0.40\cdot \mathit{XLogP} - 0.49\cdot \mathit{Fsp3} + 0.35\cdot \mathit{khs.sOH} - 0.07\cdot \mathit{Kier2} - 0.21\cdot \mathit{khs.ssNH}$	0.80	0.82	0.92
SiO_2_PEG	$\log k \sim 1.58 + 0.49\cdot \mathit{XLogP} - 0.0004\cdot \mathit{fragC} + 0.41\cdot \mathit{nHBDon} - 0.26\cdot \mathit{khs.ssssSi} - 0.42\cdot \mathit{nBase}$	0.77	0.77	0.94
SiO_2_Phosphat	$\log k \sim 1.93 + 0.48\cdot \mathit{ALogP} + 0.37\cdot \mathit{nHBDon} - 0.22\cdot \mathit{Fsp3} - 0.35\cdot \mathit{nBase} + 0.30\cdot \mathit{nAcid}$	0.84	0.86	0.93
TiO_2	$\log k \sim 1.96 + 0.40\cdot \mathit{ALogP} + 0.36\cdot \mathit{nHBDon} - 0.52\cdot \mathit{Fsp3} + 0.41\cdot \mathit{SCH.7} - 0.004\cdot \mathit{ATSm1}$	0.85	0.86	0.93
ZnO	$\log k \sim 1.62 + 0.54\cdot \mathit{ALogP} + 0.41\cdot \mathit{nHBDon} - 0.41\cdot \mathit{nB\text{–}se} - 0.32\cdot \mathit{Fsp3} + 0.95\cdot \mathit{khs.sssSiH}$	0.86	0.87	0.94
ZrO_2_Amino	$\log k \sim 1.71 + 0.53\cdot \mathit{ALogP} + 0.37\cdot \mathit{khs.sOH} - 0.0002\cdot \mathit{ATSp5} + 1.09\cdot \mathit{khs.sssSiH} + 0.30\cdot \mathit{nAcid}$	0.79	0.83	0.94
ZrO_2_PEG	$\log k \sim 2.22 + 0.60\cdot \mathit{ALogP} + 0.45\cdot \mathit{khs.sOH} - 0.07\cdot \mathit{Kier1} + 0.34\cdot \mathit{Fsp3} + 1.14\cdot \mathit{khs.sssSiH}$	0.77	0.80	0.95
ZrO_2_TODacid	$\log k \sim 1.61 + 0.46\cdot \mathit{XLogP} + 0.41\cdot \mathit{khs.sOH} - 0.002\cdot \mathit{ECCEN} + 0.22\cdot \mathit{khs.ssssSi} - 0.36\cdot \mathit{nAcid}$	0.74	0.79	0.92

a) Adjusted R^2 values are presented for the training set (R^2_{train}) and for the validation set ($R^2_{validate}$); b) AD, applicability domain; fraction of compounds from the training and validation set that are within the applicability domain thresholds of Williams plots (Fig. S6).

2.2.3 Applicability domain of the QSAR models

The set of enteric microbial metabolites that can be analyzed using the QSAR models depends on the chemical space that can be described by the molecules that were used to train the BSAI and CDK models. For all models, we determined this applicability domain (AD) using Insubria graphs. Instead of cross-validated residuals, which are used to construct Williams plots, these graphs present model predictions against the diagonal hat values of the model's design matrix (Fig. 2.2) (Gramatica et al. 2012). All molecules with a hat value smaller than the critical hat value (h^*), as defined in the Methods section, and with predicted values within predefined thresholds, are considered to be within the AD of QSAR models. Some researchers exclusively apply the h^* threshold to define the AD of QSAR models (Wang et al. 2017; Banjare et al. 2021). In this case, the AD derived using Insubria graphs shows high similarity to the AD based on Mahalanobis distances (Fig. S3).

The AD thresholds that are applied to BSAI models, determine how many molecules are available for the construction of CDK models. To investigate the effects thereof, we built CDK models using BSAI model predictions that were selected using three different AD approaches, as exemplified in Fig. 2.2. For the first AD approach, we applied both the h^* threshold and thresholds for the predicted log k value, defined by the mean ($\bar{x}$) and standard deviation (σ) of log k predictions for probe molecules ($\bar{x} \pm 3{\cdot}\sigma$) (Fig. 2.2a). These probe compounds are the 23 out of the 25 compounds that were used by Chen et al. (2014b) to derive the BSAI model, which are present in the data set

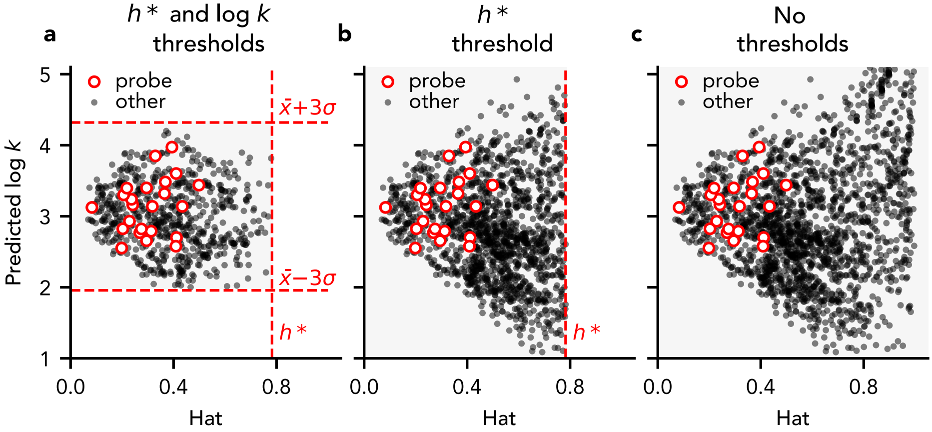

Figure 2.2: *Thresholds for the applicability domain of BSAI models.* Three different approaches are shown, using the naked SiO_2 BSAI model as an example. **a**) Thresholds defined by the predicted log k values ($\bar{x} \pm 3{\cdot}\sigma$) of probe compounds (white circles) and the critical hat value ($h^* = 0.78$). **b**) Thresholds set by h^* only. **c**) No thresholds.

with known Abraham descriptors (Bradley et al. 2014; Table S3). For the second AD approach, we only applied the h^* threshold (Fig. 2.2b). For the third approach, we applied no AD thresholds (Fig. 2.2c). This resulted in a total number of 701 molecules (h^* and log k thresholds), 1525 molecules (h^* threshold) and 1996 molecules (no thresholds) that could be used to build CDK models.

For all AD approaches, CDK models that were built at the cross-validation ratio of 80/20 (training set/validation set) explained most of the variance in log k predictions from the BSAI models (Table S5, S6, S8). According to the Williams plots (Fig. S6, S8, S12), over 93% of the training and validation compounds fell within the AD of CDK models for each of the AD thresholds (Table S5, S6, S8). We noted some deviation from normality of model residuals in Q-Q plots, potentially introducing bias to the standard error of estimates (Schmidt and Finan 2016). No issues were identified for the remaining model assumptions.

When comparing CDK models from each of the AD approaches, the best fit between BSAI and CDK models in terms of log k predictions for the training set and the validation set was obtained for CDK models that were built without AD thresholds for BSAI model predictions (Table 2.3; R^2_{train}=0.71-0.97; $R^2_{validate}$=0.77-0.98), followed by CDK models that were built with the h^* threshold only (Table S8-9; R^2_{train}= 0.75-0.90; $R^2_{validate}$=0.75-0.95), and CDK models that were built with the h^* and log k thresholds (Table S6-7; R^2_{train}= 0.65-0.83; $R^2_{validate}$=0.64-0.86). The same trend was obtained for the AD of CDK models. The largest set of enteric microbial metabolites was within the AD of all CDK models that were built without AD thresholds (60 metabolites), followed by the AD of all CDK models that were built with the h^* threshold only (51 metabolites), and the AD of all CDK models were built with the h^* and log k thresholds (38 metabolites) (Table 2.4, Table S4). These trends show that both the fit, in terms of R^2 values, and the applicability of CDK models, as determined using Insubria graphs, improve when these models are built based on a larger number of BSAI predictions. Although this favors the application of CDK models that are built without BSAI thresholds, this introduces the risk of basing CDK models on incorrect BSAI predictions. Nevertheless, given the strong correlation (ρ>0.96) between predictions of CDK models from each of the BSAI AD approaches (Fig. S2), we describe the results of CDK models that were built without applying BSAI AD thresholds in the main text, and include the results of the other CDK models in the Supporting Information. We only describe results that are supported by models from each of the AD approaches, unless specifically stated otherwise.

The applicability of CDK models, as determined based on h^*, shown in Insubria graph of Fig. S7, Fig. S9, and Fig. S13, was dependent on metabolite category (Table 2.4). The models could be applied to all ‘SCFAs’, and most ‘tryptophan metabolites’,

Table 2.4: Number of enteric microbial metabolites within the applicability domain of all CDK models.

Metabolite category [a]	*Total number of metabolites*	*h* and log k BSAI model thresholds* [b]	*h* BSAI model threshold* [b]	*No BSAI thresholds* [b]
Microbe-associated molecular patterns	21	0	0	0
Vitamins	11	1	1	1
Short-chain fatty acids	8	8	8	8
Bile acids	25	0	0	0
Tryptophan precursors and metabolites	17	8	9	14
Polyamines	4	0	0	0
Choline metabolites	6	0	4	4
Phenolic, benzoyl and phenyl derivatives	24	18	17	19
Lipids and lipid precursors	13	0	0	1
Neurotransmitters	6	0	1	1
Other	20	3	11	12
Total	155	38	51	60

[a] Proteins were excluded prior to building CDK models; [b] Columns specify the thresholds applied for the BSAI model. For all CDK models, the *h** threshold was applied, as shown in the corresponding Insubria graphs of Fig. S7, S9 and S13.

'choline metabolites', and 'phenolic, benzoyl and phenyl derivatives'. The models were less applicable to the metabolite categories 'neurotransmitters', 'vitamins', and 'lipids and lipid precursors'. For these categories, the models could only be applied to histamine (or gamma-aminobutyric acid in h^* threshold models), niacin, and linoleic acid. The CDK models could not be applied to any of the 'MAMPs', 'bile acids' and 'polyamines'. These categories comprise large metabolites, which can adopt different spatial conformations, and molecules with rich surface functionalities, including many hydroxyl- or amino-groups per metabolite. This is in agreement with the limitations of the BSAI model, which cannot successfully describe surface interactions of biomolecules with certain degrees of flexibility in bonds, cannot differentiate between the different isomeric spatial conformations of biomolecules, and are not applicable to biomolecules with diverse moieties and functional groups, like phosphate, thiophosphoryl groups, and nitrile bonds (Chen and Riviere 2017; Chen et al. 2016). For biomolecules with these characteristics, MD simulations can be used to study ENM surface interactions at higher computational cost. This could potentially lead to the identification of descriptors that can increase the AD of QSAR models (Chen and Riviere 2017; Chen et al. 2016). In the final part of our study, we apply these simulations to investigate what kind of interactions differentiate the adsorption behavior of vitamins that are within or outside the AD of QSAR models (Fig. 2.4-2.6). Vitamins were specifically selected for these investigations, rather metabolites of the other categories that are outside of the AD of CDK models, because they include relatively small molecules in terms of number of atoms, but comprise diverse structural properties. This allows to perform more simulations within a given computational time, thereby obtaining more diverse molecular information.

2.2.4 Log k predictions from the QSAR models

In the following comparison between the adsorption affinities for microbial metabolites to metal and carbon ENMs, we focus on the core set of 60 metabolites that are included in the AD of QSAR models for all ENMs (Table 2.4). The AD of the individual models was larger, as determined based on h^*, shown in the Insubria graphs presented in Fig. S7, Fig. S9 and Fig. S13. The sizes thereof ranged from 77 metabolites ('SiO_2_PEG' model) to 120 metabolites ('FullrC60' model), and can be found in the Supporting Information for more detailed investigations on specific ENMs (Table S4).

Metal and carbon ENMs could clearly be distinguished based on log k predictions for the enteric microbial metabolites. Moreover, we found a remarkable distance between log k predictions for the Buckminster fullerene (C_{60}) and predictions for all other ENMs (Fig. 2.3a; Fig. S10a, Fig. S14a). This is in line with other unique interaction properties of C_{60} fullerenes, which may act like hydrophobic organic molecules, by adsorbing to larger biomolecules, either individually, or in aggregated form, potentially changing properties of these larger biomolecules (Song et al. 2011). For this reason, log k predictions for the fullerene will be discussed separately below. All nanodescriptors except for r_e ($F_{1,13}$= 0.34, p>0.05) correlated with log k-based distances between ENMs, as detected by distance-based redundancy analysis (Fig. 2.3a). For the three nanodescriptors with the most significant correlations, namely a ($F_{1,13}$=29.32; p=0.001), b ($F_{1,13}$=22.18; p=0.001) and p_s ($F_{1,13}$=28.35; p=0.001), this result was supported by the CDK models built using the different AD approaches for the BSAI model (Fig. S10a, Fig. S14a). This indicates that in particular hydrogen-bond interactions and interactions resulting from the polarity and polarizability of metabolites distinguish the adsorption affinities for enteric microbial metabolites to ENMs. Although hydrophobicity-driven interactions contribute most to the overall predicted adsorption affinity for enteric microbial metabolites to ENM surfaces, these interactions explain less of the differences in log k predictions between metal and carbon ENMs ($F_{1,13}$=7.57; p=0.013) than the hydrogen-bond interactions, and interactions driven by polarity and polarizability.

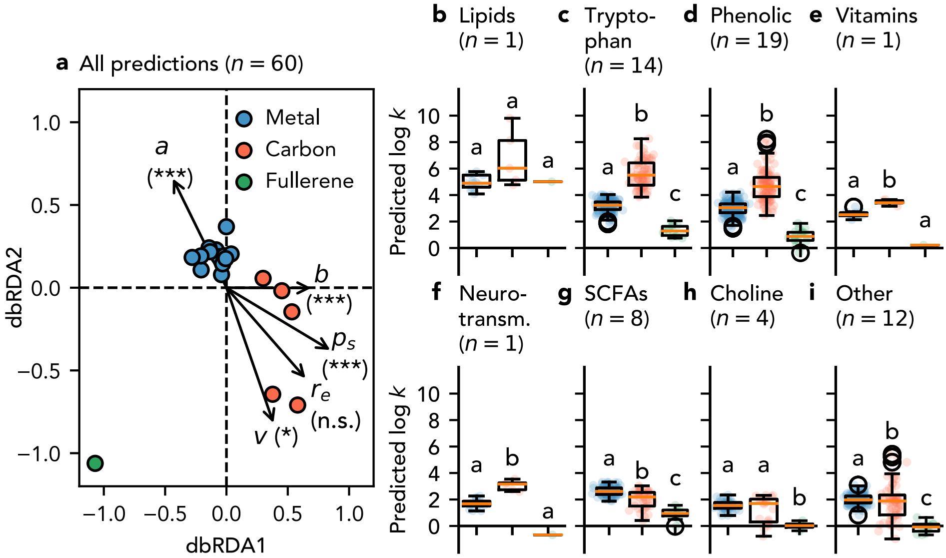

Figure 2.3: *Differences between log k predictions for enteric microbial metabolites to metal nanomaterials, carbon nanotubes, and fullerenes.* Subplot **a**) depicts the results of distance-based redundancy analysis, correlating the five nanodescriptors [r_e,p_s,a,b,v] to distances between the log *k* predictions for each of the 5 carbon nanotubes (red circles), the fullerene (green circle), and each of the 13 metal nanomaterials (blue circles). Subplots **b**) to **i**) depict log *k* predictions for: lipids and lipid precursors (**b**); tryptophan metabolites (**c**); phenolic, benzoyl and phenyl derivatives (**d**); vitamins (**e**); neurotransmitters (**f**); short-chain fatty acids (**g**); choline metabolites (**h**); and other enteric metabolites (**i**). The number of metabolites per category (*n*) is indicated between brackets. Asterisks and letters indicate significant differences. *Abbreviations*: neurotransm., neurotransmitters; n.s., not significant; *, $p<0.05$; ***, $p=0.001$.

For metabolites of most categories, predicted log *k* values were highest for carbon nanotubes, followed by metal ENMs and fullerenes (Fig. 2.3b-i; Fig. S10b-i; Fig. S14b-i). By exception, predicted log *k* values for 'choline metabolites' were similar for metal ENMs and carbon nanotubes (median (interquartile range (IQR)) log $k = 1.55$ (1.34-1.77) and 1.70 (0.30-2.03), respectively, $p > 0.05$), and predicted log *k* values for 'SCFAs' were higher for metal ENMs than for carbon nanotubes (median (IQR) log $k = 2.61$ (2.38-2.88) and 2.19 (1.50-2.54), respectively, $p<0.001$) (Fig. 2.3g, Fig. S10g, Fig. S14g). This suggests that acidic groups experience stronger interactions with metal ENMs than with carbon nanotubes. This is consistent with the results of our distance based redundancy analysis (dbRDA), identifying a highly significant contribution of nanodescriptor *a* to log *k*-based distances between metal ENMs and carbon nanotubes (Fig. 2.3a, Fig. S10a, Fig. S14a). Accordingly, computational and experimental investigations for citrate and other carboxylic acids showed that specifically the carboxylate groups of these molecules interact with Au and Fe_3O_4 ENMs (Al-Johani et al. 2017; Monti et al. 2017; Zhang et al. 2019). In contrast, and in line with our results, the QSAR models developed by Roy et al. (2019) predict a negative impact of C-O groups and aliphatic primary alcohols on the adsorption affinity for organic pollutants to carbon nanotubes. Notably, this did not result in higher log *k* estimates for 'tryptophan precursors and metabolites' and 'phenolic, benzoyl and phenyl derivatives' to metal ENMs than to carbon nanotubes. Although both of these categories comprise biomolecules with acidic functional groups, the QSAR models predicted significantly higher log *k* values for these categories to carbon nanotubes (median (IQR) log *k* = 5.50 (4.75-6.43) and 4.64 (3.88-5.33), respectively) than to metal ENMs (median (IQR)) log *k* = 3.23 (2.91-3.48) and 3.05 (2.66-3.33), respectively) (Fig. 2.3c-d; Fig. S10c-d; Fig. S14c-d). Nevertheless, in contrast to 'SCFAs' and 'choline metabolites', which solely consist of small aliphatic biomolecules, 'tryptophan precursors and metabolites' and 'phenolic, benzoyl and phenyl derivatives' comprise unsaturated (poly)cyclic molecules. This suggests that π-π stacking interactions contribute more to the interaction between these molecules and ENMs than the interactions of acidic functional groups. We further investigate the relative contributions of such different interaction types to the adsorption affinity for enteric metabolites to ENMs by way of unconstrained MD simulations as discussed below.

2.2.5 Molecular dynamics simulations: a case study

In the final part of our study, we perform MD simulations to investigate what distinguishes ENM interactions of metabolites that are within or outside of the AD of QSAR models. A recent study by Comer et al. (2015) that focuses on calculating the adsorption affinity of about 30 small aromatic compounds to carbon nanotubes, forms an inspiration and starting point for this investigation. Using a computational protocol that is very similar to ours, the authors identified an excellent correlation ($r \geq 0.9$) between calculated and measured values for the complete set of compounds. Rather than restricting ourselves to π-π stacking interactions that are important for MWCNT, we also consider the extended interaction network between a metal substrate (SiO_2) and biologically relevant molecules like vitamins. We even go one step beyond a direct comparison between adsorption affinities, and conduct a proof of principle aimed at rationalizing which of the nanodescriptors obtained by QSAR analysis contribute to key interactions identified using unconstrained MD. The small set of vitamins, including thiamine, pyridoxine, biotin and folate, was selected because of the significant spread in the predicted log *k* values by QSAR. Moreover, the set was selected to represent different structural properties, such as different numbers of aromatic rings (1-3), differences in charge (0 or +1), and different numbers of acidic and basic functional groups. Finally, the set included vitamins that are outside the AD of QSAR models for

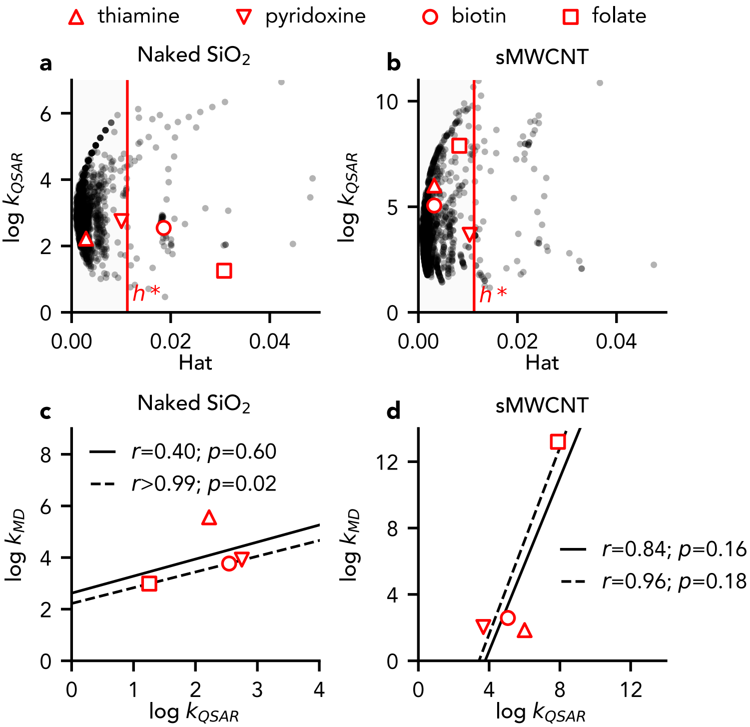

Figure 2.4: *Comparison of adsorption affinities for four vitamins with different structural properties as determined by QSAR and MD simulation to* SiO_2 (**a**,**c**) *and multiwalled carbon nanotubes (MWCNTs)* (**b**,**d**). Insubria graphs **a**) and **b**) present the applicability of QSAR models for the vitamins. Subplots **c**) and **d**) present Pearson correlations (*r*) between QSAR and MD results for the vitamins including thiamine (solid line) or excluding thiamine (dotted line).

SiO_2 (biotin and folate), as well as vitamins that are within this AD (thiamine, pyridoxine), for comparison (Fig. 2.4a). All of the four vitamins are inside of the AD of the sMWCNT model (Fig. 2.4b), while only thiamine and biotin are within the AD of the MWNT model. For this reason, log *k* predictions from the sMWCNT model are used for comparison with log *k* values determined by classical MD simulations for MWCNT. In the remainder, our MD-derived (log k_{MD}) values, calculated using eq 2.2, are directly compared to the QSAR predictions (log k_{QSAR}).

The results for the four vitamins can be found in Fig. 2.4c-d, and illustrate the significance of our direct comparison. In the case of SiO_2, log k_{QSAR} and log k_{MD} results should be compared with caution, because two out of the four vitamins are outside of the AD of the QSAR models, and because log k_{QSAR} predictions from models that were derived using the alternative AD approaches, correlate differently with the MD results (Fig. S11c, Fig. S15c). For the comparison of MWCNT results, we note that the presence of a datapoint with high leverage (folate) results in high R^2 values. Nonetheless, we find that the computed log k_{MD} and predicted log k_{QSAR} values feature the same orders of magnitude and show a reasonable, but non-significant correlation (r_{SiO2}=0.40 and r_{MWNT}=0.84; $p > 0.05$). In both cases, we find that excluding thiamine improves the correlation between log k_{MD} and log k_{QSAR} results (r_{SiO2}>0.99, p_{SiO2}=0.02 and r_{MWNT}=0.96; $p > 0.05$). While this discrepancy for thiamine is hard to pinpoint to a single cause, it may well be due to the usual choice in our MD approach to exclude electronic polarizability (Huang et al. 2014) since thiamine has an explicit +1 charge. In particular, a previous study of Wu et al. (2007) supports our suggestion that polarizability effects are essential for this particular vitamin. The study focused on the controlled release of thiamine hydrochloride with mesoporous silica tablets and showed that the pH of the medium affects thiamine release. For reasons of computational efficiency, state of the art force fields in classical MD only consider fixed atomic charges that are determined prior to simulation via more resolved (and costly) methods like density functional theory. While polarizable force fields have been developed and applied to study various phenomena, including adsorption on graphene surfaces (Hughes et al. 2014), it is difficult to assess beforehand if the substantial computational cost of including polarizability will lead to greater accuracy. In our limited case study, the improved correlation between QSAR and MD methods in terms of log *k* values when charged vitamins are omitted, indicates that it merits including polarizable force fields in MD simulations for charged enteric microbial metabolites. Next, we performed unconstrained MD to evaluate key interactions for vitamins inside of as compared to vitamins outside of the AD of QSAR models.

The interaction energies between SiO_2 and each vitamin molecule were separated into Lennard-Jones (LJ) and electrostatic contributions (Fig. 2.5a), where LJ is a combination of very short-ranged repulsion due to the overlap of the electron clouds and longer-ranged van der Waals attraction via induced dipoles. The vitamin size is accounted for by its radius of gyration r_{gyr}. We observe that the most dominant interaction for all vitamins is of a LJ type, except for thiamine. Folate (r_{gyr} = 0.57 nm) has the highest LJ contribution, irrespective of its low log *k* value, while the smaller pyridoxine (r_{gyr} = 0.24 nm) has the lowest LJ contribution but the highest log *k* value. In the case of thiamine (r_{gyr} = 0.36 nm), electrostatic (Coulomb) interactions dominate, which can be due to the explicit +1 charge that is present on the thiamine molecule.

To further investigate the relation between dominant interactions and log *k* values, we additionally considered the hydrogen bonding between these molecules and the SiO_2 slab. Using interatomic distances, we identified different chemical groups for each vitamin that are observed to form hydrogen bonds with the ENM surface during the 500 ns simulation, considering a cutoff of 0.24 nm to the SiO_2 surface (Fig. 2.5b). Time evolution plots for these hydrogen bond interactions are included in the Supporting Information (Fig. S4). Both pyridoxine and folate form on average 2-3 hydrogen bonds with the SiO_2 slab. However, considering the increased size of folate (r_{gyr} = 0.57 nm), it may also exhibit effects of steric hindrance while interacting with the slab. Different configurations extracted from the unbiased MD simulation pathway (Fig. 2.5c,d) showed a perturbed conformation, i.e. a bent folate, while its smaller size enables pyridoxine (r_{gyr} = 0.24 nm) to lie parallel to the slab without bending. As the smaller molecule does not need to adapt its conformation to the slab geometry, the hydrogen bonding gains stability, rendering pyridoxine more probable of forming hydrogen bonds with SiO_2 than folate. Overall, pyridoxine sits on the slab while folate undergoes several conformational changes to stabilize around the SiO_2 slab: see some of the simulation snapshots of folate and pyridoxine with SiO_2 shown in Fig. 2.5c-d. This is fully in line with the QSAR predictions, which infer that hydrogen bond acidity and basicity play a dominant role in the adsorption affinity of these vitamins for SiO_2.

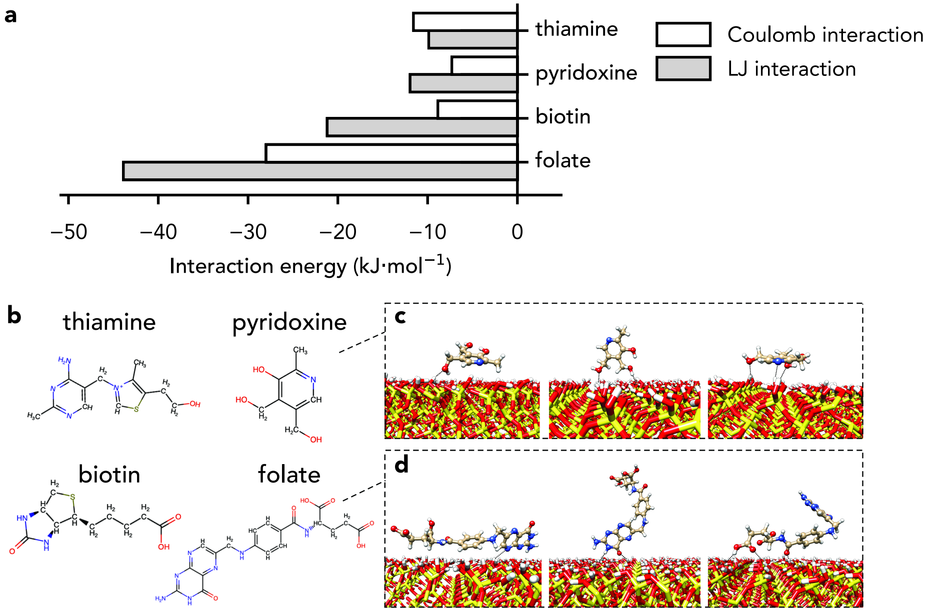

Figure 2.5: **a**) Lennard-Jones and Coulombic contributions for all the considered vitamin molecules with a SiO_2 surface. **b**) Hydrogen bond forming groups (in red and blue) identified on the four vitamin molecules. Simulation snapshots portray different configurations for **c**) pyridoxine and **d**) folate during the 500 ns molecular dynamics simulation. The positions of interacting chemical groups are indicated with dashed lines. The carbon, oxygen, nitrogen, sulfur and hydrogen atoms are shown in pale yellow, red, blue, yellow, and white, respectively.

Finally, to investigate the conformational space sampled by each molecule, we performed cluster analysis over all 500 ns MD trajectories. As a condition for defining a new cluster, we considered a difference of 0.25 nm in the root mean square displacement (RMSD, corrected for the center of mass drift). As can be expected, only a single cluster was identified for the small and rigid vitamins: thiamine, pyridoxine, and biotin. In contrast to this finding, we identified five different clusters for the longest vitamin folate. Exemplary conformations taken from each cluster are shown in Fig. S5 of the Supporting Information.

Overall, adsorption affinities determined using all-atom MD were found to agree well with values predicted by QSAR modeling for several complex molecules. The benefit of molecular simulation is that it provides molecular insight into the nature of the principal interactions between these molecules and a relevant ENM, enabling a more fundamental understanding. Moreover, *in silico* determination of adsorption affinities can be useful for part of the materials spectrum where experimental measurement is complicated, expensive or even ruled out, that is, to generate reliable training data for the computationally much more efficient (nano)QSAR in that part of the spectrum. We particularly see this limited case study as a showcase for the potential of physical modelling in this work field and for unraveling correlations that are not clarified in the QSAR approach. We believe that a broader application of this approach will help experimentalists and nanotoxicologists to further improve the applicability of QSAR and to better understand the affinity of biologically relevant molecules on the various ENM surfaces. In particular, although being computationally very costly compared to QSAR, MD simulation is an ecofriendly and cost-effective technique for performing affinity analysis prior to or even replacing *in vitro* experiments.

2.2.6 Examples for future perspectives

For future perspectives, the combination of 1) the biological functions of enteric microbial metabolites; 2) their predicted adsorption affinities to metal and carbon ENMs; 3) key interaction types inferred from QSAR models and MD simulations; and 4) the direct molecular information obtained from MD simulations, can be used to rationalize what biologically relevant interactions could occur between ingested ENMs and microbial metabolites in the gastrointestinal tract. In this section, we present two relevant examples to illustrate this rationale. We note that these examples focus on hypotheses that are based on the current understanding of the enteric microbial metabolome. Following the same principles, our results can be employed to rationalize what adsorption interactions may occur for enteric microbial metabolites that are yet to be discovered.

The first example focuses on the hypothesis that ingested ENMs can sequester essential SCFAs via the adsorption of these metabolites to the ENM surface, thereby causing nutrient deficiencies. As presented in Table 2.1, these fatty acids are synthesized by microbiota in the colon from indigestible fibers. Malfunction of intestinal microbiota can result in low availability of beneficial SCFAs, possibly causing intestinal inflammation (Venegas et al. 2019). Especially under these conditions, it is relevant to consider the potential adsorption of SCFAs to ENMs that are administered orally to treat or prevent intestinal inflammation (Xia et al. 2017, Qin et al. 2021, Zhu et al. 2019). In the case of SCFAs, which are within the AD of QSAR models, our QSAR predictions can readily be used to assess this. Log k predictions for SCFAs were significantly higher to metal ENMs than to carbon ENMs, indicating that the adsorption-driven sequestration of SCFAs forms a larger concern for metal ENMs than for carbon ENMs. Nevertheless, the results for more lipophilic metabolites put this into perspective, showing that the overall predicted adsorption affinities for SCFAs are relatively low to both carbon and metal ENMs.

The second example focuses on the hypothesis that active resorption of microbial metabolites can facilitate the transfer of ENMs across the gut epithelium when resorbed metabolites are adsorbed to ENMs. Such interactions have been demonstrated for vitamin B_{12} (Thepphankulngarm et al. 2017), but can also be expected for secondary and conjugated bile acids (Table 2.1). In contrast to SCFAs, bile acids are not in the AD of the QSAR models. In this case, the key interaction types and molecular information obtained from MD simulations can be used to assess their adsorption affinity qualitatively. First, bile acids are large, amphiphatic molecules. Given the key contribution of hydrophobicity-driven interactions to the overall adsorption affinity for metabolites, the hydrophobic face of these molecules can be expected to interact with the ENM surface, resulting in relatively high adsorption affinities for these molecules to both metal and carbon ENMs. Second, similar to other unsaturated (poly)cyclic metabolites like ‘tryptophan precursors and metabolites’ and ‘phenolic, benzoyl and phenyl derivatives’, bile acids can generally be expected to have higher affinity to carbon than to metal ENMs, as a result of π-π stacking interactions between their steroid core and the carbon ENM surface. Third, the polarity of glycine and taurine amino acid conjugates can be expected to affect the adsorption affinity for bile acids to carbon and metal ENMs differently, specifically favoring adsorption to carbon ENMs. As shown in the MD simulations for folate, the ability of these more flexible conjugates to bend toward the ENM surface can moreover improve the stability of these bile acids onto the carbon ENM surface. Thus, the probable ranking of the adsorption affinity for bile acids to ENMs, from high to low, is: conjugated bile acids and carbon ENMs – secondary bile acids and carbon ENMs – secondary bile acids and metal ENMs – conjugated bile acids and metal ENMs. This ranking, and similar qualitative assessments based on our results, can support the rationalization of biologically relevant physisorption interactions that can occur between enteric microbial metabolites and ingested ENMs. The two examples also illustrate how knowledge on adsorption interactions between ENMs and microbial metabolites can serve as a stepping stone for modeling mechanistic pathways for toxic or therapeutic nanomaterials.

2.3 Conclusions

We set out to investigate the potential interactions between ingested metal and carbon ENMs and the diverse set of enteric microbial metabolites that are available in the gastrointestinal tract. Our investigations indicate that evaluating these interactions merits an integrative approach, taking biological considerations into account, and combining different experimental or computational methods. In view of this, the overview and classification of enteric microbial metabolites, which we provide as a starting point for QSAR models and MD simulations, allows to assess the relevance of adsorption interactions from a biological perspective. Relevant considerations include the potential of biomolecules like 'MAMPs' to activate immune responses, or to mask ENMs from immunorecognition, the potential of rare and essential metabolites, like 'vitamins', to cause nutrient deficiencies following sequestration by adsorption to ENMs, and the potential of effectively resorbed metabolites, like 'vitamins' and 'bile acids', to affect the biodistribution of associated ENMs.

The QSAR models developed in the second part of our study provide a set of readily available log *k* predictions for biologically relevant metabolites like 'short-chain fatty acids' and 'tryptophan precursors and metabolites'. The correlation of these predictions to BSAI nanodescriptors, revealed that hydrophobicity-driven interactions are important to the overall interaction strength of enteric microbial metabolites, while hydrogen-bond interactions and interactions resulting from the polarizability and polarity of metabolites largely explain differences in the interactions of these metabolites with metal and carbon ENMs. Ultimately, these insights can aid in the qualitative assessment of adsorption adsorption affinities for metabolites like 'MAMPs' and 'bile acids', which cannot yet be assessed quantitatively using the QSAR models.

The MD simulation case study, which forms the third part of our study, exemplifies how conformational properties complicate extending the linear relationships of the QSAR models to larger, more flexible molecules, which may gain stability by bending toward the ENM surface. Our results furthermore indicate that it is worth including polarizable force fields in further MD investigations on charged metabolites, while computational cost can be saved by excluding these force fields for investigations on uncharged metabolites. Using unconstrained MD simulations, we moreover found excellent agreement with QSAR models on the main interaction types that facilitate the interactions between enteric microbial metabolites and ENMs. This provides confidence to evaluate the adsorption interactions for larger, flexible biomolecules to the ENM surface qualitatively, based on these interaction types. Therefore, we anticipate that the results of our study can be employed to rationalize the adsorption interactions that may occur between ingested metal and carbon ENMs and a large set of diverse enteric microbial metabolites in a biologically relevant way.

2.4 Methods

2.4.1 Literature search for enteric microbial metabolites

In order to generate an overview of microbial metabolites that occur in the intestinal lumen, we retrieved names of enteric microbial metabolites from reviews on gut microbial metabolism. The reviews were accessed through the Web of Science Core Collection database (1945-2020) via Leiden University's library, by applying the search string: "(microbiome OR microbiota OR microflora) AND (gut OR *intestine* OR enteric) AND metabolite* AND ("microbial metabol*" OR (host AND interact*))". Reviews were added to the literature search until no new categories of microbial metabolites were identified, and until the total number of identified metabolites had saturated (Fig. 2.1). Metabolites were included in the overview if they had been found to be present in the gut lumen, had been reported to be produced and excreted by gut microbiota, to be products of microbial modifications, or to be regulated by gut microbiota. In case metabolite names referred to groups of molecules (such as 'lipopolysaccharides'), one or several representative molecules were selected from the PubChem database (https://pubchem.ncbi.nlm.nih.gov). To this end, we either selected molecules that had been used in experimental work to represent the concerning metabolite groups or selected molecules that had been identified in the gut lumen. Finally, we retrieved simplified molecular-input line entry-specifications (SMILES) from the PubChem database for each of the metabolites included in the overview. In case both isomeric and canonical SMILES were available for the metabolites, isomeric SMILES were selected.

2.4.2 BSAI models for log k prediction

We built QSAR models to predict log *k* values for the identified enteric microbial metabolites to 13 metal ENMs and 6 carbon ENMs (Table 2.2). We refer to the Supporting Information of Chen et al. (2014b) for a detailed physicochemical characterization of these ENMs, including measurements by transmission electron microscopy, Brunauer-Emmlett-Teller surface area analysis, dynamic light scattering, analytical ultracentrifugation, fluorescence correlation spectroscopy, X-ray diffraction, X-ray photoelectron spectroscopy, and electron spin resonance. For each of the ENMs, we firstly applied the BSAI model published by Xia et al. (2010) (eq 2.1) to predict log *k* values for metabolites with known Abraham's molecule descriptors. We subsequently used these log *k* predictions to build QSAR models that could be applied to predict log *k* values for the enteric microbial metabolites.

For BSAI predictions, we adopted the nanodescriptors derived by Chen et al. (2014b), and obtained molecules with known Abraham's molecule descriptors from Bradley et al. (2014). We prepared the data set of Bradley et al. in three steps. First, incorrect SMILES of 14 compounds that could not be parsed in the steps described below (keys '1833', '1838', '1843', '1844', '1848', '2004', '2012', '2344', '2523', '2656', '2843', '2855', '2931', '3034'), were corrected using SMILES from the ChemSpider database (www.chemspider.com) (Table S1). Second, compounds with poor or suspicious data quality, or including metals or salts (keys '23', '2030', '2033', '2034', '2994', '4001'), were excluded following the recommendations by the authors. Third, double, triplicate and quadruplet entries of 431 compounds were removed, randomly selecting one of the references reporting Abraham descriptors for each of the concerning compounds. Similarly, isomers, which have identical values for each of the Abraham's molecule descriptors, were removed from the data set. This resulted in a data set comprising 1996 unique compounds with known Abraham descriptors.

2.4.3 Applicability domain of BSAI models

We assessed the AD of BSAI models for each of the 19 ENMs using Insubria graphs (Gramatica et al. 2012). These graphs present the diagonal hat values of the design matrix ($[E,S,A,B,V]$) on the x-axis, and QSAR predictions (log *k* values) on the y-axis. Of the 25 probe compounds that were used by Chen et al. (2014b) to derive nanodescriptors, 23 probe compounds were included in the data set with known Abraham molecule's descriptors. We used these compounds to derive the critical hat threshold (h^*) as $3\cdot(N+1)/n$, where N is the number of descriptors in the model, and n is the number of probe compounds included in the data set. For the predicted log *k* values, we defined AD thresholds by the mean of the log *k* predictions for probe compounds, and 3 times the standard deviation of these predictions ($\bar{x} \pm 3\cdot\sigma$). Subsequently, we selected compounds from Insubria graphs 1) by applying both the h^* and log *k* thresholds; 2) by applying the h^* threshold only; 3) by applying no thresholds. For the first approach, including log *k* thresholds, we only continued with compounds that fell within the log *k* thresholds for all 19 ENMs. For comparison, we also derived the BSAI

AD based on Mahalanobis distance, as described below ('Ordination Methods for QSAR Models'). We did not continue QSAR analysis with these compounds, due to the high similarity with the *h** threshold AD.

2.4.4 CDK models for log k prediction

Using BSAI log *k* predictions that were selected using each of the three aforementioned AD approaches, we applied multiple linear regression (MLR) to build QSAR models that can predict log *k* values using molecular descriptors from CDK. The molecular descriptors were computed in R (*v.* 3.6.3; www.r-project.org), accessing CDK functionality using the 'rcdk' package (*v.* 3.5.0; Guha 2007). To load molecules into the R environment, SMILES were parsed, implicit hydrogen atoms were converted to explicit hydrogen atoms, and aromaticity was checked. Thereafter, molecular descriptors were evaluated, and the data set was split into a training set and a validation set using the *createDataPartition* function of the 'caret' package (*v.* 6.0-86). The molecules with the lowest and highest BSAI model prediction, calculated as the mean predicted log *k* value for the 19 ENMs, were included in the training set. These were keys '2924 and '1700' (mean log *k* = 2.02 and 4.24), keys '2400' and '1253' (mean log *k* = 0.98 and 5.53), and keys '518' and '74' (mean log *k* = 0.40 and 10.56), when applying the *h** and log *k* threshold, the *h** threshold only, and no thresholds, respectively. The remaining molecules were divided into five quantiles, based on the predicted log *k* values from the BSAI model. Molecules of each of the quantiles were randomly divided over the training set and validation set. We evaluated the performance of four different cross-validation ratios (training set/validation sets = 90/10, 80/20, 70/30, and 60/40). Using the training set of each cross-validation ratio, MLR models were derived by forward selection. A total of five molecular descriptors were selected for the models, including the independent molecular descriptor explaining most of the model variance at each of the consequent forward selection steps. To ensure the independence of descriptors, molecular descriptors were only included if they did not result in variance-inflation factors larger than two, as assessed using the *vif* function from the 'car' package (*v.* 3.0-8).

2.4.5 Log k predictions and statistical analyses for QSAR models

We selected CDK models of the cross-validation ratio with the best internal validation score, evaluated as the mean adjusted R^2 value of models for all 19 ENMs. Diagnostic plots of the models were inspected to identify outliers (Cook's distance plot), and to evaluate the model assumptions of linearity (residuals vs. fitted values plot), normally distributed residuals (Q-Q plots), and homoscedasticity (scale-location plots). The AD of the models was assessed using Williams plots. Compounds were considered to be outside of the AD of models if cross-validated residuals are smaller than -3 or larger than 3, or if the diagonal hat values are larger than $3 \cdot (N+1)/n$, where N is the number of descriptors in the model, and n is the number of molecules in the training set. Correlations between molecular descriptors from CDK and Abraham's molecule descriptors were assessed using to the Spearman's rank correlation coefficient, calculated using the *cor.test* function of the 'stats' package (*v.* 3.6.3).

To prepare the microbial metabolite data for log *k* predictions, SMILES were parsed, implicit hydrogen atoms were converted to explicit hydrogen atoms, and aromaticity was checked. Thereafter, molecular descriptors were evaluated using 'rcdk'. Metabolites that were assigned to the metabolite category 'proteins/enzymes' were excluded due to their large size and three-dimensional conformations, which could not be accounted for using this QSAR approach. The applicability of the models for the other metabolites was assessed using Insubria graphs, by applying the h^* threshold. Log *k* predictions of metabolites that were considered to be within the AD of CDK models were compared between metal and carbon ENMs, for each metabolite category separately. To this end, the Kruskal-Wallis rank sum test was applied in combination with the Dunn's test from the 'FSA' package (v. 0.8.32; Ogle 2021). For all Dunn's tests, Holm adjusted *p*-values are reported.

2.4.6 Ordination methods for QSAR models

We used ordination methods to compare ENMs based on log *k* predictions from QSAR models and to derive the AD of BSAI models based on Mahalonobis distances. For both analyses, we used R functions that are available in the package 'vegan' (v. 2.5-6).
Log *k* data was transformed to remove negative values by subtracting the minimum log *k* value from all predicted log *k* values. Using the *vegdist* function, a Bray-Curtis dissimilarity matrix was constructed for the transformed data. The contribution of each of the five nanodescriptors to these log *k*-based distances between ENMs was tested by way of dbRDA. To this end, the *dbrda* function was used, assessing the marginal effects of the nanodescriptors.

To derive the distance-based AD for BSAI models, Mahalonobis distances were computed for the data set with known Abraham molecule's descriptors using the *vegdist* function. Subsequently, the *metaMDS* function was applied to place each of the molecules in a two-dimensional space by way of nonmetric multidimensional scaling. All compounds with equal or smaller distance to the centroid of all 23 probe compounds in this two-dimensional space were considered to be within the BSAI model AD.

2.4.7 Computational method: system description and simulation parameters

The initial structure of a solvated multiwalled carbon nanotube (MWCNTs), SiO_2, and all the four vitamins, namely, pyridoxine, folate, thiamine, and biotin were built using the CHARMM-GUI builder (Jo et al. 2008). A realistic representation of the ENM structure is required for an accurate prediction of the interaction between the nanoparticle surface and a vitamin. Hence, we considered a 5×5×4 nm^3 SiO_2 slab and a three-layered graphene sheet with an area of 6.5×6.5 nm^2 and periodic boundary conditions, resulting in infinite surface along the Cartesian x-y direction. The SiO_2 ENM used in the experiment usually occurs in a range of 20-200 nm, while the carbon nanotube typically has an outer diameter between 8-15 nm and a length of ~50 µm. We postulated that the sizes of the vitamins examined in this study are tiny compared to the considered ENMs, meaning that a flat surface representation is adequate. All the systems comprise ~40,000 atoms, each varying a little based on the size of the vitamins. All all-atom simulations were performed with GROMACS 2020 (Van der Spoel et al. 2005). The CHARMM36 force field (Pastor and MacKerell 2011) was used for all vitamins, while SiO_2 and MWCNTs parameters were procured from the INTERFACE force field (Heinz et al. 2013), which is integrated within the CHARMM force field. The water molecules were simulated using the TIP3P force field (Mark and Nilsson 2001). A Nosé-Hoover thermostat (Evans and Holian 1985) at 310 K and a Parrinello-Rahman barostat (Parrinello and Rahman 1981) at 1 atm were considered. All hydrogen atoms were constrained with the LINCS algorithm (Hess et al. 1997), and long-range electrostatics were evaluated with particle-mesh Ewald (Essmann et al. 1995). A 1.4 nm cutoff was used for both the electrostatics and LJ interactions. All MD simulations employed a 2 fs time step in the standard Leap-Frog integrator (Birdsall and Langdon 2018), and periodic boundary conditions were considered throughout the study. The setup for biotin and both considered ENMs are visualized in Fig. 2.6. Visual Molecular Dynamics 1.9.3 (VMD) (Humphrey et al. 1996) was used for visualization.

2.4.8 Constrained MD simulation

The potential of mean force (PMF) was determined using metadynamics (Laio and Gervasio 2008) as implemented in the Plumed plugin (Bonomi et al. 2009) patched with GROMACS, at all-atom resolution with explicit solvent. The considered collective variable for the generation of PMFs is the distance between the center of mass (COM) of the SiO_2 or MWCNTs slab and the COM of the respective vitamin. Each system underwent 5000 steps of energy minimization with the standard steepest descent method (Fliege and Svaiter 2000) followed by 100 ps of standard equilibration. Consequently, a 300 ns production run was conducted to generate the free energy profile. Each run was performed on 48 processors, resulting in 25-30 ns per day, that is, 10-12 days per ENM and vitamin. The reduced performance compared to the unconstrained simulations can be attributed to the more frequent output requirement while performing free energy calculations. As previously discussed by Comer et al. (2015), the adsorption affinity (k) of any given vitamin with SiO_2 surface can be calculated from the PMF as

$$k^{calc} = \int_0^c dz \exp\left[-\beta w_i^{calc}(z)\right] \qquad \text{(eq 2.2)}$$

where c is the cut-off distance provided by the onset of the (bulk) plateau region in the PMF, that is, the adsorbed region, $\beta = (k_B T)^{-1}$ corresponds to the reciprocal of the thermal energy, with the Boltzmann constant k_B and temperature T (in Kelvin), and $w_i^{calc}(z)$ is the PMF determined by constrained MD. We have omitted the usual material dependent prefactor to the right-hand side of eq 2.2, because it has to be determined experimentally, and thus introduces uncertainty. In particular, it will not change the ranking of vitamin affinities when considering a single material. In order to compare k^{calc} with log k predictions from QSAR models, the Pearson correlation coefficient (r) was calculated in R using the *cor.test* function of the stats package (*v.* 3.6.3).

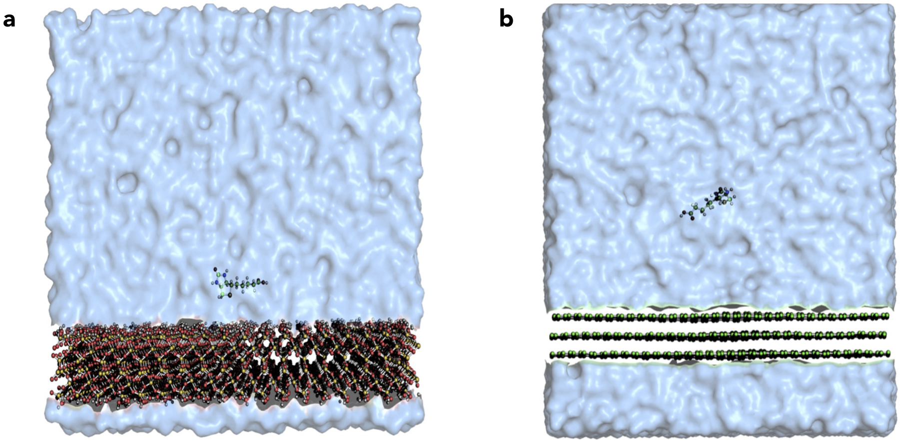

Figure 2.6: *Simulation snapshots for biotin adsorbing on a SiO2* (**a**) *and MWCNTs* (**b**) *surface.* The surfaces extend infinitely along the x-y directions due to periodic boundary conditions. All the atoms are shown as spheres, while bonds are represented as white sticks. The silicon, oxygen, carbon, sulfur, hydrogen atoms are shown in yellow, red, green, yellow and white. For reasons of visual clarity, the water molecules are represented by a blue transparent isosurface of the water density.

2.4.9 Unconstrained MD simulation

Unconstrained simulations were also required in order to differentiate between the several factors, including hydrogen bonding, π-π-stacking, charged (electrostatic) interactions, and others that may play a role in adsorption. For the unconstrained simulation, the same SiO_2 slab setup as before was considered for each vitamin. Unconstrained simulations for MWCNTs were not considered because only LJ interactions between the vitamins and this nanomaterial will play a role, meaning that a breakdown in other types of interactions is not meaningful. It can be inferred that the interaction between MWCNTs and each respective vitamin will purely be LJ interaction. Initially, we performed energy minimization, followed by 10 ns of NPT equilibration and a final production run of 500 ns. Each run was performed on 48 processors, resulting in ~70 ns per day. For the purpose of analysis, a rerun of the MD trajectories was performed to extract the different contributions to the interaction energies between the SiO_2 and each vitamin molecule. The number of hydrogen bonds formed as a function of time was computed using the GROMACS built-in routine gmx hbond.

2.4.10 Data and software availability

The QSAR models, training and validation data sets, SMILES of enteric microbial metabolites, calculated CDK descriptors, applicability domains of QSAR models, and predicted log *k* values are available free of charge as Supporting Information (DOI: 10.5281/zenodo.6800734). Data and results from MD simulations are available via Zenodo (DOI: 10.5281/zenodo.6800734).

Acknowledgment

The authors thank Jim Riviere for his recommendations on available data for the application of the BSAI model. This work was supported by the project PATROLS of the European Union’s Horizon 2020 research and innovation programme under grant number 760813, and by the project NanoInformaTIX under grant number 814426. All MD simulations were carried out on the Dutch national e-infrastructure with the support of SURF Cooperative.

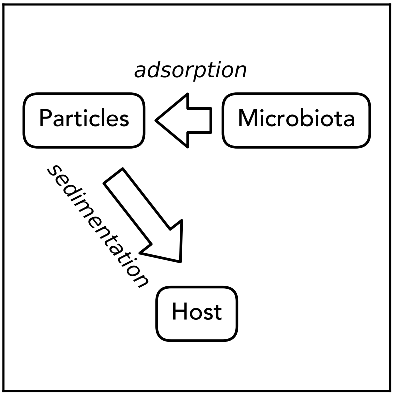
adsorption
Particles
Microbiota
sedimentation
Host

CHAPTER 3

Adsorption of titanium dioxide nanoparticles onto zebrafish eggs affects colonizing microbiota

Bregje W. Brinkmann
Wouter F. Beijk
Redmar C. Vlieg
S. John T. van Noort
Jorge Mejia
Julien L. Colaux
Stéphane Lucas
Gerda Lamers
Willie J. G. M. Peijnenburg
Martina G. Vijver

Published in *Aquatic Toxicology*, 232: 105744 (2021). DOI: 10.1016/j.aquatox.2021.105744
Data is available via *Mendeley Data*. DOI: 10.17632/2d4hcr5cb5.1

Abstract

Teleost fish embryos are protected by two acellular membranes against particulate pollutants that are present in the water column. These membranes provide an effective barrier preventing particle uptake. In this study, we tested the hypothesis that the adsorption of antimicrobial titanium dioxide nanoparticles onto zebrafish eggs nevertheless harms the developing embryo by disturbing early microbial colonization. Zebrafish eggs were exposed during their first day of development to 2, 5 and 10 mg $TiO_2 \cdot L^{-1}$ (NM-105). Additionally, eggs were exposed to gold nanorods to assess the effectiveness of the eggs' membranes in preventing particle uptake, localizing these particles by way of two-photon microscopy. This confirmed that particles accumulate onto zebrafish eggs, without any detectable amounts of particles crossing the protective membranes. By way of particle-induced X-ray emission analysis, we inferred that the titanium dioxide particles could cover 25–45 % of the zebrafish egg surface, where the concentrations of sorbed titanium correlated positively with concentrations of potassium and correlated negatively with concentrations of silicon. A combination of imaging and culture-based microbial identification techniques revealed that the adsorbed particles exerted antimicrobial effects, but resulted in an overall increase of microbial abundance, without any change in heterotrophic microbial activity, as inferred based on carbon substrate utilization. This effect persisted upon hatching, since larvae from particle-exposed eggs still comprised higher microbial abundance than larvae that hatched from control eggs. Notably, pathogenic aeromonads tolerated the antimicrobial properties of the nanoparticles. Overall, our results show that the adsorption of suspended antimicrobial nanoparticles on aquatic eggs can have cascading effects across different life stages of oviparous animals. Our study furthermore suggests that aggregation dynamics may occur that could facilitate the dispersal of pathogenic bacteria through aquatic ecosystems.

Keywords: Host-microbiota interactions; Cascading effects; Particle-Induced X-ray Emission; Two-photon multifocal microscopy; EcoPlate.

3.1 Introduction

Many vertebrate and invertebrate animals, including chordates, arthropods, echinoderms, cnidarians and mollusks, lay eggs that develop *ex vivo* in the water column. Their developing embryos are surrounded by envelopes of varying complexity, ranging from simple coats in cnidarians and nematodes, to acellular membranes with or without external jelly coating in chordates, arthropods, echinoderms and mollusks (Mazinni et al. 1984). In addition to the inner vitelline membrane, eggs of cephalopods, pterygotan insects and teleost fish are surrounded by an external chorion membrane. Together, the chorion and vitelline membranes protect the externally developing embryos against environmental stressors in the water column, including mechanical forces, predators, and pathogens (McMillan 2007).

Research on teleost fish eggs has shown that the chorion constitutes an effective physical barrier against the uptake of particulate pollutants. In medaka fish eggs, for instance, microplastic particles were found to adhere to the villi on the outside of the chorion, and could not be detected within eggs (Beiras et al. 2018). In zebrafish eggs, which do not comprise villi, microplastic particles from the water column attached to the chorion surface in a size-dependent manner. Relatively large microplastic particles, with a primary size of 10-20 μm, adhered in patches to the outside of the chorion, whereas smaller microplastic particles, with a primary size of 1-5 μm, covered the complete chorion surface (Batel et al. 2018). After hatching, only a few of these fluorescently labeled particles could be detected on the skin or in the intestinal tracts of larvae, suggesting that the uptake of the particles across the chorion surface was minor.

Similar to these micro-scaled particles, nanoparticles composed of polystyrene (Van Pomeren et al. 2017a; Lee et al. 2019; Duan et al. 2020), copper, zinc oxide, cobalt(II,III) oxide, nickel oxide (Lin et al. 2011; Brun et al. 2018), silicon dioxide (Fent et al. 2010), titanium dioxide, silver, gold and aluminum oxide (Osborne et al. 2013; Böhme et al. 2015), were found to accumulate on or in chorion structures of zebrafish eggs. A few studies have tracked particles moving through pores in the chorion membrane (Browning et al. 2009; Lee et al. 2013), or have identified nanoparticles in sections of zebrafish larvae that had been exposed to the particles prior to hatching (Lee et al. 2013, 2019). However, these first indications for potential uptake of particles across the chorion and vitelline membrane are hard to interpret due to limitations of the applied detection techniques, including the potential dissociation of the internalized fluorescent dyes that were used to localize particles (Schür et al. 2019), the potential impacts of sample fixation and sectioning on particle distribution, and the low z-confinement of the non-destructive imaging techniques that were used alternatively.

In addition to adverse effects of nanoparticles that may cross the protective membranes of zebrafish eggs, effects of particles that adsorb, and thereby accumulate, onto the chorion, could harm developing embryos. Such effects have for example been reported by Duan et al. (2020), who showed that micro- and nanoplastic particles can block the pores of zebrafish eggs, possibly lowering the oxygen supply to the embryo, resulting in hypoxia. The attached particles moreover caused delayed hatching of the embryos. Furthermore, indirect effects of particle adsorption have been described by Batel et al. (2018), who demonstrated that toxic compounds can leach out of chorion-attached polystyrene particles, onto the developing embryos. A parallel concern, posed by Böhme (2015), is the release of toxic metal ions into zebrafish eggs from chorion-attached metal nanoparticles. A fourth and hypothetical effect of chorion-attached nanoparticles, is the potential of these particles to interfere with establishing host-microbiota interactions, in particular in case the adsorbed particles exhibit antimicrobial activity. The chorion constitutes the first site of microbial colonization in developing zebrafish. After hatching, the chorion microbial community is assumed to play a key role in colonization of the initially sterile, pre-hatch embryo (Llewellyn et al. 2014). Hence, impacts of antimicrobial nanoparticles on chorion-attached microbial consortia may have cascading effects on the composition and functioning of larval microbiota. This is of concern, since already at the larval stage, microbiota is essential to zebrafish health, promoting epithelial proliferation, beta cell expansion and normal neurobehavioral development (Rawls et al. 2004; Hill et al. 2016; Phelps et al. 2017).

In this study, we investigate the hypothesized effects of nanoparticles on establishing zebrafish-microbiota interactions, focusing on the impacts of titanium dioxide nanoparticles ($nTiO_2$). These particles are amongst the most commonly applied antimicrobial metal nanoparticles on the market (Eduok and Coulon 2017), and have already been found to adsorb rapidly onto zebrafish eggs (Shih et al. 2016). We take a three-step approach to study potential adverse effects of $nTiO_2$ on zebrafish colonizing microbiota. Firstly, we investigate how $nTiO_2$ accumulates on zebrafish eggs, quantifying the total amount of titanium sorbed on zebrafish eggs using Particle-Induced X-ray Emission (PIXE) analysis (Lozano et al. 2012). We furthermore assess the effectiveness of the chorion barrier against particle uptake by localizing gold nanorods (nAu) on zebrafish eggs by way of two-photon microscopy. This detection method is non-destructive, highly sensitive and independent of potentially dissociating particle dyes. Secondly, we explore how $nTiO_2$ affects the survival of microbiota on the zebrafish chorion, combining culture-independent imaging techniques and culture-based microbiology techniques. Thirdly, we infer if impacts on egg microbiota can have cascading effects to microbiota of the larval life stage when particle exposure is discontinued, based on approximation of total microbiota abundance and carbon substrate utilization profiles of eggs and larvae. Altogether, these experiments shed light on potential consequences of nanoparticle adsorption on establishing host-microbiota interactions in aquatic oviparous animals.

3.2 Materials and methods

3.2.1 Nanoparticle dispersions

Titanium dioxide nanoparticles ($nTiO_2$) of series NM-105, with primary particles sizes around 15–24 nm, in rutile (12–19 %) and anatase (81–88 %) crystalline phase (Rasmussen et al. 2014), were purchased from the European Commission's Joint Research Centre (Ispra, Italy). For particle localization experiments (section 3.2.5), cetyltrimethylammonium bromide (CTAB)- and polyvinylpyrrolidone (PVP)-capped gold nanorods (nAu) with a diameter of 10 nm, a length of 45 nm and peak surface plasmon resonance at 850 nm, were purchased from Nanopartz (Loveland, USA). For analyses of microbiota composition (section 3.2.8), silver nanoparticles with a primary particle size of 15 nm (series NM-300K; Klein et al. 2011), kindly provided by RAS AG (Regensburg, Germany), were used as a positive control.

Nanoparticle dispersions were prepared in egg water (60 $mg{\cdot}L^{-1}$ Instant Ocean artificial sea salts in demi water; Sera GmbH, Heinsberg, Germany). Stock dispersions with a concentration of 100 $mg\ TiO_2{\cdot}L^{-1}$, 5 $mg\ Au{\cdot}L^{-1}$ (CETAB-capped nAu), 0.5 mg $Au{\cdot}L^{-1}$ (PVP-capped nAu), and 100 $mg\ Ag{\cdot}L^{-1}$, were stabilized for 10 min in an ultrasonic bath (USC200T; VWR, Amsterdam, The Netherlands) at an acoustic power of 12 W, determined following the sonicator calibration standard operation procedure (SOP) delivered in EU FP7 project NANoREG (v 1.1; Jensen et al. 2018). Immediately thereafter, stock dispersions were diluted to obtain exposure concentrations 0, 2, 5 and 10 $mg\ TiO_2{\cdot}L^{-1}$; 0, 0.03 and 0.1 $mg\ Au{\cdot}L^{-1}$; and 0 and 0.25 $mg\ Ag{\cdot}L^{-1}$.

Primary particle size and shape of $nTiO_2$ were characterized by way of transmission electron microscopy (TEM). We applied 5 µL of a 10 $mg\ TiO_2{\cdot}L^{-1}$ $nTiO_2$ dispersion onto a 200 mesh carbon-coated copper TEM grid, and the grid was incubated for > 24 h to dry. Thereafter, images from the grid were acquired at 150,000 times magnification using a 100 kV JEOL (Tokyo, Japan) 1010 transmission electron microscope. The width and length of 30 particles were measured using ImageJ (v. 2.0.0; Abràmoff et al. 2004).

The stability of the $nTiO_2$ dispersions was assessed based on zeta potential (ZP) and hydrodynamic size measurements (z-average size) after 0, 2 and 24 h of incubation in egg water, using a Zetasizer Ultra instrument (Malvern Panalytical, Malvern, UK). We applied the Smoluchowski formula to derive ZP approximations from electrophoretic mobility measurements. The refractive index and absorption value were set to 2.49 and 0.01 respectively, according to Rasmussen et al. (2014). We performed 10 runs for each of the 3 repeated measurements of hydrodynamic size per sample (*n*=3). All other procedures were adopted from the standard operating procedure developed for dynamic light scattering (DLS) analyses in NANoREG (Jensen 2018a).

The sedimentation rate of $nTiO_2$ aggregates was determined in 15 mL, 16.9 mm-diameter conical tubes comprising 9 mL of 2, 5 and 10 mg $TiO_2 \cdot L^{-1}$ (*n*=3). Following 0, 2, and 24 h of incubation, the center 3 mL of the column was sampled. The samples were acidified by adding 0.3 mL of 96 % H_2SO_4, 0.3 mL of 85 % H_3PO_4 and 0.3 mL of 65 % HNO_3, and digested by ultrasonication for 1h at 50 °C in an ultrasonic bath. Titanium concentrations in acid-digested samples were measured by inductively coupled plasma optical emission spectrometry (ICP-OES), using a 5100 ICP-OES spectrometer (Agilent Technologies, Santa Clara, USA).

For characterization of primary particle characteristics and stability of the applied batch of nAu and nAg, we refer to Van Pomeren et al. (2019) and Brinkmann et al. (2020), respectively.

3.2.2 Nanoparticle exposures

Zebrafish eggs were obtained by crossing AB×TL wildtype zebrafish, following standard procedures described in 'The zebrafish book' (https://zfin.org). Adult zebrafish were housed at Leiden University's zebrafish facility at 28 °C in a 14 h:10 h light:dark-cycle. Animal welfare was surveyed by the Animal Welfare Body of Leiden University, and complied with Dutch national regulation on animal experimentation ('Wet op de dierproeven' and 'Dierproevenbesluit 2014'), and European animal welfare regulations (EU Animal Protection Directive 2010/63/EU).

Zebrafish eggs were exposed to nanoparticle dispersions in the 24-well plate setup introduced for nanotoxicity testing by Van Pomeren et al. (2017b). Ten eggs were exposed to 2 mL of exposure medium per 17.5 mm-diameter well from 0 to 1 day post-fertilization (dpf) at 28 °C. Considering the UV-induced toxicity of $nTiO_2$ (Jovanović 2015), well plates were placed under a blacklight (F15W/T5/BL359; Sylvania, Amsterdam, The Netherlands) at a 12 h:12 h light:dark-regime. The blacklight had a UV-A irradiance optimum around 380 nm of 3–6 $\mu W \cdot cm^{-2} \cdot nm^{-1}$ (Fig. S1). Exposures to nAu were performed without UV-irradiation, in the dark.

Eggs that had been exposed from 0 to 1 dpf to $nTiO_2$, nAg or no nanoparticles, were used to investigate potential cascading effects (section 3.2.7 and section 3.2.8). To this end, the eggs were rinsed thrice with egg water immediately following the 0 to 1 dpf exposure. Subsequently, the eggs were transferred to 24-well plates, comprising 10 eggs and 2 mL egg water per well. Incubation took place in the dark at 28 °C until hatching. Possibly as a side-effect of the initial UV-radiation from 0 to 1 dpf, part of the embryos of all treatment groups died or did not hatch from 1 to 3 dpf (Table S1). As a consequence, three instead of four biological replicates were included in analyses of microbiota carbon substrate utilization (section 3.2.8). Chorions of embryos that did not hatch naturally before the end of day 3 were removed manually. Thereafter, egg water was refreshed, and incubation was continued until analyses of larval microbiota at 5 dpf.

In order to verify whether the exposure concentrations of $nTiO_2$ were sublethal to zebrafish larvae, 3 dpf-larvae were exposed for 48 h to 0, 10, 30, 35, 50 and 100 mg $TiO_2 \cdot L^{-1}$ in the 24-well setup described above. Following 24 h of exposure, dead larvae were removed from the wells and exposure media were refreshed. Mortality was scored at 24 h and 48 h of exposure. Following the same procedure, the exposure concentration of nAg (0.25 mg $Ag \cdot L^{-1}$), used as positive control, has already been found to be sublethal to zebrafish larvae (Brinkmann et al. 2020).

3.2.3 Quantification of sorbed titanium

The total amount of sorbed titanium (Ti) of zebrafish eggs was quantified by way of PIXE analysis. This approach allowed to detect 17 additional elements, which were phosphorus, chloride, potassium, sulfur, sodium, magnesium, manganese, calcium, silicon, iron, cobalt, chromium, zinc, aluminum, nickel, copper and vanadium. To prepare the sample material for analysis, 5–40 zebrafish eggs of each exposure concentration were gently rinsed thrice with 5-10 mL egg water immediately following exposure in order to remove loosely attached particles (*n*=6). Subsequently, the eggs were frozen in 1 mL egg water at -20 °C (5 of 6 replicates) or they were frozen without egg water at -20 °C (1 of 6 replicates), and were lyophilized overnight.

The lyophilized zebrafish eggs were applied onto a cylindrical sample holder consisting of three layers: a vitreous carbon substrate at the bottom, followed by a ~40 nm-thick layer of gold (theoretical thickness = 77 ± 8 $\mu g \cdot cm^{-2}$; mean ± standard error of the mean (SEM)), and a final piece of carbon tape on top. The sample material was deposited inside of a 3 mm-diameter hole in the center of the carbon tape. The gold layer, which was applied onto the carbon substrate using a physical vapor deposition system, allowed to determine the thickness of the applied sample material.

For analysis, the sample holder was placed into a vacuum chamber. An incident 2.5 MeV proton beam with a diameter of ~1 mm was directed at the analysis chamber in a 30° angle. A magnetic filter was applied to remove the flux of backscattered protons. X-rays were collected by an Ultra-LEGe detector mounted at a 135 ° angle to the incident beam direction with a magnetic filter to remove the flux of backscattered protons. Backscattered particles were collected by two passivated implanted planar silicon detectors mounted at 165° and 135° to the incident proton beam. Measurements on 4 Certified Reference Materials (MicaMg, MAN, BEN, and DRN), performed at 2.5 MeV, indicated that the energy resolution of the system was excellent, averaging 126.6 ± 1.5 eV (mean ± SEM) measured on the Fe Kα line.

Elastic backscattering spectrometry spectra were reduced with DataFurnace software (calculation code: ndf v.9.6i, graphical interface: windf 9.3.94) (Barradas and Jeynes 2008), and PIXE spectra were analyzed using GUPIX software (by J.L. Campbell; v. 2.2.0; http://pixe.physics.uoguelph.ca/gupix/main/). Masses were corrected for the elemental masses in 1 mL egg water, according to the elemental compositions of Instant Ocean salts determined by Atkinson and Bingman (1996). Elemental masses were expressed as ng per zebrafish egg, assuming that the dry mass of a zebrafish egg at 1 dpf approximates 70 μg (Hachicho et al. 2015).

3.2.4 Calculation of aggregate coverage on eggs

In order to estimate the total surface area of zebrafish eggs that could be covered by $nTiO_2$ aggregates at the measured concentrations of sorbed $nTiO_2$, we first calculated the maximum number of aggregates (N) that could theoretically attach to zebrafish eggs in one monolayer of aggregates in a hexagonal close-packing (packing factor = $\frac{\pi}{2\sqrt{3}}$), assuming that both the zebrafish eggs and aggregates are spherically shaped:

$$N = \frac{4\pi r_{egg}^{2}}{\pi r_{aggregate}^{2}} \times \frac{\pi}{2\sqrt{3}} \qquad \text{(eq 3.1)}$$

The radius of the aggregates ($r_{aggregate}$) was derived from DLS measurements (section 3.2.1) using the hydrodynamic (*z-average*) size estimates obtained at the start of exposure, and the radius of zebrafish eggs (r_{egg}) was derived from confocal microscopy images (section 3.2.6). Subsequently, the mass of this $nTiO_2$-aggregate monolayer (m_N) was calculated following:

$$m_N = \frac{4}{3}\pi r_{aggregate}^{3} \times N \times \rho_{aggregate} \qquad \text{(eq 3.2)}$$

where the effective density of aggregates ($\rho_{aggregate}$) was calculated based on the average area fraction of aggregates covered by particles ($\overline{A_{particle}}$) in TEM pictures (Fig. S2) and the particle density ($\rho_{particle}$) of 4.26 $g{\cdot}cm^{-3}$ determined by Teleki et al. (2008), following:

$$\rho_{aggregate} = \overline{A_{particle}}^{3} \times \rho_{particle} \qquad \text{(eq 3.3)}$$

Finally, the fraction of the surface area of zebrafish eggs that was covered by $nTiO_2$

aggregates was inferred by dividing the mass of one monolayer of $nTiO_2$ aggregates by the measured mass of $nTiO_2$ per egg. For comparison with previous research, the same calculation was performed for primary particles, using the primary particle radius determined by TEM (section 3.2.1) and primary particle density determined by Teleki et al. (2008), instead of aggregate radius and effective aggregate density.

3.2.5 Localization of nanoparticles on eggs

We localized nAu on zebrafish eggs by way of two-photon microscopy to assess the effectiveness of the chorion barrier against nanoparticle uptake. These rods can be detected with high sensitivity at an excitation wavelength of 850 nm, owing to their plasmon-enhanced two-photon luminescence (TPL) at this wavelength. Zebrafish eggs were mounted onto a glass slide with 1.5 % low melting agarose (CAS 39346-81-1; Sigma-Aldrich, Darmstadt, Germany) comprising 200 $\mu g \cdot mL^{-1}$ of the anesthetic tricaine (3-amino-benzoic acid; Sigma-Aldrich) in egg water. As soon as the agarose had solidified, samples were excited with a femtosecond pulsed Ti:Sa laser (Chameleon Ultra; Coherent, Santa Clara, CA, USA), operating in spiral scanning mode (n=14, A=8.912 µm, σ_G=21.166 µm; Van den Broek et al. 2013) at 4 Hz per frame, with an exposure time of 0.2 s. The microscope was equipped with a 25×/1.10 NA objective (CFI75 Apochromat 25XC W; Nikon, Tokio, Japan).

Excitation spectra were acquired between 670 nm and 900 nm at 1 nm-resolution. Laser power was set to 1.44 mW per focus. In order to obtain z-projections, optical sections of control, 0.03 mg $Au \cdot L^{-1}$ exposed and 0.1 mg $Au \cdot L^{-1}$ exposed samples were obtained at an excitation wavelength of 830 nm and with a 0.3 µm pitch over a total sample thickness of 234 µm. The exposure time was set to 0.2 s for control and 0.1 mg $Au \cdot L^{-1}$ exposed samples, and to 0.1 s for 0.03 mg $Au \cdot L^{-1}$ exposed samples. Transmitted light images were obtained using a light emitting diode. Maximum intensity projections of optical sections were computed using ImageJ.

3.2.6 Microscopy-based analysis of zebrafish egg microbiota

The survival of microbiota on eggs was studied using culture-independent imaging techniques, in combination with culture-based microbiota isolation and identification (section 3.2.7). For imaging analysis, we used the BacLight fluorophore mixture (Molecular Probes, Eugene, Oregon), comprising the green fluorescent dye Syto-9 (0.12 µM), labelling all microbes, and the red fluorescent dye propidium iodide (0.73 µM), labelling microbes with damaged cell membranes. Eggs were stained for 15 min at room temperature in 15 mL conical tubes comprising 1–1.5 mL of the fluorophore mixture in egg water (3–6 eggs per tube). Afterwards, eggs were rinsed thrice with 5–10 mL egg water. Fluorescently labeled and rinsed eggs were mounted on a glass bottom petri dish (WilCo-dish; Willco Wells, Amsterdam, The Netherlands), by covering the eggs with 1.5 % low melting agarose (Sigma-Aldrich) containing 400 $\mu g \cdot mL^{-1}$ tricaine (Sigma-Aldrich) in egg water. In total, 45 eggs were imaged of the 0 and 10 mg $TiO_2 \cdot L^{-1}$ exposures, and 24 eggs were imaged of the 2 and 5 mg $TiO_2 \cdot L^{-1}$ exposures.

Labelled microbes were detected using an inverted LSM 880 confocal laser scanning microscope (Zeiss, Oberkochem, Germany) equipped with EC Plan-Neofluar 20×/0.50 NA M27 objective (Zeiss). Syto-9 was excited at 488 nm and detected using a 505–530 BP filter. Propidium idodide was excited sequentially at 543 nm and was detected in a separate channel using a 560 LP filter. From each egg, fifteen consecutive, 2.27 µm-thick optical slices were acquired, starting at the center bottom of the eggs. Each of the optical slices had a surface of 322.56 µm × 322.56 µm. Line averaging was set to 4 to reduce noise.

Image stacks were imported into MATLAB (v. R2020a) using the TIFF-Stack module developed by Muir and Kampa (2015), and were processed in five steps using the DipImage plugin (v. 2.9; www.diplib.org/dipimage). Firstly, we applied a mask to the scanned volume, in order to exclude autofluorescence from yolk globules. The mask corresponded to the volume of a sphere with the same radius as zebrafish eggs (0.6 mm), which was shifted two 2.27 µm-thick optical sections downwards relative to the eggs. Secondly, optical sections were combined by way of maximum intensity projection. Thirdly, projections were converted to binary images, applying a threshold equal to the mean signal of the concerning projection, plus thrice the standard deviation of this signal. Fourthly, at all locations where both Syto9 (all microbes) and propidium iodide (dead microbes) were detected, the signal in the Syto9 projection was set to 0. As a result, signal in Syto9 projections corresponded to live microbes. Finally, binary images were exported in TIFF format to ImageJ, where impulse noise was removed from images using a median filter with a radius of 1 pixel. The total area fraction covered by live microbes (Syto9 projections) or dead microbes (propidium iodide projections) was quantified using ImageJ. Regions with signal that clearly did not correspond to the size and shape of microbes, were omitted. The median surface (and interquantile range (IQR)) of the omitted regions was 0.21 % (IQR= 0–0.71 %) in controls, 0.36 % (IQR= 0–0.57 %) at 2 mg $TiO_2 \cdot L^{-1}$, 0.40 % (IQR=0–1.1 %) at 5 mg $TiO_2 \cdot L^{-1}$ and 0.21% (IQR=0–0.60 %) at 10 mg $TiO_2 \cdot L^{-1}$.

3.2.7 Culture-based analysis of egg and larval microbiota

In addition to culture-independent imaging analysis (section 3.2.6), we determined the number and identity of bacterial isolates on nutrient-rich Lysogeny broth (LB) medium as an approximation of microbiota abundance and composition. Microbiota was isolated from zebrafish eggs and larvae using a tissue homogenizer (Bullet Blender model Blue-CE; Next Advance, New York, USA). From each exposure, 3 embryos or 3 larvae were transferred to a 1.5 mL SafeLock microcentrifuge tube (Eppendorf, Nijmegen, The Netherlands) comprising 200 µL autoclaved egg water and 6 zirconium oxide beads (1.0 mm-diameter; Next Advance). After initial cooling on ice for 2 min, performed to anaesthetize embryos and larvae, samples were homogenized for 15 s at speed 7. The homogenate was cooled on ice for 10 s immediately thereafter, to minimize potential damage to microbes due to heat generated in the tissue homogenizer. Subsequently, the homogenization and cooling steps were repeated seven times, to obtain a total homogenization time of 2 min. The sample homogenate was diluted 10, 100 and 1000 times in autoclaved egg water. Of each dilution, and of the non-diluted homogenate, 50 µL was plated on solid LB growth medium. After two days of incubation at 28 °C, colony-forming units (CFUs) were counted as a measure of live microbiota abundance. Incubations were continued for 2 more days, and any additional colonies were counted. Dilutions comprising 22–240 CFUs were used to assess microbiota abundance.

In order to identify what bacterial species occurred on zebrafish eggs, 10 CFUs isolated from $nTiO_2$-exposed and non-exposed zebrafish eggs (1 dpf) were selected for 16S rRNA-based identification (*n*=3). We aimed to identify as many different species as possible, and hence selected equal numbers of CFUs of each of the colony morphologies that appeared on LB plates. Colonies were selected from 1:10 dilutions of control samples, and 1:100 dilutions of exposed samples, comprising similar CFU counts (76 ± 21 CFUs per plate; mean ± SEM), to exclude potential dilution effects on microbial composition. Of each selected colony, a 1505-nt fragment of the 16S rRNA gene was amplified using universal bacterial primers (27F and 1492R). Polymerase-chain reactions, Sanger sequencing and species identification were performed as we described before (Brinkmann et al. 2020).

For two reasons, the above methods used to isolate, quantify and identify zebrafish microbes, likely underestimate microbiota abundance and diversity. Firstly, the isolation method is detrimental to a small fraction of the microbiota, as determined in our previous study (Brinkmann et al. 2020). Secondly, some bacteria may require different nutrients than present in LB medium, longer incubation times than 4 days, or alternative incubation conditions. For this reason, both the number and identity of microbial isolates as determined in this study, should be interpreted as a relative rather than an absolute representation of zebrafish larvae associated microbiota across the different experimental treatments.

3.2.8 Carbon-substrate utilization profiles of eggs and larval microbiota

We used EcoPlates (Biolog, Hayward, California) to characterize the carbon substrate utilization of zebrafish microbiota. These plates are commercially available and comprise 96-wells with 31 different lyophilized carbon substrates and 1 blank in triplo. In addition to the carbon substrates, each EcoPlate well comprises the redox dye tetrazolium violet that can be used to quantify the utilization of the corresponding carbon substrates colorimetrically at a wavelength of 590 nm.

Microbiota for EcoPlate analyses was isolated from 12 larvae of each biological replicate (*n*=3, three tubes with four larvae each), following the procedure described in section 3.2.7. Larvae homogenate was pooled and diluted with 14.4 mL sterile egg water. We inoculated EcoPlates with 100 µL of diluted microbiota per well, and incubated the plates in the dark at 28 °C. In order to test if zebrafish enzymes contribute to color development on EcoPlates, homogenate of germ-free zebrafish larvae at 5 dpf, obtained following Brinkmann et al. (2020), was inoculated on an additional EcoPlate. The optical density (*OD*) of EcoPlates was measured daily, from 1 to 4 days of incubation, at 590 nm with an Infinite M1000 plate reader (Tecan, Männedorf, Switzerland).

Ecoplate substrate utilization profiles of zebrafish larvae microbiota were compared between the different experimental conditions, based on the rate of color development between 1 and 2 days of incubation, expressed in *OD* units per hour. During this part of the incubation, color development increased linearly (Fig. S3). Additionally, four functional community parameters were derived from EcoPlate well-color development. Firstly, the average well color development (*AWCD*) was calculated following (Garland and Mills 1991):

$$AWCD = \frac{\sum_{i=1}^{S} OD_i - OD_c}{31} \qquad \text{(eq 3.4)}$$

where OD_i is the well color development for the *i*th carbon substrates *S*, and OD_c is the color development in the control well without carbon substrate. In some cases, where $OD_i < OD_c$, this produced negative values, which were set to 0. Secondly, Ecoplate carbon substrate utilization richness (*R*) was calculated as the sum of all substrates where $OD_i > 0.25$, according to Sillen et al. (2015):

$$R = \sum_{\{i \mid (OD_i > 0.25)\}}^{S} S(i) \qquad \text{(eq 3.5)}$$

Thirdly, color development was normalized, and the Shannon diversity index (*H'*) was calculated as a measure of the diversity in utilized carbon substrates, following:

$$p_i = \frac{\sum_{i=1}^{S} OD_i - OD_c}{AWCD} \qquad \text{(eq 3.6a)}$$

$$H' = -\sum_{i=1}^{S}(p_i \ \ln p_i) \qquad \text{(eq 3.6b)}$$

where p_i represents the normalized color development. Fourthly, to characterize the evenness of carbon utilization across the different substrates, the Pielou's evenness index (*J'*) was calculated as:

$$J' = \frac{H'}{\ln{(R)}} \qquad \text{(eq 3.7)}$$

3.2.9 Statistical analyses

Statistical analyses were performed in R (v. 3.6.3; www.r-project.org). Mean and SEM are presented, calculated using the 'bear' package (v. 2.8.7; pkpd.kmu.edu.tw/bear). In case data did not follow a normal distribution, median and IQR values are presented. Figures were plotted using Python (v. 3.6.5) with packages 'numpy' (v.1.19.1), 'pandas' (v.0.23.3), 'matplotlib' (v.3.1.3), and 'scipy' (v.1.5.0).

An overview of the applied statistical models is presented in Table 3.1. Only significant interactions between explanatory variables were included in statistical models. In case explanatory variables were factorial, two-way ANOVA tests were combined with Tukey's HSD post-hoc test. Spearman rank correlations between elemental concentrations of the 18 elements determined by PIXE analysis, were computed using the 'Hmisc' package (v. 4.4–0). For CLSM and EcoPlate data, data included repeated measurements from the same exposure well (CLSM data) or EcoPlate. We accounted for this in a nested ANOVA design using the 'nlme' (v.3.1–144) package, including exposure well or EcoPlate as the random variable. Cluster analyses of EcoPlate data were performed using the 'vegan' package (v.2.5–6), based on Bray-Curtis dissimilarity matrices, computed using the *vegdist* function. We compared dissimilarity matrices by way of Permutational multivariate analysis of variance (PERMANOVA) with 999 permutations, using the *adonis* function. Permutations were restricted to the exposure treatment groups and were not allowed to occur among replicates of the same exposure. Clusters were visualized in non-metric multidimensional scaling (nMDS) plots, obtained using the *metaMDS* function.

For all models, model assumptions were checked by inspecting the model's diagnostic Q-Q plot and residuals vs. fit plot. Equality of variance between groups was tested using Levene's test from the 'car' package (v. 3.0–7). For cluster analyses, the *betadisper* function was used to test if multivariate spread across matrices was similar. The Shapiro-Wilk test for normality was performed to test if residuals followed a normal distribution. In several cases, square-root, logarithmic or rank transformation was required to ensure this (Table 3.1). Skewness was quantified using the 'e1071' package (v. 1.7–3).

Table 3.1: Performed statistical analyses. *Abbreviations*: ANOVA, analysis of variance; AWCD, average well-color development; CLSM, confocal laser scanning microscopy; CFU, colony-forming unit; DLS, dynamic light scattering; log, logarithmic; PERMANOVA, permutational analysis of variance; PIXE, particle-induced X-ray emission; sqrt, square root; ZP, zeta potential.

Experimental analysis	*Response variable*	*Statistical model*	*Explanatory variables*	*Significant interaction*	*Transformation*
DLS	Hydrodynamic size	Two-way ANOVA	Incubation time × exposure concentration	yes	none
	ZP	Two-way ANOVA	Incubation time + exposure concentration	no	none [a]
PIXE	TiO_2 concentration per egg	Two-way ANOVA	Exposure concentration [b]	N.A.	log
	Elemental concentrations per egg	Spearman rank correlations	N.A.	N.A.	none
CLSM	Total microbial cover	Nested ANOVA	Exposure concentration	N.A.	sqrt
	Dead or live microbial cover	Nested ANOVA	Fraction (dead or live)	N.A.	log (at 0 mg $TiO_2 \cdot L^{-1}$), none (at 2 mg $TiO_2 \cdot L^{-1}$), sqrt (at 5 and 10 mg $TiO_2 \cdot L^{-1}$) [c]
CFU abundances	CFU count	Two-way ANOVA	Life stage + exposure concentration	no	log
EcoPlate	Carbon substrate profile	PERMANOVA	Life stage × exposure concentration	yes	none
	AWCD	Nested ANOVA	Life stage + exposure concentration	no	none
	Richness	Nested ANOVA	Life stage + exposure concentration	no	none
	Shannon diversity index	Nested ANOVA	Life stage + exposure concentration	no	none
	Evenness	Nested ANOVA	Life stage + exposure concentration	no	log (data without nAg) none (data with nAg)

[a] Only if one outlier with positive ZP was excluded, residuals followed a normal distribution. As this did not affect the results of the ANOVA test, the outlier was not excluded from the model.

[b] Exposure concentration was included as a factor, in order to obtain a normal distribution of model residuals. Despite log transformation of the data, the distribution of variance over the different exposure concentrations remained slightly unequal ($F_{3,20}$=3.61, p=0.03), and hence results should be treated with care.

[c] Residuals from the 10 mg $TiO_2 \cdot L^{-1}$ model deviated slightly from a normal distribution according to a Shapiro-Wilk test for normality (W=0.98, p=0.03). As both histogram shape and skewness (-0.02) did not indicate clear deviations from normality, the ANOVA results are presented nonetheless.

3.3 Results

3.3.1 Nanoparticle shape, size and stability

Primary $nTiO_2$ particles had irregular, angulated shapes with a width of 21.3 ± 1.2 nm and a length of 28.0 ± 1.5 nm ($n = 30$) (Fig. 3.1a). Following dispersion, the particles formed aggregates with a hydrodynamic size of 1.31 ± 0.17 µm, irrespective of the exposure concentration (Table 3.2). Over the 24-h exposure time, the size of the aggregates changed ($F_{1,23}=14.6$, $p=0.0009$) in a concentration-dependent manner ($F_{1,23}=11.3$, $p=0.003$), reaching hydrodynamic sizes of 1.22 ± 0.38 µm, 2.50 ± 0.89 µm, and 4.08 ± 1.08 µm at the end of exposure, at the nominal exposure concentrations of 2, 5 and 10 mg $TiO_2 \cdot L^{-1}$, respectively ($F_{1,23}=6.3$, $p=0.02$). The sedimentation analysis indicated that all aggregates had reached the bottom of the well in 14.0 h, 11.4 h and 10.5 h at the 2, 5 and 10 mg $TiO_2 \cdot L^{-1}$ exposures, respectively (Fig. S4). This suggests that particle stability decreased at increasing exposure concentrations. Accordingly, the zeta potential of aggregates was concentration-dependent ($F_{1,23}=33.3$, $p=6.1 \cdot 10^{-6}$), averaging -19.1 ± 0.30 mV, -14.2 ± 0.92 mV, and -10.0 ± 1.7 mV at nominal exposure concentrations of 2, 5 and 10 mg $TiO_2 \cdot L^{-1}$, respectively. At all concentrations, the zeta potential of the aggregates did not change over time ($F_{1,23}=1.5$, $p>0.05$) (Table 3.2).

3.3.2 Sorption of nanoparticles to zebrafish eggs

Akin to the aggregation of $nTiO_2$, sorption of $nTiO_2$ to zebrafish eggs was concentration-dependent ($F_{3,20} = 1.0 \cdot 10^3$, $p < 2.0 \cdot 10^{-16}$; Fig. 3.1b). No titanium could be detected in zebrafish eggs that were not exposed to $nTiO_2$ (with a limit of detection of 3.6 ± 1.0 ng per egg). A lower concentration of titanium was detected at the exposure concentration of 2 mg $TiO_2 \cdot L^{-1}$, averaging 30.4 ± 9.0 ng per egg, than at the highest two

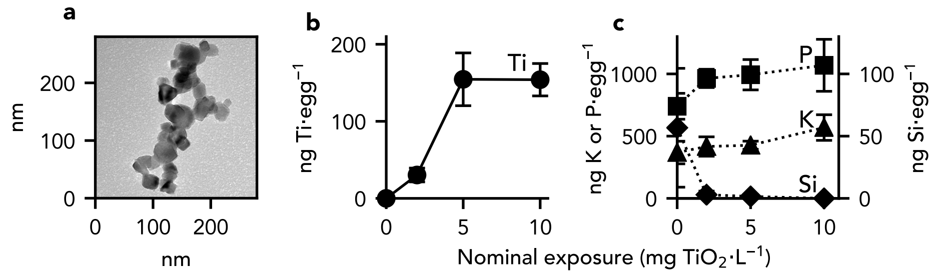

Figure 3.1: *Quantification of the sorption of titanium (Ti) and correlated elements on zebrafish eggs.* Subplots show a TEM picture of the TiO_2 nanoparticles (**a**), quantification of total ad- and/or absorbed Ti at the nominal exposure concentrations (circles) (**b**), and quantification of phosphorus (P, squares), potassium (K, triangles) and silicon (Si, diamonds) (**c**). Mean and SEM concentrations of all quantified elements (*n*=6) are presented in Table S2.

Table 3.2: Mean hydrodynamic size and zeta potential of $nTiO_2$ aggregates over one day of incubation in egg water. Mean and standard error of the mean are presented (*n*=3).

	Exposure	*Incubation time (h)*		
	(mg $TiO_2 \cdot L^{-1}$)	*0*	*1.5*	*24*
Hydrodynamic size (μm)	2	1.63 ± 0.40	1.31 ± 0.38	1.22 ± 0.38
	5	0.94 ± 0.12	1.00 ± 0.13	2.50 ± 0.89
	10	1.34 ± 0.19	1.55 ± 0.09	4.10 ± 1.08
Zeta potential (mV)	2	-18.9 ± 0.4	-18.4 ± 0.3	-19.8 ± 0.5
	5	-15.4 ± 1.6	-12.8 ± 0.5	-14.2 ± 2.3
	10	-6.5 ± 4.2	-9.9 ± 2.0	-13.5 ± 0.7

exposure concentrations, averaging 155 ± 34 ng at 5 mg $TiO_2 \cdot L^{-1}$ and 154 ± 21 ng at 10 mg $TiO_2 \cdot L^{-1}$ ($p=9.0 \cdot 10^{-6}$). The latter two concentrations did not differ significantly ($p>0.05$), suggesting that sorption of $nTiO_2$ had saturated at this concentration of sorbed Ti, averaging 153 ± 19 ng Ti (257 ± 32 ng TiO_2) per egg. Based on the size of the $nTiO_2$ aggregates determined by DLS (Table 3.2), the effective density of aggregates (0.328 $g \cdot cm^{-3}$) determined from TEM pictures (Fig. S2), and the radius of zebrafish eggs determined from CLSM images (0.6 mm), aggregates of this amount of $nTiO_2$ could cover 25.2 % of the egg surface in a hexagonal close-packing. In non-aggregated form, the corresponding number of primary particles could cover 44.8 % of the zebrafish egg surface.

Fifteen other elements were detected on zebrafish eggs, including phosphorus, chloride, potassium, sulfur, sodium, magnesium, manganese, calcium, silicon, iron, cobalt, chromium, zinc, aluminum and nickel (Table S2). Of all these elements, only the concentration of potassium correlated positively with the concentration of titanium ($r_s=0.45$, $n=24$, $p=0.03$). There was a slight but insignificant correlation between concentrations of titanium and phosphorus ($r_s=0.33$, $n=24$, $p=0.12$). The concentrations of silicon per egg correlated negatively with concentrations of titanium ($r_s=-0.46$, $n=24$, $p=0.02$) (Fig. 3.1c).

3.3.3 Internalization of nanoparticles by zebrafish eggs

In order to investigate if nanoparticles can be internalized by zebrafish eggs, we localized nAu on zebrafish eggs following 24 h of exposure by way of two-photon multifocal microscopy (Fig. 3.2). We firstly used CETAB-stabilized nanorods to study how nAu appears in two-photon images. Due to their high stability, these particles can be identified based on their TPL optimum at an excitation wavelength around 850 nm, resulting from plasmon resonance. nAu appeared as bright spots in two-photon images (Fig. 3.2a–c). Background fluorescence, as detected in images of non-exposed eggs, was visible as a blur comprising dim spots that lacked the characteristic emission optimum

(Fig. 3.2d–f). We subsequently used this information to localize PVP-coated nanorods with much lower toxicity, at increasing exposure concentrations. It was not possible to localize these rods based on their emission optima directly, because aggregation of these rods, resulting from their lower stability, can shift the wavelength of emission optima. In z-projections of zebrafish eggs exposed to increasing concentrations of nAu, increasing amounts of nAu could be detected on the surface of zebrafish eggs (Fig. 3.2g–l). Inside of the zebrafish eggs, a background blur was visible at the location of the head of the developing embryo. However, no bright spots corresponding to excited nAu could be detected inside of zebrafish eggs (Fig. 3.2i, Fig. S5).

3.3.4 Survival of microbiota on zebrafish eggs

Using fluorescence microscopy, ovoid and rod-shaped microbes could be identified on the surface of zebrafish eggs (Fig. 3.3a). Without exposure to $nTiO_2$, the microbes were spread homogeneously over the chorion, covering 0.43 ± 0.06 % of the total chorion surface. A 2-fold higher surface area of the chorion was covered by live microbes (0.29 ± 0.06 %) than by dead microbes (0.14 ± 0.01 %). However, this difference was not significant ($F_{1,79} = 1.48$, $p > 0.05$), possibly due to the required log-transformation of the data on coverage. Exposure to $nTiO_2$ resulted in a higher total cover of live and dead microbes on zebrafish eggs ($F_{1,127} = 7.77$, $p=0.006$) (Fig. 3.3b; Table S3). It moreover affected to ratio between the cover of dead and live microbes on the chorion. At 2 mg $TiO_2 \cdot L^{-1}$, dead microbes covered a larger surface area of zebrafish eggs than live microbes ($F_{1,41} = 8.58$, $p = 0.006$). In contrast, at 5 and 10 mg $TiO_2 \cdot L^{-1}$, equal surface areas were covered by dead and live microbes ($F_{1,41} = 1.52$, $p > 0.05$ and $F_{1,79} = 0.30$, $p > 0.05$, respectively).

The bacteria that could be isolated from zebrafish eggs belonged to five different genera (Fig. 3.3c, Table S4). Most (33) of the isolated 16S rRNA sequences had high sequence similarity (98-100 % identity) to sequences of identified bacterial species included in the NCBI database. The seven sequences with lower similarity (93–98 % identity) corresponded to the same bacterial species as the sequences with high similarity. Eggs of both $nTiO_2$-exposed and non-exposed conditions comprised bacteria of the genera *Aeromonas*, *Pseudomonas* and *Delftia*. The aeromonads had highest 16S rRNA sequence similarity to the species *A. hydrophila, A. sobria. A. salmonicida, A. veronii,* or *A. diversa*; the pseudomonads were most similar to *P. mosselii, P. putida, P. fluorescens, P. entomophila, P. hunanensis,* or *P.* cf. *monteilii*; and the *Delftia* bacteria had highest sequence similarity to either *D. lacustris* or *D. tsuruhatensis*. In addition to these genera, the bacteria *Chryseobacterium massiliae* and *Stenotrophomonas maltophilia* could be identified among bacterial isolates from exposed eggs.

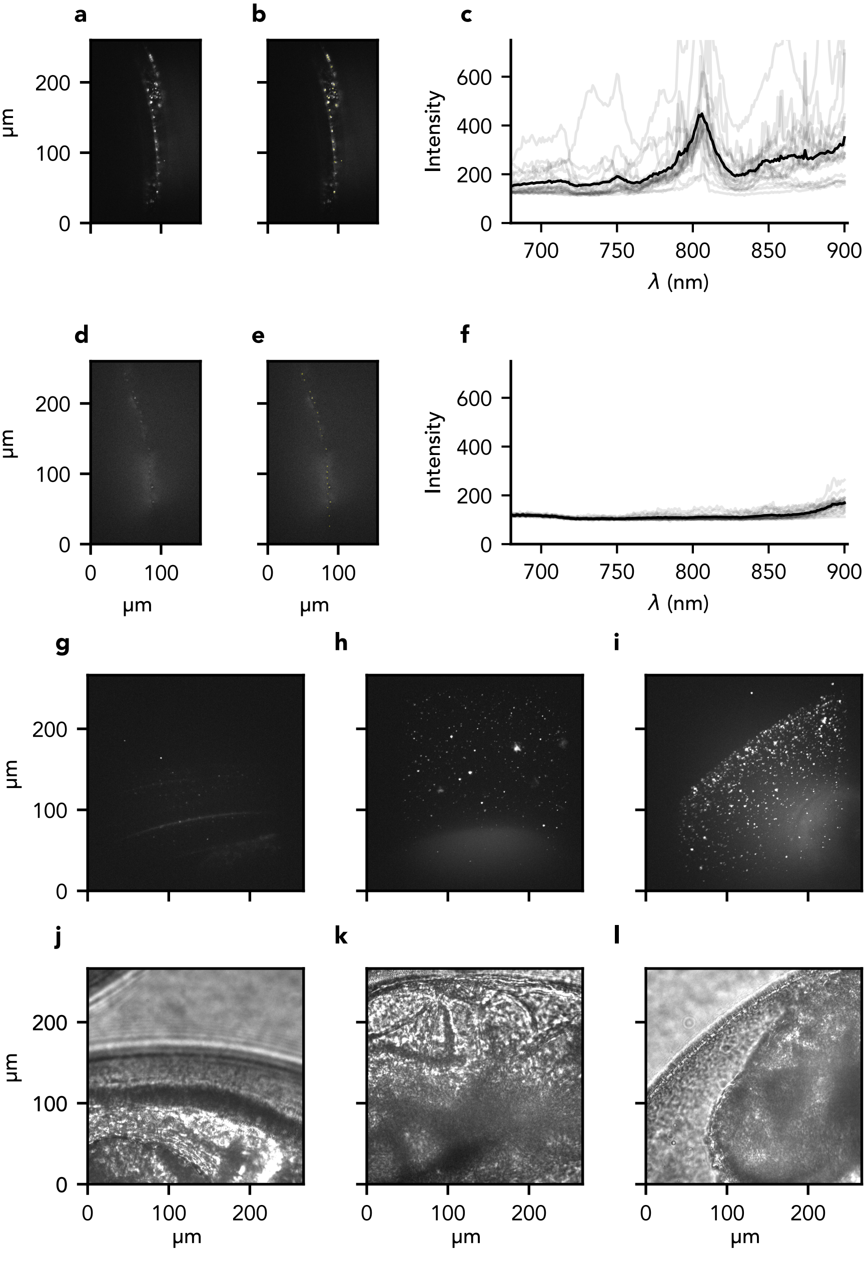

Figure 3.2: *Two-photon microscopy detection of gold nanorods on zebrafish eggs at 1 day post-fertilization.* Subplots show representative images of a zebrafish embryo following 24 h-exposure to 0.03 mg Au·L^{-1} CETAB-coated gold nanorods (**a**), with 20 regions of interest (ROIs) (**b**) used to obtain excitation spectra (**c**); a zebrafish embryo that had not been exposed to nanorods (**d**), with 20 ROIs (**e**) that were used to obtain excitation spectra (**f**); and z-projections of embryos that had been exposed for 24 h to no nanorods (**g**), 0.03 mg Au·L-1 PVP-coated gold nanorods (**h**), and 0.1 mg Au·L^{-1} PVP-coated gold nanorods (**i**). Transmitted light images **j**), **k**), and **l**) correspond to emitted light images **g**), **h**) and **i**), respectively. The black line in graph **c**) and **f**) depict the mean intensity of the intensity of all 20 ROIs, indicated with gray lines.

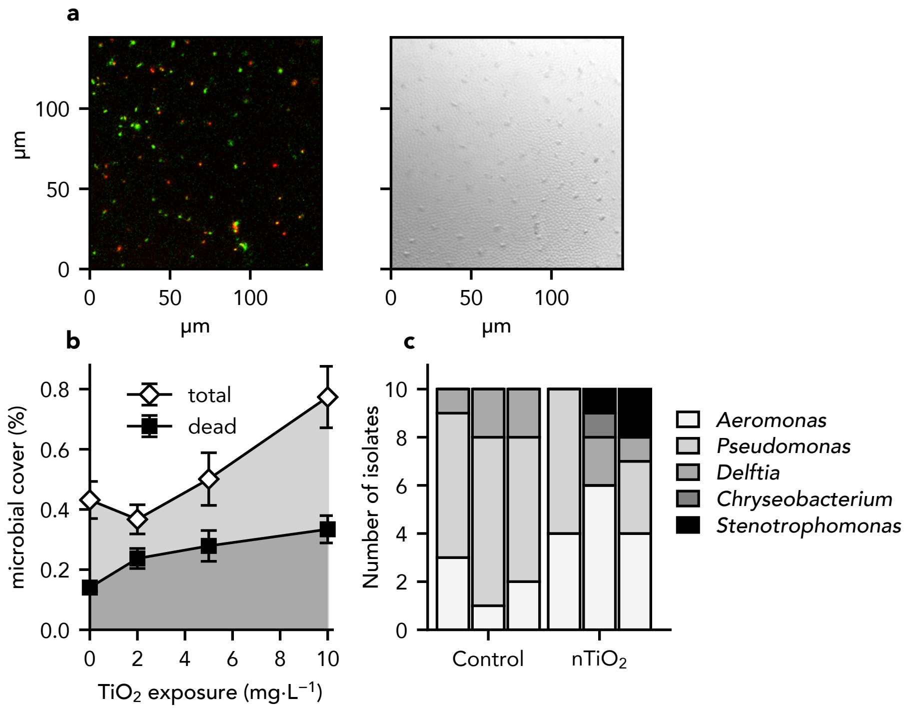

Figure 3.3: *Impacts of $nTiO_2$ on microbial communities establishing on zebrafish eggs.* Subplots show a CLSM picture of dead (red) and live (green) microbes (**a**, left picture) on the surface of a zebrafish egg (**a**, right picture); the impact of 24 h-exposure to $nTiO_2$ on total microbial cover (white diamonds) and dead microbial cover (black squares) on the surface of zebrafish eggs (n=24–45; mean ± SEM are presented) (**b**); and the identity of bacteria isolated from zebrafish eggs exposed for 24 h to no nanoparticles ('Control'; left bars) and 5 mg $nTiO_2 \cdot L^{-1}$ ('$nTiO_2$'; right bars). Each bar represents 10 bacterial isolates from 1 biological replicate. The corresponding BLAST results are included in Supplementary Table S4.

3.3.5 Cascading effects on microbiota of zebrafish larvae

All of the applied concentrations of $nTiO_2$ were sublethal to zebrafish larvae during 24 h of exposure (Fig. S6). Given the saturation of $nTiO_2$ on zebrafish eggs at an exposure concentration of 5 mg $TiO_2 \cdot L^{-1}$, we selected this embryonic exposure scenario to study potential cascading effects on larval microbiota abundance and composition. As a positive control, the highest sublethal concentration of nAg (0.25 mg $Ag \cdot L^{-1}$) was selected, which has previously been confirmed to exert high antimicrobial activity. In accordance with confocal microscopy results, exposure to $nTiO_2$ resulted in a significantly higher number of colony-forming units (CFUs) per egg than incubation in egg water without nanoparticles ($F_{1,13}$=22.95, p=0.00035) (Fig. 3.4, Table S3). From

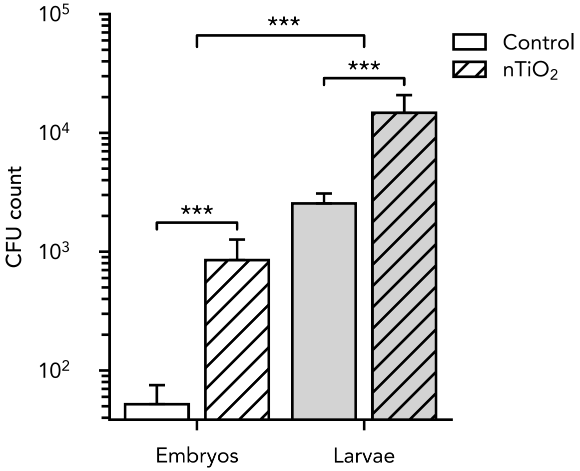

Figure 3.4: *Total count of colony-forming units* (CFUs) associated per zebrafish embryo (1 dpf; white bars) or per zebrafish larva (5 dpf; gray bars) following embryonic exposure (0-1 dpf) to egg water without nanoparticles ('Control'; non-hatched, white fill), and egg water comprising $nTiO_2$ (5 mg $TiO_2 \cdot L^{-1}$; hatched fill). Bars represent means with standard error of the mean (*n*=3). Asterisks indicate significant differences ($p<0.001$).

surrounding water without $nTiO_2$, a median number of $8.2 \cdot 10^2$ $CFUs \cdot mL^{-1}$ (IQR = $4.2 \cdot 10^2$–$1.8 \cdot 10^3$ $CFUs \cdot mL^{-1}$, *n*=23) could be isolated at 6 hpf, which corresponded to $1.6 \cdot 10^2$ $CFUs \cdot egg^{-1}$ (IQR = 83–$3.7 \cdot 10^2$ $CFUs \cdot egg^{-1}$, *n*=23). Larvae comprised higher numbers of CFUs than eggs ($F_{1,13}$=50.90, $p=3.5 \cdot 10^{-6}$). This difference in microbial abundance between the exposed and non-exposed group persisted until 5 dpf (Fig. 3.4; Table S3).

We used EcoPlates to assess the functional composition of heterotrophic zebrafish microbiota based on carbon substrate utilization. The activity of zebrafish enzymes did not interfere with this analysis, since carbon substrate utilization by germ-free larvae resulted in a negligible average well-color development (AWCD) of 0.007 ± 0.0008 in comparison to carbon substrate utilization of microbially colonized larvae (AWCD = 0.45 ± 0.01). In contrast to microbiota abundance, the functional composition of the zebrafish egg microbiota did not differ between exposed and non-exposed groups, as determined based on carbon substrate utilization ($F_{1,28}$=0.68, $p>0.05$; Fig. 3.5a, Fig. S8a). Larvae had a functionally distinct microbiota composition ($F_{1,28}$=11.21, $p=0.001$), which diverged slightly following exposure to $nTiO_2$, as indicated by a significant interaction between life stage and exposure ($F_{1,28}$= 5.63, $p=0.001$; Fig. 3.5a, Fig. S8b). However, compared to the effects of embryonic exposure to sublethal concentrations of nAg, impacts of sublethal concentrations of $nTiO_2$ on the functional microbiota composition of zebrafish larvae were minor (Fig. S8-S9). Accordingly, exposure to $nTiO_2$ did not result in differences in AWCD (0.45 ± 0.01; $F_{1,31}$= 0.27, *p*>0.05; Fig. 3.5b), the diversity in utilized carbon substrates ($F_{1,31}$= 0.57, *p*>0.05; 2.75 ± 0.017 in larvae and 2.63 ± 0.041 in eggs, $F_{1,31}$=15.0; *p*=0.0005; Fig.3.5c), and the richness in utilized carbon substrates (14.5 ± 0.34; $F_{1,31}$=1.34, *p*>0.05; Fig. 3.5d). For comparison, although nAg exposed and non-exposed larvae had similar microbiota abundance (Fig. S7), exposure to nAg resulted in significantly lower AWCD of larval microbiota (0.33 ± 0.02; $F_{2,22}$=18.13, *p*<0.0001; Fig. S8b). No difference in the diversity in utilized carbon substrates (2.77 ± 0.02; $F_{2,22}$=1.51, *p*=0.24; Fig. S8c) and richness of utilized carbon substrates (14.85 ± 0.40; $F_{2,22}$=0.055, *p*>0.05; Fig. S8d) of larval microbiota could be detected following exposure to nAg. The evenness of the egg and larval microbiota carbon substrate utilization could only be compared with care, as residuals did not follow a normal distribution, even following log or rank transformation. However, the carbon substrate utilization profile of embryos appeared to be slightly more even (1.00 ± 0.004) than that of larvae (1.02 ± 0.006; $F_{1,31}$=8.78, *p*=0.006). The evenness of larval microbiota carbon substrate utilization was not affected by exposure to $nTiO_2$ or nAg (1.03 ± 0.007; $F_{2,22}$=2.65, *p*>0.05; Fig. S8e).

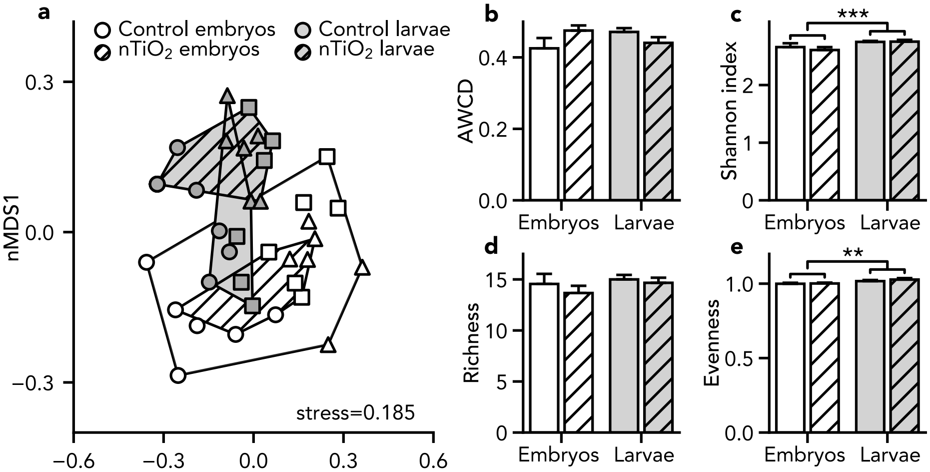

Figure 3.5: *Carbon substrate utilization characteristics of microbiota isolated from zebrafish embryos* (1 dpf) *and zebrafish larvae* (5 dpf) following embryonic exposure (0-1 dpf) to egg water without nanoparticles (non-hatched), and egg water comprising $nTiO_2$ (5 mg $TiO_2 \cdot L^{-1}$; hatched fill). Subplots represent carbon substrate utilization profiles (**a**), total well color development (TWCD) (**b**), Shannon index (**c**), richness (**d**), and evenness (**e**). Each biological replicate, comprising three measurement replicates, is depicted with a unique marker shape. Bars represent means with standard error of the mean (n=3). Asterisks indicate significant differences (**, *p*<0.01; ***, *p*<0.001).

3.4 Discussion

Teleost fish embryos, developing *ex vivo* in the water column, are protected against particulate pollutants by two acellular envelopes: the inner vitelline and the outer chorion membrane. Despite the efficacy of this physical barrier against particles in the environment, as confirmed in several studies (Böhme 2015; Van Pomeren et al. 2017a; Batel et al. 2018; Brun et al. 2018; Lee et al. 2019; Duan et al. 2020), the adsorption and enrichment of particles on the chorion surface has been related to several adverse effects. These include the obstruction of gas exchange across the chorion surface (Duan et al. 2020), and the leaching of toxic chemicals and ions out of chorion-attached particles into the eggs (Böhme 2015; Batel et al. 2018). Given the antimicrobial nature of many metal nanoparticles, and the importance of early microbial colonization to larval development (Rawls et al. 2004; Hill et al. 2016; Phelps et al. 2017), we hypothesized that the disruption of the chorion-attached microbial community constitutes a hitherto unexplored adverse effect of concern. In this study, we took a three-step approach to investigate this, focusing on the impacts of titanium dioxide nanoparticles on zebrafish embryos. Firstly, we inferred if the particles accumulated on the chorion surface; secondly, we studied how this affected the microbial community that establishes on the chorion surface; and thirdly, we examined if this resulted in any cascading effects on the larval microbial community.

3.4.1 Internalization of nanoparticles by zebrafish eggs

As a first step, we assessed if nanoparticles can cross the external membranes of zebrafish eggs, employing the advantages of two-photon microscopy for the localization of nAu. This approach builds on previous knowledge obtained using fluorescently labeled particles, or using destructive analyses such as Laser Ablation Inductively Coupled Plasma Mass Spectrometry (LA-ICP-MS), enabling live imaging without the risk of fluorescent dye dissociation, with less autofluorescence background than with the use of fluorophores, and providing a high z-confinement with large penetration depth (Van Den Broek 2013). Using this approach, we did not detect any particles inside of zebrafish eggs, yet observed a high and concentration-dependent accumulation of nanoparticles on the chorion surface. Considering the high sensitivity of two-photon microscopy detection of nAu, this suggests that the particles did not cross the chorion surface. Moreover, in view of the lower stability of $nTiO_2$ than nAu, resulting in larger aggregate sizes, it is even less likely that $nTiO_2$ aggregates can cross the chorion pores. These findings agree with previous results, showing an accumulation of polystyrene nanoparticles (Van Pomeren et al. 2017a; Duan et al. 2020), silicon nanoparticles (Fent et al. 2010), copper nanoparticles (Brun et al. 2018), titanium dioxide, silver, gold, and aluminum oxide nanoparticles (Osborne et al. 2013; Böhme et al. 2015) onto or inside of zebrafish chorions, with limited or no detectable uptake of particles by the embryos.

Using PIXE to quantify elemental concentrations of Ti, we observed a concentration-dependent accumulation of $nTiO_2$ onto zebrafish eggs, reaching a maximum of 154.3 ± 19.2 ng Ti (257.4 ± 32.0 ng TiO_2) per egg at a nominal exposure concentration of 5 mg $TiO_2{\cdot}L^{-1}$. Previous studies have shown that small (1-5 µm) microplastic particles (Batel et al. 2018) and metal nanoparticles (Böhme 2015; Shih et al. 2016) can cover the zebrafish chorion completely. Although our estimates of the chorion coverage are lower, we nevertheless estimated that a relatively large surface of the chorion could be covered by TiO_2 aggregates (25.2 %) or primary particles (44.8 %), as compared to the surface of the chorion that is occupied by microbes (<1%). Studies applying more optimal sorption conditions, obtained even higher particle coverages. In an experimental setup where eggs were exposed to nanoparticles in a rotating glass vial, Shih et al. (2016) reached a maximum of 6 tightly bound layers of $nTiO_2$ in a hexagonal close-packing of primary particles. Comparably, Lin et al. (2015) calculated that 2–17 layers of primary TiO_2 particles attached to cells of algae *Raphidocelis subcapitata* in a hexagonal close-packing.

The accumulation of TiO_2 coincided with changes in the elemental concentrations of silicon and potassium of zebrafish eggs. Concentrations of Ti correlated negatively with silicon, which could result from competition in binding sites of Ti and silicon on the chorion, or from lower internalization rates of silicon by the TiO_2-exposed embryos. In view of indications for the contribution of silicon to immune and inflammatory responses, osteogenesis, and the formation of connective tissue (Nielsen 2014), the latter scenario merits further investigation.

A positive correlation was found between concentrations of Ti and potassium of zebrafish eggs. A similar, yet insignificant trend was observed for the concentration of phosphorus. Of all detected elements by PIXE (Table S2), potassium constitutes the most abundant element in bacteria, followed by phosphorus (Novoselov et al. 2013). This suggests that the higher concentrations of both potassium and phosphorus were detected on zebrafish chorions as a result of the accumulation of bacteria on zebrafish chorions.

3.4.2 Survival of microbiota on zebrafish eggs

To address our second research question, we characterized the effects of $nTiO_2$ on microbial consortia that establish on the chorion of zebrafish eggs. In accordance with the reported antimicrobial activity of $nTiO_2$, we detected a higher cover of dead microbes on the chorion surface of zebrafish eggs following exposure to $nTiO_2$.

However, imaging analyses also showed that exposure concentrations above 2 mg $TiO_2 \cdot L^{-1}$ resulted in an overall increase in total microbial abundance. For this reason, the antimicrobial effects of $nTiO_2$ could not have been identified using culture-dependent microbial techniques only. For future research, this shows the importance to support culture-dependent analysis of microbiota composition with culture-independent techniques to assess microbiota composition, specifically using microbial profiling techniques that are based on RNA, or include initial removal of relic DNA, to allow to distinguish dead from live microbiota (Knight et al. 2018).

Similar to our results, Zhai et al. (2019) detected a concentration-dependent increase in soil microbiota abundance following 24 h-exposure to $nTiO_2$, with higher microbial abundance at 500 and 2000 mg $TiO_2 \cdot kg^{-1}$ soil than at 0 and 1 mg $TiO_2 \cdot kg^{-1}$ soil. Nevertheless, these effects were of transient nature, and the adverse effects of $nTiO_2$ on microbial abundance gradually appeared from 15 to 60 days of exposure. In the present study, such adverse effects of prolonged exposure to $nTiO_2$ might explain why the acute growth-promoting effects of $nTiO_2$ did not result in higher AWCD over the two days longer Ecoplate incubations.

Following 24 h of exposure to 5 mg $TiO_2 \cdot L^{-1}$, over 16 times more CFUs were isolated from TiO_2-exposed embryos than from control embryos. One explanation to this difference could be potential growth-promoting effects of $nTiO_2$ on certain bacterial isolates; only four generation cycles are required to obtain a 16-times difference in microbial abundance. An alternative and non-exclusive explanation follows from our DLS results. Above exposure concentrations of 2 mg $TiO_2 \cdot L^{-1}$, we measured a more neutral zeta potential, and observed a corresponding increase in the hydrodynamic size of aggregates over time. This suggests that particle stability was lower at exposure concentrations above 2 mg $TiO_2 \cdot L^{-1}$. Accordingly, imaging analyses indicated that only at exposure concentrations above 2 mg $TiO_2 \cdot L^{-1}$, exposure to $nTiO_2$ resulted in higher microbial abundance on zebrafish eggs. Combined, these results may imply that the increased microbial abundance at exposure concentrations above 2 mg $TiO_2 \cdot L^{-1}$ resulted from the formation of heteroaggregates of microbes and TiO_2 in the water column, which subsequently settled onto zebrafish eggs. In agreement with this reasoning, the total number of CFUs in the water column without exposure to TiO_2 ($1.6 \cdot 10^2$ CFUs$\cdot$egg^{-1}; IQR = 83–$3.7 \cdot 10^2$ CFUs$\cdot$egg^{-1}, n=23), can explain a large part of the difference in CFU counts between non-exposed eggs (52 ± 23 CFUs$\cdot$egg^{-1}) and $nTiO_2$-exposed eggs ($8.5 \cdot 10^2 \pm 4.2 \cdot 10^2$ CFUs$\cdot$egg^{-1}). Heteroaggregation dynamics of $nTiO_2$ with microbes have already been described for the unicellular alga *R. subcapitata* (Lin et al. 2015). Moreover, the aggregation and subsequent sedimentation of microbes with suspended particles is a well-described phenomenon in the water column of pelagic water bodies, known as marine snow (Suzuki and Kato 1953) or lake snow (Grossart and Simon 1998).

3.4.3 Cascading effects on microbiota of zebrafish larvae

The third part of our study concerned the potential consequences of altered embryonic microbiota to zebrafish larvae health. Specifically, we inferred if nTiO$_2$-induced changes in chorion-attached microbiota resulted in different larval microbiota abundance and composition. Considering the potential functional redundancy of microbes, we used carbon substrate utilization as a functional measure of microbiota composition. We found that the higher microbial abundance on zebrafish eggs that had been exposed to nTiO$_2$, persisted until the 5 dpf-larval stage. This indicates that microbes which grow on zebrafish eggs as a result of nTiO$_2$ exposure, possibly due to the adsorption of aggregates consisting of microbes and nTiO$_2$ onto the chorion surface, can colonize the larvae upon hatching. In our experiment, this did not result in different functional composition of larval microbiota, as determined based on carbon-substrate utilization. However, there is a risk that hazardous microbes are transferred to eggs following heteroaggregate formation in aquatic ecosystems. In the Baltic Sea, for instance, potentially pathogenic *Vibrio* bacteria have been identified on microplastic particles (Kirstein et al. 2016). Of comparable concern, we identified *Aeromonas* species on zebrafish eggs which are known to be pathogenic to fish (Fernández-Bravo and Figueras 2020), which were one of the species *A. hydrophila* (infecting salmonids and eel), *A. salmonicida* (infecting salmonids), *A. sobria* (infecting tilapia and common carp) or *A. veronii* (infecting catfish, common carp, and eel). More broadly, aeromonads have been associated with infections in echinoderms, mollusks, copepods, crocodiles, frogs, rabbits, cats, dogs, horses and humans (Fernández-Bravo and Figueras 2020). The presence of these aeromonads on nTiO$_2$-exposed eggs suggests that these bacteria are able to cope with the particles' antimicrobial properties. Therefore, it is possible that pathogenic aeromonads are transferred throughout aquatic ecosystems, and to aquatic eggs, via attachment to suspended nTiO$_2$ particles and aggregates.

Although the nAg-exposed eggs of the positive control developed functionally different larval microbiota than zebrafish eggs that had not been exposed to nanoparticles, larval microbiota of nTiO$_2$-exposed eggs did not differ from non-exposed eggs in carbon substrate utilization. This lower impact of nTiO$_2$ on microbiota composition, as compared to nAg, at concentrations that are sublethal to the host, has been reported for soil microbes (Ahmed et al. 2020), intestinal microbiota of mice (Chen et al. 2017), and human gut simulator microbiota (Agans et al. 2019). Nevertheless, even though we exclusively isolated the bacteria *C. massiliae* and *S.*

maltophilia from $nTiO_2$-exposed eggs, which could indicate that the composition of exposed and non-exposed egg microbiota differed taxonomically, also microbiota of eggs did not differ in carbon substrate utilization profiles. This may imply that $nTiO_2$-exposure can induce shifts in microbiota composition that do not result in different microbiota functioning, as a result of functional redundancy. Interestingly, Zhai et al. (2019) obtained similar results for the impacts of $nTiO_2$ on soil microbiota. This remarkable similarity in the impacts of $nTiO_2$ on microbiota from different environments warrants further research, investigating the generalizability of these results.

On a similar note, comparing the particle-specific protection of the external structures surrounding the embryos of different taxa merits further investigation. At a large phylogenetic distance to teleost fish, for instance, it can be questioned if egg coatings facilitate early microbial colonization, given the bactericidal or bacteriostatic activity of the jelly layer of amphibian eggs (Mazzini et al. 1984). Even at low phylogenetic distances, a remarkable diversity of egg surfaces exists. Demersal fish, for example, generally produce eggs with much thicker and harder chorion structures than pelagic fish (McMillan 2007). Moreover, chorions can have diverse kinds of protrusions, such as threads, fibrils, or spikes, increasing their surface area. Additionally, differences between the environments where these eggs develop – including turbidity, water column depth, currents, salinity, and the presence of other pollutants or stressors – will affect the interactions between suspended particles and microbiota colonizing aquatic eggs externally. In view of this diversity in the external surface and environment of aquatic eggs, the adverse effects of nanoparticle adsorption on the eggs of oviparous animals, as examined in this study, may contribute to variation in nanoparticle sensitivity across different taxa. Further characterization thereof may help to refine the assessment of environmental risks of nanoparticle exposure on early life stages of oviparous animals.

3.5 Conclusions

Early host-microbiota interactions are of key importance to the development of zebrafish larvae. In this study, we tested the hypothesis that the adsorption of antimicrobial titanium dioxide nanoparticles on zebrafish eggs can perturb microbial communities that establish on the egg surface, indirectly affecting the subsequent colonization of hatched larvae. Our results confirmed that both nanoparticles and microbes accumulated on the surface of zebrafish eggs, whereas no particles could be detected inside of the eggs. At increasing exposure concentrations, this resulted in higher dead and total microbial abundance, and altered concentrations of potassium and silicon. These impacts of titanium dioxide nanoparticles on egg microbiota had cascading effects on later life stages, as indicated by a persisting increased microbial abundance of larvae. Combined with measurements on particle stability, this overall stimulatory effect of nTiO_2 on egg- and larval microbial abundance can potentially be explained by the formation of heteroaggregates of microbes and nanoparticles that settle on the egg surface. Given the tolerance of pathogenic aeromonads against antimicrobial properties of titanium dioxide particles, these dynamics potentially come at the expense of increased dispersal of pathogenic bacteria through aquatic ecosystems, as well as across different life stages of oviparous animals.

Author contributions

Bregje W. Brinkmann: Conceptualization, Investigation, Supervision, Formal analysis, Writing – Original Draft, Review & Editing. ***Wouter F. Beijk***: Investigation, Methodology, Writing – Review & Editing. ***Redmar C. Vlieg***: Investigation, Methodology, Writing – Review & Editing. ***S. John T. van Noort***: Supervision, Funding acquisition, Writing – Review & Editing. ***Jorge Mejia***: Investigation, Methodology, Writing – Review & Editing. ***Julien L. Colaux***: Investigation, Methodology, Writing – Review & Editing. ***Stéphane Lucas:*** Supervision, Funding acquisition. ***Gerda Lamers***: Methodology, Writing – Review & Editing. ***Willie J. G. M. Peijnenburg***: Supervision, Writing – Review & Editing. ***Martina G. Vijver***: Supervision, Funding acquisition, Writing – Review & Editing.

Data availability statement

Data is available via Mendeley Data: DOI:10.17632/2d4hcr5cb5.1

Supporting material is made available by *Aquatic Toxicology* [online]:
DOI: 10.1016/j.aquatox.2021.105744

Acknowledgements

We thank Ilaria Zanoni for performing the nTiO_2 sedimentation measurements, Rian van den Nieuwendijk for providing technical support and equipment for the lyophilization of zebrafish eggs; Emilie Didaskalou for help with the concerning sample preparation; and RAS AG for providing the applied silver nanoparticles. John van Noort and Redmar Vlieg were supported by the Netherlands Organization for Scientific Research [VICI 680.47.616]. This work was supported by the project PATROLS of European Union's Horizon 2020 research and innovation programme [grant number 760813].

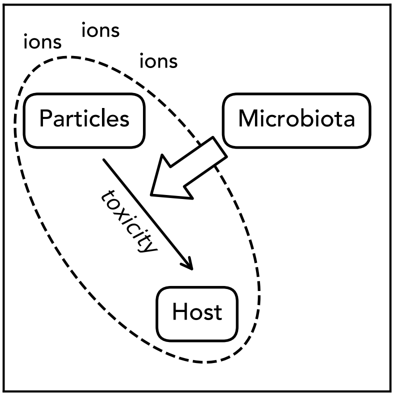
ions
ions
ions
Particles
Microbiota
toxicity
Host

CHAPTER 4

Colonizing microbiota protect zebrafish larvae against silver nanoparticle toxicity

Bregje W. Brinkmann

Bjørn E. V. Koch

Herman P. Spaink

Willie J. G. M. Peijnenburg

Martina G. Vijver

Published in *Nanotoxicology*, 14(6): 725-739 (2020). DOI: 10.1080/17435390.2020.1755469

Data is available via *Figshare*. DOI: 10.6084/m9.figshare.c.4923261

Abstract

Metal-based nanoparticles exhibiting antimicrobial activity are of emerging concern to human and environmental health. In addition to their direct adverse effects to plants and animals, indirect effects resulting from disruption of beneficial host-microbiota interactions may contribute to the toxicity of these particles. To explore this hypothesis, we compared the acute toxicity of silver and zinc oxide nanoparticles (nAg and nZnO) to zebrafish larvae that were either germ-free or colonized by microbiota. Over two days of exposure, germ-free zebrafish larvae were more sensitive to nAg than microbially-colonized larvae, whereas silver ion toxicity did not differ between germ-free and colonized larvae. Using response addition modeling, we confirmed that the protective effect of colonizing microbiota against nAg toxicity was particle-specific. Nearly all mortality among germ-free larvae occurred within the first day of exposure. In contrast, mortality among colonized larvae increased gradually over both exposure days. Concurrent with this gradual increase in mortality was a marked reduction in the numbers of live host-associated microbes, suggesting that bactericidal effects of nAg on protective microbes resulted in increased mortality among colonized larvae over time. No difference in sensitivity between germ-free and colonized larvae was observed for nZnO, which dissolved rapidly in the exposure medium. At sublethal concentrations, these particles moreover did not exert detectable bactericidal effects on larvae-associated microbes. Altogether, our study shows the importance of taking host-microbe interactions into account in assessing toxic effects of nanoparticles to microbially-colonized hosts, and provides a method to screen for microbiota interference with nanomaterial toxicity.

Keywords: Fish Embryo Acute Toxicity Test; Host-microbiota interactions; Particle-specific toxicity; Gnotobiotic techniques; Germ-free.

4.1 Introduction

Microbiota that reside in and on plants and animals, interact closely with their hosts, modulating immune responses, nutrient uptake and energy metabolism (Hacquard et al. 2015; Brugman et al. 2018). Healthy hosts with beneficial microbiota harbor diverse mutualistic and commensal microbes, yet restrict growth of pathogenic microbes. Perturbation of the interactions between hosts and interacting microbiota, called 'dysbiosis', has been related to severe infections, metabolic disorders and immune diseases across humans, animals and plants (Willing et al. 2011). For this reason, the release of antimicrobial agents into the environment, potentially disturbing host-associated microbiota, raises concerns about human and environmental health (Adamovsky et al. 2018; Trevelline et al. 2019).

Of emerging concern are metal-based nanoparticles that appear as new antimicrobial agents on the market (Seil and Webster 2012). Examples of antimicrobial nanoparticles include silver, zinc oxide, titanium dioxide, copper and iron oxide particles. These metal nanoparticles can disrupt and damage cellular membranes, DNA and proteins, either as a result of their physical interaction with these cellular components, or by inducing the formation of reactive oxygen species (Bondarenko et al. 2013; Brandelli et al. 2017). Additionally, metal nanoparticles release toxic metal ions, either in- or outside of cells, that exert similar adverse effects (Seil and Webster 2012; Brandelli et al. 2017). Notably, nanoparticles and their shed ions do not only affect microbial cells, but can also exert adverse effects on plants and animals (Yang et al. 2017b; Sukhanova et al. 2018).

Whilst at risk of the negative consequences of dysbiosis, some microbes can interact with antimicrobial nanoparticles, potentially reducing the nanoparticles' toxicity to the host. *In vitro* studies, for instance, have demonstrated that several bacteria can reduce toxic silver ions back into their less toxic particulate form (Lin et al. 2014). Moreover, experiments in micro- and mesocosm setups revealed that microbiota can enhance their production of extracellular polysaccharides in response to chronic nanoparticle exposure (Eduok and Coulon 2017). By trapping antimicrobial nanoparticles, extracellular polysaccharides presumably offer protection against toxic nanoparticles. Whether such interactions occur among host-associated microbiota *in vivo*, and whether these interactions significantly affect the toxicity of nanoparticles to the host, is still unknown. Nevertheless, human gut microbiota have already been found to affect the toxicity of other environmental pollutants, either bioactivating or detoxifying compounds such as (nitro-)polycylic aromatic hydrocarbons, nitrotoluenes, polychlorobiphenyls, metals, and benzene derivatives (Claus et al. 2016).

In recent years, zebrafish larvae have proven to be a useful model organism to study host-microbiota interactions *in vivo* (Rawls et al. 2004; Meijer et al. 2014). Zebrafish larvae also continue to be an important model organism in toxicology for both human and environmental hazard assessment (Bambino and Chu 2017; Horzmann and Freeman 2018). Similar to embryos of other teleost fish species, zebrafish embryos are assumed to develop in a sterile environment inside of the chorion, until they hatch at 2 days post-fertilization (dpf). Then, microbes that densely colonize the outer surface of chorions, and microbes from the surrounding water, likely colonize zebrafish larvae externally. Quickly thereafter, zebrafish open their mouth (at 3 dpf) and start feeding (at 5 dpf), allowing microbial colonization of their gastrointestinal tracts (Llewellyn et al. 2014). Based on this colonization cycle, Rawls et al. (2004) established gnotobiotic techniques that enable quick and easy derivation of zebrafish larvae that are either germ-free or colonized by specific microbes or microbiota.

In this study, we combined gnotobiotic techniques for zebrafish larvae with standardized toxicity tests (Fish Embryo Acute Toxicity Test, OECD Test No. 236) enabling to explore the impact of host-associated microbiota on the acute toxicity of silver and zinc oxide nanoparticles (nAg and nZnO). Specifically, we investigated 1) how colonizing microbiota affect the sensitivity of zebrafish larvae to nAg and nZnO; 2) to what extent these impacts of microbiota-host interactions relate to the particle-specific toxicity of nAg and nZnO, rather than to the toxicity of their shed Ag^+ and Zn^{2+} ions; and 3) how nAg and nZnO affect the abundance and the composition of colonizing microbiota. To this end, we compared the acute toxicity of nAg and nZnO between germ-free and microbially-colonized zebrafish larvae. Using response addition modeling, we derived the relative contribution of nanoparticles and their shed ions to the toxicity of nanoparticle suspensions. At the end of the exposures, we isolated bacteria from zebrafish larvae, and counted their abundance as an estimation of microbiota quantity. Finally, we identified the isolated colony-forming units based on 16S rRNA gene sequencing, to reveal what bacterial species associating with zebrafish larvae are potentially resilient to nanoparticle toxicity.

4.2 Materials and methods

4.2.1 Nanoparticle dispersions

Silver nanoparticles (nAg) with a primary particle size of 15 nm (NM-300K; Klein et al. 2011) were kindly provided by RAS AG (Regensburg, Germany). These particles are commercially available as an aqueous suspension (agpure® W10) comprising 10% (w/w) Ag nanoparticles, 4% ammonium nitrate, 4% (w/w) polyoxyethylene glycerol trioleate, and 4% (w/w) polyoxyethylene sorbitan mono-laurat. Uncoated zinc oxide nanoparticles (nZnO) with a primary particle size of 42 nm (NM-110) (Singh et al. 2011) were purchased from the Joint Research Centre (Ispra, Italy) of the European Union (EU).

Immediately prior to exposure, stock suspensions of both nanoparticles were prepared in egg water (60 mg·L^{-1} Instant Ocean sea salts; Sera GmbH, Heinsberg, Germany) at a final concentration of 100 mg·L^{-1}. According to the batch dispersion protocol of the EAHC NANOGENOTOX project (v.1; Jensen 2018b), nAg was handled in an argon atmosphere to prevent particle oxidation. Stock suspensions were stabilized by sonication for 10 min in an ultrasonic water bath (USC200T; VWR, Amsterdam, The Netherlands). The acoustic power of the sonicator was 12 W, as determined following the sonicator calibration standard operation procedure delivered in the EU FP7 NANoREG project (v. 1.1; Jensen et al. 2018). The stock solutions were diluted to the appropriate test concentrations in egg water.

The size and morphology of both nanoparticles were characterized by transmission electron microscopy. To this end, dispersions of 10 mg·L^{-1} nAg and nZnO were prepared in egg water as described above. Five µL of these dispersions were transferred onto 200 mesh carbon-coated copper transmission electron microscopy grids (Ted Pella, Redding, California). The grids were dried at room temperature in the dark for at least 24 h. Particles on the grids were imaged with a 100 kV JEOL (Tokyo, Japan) 1010 transmission electron microscope at 50k-60k times magnification. The size of 50 particles from TEM images of nAg and nZnO was measured using ImageJ software (v. 1.51h; Abramoff et al. 2004).

The hydrodynamic size and zeta potential of nAg and nZnO aggregates were determined using a Zetasizer Ultra instrument (Malvern Panalytical, Malvern, United Kingdom) following 0, 2, 4, 6 and 24 h of exposure (section 4.2.3). We applied the standard operation procedure (SOP) delivered in NANoREG (v. 1.1; Jensen 2018a), but used a fixed number of 10 runs and 3 repeated measurements per sample (n=3). We selected the Smoluchowski formula for approximation of zeta potentials from electrophoretic mobility. For nAg, the refractive index (R_i) and absorption value (R_{abs}) were set to 0.180 and 0.010 respectively, in accordance with Bove et al. (2017). For nZnO, R_i and R_{abs} were set to 2.02 and 0.40 respectively, following the aforementioned SOP. Exposure concentrations below 1.5 mg nAg·L^{-1}, and below 10 mg nZnO·L^{-1} are omitted, as high variation between repeated measurements (SEM > 30% of the mean hydrodynamic size) and high polydispersity indices (≥0.70), indicate that the concentration of aggregates in these samples was too low for accurate dynamic light scattering analyses.

4.2.2 Zebrafish larvae and colonizing microbiota

Embryos and larvae of AB×TL wild-type zebrafish were used for all experiments. Adult zebrafish were kept at 28 °C in a 14 h:10 h light:dark-cycle. Zebrafish husbandry and handling were in compliance with local and European animal welfare regulations (EU Animal Protection Directive 2010/63/EU), as surveyed by the Animal Welfare Body of Leiden University. Standard protocols (https://zfin.org) were used for the maintenance and handling of zebrafish adults and their larvae.

We divided fertilized embryos over two groups:

1. Embryos of the first group were raised according to standard protocols (https://zfin.org). It is assumed that larvae of this group are colonized by microbes from the surrounding water and from chorions, directly upon hatching (Llewellyn et al. 2014).
2. Embryos of the second group were sterilized and raised in autoclaved egg water, in order to exclude any microbial colonization. We sterilized these embryos using the 'Natural breeding method' described by Pham et al. (2008), with the adaptations made by Koch et al. (2018). We further adapted the protocol by Koch et al. (2018) by using half of the concentration of sodium hypochlorite recommended, to ensure that all embryos hatched naturally. Briefly, embryos were incubated from 0-6 hours post fertilization (hpf) in antibiotic- and antimycotic-containing egg water (100 $\mu g \cdot mL^{-1}$ Ampicillin, 5 $\mu g \cdot mL^{-1}$ Kanamycin, 250 $ng \cdot mL^{-1}$ Amphothericin B). From these, 150 embryos were collected in 15 mL conical tubes at 6 hpf. Under sterile conditions, the embryos were washed with 3 mL 0.2% PVP-iodine in egg water for 45-60 s and rinsed twice with 10 mL sterile egg water. Thereafter, the embryos were washed twice with 6 mL 0.03% sodium hypochlorite (3.5% Cl_2; VWR International, Radnor, PA) in egg water for 5 min. Embryos were rinsed once with 10 mL sterile egg water in between these washing steps, and were rinsed thrice with 10 mL sterile egg water following both sodium hypochlorite washing steps. Only if we could not isolate any bacterial colonies from the resulting larvae on solid LB growth medium, as described in section 4.2.5, larvae were included in this germ-free group.

As a control for the sterilization treatment, embryos of a third group were first sterilized as described for group 2, and were recolonized immediately thereafter by placing the embryos in egg water of the non-sterilized group 1. However, in agreement with the principles of ecological succession (Odum 1969), specifically microbes with high growth rates, such as *Pseudomonas aeruginosa,* appeared to recolonize zebrafish embryos following initial sterilization, in favor of microbes with slower growth rates, such as *Phyllobacterium myrsinacearum* and *Sphingomonas leidyi* (Fig. S1). For this reason, we continued our experiments with embryos of group 1 and 2 only. The embryos of both groups were incubated at 28 °C in petri dishes with 30 mL egg water until the start of exposure.

4.2.3 Exposures

Microbially-colonized and germ-free zebrafish larvae were exposed to nanoparticle dispersions from 3 to 5 dpf in 24-well plates as described by Van Pomeren et al. (2017b). This setup is based on OECD guideline No. 236 (OECD 2013), with the modification of exposing 10 larvae for each test concentration together in one well, instead of exposing 20 larvae for each test concentration in separate wells. This modification reduces the total amount nanomaterial that is required per test, and produces similarly robust data to the original test (Van Pomeren et al. 2017b). Three biological replicates were tested for each nominal test concentration. These were 0, 0.25, 0.75, 1, 1.5 and 2.5 mg $nAg{\cdot}L^{-1}$, and 0, 2.5, 5, 8, 10 and 20 mg $nZnO{\cdot}L^{-1}$. Additionally, to test the impacts of potentially shed ions, zebrafish larvae were exposed to solutions of $AgNO_3$ and $Zn(NO_3)_2$ in egg water. The nominal test concentrations to derive dose-response curves for these salt solutions were 0, 0.025, 0.05, 0.1, 0.2 and 0.4 mg $Ag^+{\cdot}L^{-1}$; and 0, 2.5, 5, 6, 7.5, and 15 mg $Zn^{2+}{\cdot}L^{-1}$. Because Ag^+ and Zn^{2+} ions exert antimicrobial activity, the $AgNO_3$ and $Zn(NO_3)_2$ stock solutions can be expected to be sterile. However, since exposure of germ-free zebrafish larvae to microbes can induce a major transcriptional response, resulting in altered leukocyte infiltration in the intestines (Koch et al. 2018), $AgNO_3$ and $Zn(NO_3)_2$ stock solutions were autoclaved for this group out of precaution. Control groups were exposed to egg water without nanoparticles or corresponding salt solutions. Exposure took place in the dark at 28 °C. After 24 h of exposure, dead embryos were removed, and nanoparticles and salt solutions were refreshed. Mortality was scored following 24 h and 48 h of exposure.

The above setup is based on two assumptions, which we tested. Firstly, we assumed that mortality in nAg exposures resulted either directly from the particles, or indirectly from their shed ions, but was not caused by the dispersion medium itself. In order to verify this assumption, particles from a 100 $mg{\cdot}L^{-1}$ stock dispersion of nAg were spun down thrice at 20 000 × *g* for 30 min, and zebrafish larvae were exposed to the autoclaved supernatant following the above setup. Secondly, we assumed that the iodine and sodium hypochlorite rinsing steps that are part of the sterilization protocol, do not alter the dissolution of particles. To test this assumption, we compared particle dissolution in microbially-colonized and germ-free exposures as described in section 4.2.4.

4.2.4 Derivation of particle-specific toxicity

Actual concentrations of nanoparticles and their shed ions were determined using atomic adsorption spectrometry. At 0 h and 24 h following the start of exposure, 3-5 mL of the nanoparticle dispersions at each test concentration were sampled to determine total metal concentrations (n=3). Another 4 mL of each nanoparticle dispersion was centrifuged for 30 min at 20 000 × g, and 3 mL of the supernatant was sampled to determine metal ion concentrations (n=3). The samples were acidified with 0.5% HCl and 1% HNO_3, and were stored in the dark until further analysis. Elemental concentrations of Zn and Ag in the acidified samples were measured using an Analyst 100 flame atomic absorption spectrometer (Perkin Elmer, Waltham, Massachusetts). Elemental particle concentrations were calculated by subtracting ion metal concentrations from total metal concentrations. In a few cases for nZnO, where particle concentrations were below the detection limit (as indicated by <D.L.), this calculation produced negative values, which we set to zero. Particulate and total ZnO concentrations were derived from the elemental Zn concentrations based on differences in molar mass. Subsequently, replicate measurements were averaged, and the time weighted average concentration (C_{TWA}) was calculated for ions, particles and total metals, as proposed for nanosafety research by Zhai et al. (2016):

$$C_{TWA} = \frac{c_{t=0h} + c_{t=24\,h}}{2} \qquad \text{(eq 4.1)}$$

where $c_{t=0h}$ is the average concentration at 0 h, and $c_{t=24h}$ is the average concentration at 24 h following the start of exposure. Finally, the mean particle-specific contribution to mortality ($\overline{E_{particle}}$) was determined for each nanoparticle test concentration by way of response addition (Bliss 1939):

$$\overline{E_{total}} = 1 - [(1 - \overline{E_{ion}})(1 - \overline{E_{particle}})] \qquad \text{(eq 4.2)}$$

where $\overline{E_{total}}$ corresponds to the mean mortality in nanoparticle exposures at the total CTWA, and $\overline{E_{ion}}$ corresponds to the mean mortality in $AgNO_3$ and $Zn(NO_3)_2$ exposures at the ion CTWA. The standard deviation of $\overline{E_{particle}}$ was derived by propagating the standard deviation of $\overline{E_{total}}$ following:

$$\sigma_{\overline{E_{particle}}} = \overline{E_{particle}} \sqrt{\left(\frac{\sigma_{\overline{E_{total}}}}{\overline{E_{total}}}\right)^2} \qquad \text{(eq 4.3)}$$

where $\sigma_{\overline{E_{particle}}}$ and $\sigma_{\overline{E_{total}}}$ represent the standard deviations of $\overline{E_{particle}}$ and $\overline{E_{total}}$.

4.2.5 Microbiota colony-forming units

Microbiota were isolated from zebrafish larvae at 5 dpf using a tissue homogenizer. To this end, 3 larvae were transferred to a 1.5 mL SafeLock microcentrifuge tube (Eppendorf, Nijmegen, the Netherlands) comprising 200 µL autoclaved egg water and 6 zirconium oxide beads (1.0 mm-diameter; Next Advance, New York, New York). The larvae were anaesthetized for 2 min on ice, homogenized for 15 s in a tissue homogenizer (Bullet Blender model Blue-CE; Next Advance) at speed 7, and cooled for 10 s on ice immediately thereafter. The homogenization and cooling steps were repeated 7 times to obtain a total homogenization time of 2 min.

As a measure of microbiota abundance, we determined the number of colony-forming units (CFUs) associated with larvae from the lowest exposure concentrations and controls at the end of exposures. Microbes were isolated from zebrafish larvae as described in section 4.2.5, using 3 instead of 5 larvae per microcentrifuge tube. Isolated microbiota were diluted in autoclaved egg water (10, 100 and 1000 times) to reach appropriate CFU densities, and 100 µL of the diluted microbiota was plated on LB agarose. Undiluted isolates from germ-free larvae were also plated (100 µL). Following 2 days of incubation at 28 °C, CFUs were counted. We continued the incubation at 28 °C for 3 additional days, to check if any new colonies appeared. If colonies appeared in the germ-free group, data from the corresponding larvae were excluded from the experiment. Dilutions with the highest countable number of CFUs below 200 were used to estimate microbiota abundances. It should be noted that we used our CFU estimates as a relative rather than absolute measure of microbiota abundance. Many bacteria can still not be cultured, and will thus not grow on LB growth medium. Moreover, we showed that our isolation method is detrimental to a small fraction of the isolated bacteria as presented in the Supplementary Fig. S2.

Thirty colonies of nAg-exposed larvae and their controls were selected for 16S rRNA-based bacterial identification (60 colonies in total). Individual colonies were freshly grown on solid LB growth medium overnight at 28 °C, and a swap of each colony was lysed for 3 min in 100 µL nuclease free water at 100 °C. Of these, a 1505-nt fragment of the 16S rRNA gene was amplified in polymerase chain reactions (PCR) with 27F (5’-AGAGTTTGATCMTGGCTCAG-3’) and 1492R (5’-TACGGYTACCTTGTTACGACTT-3’) universal bacterial primers (Lane 1991). The PCR reactions had a total volume of 50 µL and contained 1 µL colony lysate, 5 µL 10× PCR buffer (200 mM Tris-HCl pH 8.4, 500 mM KCl), 5 µL dNTP mix (2mM), 1 µL $MgCl_2$ (50 mM), 0.5 µL of each primer (100 µM) and 0.5 µL Taq DNA polymerase (5 $U \cdot \mu L^{-1}$) in nuclease free water. The reactions were performed with an initial denaturation step of 5 min at 94 °C, followed by 30 cycles of denaturation (30 s at 94 °C), annealing (30 s at 58°C), and extension (30 s at 72 °C), and a final extension step of

10 min at 72 °C. The DNA sequence of PCR products was determined by BaseClear, Leiden by way of Sanger sequencing with 27F primers. We trimmed low-quality areas of the obtained sequence chromatograms, and corrected chromatograms manually where necessary using 4Peaks software (by A. Griekspoor and Tom Groothuis; nucleobytes.com). For each of the resulting sequences, we performed a BLASTn search against NCBI's nucleotide database (https://blast.ncbi.nlm.nih.gov/) to identify the corresponding species.

4.2.6 Statistical analyses

All statistical analyses were performed in R (v. 3.4.0; www.r-project.org). Results are reported as mean ± standard error of the mean (SEM), calculated using the 'bear' package (v. 2.8.3; pkpd.kmu.edu.tw/bear). All figures were plotted using Python (v. 3.6.5) with the 'numpy' (v. 1.15.0), 'matplotlib' (v. 2.2.2) and 'pandas' (v. 0.23.3) packages.

In order to investigate particle dissolution, mean nanoparticle concentrations at 0 h and 24 h following exposure were compared for each of the five exposure concentrations in a two-way ANOVA design without interaction between exposure concentration and exposure time. The mean concentrations of shed ions at 0 h and 24 h were compared in a similar model. Subsequently, to test if the sterilization procedure affected nAg dissolution, we compared mean nAg and Ag^+ concentrations between exposure wells with microbially-colonized and germ-free larvae using a Welch Two Sample t-test (for nAg) and Two Sample t-test (for Ag^+) respectively. Diagnostic plots were inspected to verify if the model assumptions were met. Additionally, the Shapiro-Wilk test for normality was performed to check if residuals of the ANOVA and t-tests followed a normal distribution. We performed an F test to compare two variances to check if the variance was equally distributed over the microbially-colonized and germ-free groups.

For dose-response analyses, mortality data were fitted to a three-parameter log-logistic model using the *drm* function of the 'drc' package (v. 3.0-1; Ritz et al. 2005). The lower limit of the models was set to 0, and slope, inflection point (LC_{50}) and upper limit were estimated. LC_{50} estimates were compared between colonized and germ-free larvae using the *compParm* function. We obtained mortality estimates (mean and SEM) from ion (Ag^+/Zn^{2+}) and nanoparticle (nAg/nZnO) dose-response curves, at the measured ion C_{TWA} and total C_{TWA} respectively, by interpolation using the *predict* function. From these mortality estimates, we derived particle-specific mortality estimates (mean and SEM) by way of response addition as described before (section 4.2.4). We used these mean and SEM particle-specific mortality estimates to simulate particle-specific mortality data at each of the exposure concentrations (*n*=3) using the *rnorm* function of the stats package (v. 3.5.1). Finally, we fitted a three-parameter log-logistic function to these particle-specific mortality data and particle C_{TWA} estimates, and compared particle-specific LC_{50} estimates of germ-free and colonized larvae using the *compParm* function.

The CFU counts of control larvae, and larvae that were exposed to the lowest exposure concentrations of nAg, Ag^+, nZnO and Zn^{2+}, were compared using an ANOVA test, combined with Tukey's HSD post-hoc test. For this model, log(x+1) transformation of CFU counts was required to ensure that the residuals of the model followed a normal distribution, as indicated by the Q-Q plot and Shapiro-Wilk test for normality. We used the diagnostic plots of the model to check for equal variance of residuals across larvae of the control, nAg, Ag^+, nZnO and Zn^{2+} exposures.

4.3 Results

4.3.1 Nanoparticle size, shape, aggregation and dissolution

Dispersions of nAg comprised spherically shaped primary particles with a diameter ranging from 8 nm to 42 nm (average 24 nm; *n*=50; Fig. 4.1). Following dispersion in the exposure medium, the particles formed aggregates with mean hydrodynamic sizes of 218 ± 109 nm and 140 ± 59 nm at nominal exposure concentrations of 1.5 mg $nAg{\cdot}L^{-1}$ and 2.5 mg $nAg{\cdot}L^{-1}$, respectively. The size of nAg aggregates remained similar over the first 6 h of incubation, and reached a mean hydrodynamic size of 67 ± 7 nm at 24 h of incubation (Fig. S3a), the time at which the exposure medium was replaced. Accordingly, the mean zeta potential of aggregates remained around -20 mV over 24 h of incubation, indicating that particles remained stable over the incubation time (Fig. S3b).

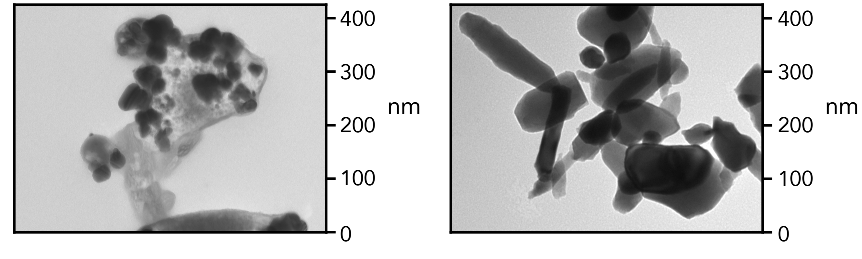

Figure 4.1: *Transmission electron microscope images of nAg and nZnO particles* at 60k and 50k magnification respectively.

Primary particles of nZnO had irregular shapes, with a width ranging from 12 nm to 109 nm (average 47 nm; n=50), and a length ranging from 17 nm up to 234 nm (average 94 nm; n=50; Fig. 4.1). At nominal exposure concentrations of 10 and 20 mg nZnO·L^{-1}, these primary particles formed aggregates with hydrodynamic sizes of 1086 ± 326 nm and 822 ± 193 nm at the start of incubation, and 806 ± 176 nm and 423 ± 73 nm at 24 h of incubation, respectively (Fig. S3c). The corresponding zeta potential measurements indicated that nZnO aggregates stabilized over the first 2 h of incubation, reaching a zeta potential of around -30 mV (Fig. S3d).

Immediately following dispersion, nAg and nZnO released ions into the exposure medium (Fig. 4.2a,c). No ions could be detected in controls without particles. Following 24 h of incubation, mean concentrations of Ag^+ ions in the exposure medium were still similar to those at the start of exposures (Fig. 4.2a,b; Table S1; $F_{1,24}$= 0.025, p>0.05). We note that this result needs to be interpreted with caution, as the assumption of normally distributed model residuals was not met, even following log or rank transformation. In accordance with the similar concentrations of Ag^+ ions measured at 0 h and 24 h of incubation, we could not detect any differences between mean mass-based particle concentrations at 0 h and 24 h of incubation for nAg (Fig. 4.2a,b; Table S1; $F_{1,24}$=1.1, p>0.05). Furthermore, the sterilization procedure to obtain germ-free larvae, including rinsing steps with sodium hypochlorite and PVP-iodine, did not result in higher concentrations of Ag^+, or lower concentrations of nAg, in the exposure medium (Table S2). In contrast to Ag^+, mean concentrations of Zn^{2+} were significantly higher following 24 h of incubation than at the start of exposures (Fig. 4.2c,d; Table S1; $F_{1,24}$= 26.9, p=2.6·10^{-5}). The dissolution of nZnO appeared to be concentration-dependent, where the release of Zn^{2+} seemed to have saturated already at the start of exposure at nominal concentrations below 8 mg ZnO·L^{-1}, whereas concentrations of Zn^{2+} in the exposure medium increased over 24 h of exposure at nominal concentrations above 8 mg ZnO·L^{-1}. Despite this release of ions, we did not detect differences between mass-based nZnO concentrations between 0 h and 24 h of incubation in the exposure medium (Fig. 4.2c,d; Table S1; $F_{1,24}$= 0.26, p>0.05).

4.3.2 Impact of microbiota on nanoparticle toxicity

Zebrafish larvae that were colonized by microbes responded differently to dispersions of nAg than germ-free zebrafish larvae (Fig. 4.3a). Following 48 h of exposure, median lethal toxic concentrations (LC_{50}) were significantly higher for microbially-colonized larvae (LC_{50}= 0.94 ± 0.14 mg Ag·L^{-1}), than for germ-free larvae (LC_{50}= 0.34 ± 0.06 mg Ag·L^{-1}; p=0.0006; Fig. 4.3a). Mortality among microbially-colonized larvae increased from 24 h to 48 h of exposure. In contrast, nearly all mortality among germ-free larvae

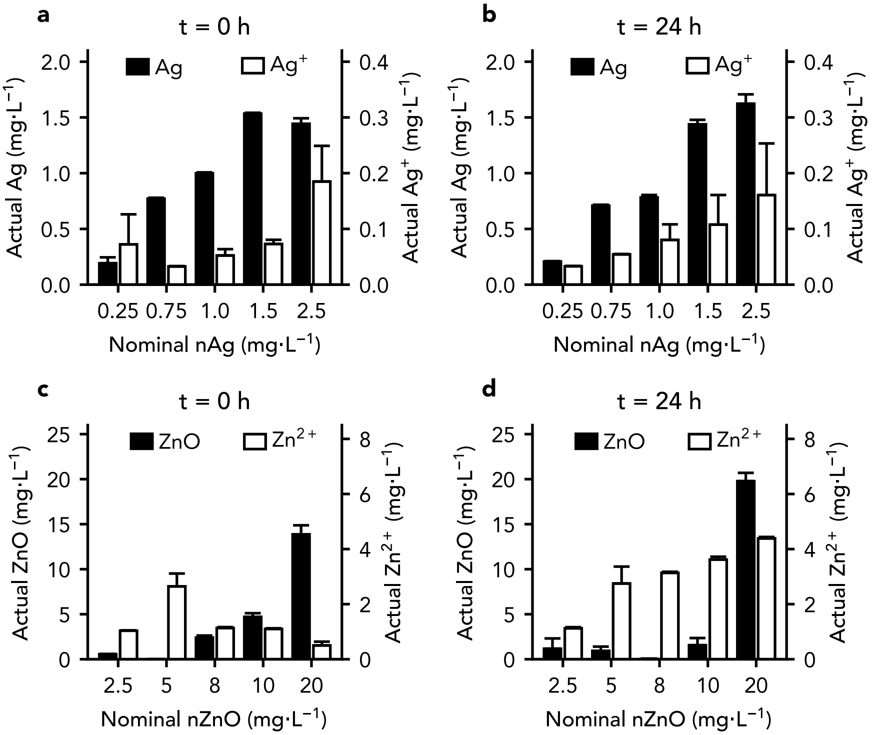

Figure 4.2: *Dissolution of nAg* (**a**,**b**) *and nZnO* (**c**,**d**) *nanoparticles.* Bars depict the mean concentrations of particles (black bars, left axis) and their shed ions (white bars, right axis) at 0 h (**a**,**c**) and 24 h (**b**,**d**) following dispersion, for each of the nominal test concentrations. Error bars indicate standard error of the mean (*n*=3). Values are provided in Table S1.

occurred within the first day of exposure. When nAg was removed from the dispersion medium by centrifugation prior to exposure, and larvae were exposed for 48 h to the nAg-dispersion medium without particles, we did not observe any mortality among larvae of each microbiota group.

In contrast to the effects of nAg, median lethal toxic concentrations of Ag^+ did not differ between the microbially-colonized larvae (0.14 ± 0.02 mg $Ag^+·L^{-1}$) and germ-free larvae (0.16 ± 0.06 mg $Ag^+·L^{-1}$; $p=0.74$; Fig. 4.3b) following two days of exposure. However, similar to the results of nAg exposures, nearly all mortality among germ-free larvae occurred during the first day of exposure to Ag^+, while mortality among colonized larvae gradually increased over the two days of exposure.

No differences in median lethal concentrations of nZnO dispersions were observed between germ-free larvae (4.91 ± 0.43 mg $ZnO·L^{-1}$) and colonized larvae (4.68 ± 0.62 mg $ZnO·L^{-1}$; $p>0.05$; Fig. 4.3c) following two days of exposure. Moreover, mortality among both germ-free and colonized larvae increased from 24 h to 48 h of exposure to nZnO.

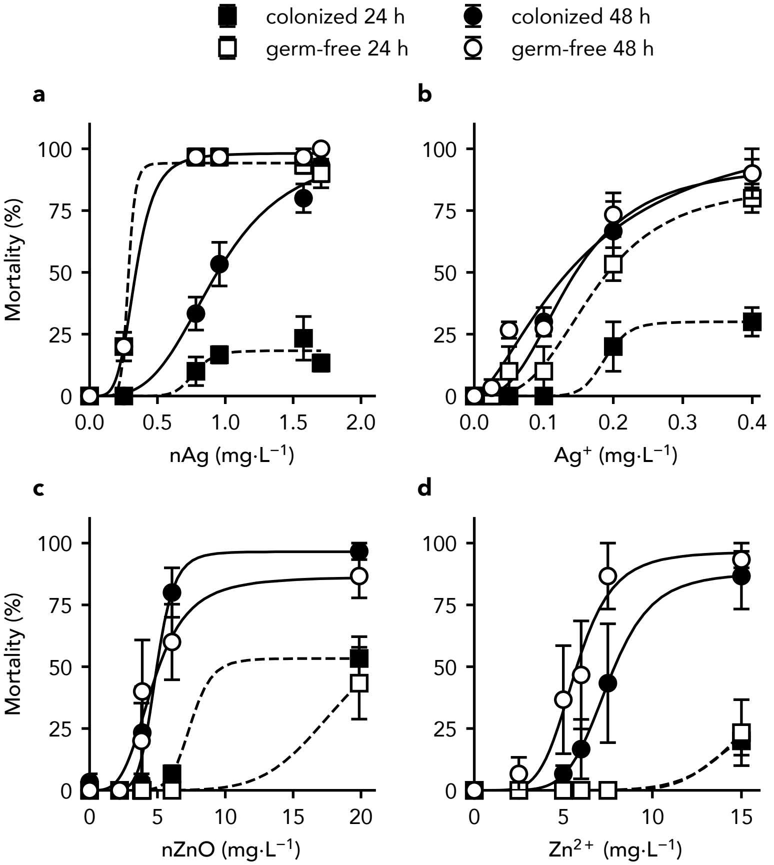

Figure 4.3: *Dose response curves of microbially-colonized* (black markers) *and germ-free* (white markers) *zebrafish larvae* exposed to nAg (**a**), Ag^+ (**b**), nZnO (**c**), and Zn^{2+} (**d**) following 24 h (squares) and 48 h (circles) of exposure. Error bars depict the standard error of the mean (*n*=3).

Similar to nZnO, we did not detect differences between median lethal concentrations of Zn^{2+} for colonized larvae (7.54 ± 0.82 mg $Zn^{2+}\cdot L^{-1}$) and germ-free larvae (5.68 ± 0.47 mg $Zn^{2+}\cdot L^{-1}$; $p>0.05$; Fig. 4.3d). Furthermore, mortality among Zn^{2+}-exposed larvae increased over the second day of exposure, independent of microbial colonization.

In order to explore the particle-specific contributions to the observed toxicity of nAg and nZnO, dose response curves were corrected for the effects of shed ions in the exposure medium by way of response addition (Fig. 4.4). The particle-specific LC_{50} estimates that were obtained for nAg in this way, still differed significantly between colonized (0.84 ± 0.06 mg particulate $Ag\cdot L^{-1}$) and germ-free larvae (0.34 ± 0.20 mg particulate $Ag\cdot L^{-1}$; t=2.35, df=4, $p=0.03$). At median lethal concentrations of total silver,

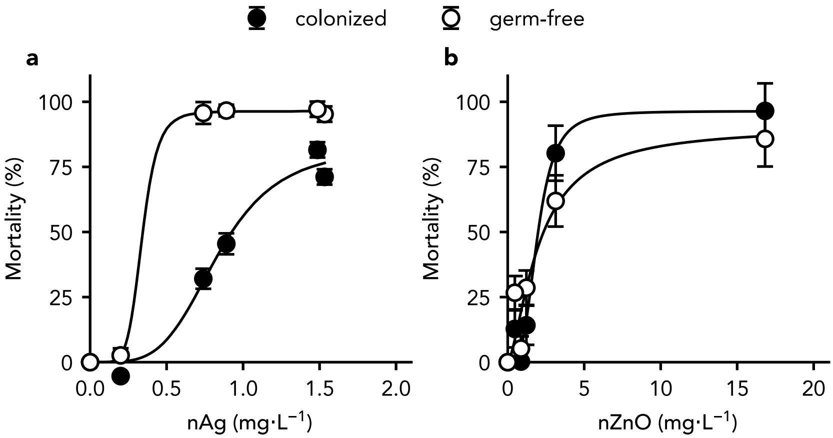

Figure 4.4: *Particle-specific dose response curves of microbially-colonized* (black markers) *and germ-free* (white markers) *zebrafish larvae* exposed to nAg (**a**), and nZnO (**b**) following 48 h of exposure. Error bars depict the standard error of the mean (*n*=3).

93 ± 13 % and 42 ± 57 % of the mean mortality under colonized and germ-free conditions respectively, could be explained by the particle-specific contribution to toxicity. For nZnO, particle-specific median lethal toxic concentrations did not differ between microbially-colonized conditions (1.94 ± 0.25 mg particulate ZnO·L^{-1}) and germ-free conditions (2.04 ± 0.48 mg particulate ZnO·L^{-1}; t= -0.17, df=4, $p>0.05$). Despite the quick dissolution of these particles, the relative contribution of nZnO particles accounted 97 ± 396 % and 88 ± 431 % of the mean total observed mortality at median lethal concentrations for colonized and germ-free larvae respectively.

4.3.3 Impact of nanoparticles on microbiota

In order to investigate the impacts of nAg and nZnO on zebrafish microbiota, we isolated colony-forming units (CFUs) from zebrafish larvae of the colonized group. At the end of the exposure time, $8.4{\cdot}10^3 \pm 3.6{\cdot}10^3$ CFUs per larvae could be isolated from the control group (Fig. 4.5). Exposure to the lowest test concentrations of nAg (0.25 mg·L^{-1}), Ag^+ (0.025 mg·L^{-1}), nZnO (2.5 mg·L^{-1}), and Zn^{2+} (2.5 mg·L^{-1}) affected this CFU count ($F_{4,10} = 45.5$, $p=2.2{\cdot}10^{-6}$; Fig. 4.5). Fewer CFUs could be isolated from larvae that were exposed to nAg (0.89 ± 0.59 CFUs per larvae; $p=0.00002$) and Ag^+ ($1.3{\cdot}10^2 \pm 1.1{\cdot}10^2$ CFUs per larvae; $p=0.001$). Exposure to nZnO or Zn^{2+} did not result in different CFU counts per larvae, as compared to control larvae ($p>0.05$).

Considering the bactericidal effects of nAg, we further explored what bacterial species remained among the isolated CFUs following exposure to nAg, selecting 30 CFU

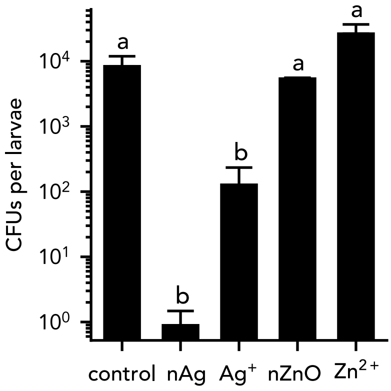

Figure 4.5: *Number of colony-forming units (CFUs) associated with zebrafish larvae* at the lowest exposure concentrations of nAg (0.25 mg·L^{-1}), Ag^+ (0.025 mg·L^{-1}), nZnO (2.5 mg·L^{-1}) and Zn^{2+} (2.5 mg·L^{-1}). Bars depict the mean CFU count per larvae (n=3), error bars depict the standard error of the mean, and letters indicate significant differences (p<0.05).

isolates of nAg-exposed larvae and 30 CFU isolates of control larvae for 16S rRNA gene-based identification. In total, we identified 52 of 60 selected bacteria with >98% sequence identity (Table S3). The other 8 CFUs had low sequence quality, resulting in 16S rRNA identity <98%. Nevertheless, BLAST results suggested similar bacterial species for these CFUs, as for the CFUs with >98% sequence identity. Hence, these records were included in the sequence identities presented below.

Based on 16S rRNA sequence identity, we identified 6 different bacterial species among isolated CFUs (Fig. 4.6). Additionally, we identified 3 groups of bacteria that we could not distinguish based on 16S rRNA sequences. Most of the isolated CFUs corresponded to *Phyllobacterium myrsinacearum* (30%), followed by bacteria of the genus *Pseudomonas* (30%; 13% of which was *P. aeruginosa*), *Delftia lacustris/D. tsuruhatensis* (17%), *Rhizobium rhizoryzae* (17%), and *Sphingomonas leidyi* (7%). Exposure to nAg and Ag^+ changed the relative abundance of these bacteria among isolated CFUs. The relative abundance of *P. myrsinacearum* was higher (63%) among CFUs of exposed larvae compared to non-exposed larvae. Additionally, we identified several bacterial species that did not appear among selected CFUs of non-exposed larvae, including *Bosea* sp. (13%), bacteria of the genus *Microbacterium* (17%), and *Staphylococcus* bacteria/*Sulfitobacter donghicola* (7%).

4.4 Discussion

Multicellular organisms live in association with diverse microbiota that contribute to host health and development. The emergence of metal-based nanoparticles on the

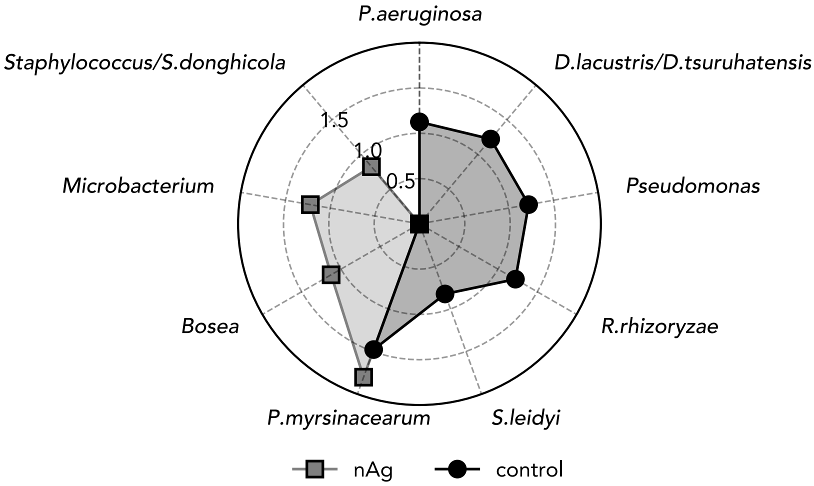

Figure 4.6: *Impacts of nAg* (0.25 mg·L^{-1}) *on the composition of colony-forming units (CFUs) isolated from zebrafish larvae* (30 colonies each). Radial axes depict log$_{10}$-transformed relative abundances (%) of bacterial species. The corresponding BLAST results are included in Table S3. *Abbreviations*: *D. lacustris/D. tsuruhatensis*, *Delftia lacustris/Delftia tsuruhatensis*; *P. aeruginosa*, *Pseudomonas aeruginosa*; *P. myrsinacearum*, *Phyllobacterium myrsinacearum*; *R. rhizoryzae*, *Rhizobium rhizoryzae*; *S. donghicola*, *Sulfitobacter donghicola*; *S. leidyi*, *Sphingomonas leidyi*.

market poses a threat to these host-associated microbiota, owing to the inherent antimicrobial properties of these particles. Ultimately, nanoparticle-induced perturbation of host-associated microbiota might affect both human and environment health (Adamovsky et al. 2018; Trevelline et al. 2019). For this reason, we set out to explore the role of zebrafish larvae-associated microbiota in the acute toxicity of the two commonly applied antimicrobial nanoparticles nAg and nZnO, explicitly quantifying the relative contributions of particles and shed ions to toxicity.

4.4.1 Protection of host-associated microbiota against nanoparticles

By combining standardized acute toxicity tests and established gnotobiotic techniques, we found that colonizing microbiota protect zebrafish larvae against particle-specific lethal effects of nAg, increasing the LC_{50} from 0.34 ± 0.20 mg particulate Ag·L^{-1} under germ-free conditions to 0.84 ± 0.06 mg particulate Ag·L^{-1} under microbially-colonized conditions. Following two-days of exposure, we did not detect this microbially-mediated protection against Ag^{+}, observing similar LC_{50} values for microbially-colonized and germ-free larvae. This suggests that interactions between microbes and particles, rather than interactions between microbes and particle-shed ions, underlie the protective effect of microbiota. We also did not observe any differences between the sensitivity of germ-free and colonized larvae to nZnO and Zn^{2+}. This similar sensitivity of germ-free and colonized larvae to nZnO and Zn^{2+} indicates that the protective effect against nAg results from specific interactions between microbes and particles, rather than general differences in health between germ-free and colonized larvae.

It is still unclear what mechanisms underlie the microbially-mediated protection against nAg. Notably, the majority of zebrafish larvae that died from nAg exposure under germ-free conditions, already died within the first day of exposure, whereas mortality under microbially-colonized conditions gradually increased over the two days of exposure. Given this acute mortality under germ-free conditions, it is possible that nAg induces an intense pro-inflammatory immune response in zebrafish larvae, which results in increased acute mortality under germ-free conditions. Diverse metal nanoparticles, including silver, copper and gold nanoparticles, have already been found to induce an acute immune response in zebrafish larvae (Brun et al. 2018; Poon et al. 2019; Van Pomeren et al. 2019). Moreover, Poon et al. (2019) found that nAg, but not nZnO, induces inflammatory immune responses in THP-1 cells. In case immune responses underly the differences in sensitivity between germ-free and colonized conditions, the absence of immune responses in response to nZnO might explain why we did not observe differences in sensitivity between germ-free and colonized larvae to nZnO. Interestingly, Koch et al. (2018) have shown that colonizing microbiota can suppress immune responses in zebrafish larvae via Myd88 signaling. Combined, these findings suggest that colonizing microbiota could protect zebrafish larvae against nAg, by suppressing pro-inflammatory immune responses that are induced by these particles.

4.4.2 Effects of nanoparticles on host-associated microbiota

Concurrent to the mortality among zebrafish larvae, nAg and Ag^{+} killed the majority of zebrafish larvae-associated microbes, with barely any culturable microbes remaining after two days of exposure to nAg. Similarly high bactericidal activity of nAg has been demonstrated *in vitro*, with 4-h EC_{50} values based on growth inhibition ranging from 0.35 to 18.7 mg $Ag{\cdot}L^{-1}$ for gram-negative bacteria (including several *Pseudomonas* species, *Bacillus subtilis* and *Escherichia coli*), and 46.1 mg $Ag{\cdot}L^{-1}$ for the gram-positive bacterium *Staphylococcus aureus* (Bondarenko et al. 2013). In contrast, exposure of zebrafish larvae to sublethal concentrations of nZnO and Zn^{2+} did not result in a lower abundance of isolated microbes. Accordingly, *in vitro* studies have shown that zinc oxide particularly exhibits antimicrobial activity against Gram-positive bacteria, whilst the majority our isolates from zebrafish larvae were Gram-negative bacteria (Seil and Webster 2012). Moreover, the lowest concentrations of nZnO that reduced viability of the Gram-positive bacterium *S. aureus* and the Gram-negative bacterium *Escherichia* *coli,* as determined in 24 h-*in vitro* exposures (> 400 mg ZnO·L^{-1}; Nair et al. 2009), were well above the sublethal concentration of nZnO applied in our study (2.5 mg ZnO·L^{-1}). This could imply that nZnO and Zn^{2+} did not exert any bactericidal activity against the bacterial isolates of our study. Alternatively, growth of resistant bacteria might have compensated for the loss of affected bacteria.

Considering the bactericidal effects of nAg, we further investigated the effects of these particles on microbiota composition. Without exposure to nAg, CFU isolates included the opportunistic pathogenic bacteria *P. aeruginosa, D. lacustris* and/or *D. tsuruhatensis,* and *S. maltophilia* (Preiswerk et al. 2011; Brooke 2012; Shin et al. 2012; Gellatly and Hancock 2013), and possibly *S. epidermis* (Otto 2009). Following exposure to nAg, we did not isolate any of these species anymore from microbially-colonized larvae. It is still unclear whether nAg elicits immune responses that contribute to the loss of opportunistic bacteria. Only one of the bacterial isolates – *P. myrsinacearum* – appeared to be resistant against nAg. Surprisingly, this species was initially isolated from *Ardisia* leaf nodules (Knösel 1984), and is known to be capable of nitrate reduction (Mergaert et al. 2002). Since nitrate-reducing enzymes can reduce Ag^{+} (Lin et al. 2014), it is tempting to hypothesize that *P. myrsinacearum* is resistant to nAg, and protects zebrafish larvae against nAg, by reducing Ag^{+} ions that are released from nAg back into their less toxic particulate form. However, considering other bacterial resistance mechanisms to silver compounds including nAg that have been identified *in vitro* (Silver 2003; Panáček et al. 2018), it remains to be determined what mechanisms drive bacterial resistance to nAg *in vivo*.

4.4.3 General applicability of the test approach

This study, at the interface between toxicology and host-microbe interaction studies, is to the best of our knowledge the first of its kind. We investigate how microbial colonization affects the sensitivity of a vertebrate host to nanoparticle toxicity. In our experimental setup, we include germ-free conditions in nanoparticle toxicity tests, thereby combining multiple stressors using standardized and established techniques that do not require advanced laboratory equipment (OECD 2013; Pham et al. 2018). We note that this multi-stressor research design can be applied to detect effects of nanoparticles at concentrations below the lowest-observed-effect concentrations in conventional toxicity tests. More specifically, it can be used to screen for the interaction of host-associated microbiota with the toxicity of nanoparticles and other compounds of interest. Although zebrafish that are raised in the laboratory harbor different microbiota as compared to zebrafish in their natural habitats, core groups of their microbiota are strikingly similar (Roeselers et al. 2011). Moreover, despite differences in microbiota composition, hosts respond to their associated microbiota in conserved ways (Rawls et al. 2016). This supports the use of our laboratory approach to include the role of host-associated microbiota in human and environmental toxicology. Similar opportunities have been established to derive germ-free *Daphnia magna* water fleas (Sison-Mangus et al. 2015; Callens et al. 2016; Manakul et al. 2017), extending these possibilities to include the role of invertebrate microbiota in toxicological research.

Our results imply that longer-term exposure to bactericidal concentrations of nanoparticles might increase the susceptibility of the host to nAg over time due to the loss of protective microbiota. This insight can serve as an early warning for potential chronic toxic effects of nanoparticles. Nevertheless, chronic effects of nanoparticles depend on many variables and thus remain hard to predict. Some bacteria, for instance, may gain resistance against nAg, and the effects thereof are still unknown. The opportunistic pathogens *P. aeruginosa* and *Escherichia coli* have already been found to be able protect themselves against nAg by producing adhesive proteins that enhance nanoparticle aggregation (Panáček et al. 2018). In case such opportunistic pathogens thrive following nAg-exposure *in vivo*, they might cause infections. Although the complete understanding of the effects of long-term exposure to nAg is beyond the scope of this study, the finding in our study, of a profound impact of colonizing microbiota on silver nanoparticle toxicity, contributes to a better understanding of potential effects of antimicrobial nanoparticles on humans and the environment, and merits further experimental attention.

4.5 Conclusions

In this study, we integrate the disciplines of host-microbiota research and nanotoxicology. By combining gnotobiotic techniques with acute toxicity tests, we showed that host-associated microbiota protect zebrafish larvae against particle-specific toxic effects of silver nanoparticles. This protective effect was lost over time, possibly due to the bactericidal effects of silver particles killing protective microbes. Such indirect adverse effects of nanoparticles, in addition to the direct impacts of nanoparticles on the hosts, can be employed in multi-stressor experimental designs that allow detecting otherwise hidden effects of nanoparticles. The results of our study may also contribute to understanding long-term toxic effects of nanoparticles, since chronic exposure of microbially-colonized organisms to low, yet bactericidal concentrations of nanoparticles may enhance their sensitivity to nanoparticles over time. The observed protective effect of colonizing microbiota against silver nanoparticle toxicity moreover suggests that the effects of silver nanoparticles to humans and to the environment may be more severe following pre-exposure to antimicrobial agents. Hence, our results highlight the importance of taking microbiota interactions into account in human and environmental hazard assessment of silver nanoparticles.

Data availability statement

Data and supporting material are available via Figshare:
https://doi.org/10.6084/m9.figshare.c.4923261 (data)
https://doi.org/10.6084/m9.figshare.12181941.v1 (supporting material)

Acknowledgement

We thank Wouter Beijk for assistance in the laboratory, Gerda Lamers for help with transmission electron microscopy, Rudo Verweij for supervising atomic adsorption spectrometry measurements and Yujia Zhai for supportive discussions about the project. We are grateful to RAS AG for providing silver nanoparticles. This work was supported by the project PATROLS of European Union's Horizon 2020 research and innovation programme under Grant number 760813.

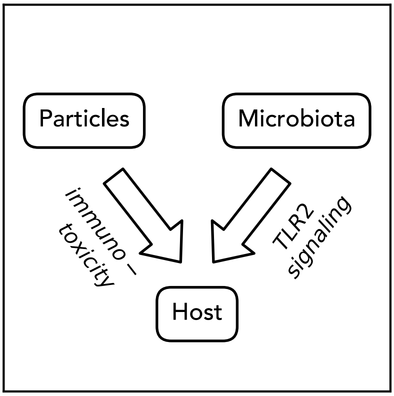
Particles
Microbiota
immuno – toxicity
TLR2 signaling
Host

CHAPTER 5

Microbiota-dependent TLR2 signaling reduces silver nanoparticle toxicity to zebrafish larvae

Bregje W. Brinkmann
Bjørn E. V. Koch
Willie J. G. M. Peijnenburg
Martina G. Vijver

Published in *Ecotoxicology and Environmental Safety*, 237: 113522 (2022). DOI: 10.1016/j.ecoenv.2022.113522

Data is available via *Mendeley Data*. DOI: 10.17632/4nfg69v8hy.1

Abstract

Many host-microbiota interactions depend on the recognition of microbial constituents by toll-like receptors of the host. The impacts of these interactions on host health can shape the host's response to environmental pollutants such as nanomaterials. Here, we assess the role of toll-like receptor 2 (TLR2) signaling in the protective effects of colonizing microbiota against silver nanoparticle (nAg) toxicity to zebrafish larvae. Zebrafish larvae were exposed to nAg for two days, from 3-5 days post-fertilization. Using an *il1ß*-reporter line, we first characterized the accumulation and particle-specific inflammatory effects of nAg in the total body and intestinal tissues of the larvae. This showed that silver gradually accumulated in both the total body and intestinal tissues, yet specifically caused particle-specific inflammation on the skin of larvae. Subsequently, we assessed the effects of microbiota-dependent TLR2 signaling on nAg toxicity. This was done by comparing the sensitivity of loss-of-function zebrafish mutants for TLR2, and each of the TLR2-adaptor proteins MyD88 and TIRAP (Mal), under germ-free and microbially-colonized conditions. Irrespective of their genotype, microbially-colonized larvae were less sensitive to nAg than their germ-free siblings, supporting the previously identified protective effect of microbiota against nAg toxicity. Under germ-free conditions, *tlr2*, *myd88* and *tirap* mutants were equally sensitive to nAg as their wildtype siblings. However, when colonized by microbiota, *tlr2* and *tirap* mutants were more sensitive to nAg than their wildtype siblings. The sensitivity of microbially-colonized *myd88* mutants did not differ significantly from that of wildtype siblings. These results indicate that the protective effect of colonizing microbiota against nAg-toxicity to zebrafish larvae involves TIRAP-dependent TLR2 signaling. Overall, this supports the conclusion that host-microbiota interactions affect nanomaterial toxicity to zebrafish larvae.

Keywords: Host-microbiota interactions; Toll-like receptor; Zebrafish mutants; Inflammation; IL1ß; NM-300K.

5.1 Introduction

Vertebrate animals depend on their interactions with commensal microbes, residing in and on their tissues, to maintain optimal health. These host-microbiota interactions in, amongst others, immune responses, nutrient uptake and energy metabolism (Hacquard et al. 2015; Brugman et al. 2018), can enhance the resilience of the host to environmental pollutants, including engineered nanoparticles. Microbes have also been shown to directly interact with environmental pollutants, for instance by excreting ligands and other biomacromolecules, by facilitating redox reactions, and by decomposing organic chemicals and coatings (Claus et al. 2016; Desmau et al. 2020). In the case of nanoparticles, this can transform the aggregation state, dissolution rate and surface chemistry of the particles, potentially altering their bioavailability, reactivity, persistence, and toxicity (Lowry et al. 2012). Additionally, nanoparticles can adsorb onto the surface of microbes and microbial spores, forming microbe-particle complexes, which can change the fate and (patho)biological effects of the concerning microbes and particles in relevant, yet largely understudied ways (Westmeier et al. 2018). It is difficult to differentiate between the impacts such microbe-particle interactions, and the effects of host-microbiota interactions when studying nanoparticle toxicity *in vivo*.

Many of the balanced interactions between hosts and commensal microbiota are based on evolutionarily conserved principles, where receptors of the toll-like receptor (TLR) family function to sense microbial cells (Fig. 5.1a). The receptors of this family, which are either located in cell membranes (such as TLR1, -2, -4, -5, -6 and -10) or in intracellular vesicles (like TLR3, -7, -8, -9, -11 and -13), were initially found to detect invading pathogens by sensing common constituents of their cells, termed pathogen-associated molecular patterns (PAMPs), or more generally, microbe-associated molecular patterns (MAMPs). Upon recognition of these ligands, TLR receptors form dimers with intracellularly oligomerized Toll/IL-1 receptor (TIR) domains. Dimerized TLRs subsequently recruit TIR-domain including adaptor proteins such as Myeloid Differentiation factor 88 (MyD88) and Toll/Interleukin-1 Receptor domain-containing Adaptor Protein (TIRAP), also known as MyD88 Adaptor-Like (Mal). The recruitment of these adaptor proteins results in a pro-inflammatory signaling cascade that functions to clear the infection (Li et al. 2017; Hu et al. 2019).

Over the past decade, some TLRs, such as TLR2 (Round et al. 2011; Koch et al. 2018), have also been found to detect MAMPs of commensal microbes. As opposed to host-pathogen interactions, this has been found to dampen pro-inflammatory responses (Koch et al. 2018) (Fig. 5.1a), and has moreover been shown to induce mucin secretion (Birchenough et al. 2016; Paone and Cani 2020), thereby enabling commensal microbes to colonize host tissue without penetrating the mucosal barrier. Theoretically, such immuno-suppressive effects of commensal microbiota could also inhibit the pro-

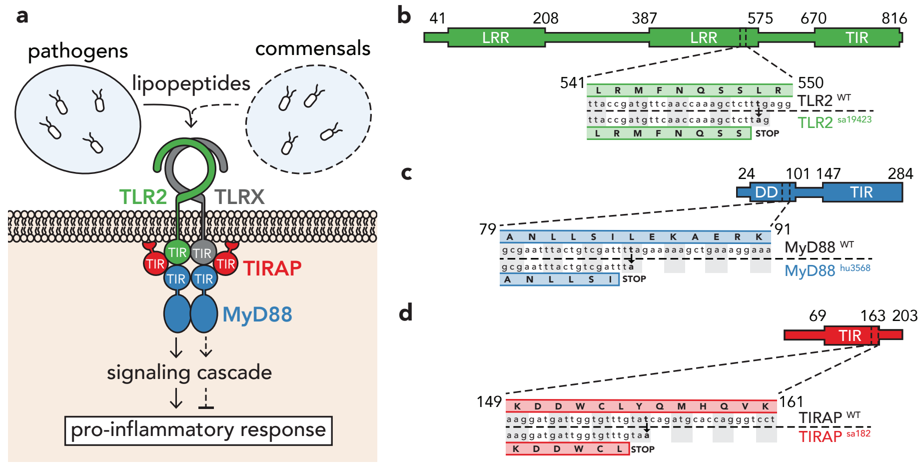

Figure 5.1: *Mutant zebrafish lines in the TLR2 signaling pathway.* **a**) Schematic representation of TLR2 with its adaptor proteins MyD88 and TIRAP (Mal). The Toll/IL-1 receptor (TIR) domain of MyD88 and TIRAP (Mal) can interact with the TIR domain of TLR2. Pathogens have been found to induce pro-inflammatory immune responses via TLR2 (solid line), while commensal microbiota have been shown to dampen pro-inflammatory responses via TLR2 (dashed line). **b**) - **d**) Mutant and wildtype alleles with encoded proteins for TLR2 (*tlr2*^{sa19423} mutant allele) (**b**); MyD88 (*myd88*^{hu3568} mutant allele) (**c**); and TIRAP (Mal) (*tirap*^{sa182} mutant allele) (**d**). In all mutant alleles, a threonine to alanine point mutation results in a premature stop codon prior to or inside of the open reading frame for the TIR domain. As a consequence, the mutants produce truncated versions of TLR2, MyD88 or TIRAP, lacking a functional TIR domain. *Abbreviations*: DD, death domain; LRR, leucine rich repeat; Mal, MyD88 Adaptor-Like; MyD88, Myeloid Differentiation factor 88; TIR, Toll/IL-1 receptor domain; TIRAP, Toll/Interleukin-1 Receptor domain-containing Adaptor Protein; TLR, Toll-Like Receptor.

inflammatory responses of vertebrate hosts to immuno-toxic nanoparticles. Additionally, colonizing microbiota were found to stimulate the proliferation of epithelial cells in the small intestines by enhancing TLR2 expression (Hörmann et al. 2014). As suggested by Hörmann et al. (2014), in addition to potentially beneficial effects of this response to host-microbiota homeostasis, it may explain the protective effects of TLR2 against chemical (DSS)-induced epithelial injury (Rakoff-Nahoum et al. 2004). Similar protective effects of TLR2 signaling can be expected for nanoparticle-induced epithelial injury.

In this study, we investigate the hypothesis that host-microbiota interactions can protect vertebrate hosts against the pro-inflammatory effects of nanoparticles, focusing on the acute toxicity of silver nanoparticles (nAg) to zebrafish larvae. We have previously shown that colonizing microbiota protect zebrafish larvae against the toxicity of these particles (Brinkmann et al. 2020). Moreover, nAg has been shown to induce acute immuno-toxic adverse effects in both animal models and *in vitro* systems (Poon et al. 2019; Cronin et al. 2020). Here, we aim to deepen our understanding on the marked protection of colonizing microbiota against nAg toxicity to zebrafish larvae, investigating the role of TLR signaling.

To test our hypothesis, we take a threefold approach. Firstly, to characterize nanoparticle exposures, we measured the total accumulation of silver in total and intestinal tissues of exposed larvae. Secondly, to verify the pro-inflammatory effects of the particles, we quantified and localized the particle-specific expression of *il1ß*, encoding the pro-inflammatory cytokine IL1ß, using a fluorescent zebrafish reporter line. Thirdly, to evaluate the role of TLR2 signaling in the protective effect of microbiota against these adverse effects, we compared the sensitivity of three mutants in the TLR2 signaling pathway to that of wildtype siblings under germ-free and microbially-colonized conditions. We focused on a loss-of-function mutant for TLR2, as well as on loss-of-function mutants for the TLR2 adaptor proteins MyD88 and TIRAP. Given the key role of TLR2-signaling in host-microbiota interactions, these efforts help to elucidate the impact of host-microbiota interactions on nAg toxicity to zebrafish larvae. More generally, this work provides a proof-of-principle to discriminate between the effects of microbe-pollutant and host-microbiota interactions on toxicity based on evolutionarily conserved pathways in host-microbiota signaling.

5.2 Methods

5.2.1 Nanoparticle dispersions

Silver nanoparticles (nAg) of series NM300-K (Klein et al. 2011) were kindly provided by HeiQ RAS AG (Regensburg, Germany). Non-dispersed particles were handled in an argon atmosphere to prevent particle oxidation, following the EAHC NANOGENOTOX batch dispersion protocol (v.1) (Jensen 2018b). Particle dispersions were prepared from a 100 mg nAg·L^{-1} stock suspension of nAg in autoclaved egg water (60 mg·L^{-1} Instant Ocean sea salts in demi water; Sera GmbH, Heinsberg, Germany). Stock suspensions were dispersed for 10 min in an ultrasonic bath (USC200T; VWR, Amsterdam, The Netherlands) at an acoustic power of 12W, as determined following the EU FP7 NANoREG sonicator calibration standard operation procedure (v.1.1) (Jensen et al. 2018).

Immediately following dispersion, stock suspensions were diluted to nominal exposure concentrations of 2.5, 1.5, 1.0, 0.75 and 0.25 mg nAg·L^{-1} in autoclaved egg water. As determined in our previous study (Brinkmann et al. 2020), this corresponded to actual concentrations averaging 1.53, 1.49, 0.89, 0.74 and 0.20 mg nAg·L^{-1}, and shed ion concentrations averaging 0.17, 0.09, 0.07, 0.04, and 0.05 mg Ag^{+}·L^{-1}, respectively.

Our previous characterization of the exposure media furthermore indicated that primary particles were spherically shaped, had a mean diameter of 8 to 42 nm (average 24 nm, *n*=50), and formed aggregates with a hydrodynamic size of 140 ± 59 to 218 ± 109 nm at nominal exposure concentrations of 2.5 and 1.5 mg nAg·L^{-1}, respectively. The zeta potential of aggregates remained stable around -20 mV.

5.2.2 Zebrafish lines

Zebrafish were housed at Leiden University's zebrafish facility at 28 °C and with the photoperiod set to 14 h light:10 h dark. Husbandry and handling of the fish complied with Dutch national regulation on animal experimentation ('Wet op dierproeven' and 'Dierproevenbesluit 2014'), and European animal welfare regulations (EU Animal Protection Directive 2010/63/EU), as supervised by the Animal Welfare Body of Leiden University. Fish were bred and larvae were handled following the standard protocols included in 'The zebrafish book' (https://zfin.org).

Experiments were performed with larvae of AB×TL wildtype zebrafish, the transgenic reporter line *Tg(il1ß:eGFP-F)*, expressing farnesylated GFP under control of the *il1ß* promotor (Nguyen-Chi et al. 2014), and three loss-of-function mutants in the TLR2 signaling pathway. These mutants included a *tlr2-/-* mutant, a *myd88-/-* mutant and a *tirap-/-* mutant, comprising the *tlr2^{sa19423}* allele (ZFIN Cat# ZDB-ALT-131217-14694, RRID:ZFIN_ZDB-ALT-131217-14694), *myd88^{hu3568}* allele (ZFIN Cat# ZDB-ALT-130729-6, RRID:ZFIN_ZDB-ALT-130729-6) and *tirap^{sa182}* allele (ZFIN Cat# ZDB-ALT-100831-10, RRID:ZFIN_ZDB-ALT-100831-10), respectively. All mutant alleles were obtained in ENU mutation screens and comprised a threonine to alanine point mutation resulting in a pre-mature stop codon prior to (*tlr2^{sa19423}* and *myd88^{hu3568}*) or inside of (*tirap^{sa182}*) the TIR domain encoding sequence (Fig. 5.1b-d). The mutant alleles therefore encode truncated proteins without a functional TIR domain. All loss-of-function mutants and the transgenic line have an AB×TL background and have been approved by the Animal Welfare Body.

For the loss-of-function mutants, germ-free zebrafish larvae were obtained following 'Natural breeding method' described by Pham et al. (2008), with the modifications made by Koch et al. (2018). To this end, zebrafish eggs acquired from synchronized crosses were incubated for 6 h in egg water containing the antimycotic Amphothericin B (250 ng·mL^{-1}), and the antibiotics Ampicillin (100 µg·mL^{-1}) and Kanamycin (5 µg·mL^{-1}). Thereafter, 150 eggs were rinsed for 45 to 60 s with 3 mL 0.2% PVP-iodine solution in 15 mL conical tubes, and were subsequently rinsed twice with 10 mL autoclaved egg water. This procedure was followed by two rinsing steps of 5 min with 6 mL 0.03% sodium hypochlorite (3.5% Cl_2; VWR International, Radnor, PA).

Notably, this hypochlorite concentration is twice as low as the concentration used by Koch et al. (2018), to ensure that all embryos hatched naturally. In between hypochlorite rinsing steps, eggs were rinsed once with 10 mL autoclaved egg water. After the hypochlorite rinsing steps, eggs were rinsed thrice with 10 mL autoclaved egg water. Sterilized eggs were maintained in the dark under sterile conditions at 28 °C until the start of exposures at 3 days post-fertilization (dpf) (section 5.2.3). The sterility these 3-dpf larvae was checked by plating homogenized larvae on LB-medium, as described by Brinkmann et al. (2020).

5.2.3 Nanoparticle exposures

Zebrafish larvae were exposed to silver dispersions from 3-5 dpf. For exposures, the 24-well plate setup introduced by Van Pomeren et al. (2017b) was used. In this setup, ten larvae were exposed to 2 mL of exposure medium in one well of the 24-well plate. Larvae of controls were exposed to autoclaved egg water without nanoparticles. Three replicates were included per exposure concentration or control. Larvae in well plates were incubated in the dark at 28 °C, and mortality was scored at 0, 3, 7, 24 and 48 h post-exposure. At 24 h post-exposure, dead larvae were removed, and exposure media were refreshed.

Three different sets of exposures were tested, depending on the research question. Firstly, to study the accumulation of silver (section 5.2.4), AB×TL larvae were exposed to the lowest, sublethal nominal exposure concentration of 0.25 mg $nAg \cdot L^{-1}$. Secondly, to study inflammatory responses (section 5.2.5), *Tg(il1ß:eGFP-F)* larvae were exposed to the sublethal nominal exposure concentration of 0.25 mg $nAg \cdot L^{-1}$, and the corresponding shed ion concentration of 0.05 mg $Ag^{+} \cdot L^{-1}$, as prepared from a $Ag(NO_3)$ stock solution. This enabled assessing the particle-specific inflammatory effects of nAg. Thirdly, to test the nAg-sensitivity of TLR2 signaling mutants (section 5.2.6.2), a full factorial exposure design, including each mutant and its sibling under both microbially-colonized and germ-free conditions, was applied for exposure to all nAg exposure concentrations.

5.2.4 Accumulation of silver in larvae and intestines

The uptake and adsorption of nAg by zebrafish larvae was determined by measuring total silver concentrations in larvae and their intestines. At 0, 7, 24 and 48 h post-exposure, larvae were sampled and anaesthetized with tricaine (200 $\mu g \cdot L^{-1}$; 3-amino-benzoic acid; Sigma-Aldrich, Darmstadt, Germany). Intestines of anaesthetized larvae were extracted using two pairs of dissection tweezers, by pinching one pair of the tweezers in between the swim bladder and the intestines of the larvae, and gently pulling the mid- and posterior intestine out of the tail of the larvae using the other pair of tweezers. Thereafter, the tissue covering the intestinal bulb was carefully removed, and intestines were cleaved at the basal side of the intestinal bulb. Intestines could not be collected at the start of exposures, as the intestinal tissue was still too fragile at this developmental stage. For three replicates at each exposure time, ten intestines were collected on one 2% agarose slice. Similarly, ten non-dissected larvae were collected on one 2% agarose slices at each exposure time *in triplo*. Agarose slices with intestines or larvae were transferred to pre-weighed 2.0 mL SafeLock microcentrifuge tubes (Eppendorf, Nijmegen, The Netherlands), and weighed again to determine the volume of agarose slices, which did not exceed 15 µL. Larvae and intestines were digested overnight at 70 °C in 200 µL 0.76× *aqua regia* (HNO_3 : HCl; 1 : 3), accounting for the volume of agarose slices. Digested samples were diluted to a final concentration of 2.25% HCl (1.06% HNO_3). Total silver in larval samples was measured by graphite furnace atomic absorption spectrometry (GFAAS; PinAAcle 900Z, Perkin Elmer, The Netherlands), and total silver in intestinal samples was measured by inductively coupled plasma mass spectrometry (ICP-MS; NexIon 2000, Perkin Elmer). Silver concentrations in larvae and their intestines were expressed as the total mass of Ag per larvae, and total mass of Ag per intestine, respectively.

5.2.5 Particle-specific inflammation

The pro-inflammatory effects of nAg were assessed using *Tg(il1ß:eGFP-F)* reporter larvae. At 48 h post-exposure, larvae of controls and larvae exposed to nAg (0.25 $mg{\cdot}L^{-1}$) or Ag^+ (0.05 $mg{\cdot}L^{-1}$) were transferred to a 0.5 % methylcellulose solution in egg water comprising the anesthetic tricaine (200 $\mu g{\cdot}L^{-1}$). Anaesthetized larvae were laterally positioned on a 1% agarose plate for imaging using a stereo fluorescence microscope. Images were acquired of the green fluorescent signal, as detected using a GFP emission filter, and total transmitted light, as detected without emission filter. The sum of all pixel values in green fluorescence images was quantified from the posterior side of the swimbladder to the apical side of the tail using the 'RawIntDen' measurement in ImageJ (v. 2.0.0; Abràmoff et al. 2004). The area posterior of the swimbladder was excluded from the image analysis due to the high expression of GFP in the retina of control *Tg(il1ß:eGFP-F)* larvae (Nguyen-Chi et al. 2014). Ten larvae were imaged for each of the three replicates per treatment.

5.2.6 Statistical analysis

All statistical analyses were performed in R (v. 3.6.3; www.r-project.org), and all figures were plotted using Python (v. 3.6.5) with the packages 'numpy' (v. 1.19.1), 'pandas' (v.0.23.3), and 'matplotlib' (v.3.1.3). Mean and standard error of the mean (SEM) are reported.

5.2.6.1 Il1ß expression of reporter larvae

The GFP signal of *Tg(il1ß:eGFP-F)* larvae was compared between control larvae, nAg-exposed larvae and Ag^+-exposed larvae by way of a one-way analysis of variance (ANOVA) combined with a Tukey's HSD post-hoc test. Logarithmic transformation was required to ensure that residuals followed a normal distribution, as assessed by inspecting histograms and Q-Q plots. Model residuals were plotted against fitted values to check for the equal distribution of variance across the treatments.

5.2.6.2 Sensitivity of TLR2 signaling mutants to nAg

The sensitivity of the TLR2 signaling mutants was compared to that of their wildtype siblings under germ-free and microbially colonized conditions by fitting time-response curves to mortality data using generalized linear mixed models. These models were fitted using the *glmer* function of the 'lme4' package (v. 1.1-23), for all five exposure concentrations, excluding controls. All models included the 'dead' or 'live' state of larvae as binary response variable, and exposure time, exposure concentration, genotype ('mutant' vs. 'wildtype') and colonization condition ('colonized' or 'germ-free') as explanatory variables. Significant interactions between these four explanatory variables, as indicated in Table 5.1, were also included in the models. Additionally, exposure well was included as random variable in all models, to account for the repeated scoring of mortality over time for these wells. The *logit* link function was used to specify the binomial family of the generalized linear mixed models. Moreover, a *bobyqa* optimizer function with 2^5 iterations was applied for TLR2 and TIRAP models to solve convergence failure. To plot the fitted time-response curves, predicted probabilities were obtained from mixed models using the *predict* function.

To check model assumptions, Q-Q plots were computed using the 'car' package (v. 3.0-8), to examine if model residuals followed a normally distributed. Furthermore, Pearson model residuals were plotted against fitted values, to verify the equal spread of variance across the treatments. Theta values of the mixed effect were extracted to check for potential singularity. In case none of these assumptions were violated, post-hoc comparisons were performed using the *glth* function of the 'multcomp' package (v.1.4-13) in four consecutive steps. Firstly, we tested if microbiota indeed offered protection against nAg, by comparing the nAg-sensitivity of wildtype siblings under germ-free and

Table 5.1: Significant interactions included in dose-response models.

Interactions	*TLR2*	*MyD88*	*TIRAP*
Hours : Condition	x	x	x
Hours : Genotype	x		
Hours : Concentration	x	x	
Genotype : Condition			x
Genotype : Concentration			x
Hours : Genotype : Condition	x		x
Hours : Genotype : Concentration			x

microbially-colonized conditions. Secondly, we tested if this protective effect was lost in the loss-of-function mutants, by comparing the nAg-sensitivity of TLR2 signaling mutants under germ-free and microbially colonized condition. Thirdly, we examined if there were any microbiota-independent effects of TLR2 signaling on nAg-sensitivity, by comparing the nAg-sensitivity of TLR2 signaling mutants and wildtype siblings under germ-free conditions. Fourthly, in case no microbiota-independent effects could be detected, we evaluated if the level of protection against nAg offered by colonizing microbiota was affected in TLR2 signaling mutants, by comparing the nAg-sensitivity of TLR2 signaling mutants and their wildtype siblings under microbially colonized conditions.

5.3 Results

5.3.1 Accumulation of silver in total and intestinal tissues

Zebrafish larvae gradually accumulated silver in and on their tissues over the two-day exposure to sublethal concentrations of nAg (0.25 mg $nAg \cdot L^{-1}$) (Fig. 5.2). The concentration of silver associated with the total larval tissue increased linearly over time, reaching a final concentration of 0.29 ± 0.01 ng $Ag \cdot larva^{-1}$ at the end of exposure (Fig. 5.2, black circles). Less than 10% of this total amount of tissue-associated silver accumulated in the intestines of larvae (Fig. 5.2, white circles). Most of this silver accumulated in the intestines over the first day of exposure, reaching an average concentration of 0.008 ± 0.0003 ng $Ag \cdot intestine^{-1}$ at 24 h of exposure. Over the second exposure day, only a slight increase to 0.011 ± 0.0009 $Ag \cdot intestine^{-1}$ was detected, indicating a saturation of the intestinal exposure to nAg.

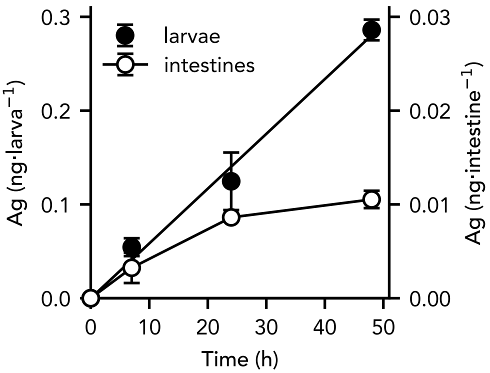

Figure 5.2: *Accumulation of total silver in zebrafish larvae.* Black circles (left axis) represent silver concentrations in and on the entire larvae, white circles (right axis) represent silver concentrations in the intestines of larvae.

5.3.2 Particle-specific inflammation induced by silver nanoparticles

The intensity and localization of pro-inflammatory effects of nAg were assessed based on the expression of the pro-inflammatory cytokine encoding gene *il1ß* in transgenic *Tg(il1ß:eGFP-F)* reporter larvae. Following two days of exposure, sublethal concentrations of nAg (0.25 mg·L^{-1}) resulted in enhanced expression of *il1ß* in patches along the complete surface of the skin of zebrafish larvae (Fig. 5.3a). At some of these patches, tissue damage could clearly be observed using stereo microscopy. The total *il1ß* signal, as quantified by the log-transformed integrated density of GFP signal in microscopy images, was significantly higher in nAg-exposed larvae (14.38 ± 0.07) than in control larvae (13.82 ± 0.03) ($p < 0.001$). No tissues with enhanced *il1ß* expression could be observed in larvae that were exposed to silver ions at concentrations that correspond to the dissolved fraction of nAg in particle exposures (0.05 mg Ag^+·L^{-1}) (Fig. 5.3b). Similarly, no indications of an enhanced *il1ß* signal could be observed in controls that had not been exposed to silver ions and particles (Fig. 5.3c). Accordingly, the total *il1ß* signal in Ag^+-exposed larvae (13.92 ± 0.05) and controls (13.82 ± 0.03) did not differ significantly ($p = 0.42$).

5.3.3 Microbiota-dependent sensitivity of TLR2 signaling mutants to silver nanoparticle toxicity

To gain further mechanistic understanding of the protective effect of microbiota against the adverse effects of nAg, resulting from aquatic exposure as characterized above, we compared the sensitivity of three loss-of-function mutants in the TLR2 signaling pathway in acute toxicity tests. We specifically focused on mutants for TLR2 (Fig. 5.4), and TLR2 adaptor proteins MyD88 and TIRAP (Fig. 5.5). To allow detecting subtle

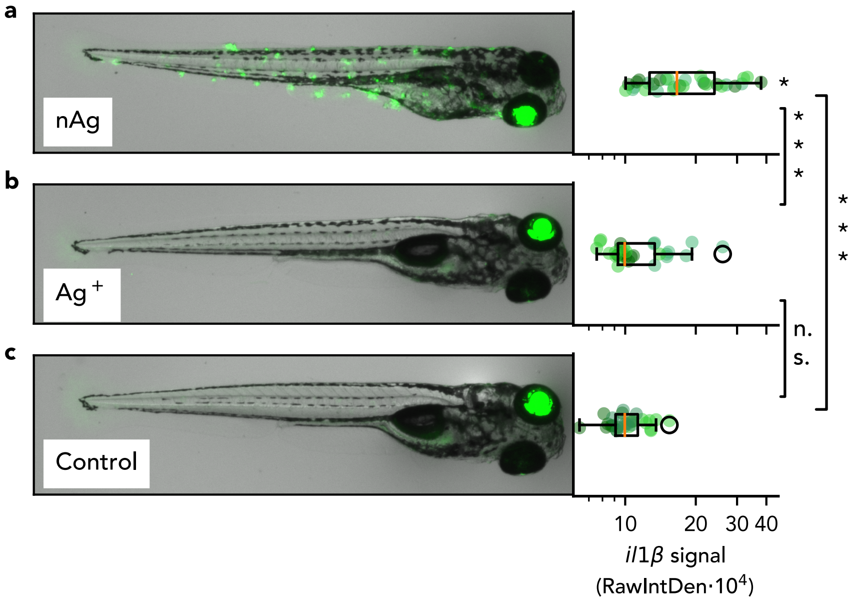

Figure 5.3: *Particle-specific inflammatory effect of silver nanoparticle exposures.* Inflammatory effects were studied using *Tg(il1ß:eGFP-F)* reporter zebrafish larvae. Pictures show representative images of larvae, with quantification of GFP signal from the anterior side of the swim bladder up to and including the tail fin, following exposure to nAg (0.25 mg nAg·L^{-1}; *n*=30) (**a**), their shed ions (0.05 mg Ag^{+}·L^{-1}; *n*=30) (**b**), and egg water lacking nAg and shed ions (*n*=28) (**c**). Asterisks indicate significant differences: ***, *p*<0.001. *Abbreviations*: RawIntDent, Raw integrated density; n.s., non-significant.

differences in the protective effects of microbiota between the TLR2 signaling mutants, time response curves for the full range of exposure concentrations were used in all acute toxicity comparisons.

Before we evaluated the effects of microbial interactions with the TLR2, MyD88 and TIRAP proteins on nAg toxicity to zebrafish larvae, we first checked if the genetic background of these mutants affected nAg sensitivity. For siblings of all mutants, microbially-colonized larvae were less sensitive to nAg than germ-free larvae (TLR2: $p < 0.001$, $z = -8.21$; MyD88: $p < 0.001$, $z = -9.83$; TIRAP: $p < 0.001$, $z = -8.92$). The mortality of nAg-exposed siblings followed similar time-response patterns, where the difference in mortality between germ-free and colonized conditions was largest at the start of exposure and decreased gradually over time (Fig. 5.4 and Fig. 5.5, black curves). These results indicate that, irrespective of genetic background, colonizing microbiota protected zebrafish larvae against nAg toxicity, while this protective effect dissipated over time. We subsequently examined if there were any microbiota-independent effects of the loss-of-function mutations on nAg toxicity. Since, under germ-free conditions,

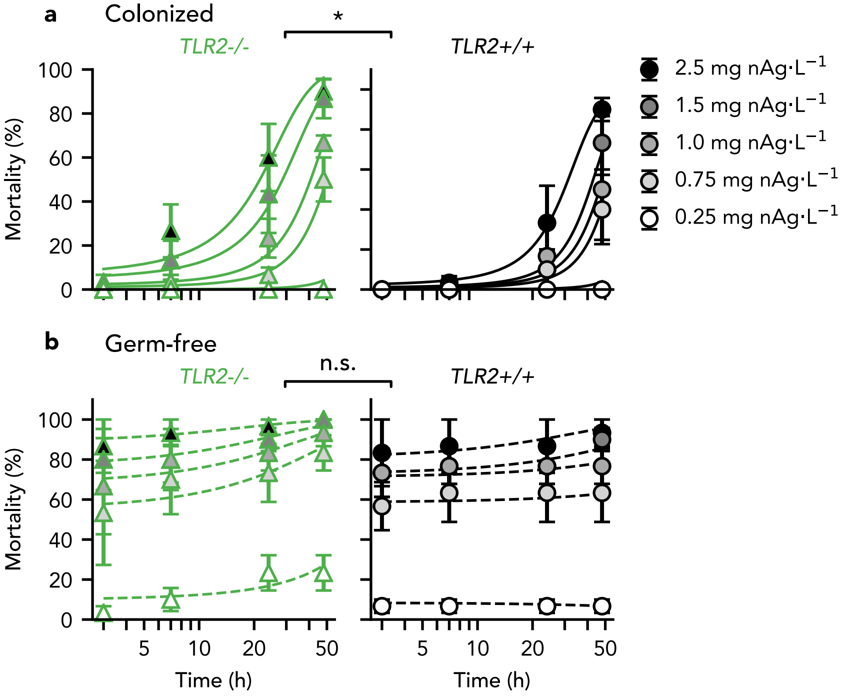

Figure 5.4: *TLR2-dependent effects of colonizing microbiota on silver nanoparticle toxicity to zebrafish larvae.* Sensitivity of *tlr2*$^{-/-}$ as compared to *tlr2*$^{+/+}$ zebrafish larvae under microbially-colonized conditions (**a**) and germ-free conditions (**b**). Asterisks indicate significant differences (*n*=3).

the nAg-sensitivity of all mutants did not differ from that of their wildtype siblings (TLR2: $p = 0.90$, $z = -0.12$; MyD88: $p = 0.73$, $z = 0.35$; TIRAP: $p = 0.14$, $z = -1.49$) (Fig. 5.4b, Fig. 5.5c,d), these effects could not be detected.

The lack of microbiota-independent effects on nAg-sensitivity for all mutant lines allowed us to explore to what extent microbiota-dependent effects on nAg-sensitivity involve signaling through TLR2, MyD88 or TIRAP. All loss-of-function mutants were less sensitive to nAg under microbially-colonized conditions than under germ-free conditions (TLR2: $p < 0.001$, $z = -7.14$; MyD88: $p < 0.001$, $z = -9.23$; TIRAP: $p <0.001$, $z = -8.08$), indicating that the protective effect of microbiota against nAg was maintained in the absence of functional TLR2, MyD88 or TIRAP protein. Nevertheless, the level of protection offered by colonized microbiota against nAg toxicity depended on the loss-of-function mutations. Under microbially-colonized conditions, *tlr2* mutants were more sensitive to nAg than their wildtype siblings ($p = 0.04$, $z = 2.01$) (Fig. 5.4a). Similarly, *tirap* mutants were more sensitive to nAg under microbially-colonized conditions than wildtype siblings ($p < 0.001$, $z = 4.51$) (Fig. 5.5b). This implies that

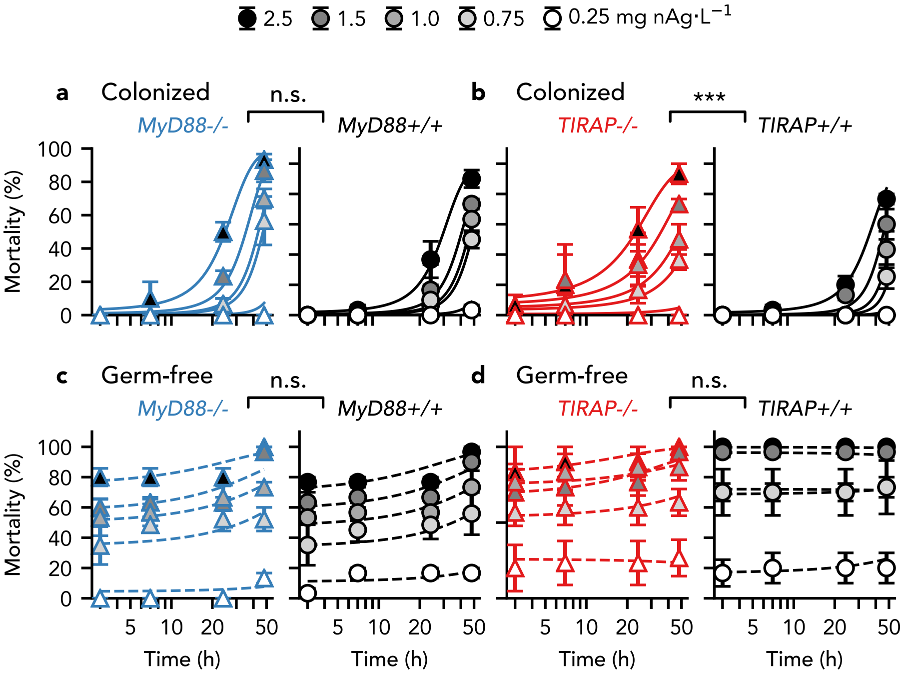

Figure 5.5: *TLR2 adaptor-dependent effects of colonizing microbiota on silver nanoparticle toxicity to zebrafish larvae.* **a**) and **c**) Sensitivity of *myd88*$^{-/-}$ as compared to *myd88*$^{+/+}$ zebrafish larvae, under microbially-colonized conditions (**a**) and germ-free conditions (**c**). **b**) and **d**) Sensitivity of *tirap*$^{-/-}$ as compared to *tirap*$^{+/+}$ zebrafish larvae, under microbially-colonized conditions (**b**) and germ-free conditions (**d**). Asterisks indicate significant differences (*n*=3).

microbial interactions with TLR2 affect the sensitivity of zebrafish larvae to nAg in a TIRAP-dependent manner. In contrast to *tlr2* and *tirap* mutants, the sensitivity of the *myd88* mutant did not differ significantly from that of wildtype siblings under microbially-colonized conditions ($p = 0.52$, $z = 0.47$) (Fig. 5.5a).

5.4 Discussion

Studies investigating the role of host-microbiota interactions in nanomaterial toxicity face the common challenge to differentiate between the direct effects of microbe-particle interactions on the fate, behavior and reactivity of nanoparticles (Lowry et al. 2012), and the effects of host-microbiota interactions on the host's sensitivity to particle toxicity. In diverse animals, with most evidence provided for vertebrates (Dierking and Pita 2020), interactions between commensal microbiota and the host have been shown to depend on the recognition of microbial constituents by receptors of the TLR family. Here, we explored if we could identify impacts of host-microbiota interactions on nanomaterial toxicity based on TLR2 signaling. To this end, we focused on the protective effect of colonizing microbiota against nAg toxicity to zebrafish larvae, employing the experimental benefits and available mutant lines for this widely used model organism.

The first step towards understanding the protective effects of colonizing microbiota against nAg toxicity, was to characterize the actual exposure to nAg over time, as well as to quantify and localize the adverse effects that this imposes on the larvae. Briefly, we found that silver accumulated gradually in and on the larval bodies from the start of exposure onwards, with a small fraction reaching the intestines. This intestinal silver exposure accounted less than 10% of the total body burden. In contrast to the total body burden, the accumulation of silver in intestines saturated over time. It is plausible that this saturation resulted from the impaired swallowing activity of larvae that have been affected by the pro-inflammatory effects of nAg.

To characterize these pro-inflammatory effects of nAg, we used fluorescent reporter larvae expressing GFP under control of the *il1ß* promotor. Imaging of these larvae showed that nAg exposure resulted in enhanced *il1ß* expression in patches across the full skin of larvae. The transcriptional investigations of Kang et al. (2016), showing a >2-fold higher expression of *il1ß* (BC098597 / NM_212844) by zebrafish larvae that were exposed to a sublethal concentration of nAg, as compared to control larvae, corroborate this finding. Because we also observed tissue damage at these locations with enhanced *il1ß* expression, the pre-cytokine had likely been activated by pyrin containing protein-3 (NLRP3) and caspase-1 (Dinarello 2018). Notably, these pro-inflammatory effects could not be detected in zebrafish larvae that had been exposed to silver ions at concentrations corresponding to the dissolved fraction of the particle exposures. Although the applied analytical techniques do not allow for the quantification of silver in dermal versus internal tissues, and can neither discriminate between the particulate and dissolved fractions of silver, these particle-specific adverse effects suggest that nAg adsorbed onto the skin of zebrafish larvae, causing local dermal inflammation. Similar dermal pro-inflammatory effects of nanoparticles have previously been described by Brun et al. (2018) for both copper and plastic nanoparticles.

Although the *il1ß* reporter larvae allow to detect pro-inflammatory cytokine responses in internal tissues (Nguyen-Chi et al. 2014), we only detected increased *il1ß* expression on the skin of larvae. Previous research on the adverse effects of nAg to zebrafish larvae revealed that ionocytes, a skin cell type, and sensory systems, including the olfactory bulb and neuromasts, are particularly sensitive to nAg-induced oxidative stress, showing responses at concentrations from 4 $\mu g \cdot L^{-1}$ to 1 mg $nAg \cdot L^{-1}$ (Osborne et al. 2016; Horng et al. 2022). At higher exposure concentrations, starting at 1 mg $nAg \cdot L^{-1}$, oxidative stress could also be observed in the intestines of zebrafish larvae (Liu et al.

2019; Lee et al. 2022). In nanomaterial toxicity, levels of oxidative stress that cannot be compensated via the regulation of cytoprotective (antioxidant) genes (‘tier 1’ oxidative stress) are hypothesized to result in inflammatory responses (‘tier 2’ oxidative stress), and eventually, if ROS levels increase even further, in cytotoxic and genotoxic responses (‘tier 3’ oxidative stress) (Johnston et al. 2018). Since both neuromasts and ionocytes are located on the skin of zebrafish larvae, it is possible that the dermal inflammation observed in our study originates from nAg-induced oxidative stress in these sensory systems and cells.

Next, to study the protective effect of microbiota against nAg, we compared the lethal effects of nAg between larvae raised under microbially-colonized and germ-free conditions. The difference in mortality between these conditions can be attributed to the protective effect of colonizing microbiota against nAg toxicity to zebrafish larvae. In the absence of microbiota, nAg induced high and nearly instant mortality at concentrations that were only lethal to microbially-colonized larvae by the second day of exposure. Such nearly instant mortality has been associated with septic shock, which can be induced by exposing zebrafish larvae to immunostimulants such as lipopolysaccharides (Philip et al. 2017). Similar to the protective effect of microbiota against acute nAg-induced mortality, synbiotics comprising commensal microbes have been reported to protect early infants against sepsis (Panigrahi et al. 2017). These remarkable commonalities could indicate that nAg toxicity and sepsis involve similar hyperinflammatory states.

In our study, we showed that a loss-of-function mutation in TLR2 limits the protective effect of colonizing microbiota against nAg toxicity to zebrafish larvae. This indicates that microbial interactions with TLR2 confer protection against nAg toxicity to zebrafish larvae. Crucially, under germ-free conditions we could not detect any difference in sensitivity between *tlr2* mutants and their wildtype siblings. This supports two important assumptions that are inherent to our experimental setup. It firstly suggests that interactions of colonizing microbiota with TLR2, rather than interactions of sterile TLR2 agonists, such as damage-associated molecular patterns (DAMPs) that are released upon wounding, affect nAg toxicity to zebrafish larvae. It secondly shows that differences in sensitivity between mutants and their siblings do not result from direct effects of nAg on TLR2 signaling. This is an important assumption to validate, as nAg has previously been found to affect lipopolysaccharide-induced TLR signaling in THP-1 cells (Gliga et al. 2019).

Downstream signaling from TLR2 requires the intracellular recruitment of TLR2 adaptor proteins TIRAP and MyD88. Together with interleukin 1 receptor (IL-1R) associated kinase 4 (IRAK-4), and IRAK-1 or IRAK-2, these adaptor proteins form a protein complex called the ‘Myddosome’, which transduces the TLR2 signal intracellularly (Lin et al. 2010). In view of this signaling cascade, reproducing the results obtained for the *tlr2* mutant in loss-of-function mutants for TIRAP or MyD88 could provide further support for the hypothesis that colonizing microbiota protect zebrafish larvae against nAg toxicity via signaling through TLR2. However, only the loss-of-function mutant for TIRAP, but not the loss-of-function mutant for MyD88, could reproduce the higher microbiota-dependent sensitivity to nAg toxicity observed for the *tlr2* mutant. This discrepancy could indicate that the protective effect of colonizing microbiota against nAg toxicity involves MyD88-independent TLR2 signaling pathways, as have been described by Bernard and O'Neill (2013) and Rajpoot et al. (2021). Alternatively, the contrasting results for MyD88 and TIRAP could reflect the more complex role of MyD88 in intracellular signaling. While, to our current understanding, TIRAP is only involved in signaling from TLR2 and TLR4, and in signaling from the receptor for advanced glycation end-products (RAGE), MyD88 interacts with intracellular signaling pathways from all TLRs except for TLR3, and moreover interacts with the interleukin receptors IL-1R and IL-18R (Adachi et al. 1998), as well as RAGE (Rajpoot et al. 2021) and IFN-γR (Sun and Ding 2006). Potentially, the effects of the loss-of-function mutation for MyD88 on signaling from these receptors could mask its effects on TLR2 signaling. Despite the complexity in these signaling pathways, the finding that loss-of-function mutations in two key proteins of the TLR2 signaling pathway result in higher, microbiota-dependent sensitivity of zebrafish larvae against nAg toxicity, strengthens the support for the identified role of TLR2 signaling in the protective effect of colonizing microbiota against nAg toxicity.

The observed responses of zebrafish larvae to nAg, including protective TLR2 signaling and enhanced *il1ß* expression, could be part of a pathophysiological manifestation initiated by particle-induced oxidative stress, and resulting in tissue damage. Here, the elevated *il1ß* expression can be an indication of the inflammatory response to 'tier 2' oxidative stress, in which neutrophils and macrophages infiltrate the particle-exposed tissue (Johnston et al. 2018). The enhanced *il1ß* expression by epithelial cells can also stimulate the regeneration of injured tissue via the expression of regenerative genes (Hasegawa et al. 2017). Similarly, microbiota-induced TLR2 expression can promote cell proliferation via ERK and AKT signaling (Hörmann et al. 2014). This is consistent with the expression study of Kang et al. (2016), showing that not only the expression of *il1ß*, but also the expression of genes from the TLR, MAPK/ERK and cell cycle pathways were upregulated in response to nAg. Nevertheless, if inflammatory cytokines and immune cells are not cleared from the target site, chronic inflammation can result in cytotoxicity, genotoxicity (Johnston et al. 2018) and apoptosis of regenerative cells (Hasegawa et al. 2017).

Irrespective of what intracellular signaling pathways confer the protective effect of colonizing microbiota against nAg toxicity to zebrafish larvae, only a small fraction of the mortality that could be prevented by microbial colonization was TLR2-dependent. Part of the remaining mortality that is specific to the germ-free condition may be attributed to the lack of host-microbiota interactions through other receptors. In fact, adult zebrafish express at least seventeen putative TLR variants, including counterparts for human TLRs (TLR-1,-2,-3,-4,-5,-7,-8,-9), several non-mammalian TLRs (TLR-18, -19, -20, -21, and -22), and variants resulting from the genome duplication event in teleost fish (tlr4ba/tlr4bb for TLR-4; tlr5a/tlr5b for TLR-5; tlr8a/tlr8b for TLR-8; tlr20a/trl20b for TLR-20) (Meijer et al. 2004; Li et al. 2017). Additionally, direct interactions between microbes and nanoparticles would be expected to alter nAg toxicity to zebrafish larvae by affecting particle fate, biodistribution and reactivity (Lowry et al. 2012; Westmeier et al. 2018). Intuitive examples of such interactions include the enhanced aggregation of nAg in the presence of microbial exudates like flagellin (Panáček et al. 2018), as well as the reduction of toxic silver ions by microbial activity (Lin et al. 2014). It is beyond the scope of the present work to assess the relative contributions of these microbe-particle interactions, compared to the effects of host-microbiota interactions on nanomaterial toxicity. Nonetheless, for the first time, our study provides evidence that the recognition of colonizing microbiota by TLR2 affects nanomaterial toxicity *in vivo*. This demonstrates the importance of considering the intricate interactions between hosts and their microbiota in nanomaterial hazard assessment.

5.5 Conclusions

In this study, we show that suspended nAg can accumulate on the skin of zebrafish larvae, causing particle-specific dermal inflammation at sublethal exposure concentrations. At lethal exposure concentrations, nAg induced more acute mortality patterns under germ-free conditions than under microbially-colonized conditions. The nearly instant mortality under germ-free conditions could potentially result from hyperinflammatory states that have been described for septic shock. We found that colonizing microbiota can protect against this nAg-toxicity in a partly TLR2- and TIRAP-dependent manner. Since TLR2 and TIRAP are key proteins of the TLR2 signaling pathway, this reveals that microbiota-host interactions can shape the response of the host to immuno-toxic nanoparticles. This confirms the importance of including the role of host-microbiota interactions in nanoparticle effect assessment.

Author contributions

Bregje W. Brinkmann: Conceptualization, Investigation, Formal analysis, Writing – original draft, Writing – review & editing. ***Bjørn E.V. Koch***: Conceptualization, Writing – review & editing. ***Willie J.G.M. Peijnenburg***: Supervision, Writing – review & editing. ***Martina G. Vijver***: Supervision, Funding acquisition, Writing – review & editing.

Data availability statement

Data is available via Mendeley Data DOI: 10.17632/4nfg69v8hy.1

Acknowledgments

The authors are grateful to Rudo Verweij for his support with GFAAS measurements, Sipeng Zheng for performing ICP-MS measurements, Wouter Beijk for help with stereo fluorescence imaging, Wanbin Hu for help with maintenance and genotyping of the mutant zebrafish lines, Mónica Varela for maintaining the *il1ß*-reporter zebrafish, Annemarie Meijer for providing the *myd88-/-* mutant, Herman Spaink for providing the *tlr2-/-* mutant, as well as for his valuable input in scientific discussions, and the anonymous reviewer for providing constructive comments. The authors thank HeiQ RAS AG for providing silver nanoparticles for this study. This work was supported by the project PATROLS of European Union's Horizon 2020 research and innovation programme [grant number 760813].

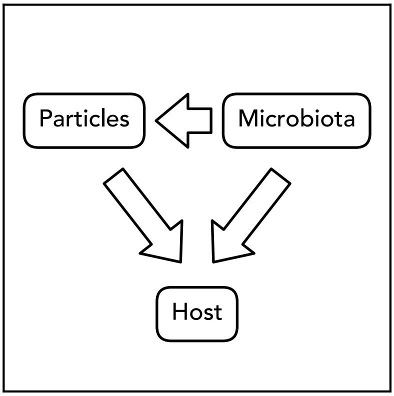
Particles
Microbiota
Host

CHAPTER 6

General discussion

In the four years spanning the timeframe of this thesis (2018-2022), nanosafety research has made considerable progress by incorporating more realistic exposure scenarios in testing strategies, and by obtaining mechanistic insight into physiological responses to nanomaterials that can support predictive hazard assessment (e.g. Johnston et al. 2018; Kämpfer et al. 2020; Doak et al. 2022). As part of the progress made, the importance of microbiota-mediated toxicity, resulting from nanomaterial-induced changes in microbiota composition, has increasingly been demonstrated. In this thesis, we showed that an even wider array of interactions between hosts, microbiota and nanoparticles can influence nanomaterial toxicity. These interactions relate to key nanomaterials properties, including the large surface area of nanomaterials that is available for physisorption interactions, as well as particle-specific toxicity mechanisms. As described in this general discussion, this understanding of microbiota-dependent nanomaterial toxicity can further support the design of innovative tools and methods in support of regulatory decision-making. Ultimately, such a transition to microbiota-inclusive nanosafety testing can contribute to the evolving strategy of the European Union that is aimed to minimize the use of hazardous substances, including their (nano)forms, and where possible, detect and replace substances of concern early in the development pipeline, to continue to protect human and environmental health.

6.1 A new viewpoint on host-microbiota interactions in nanomaterial toxicity

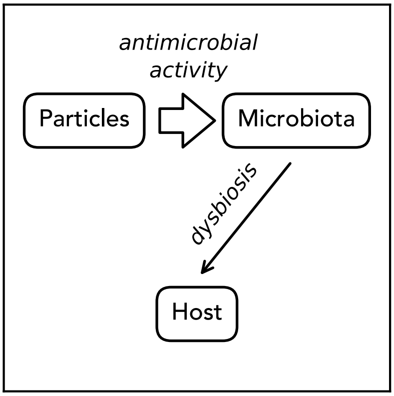

Many experimental studies preceding the investigations presented in this thesis have shown that nanomaterials can disturb the composition and abundance of host-associated microbiota. When this results in dysbiosis, this can have detrimental consequences to hosts. It is hard to predict *if*, and under *what circumstances*, changes in microbiota composition affect host health. Due to functional redundancy between microbiota members, changes in microbiota composition do not necessary alter microbiota functioning, for instance, in terms of metabolic activity, or immune system modulation. Moreover, it is still unclear *if*, and *at what pace*, host-associated microbiota can recover from nanomaterial-induced changes in composition. Nevertheless, the fact that many nanomaterials can alter the composition of microbiota, across diverse hosts, and following various exposure pathways, as summarized in **chapter 1**, is of concern to human, animal and environmental health.

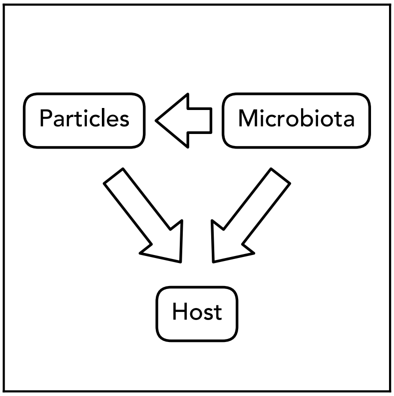

In this thesis, we took the opposite viewpoint on the role of host-associated microbiota in nanomaterial toxicity. We did so by examining how colonizing microbiota affect nanomaterial toxicity to the host. In principle, both the effects of microbiota on nanoparticle fate, bioavailability and biodistribution, as well as the effects of microbiota on the host's response to nanomaterials can alter nanomaterial toxicity to hosts. Differentiating between these effects is challenging, but it can be achieved by using computational techniques (**chapter 2**), by focusing on specific life stages of host models (**chapter 3**), and by employing and combining different experimental strategies that are available for toxicological model organisms (**chapters 4,5**). This chapter elaborates on what we have learnt from this new viewpoint, specifically addressing particle-specific characteristics of nanomaterial toxicity. Firstly, interactions between microbes and particles that influence realistic nanomaterial exposure scenarios will be discussed (section 6.2), followed by the impacts of microbiota on particle-specific adverse effects of nanomaterials (section 6.3).

6.2 Accounting for microbiota in more realistic nanomaterial exposure scenarios

Microbiota-mediated physisorption interactions can affect the fate of nanoparticles and microbes. This section discusses how future tools for nanomaterial safety testing can account for these effects based on the findings of this thesis.

Nanoparticles can be purchased in a pristine form, free from endotoxins, as bare particles or with specific surface modifications. This pristine nature rapidly changes once nanoparticles enter the environment. In the environment, biomolecules adsorb onto the large surface area of nanoparticles, forming biocoronae, consisting of tightly and loosely bound metabolite layers on the particle surface. Like any other chemical modification of the nanomaterial surface, including the application of surface coatings (e.g. consisting of polymers like polyethylene glycol or polyvinylpropylene) and functional groups (e.g. hydroxyl, amino, or phosphate groups), this can influence the colloidal stability (Gebauer et al. 2012; Panáček et al. 2018), circulation time (Li and Huang 2010) and biodistribution (Hussain et al. 1998; Thepphankulngarm et al. 2017) of nanomaterials in both in- and external environments. In **chapter 2**, we provide an overview of microbial biomolecules that can contribute to biocorona formation in the gastrointestinal tract. Many of these biomolecules fulfill essential roles in host-microbiota interactions, supporting amongst others the digestion of dietary fibers, energy supply to cells of the intestinal lining, signal transduction, and the control of inflammatory responses. For this reason, the potential interactions of these biomolecules with the nanomaterial surface should not be overlooked.

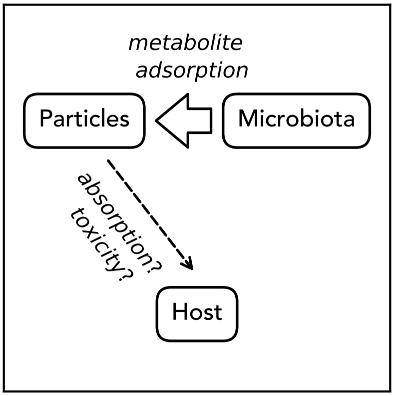

The results of **chapter 2** can be used to incorporate the effects of microbial metabolite physisorption into mechanistic pathways for nanomaterial safety assessment. To this end, the chapter (section 2.2.6) describes in detail how the adsorption affinity for microbial metabolites to metal and carbon nanomaterials can be predicted both quantitatively and qualitatively, as based on our results. Instead of repeating this rationale, we highlight three additional considerations for the relevance of this practice to exposure scenarios for nanomaterials. Firstly, the models and simulations of **chapter 2** predict that it is particularly relevant to consider biocorona interactions for microbial metabolites from categories like lipids and bile acids. These categories comprise metabolites with hydrophobic sites that can interact with the hydrophobic regions of nanomaterials. This interaction type was inferred to contribute most to the overall adsorption affinity of microbial metabolites to nanomaterials. Secondly, our results indicate that differences between experimental results for metal and carbon nanomaterials can result from microbiota-mediated biocorona effects. The predictions of the adsorption affinity for many metabolite categories differed between metal and carbon nanomaterials. Therefore, by affecting the extrinsic properties of metal and carbon nanomaterials differently, the adsorption of microbial metabolites to nanomaterials could contribute to different, microbiota-dependent responses of the host to these nanomaterials. Thirdly, in order to rationalize how microbiota-mediated biocorona formation can affect the responses of a host, advanced nanomaterials such as nanocarriers and biosensors can serve as examples. As noted before, vitamin B_{12}, has for instance been employed to target pharmaceutical-loaded nanocarriers to specific cell types comprising transcobalamin (vitamin B_{12}) receptors (Thepphankulngarm et al. 2017). Other nanomaterials have been designed for the detection and remediation of inorganic and organic environmental pollutant, like mercury (Chen et al. 2014a) and pesticides (Chen et al., 2016). Following similar principles, ingested nanomaterials may sequester enteric microbial metabolites, or may interact with specific cell types due to interactions between adsorbed metabolites and cell surface receptors.

Physisorption interactions can also influence the fate of nanoparticles and microbes in *in vitro* and *ex vivo* test systems for nanosafety testing. In these systems, nanoparticles are typically applied to the aqueous culture medium covering cells, tissues or organoids sitting on the bottom of a culture plate. This is similar to the acute toxicity test setup that is applied for the zebrafish larvae experiments in this thesis, where embryos or larvae sit on the bottom of a well plate, covered by a nanoparticle dispersion. In aqueous media, the exposure concentrations of nanomaterials are influenced by collisions between suspended particles, resulting in the continuous formation and breakup of aggregates in the water column. We observed such aggregates in all nanomaterial exposures that were performed for this thesis (**chapters 3,4,5**), and found that these aggregates increased in size, and settled to the bottom of exposure wells during the exposure time of the toxicity tests that were performed (1-2 days). Thus, vertical concentration gradients develop in many exposure setups for nanosafety testing, where the particle concentration at the bottom of the system increases gradually over time, until all particles have been deposited, or until a steady state with stably dispersed particles is reached. This has led to the development of dosimetry models for nanosafety testing (e.g. Hinderliter et al. 2010; DeLoid et al. 2016), that can be used to predict the delivered exposure concentrations as a function of time at the location of the test species or specimen.

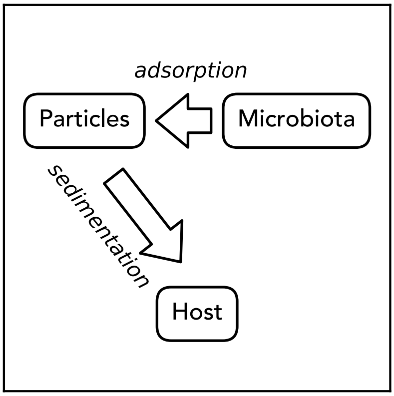

The results of **chapter 3** indicate that colliding nanoparticles do not only affect the exposure concentrations of nanomaterials, but can also influence microbial colonization dynamics. Briefly, focusing on nano-titanium dioxide ($nTiO_2$), our results indicate that colliding particles and microbes can form heteroaggregates that facilitate the transfer of microbes to eggs, by way of the sedimentation of these aggregates onto the egg surface. Similarly, in both marine and freshwater ecosystems, microbes have already been found to colonize the 'plastisphere', forming biofilms onto the surface of suspended microplastic particles (Kirstein et al. 2016; Arias-Andres et al. 2018). This contribution of this thesis to this insight is twofold. Firstly, we show that opportunistic pathogens do not only survive the antimicrobial activity of $nTiO_2$, but are also transferred to later (larval) life stages upon hatching (**chapter 3**). This underscores the concern that nanoparticles can facilitate the transfer of pathogenic bacteria to oviparous animals. Secondly, we show that these physisorption interactions between particles and microbes are also relevant to experimental test setups, which are a simplification of natural systems: even stagnant waters with little mixing induced by wind flow, tidal changes, and thermal convection are much more complex than our laboratory setup. This indicates that other laboratory setups that include microbial strains, such as advanced *in vitro* models for the intestine that mimic more realistic exposure scenarios by adding colonizing microbes (Kämpfer et al. 2020), should also account for the effects of nanoparticles on microbial colonization. For instance, temporarily separating the microbial colonization and nanoparticle exposure in experiments could minimize potential confounding effects of nanoparticle exposure on microbial colonization. Additionally, researchers can consider including non-toxic particles with similar physicochemical properties as the tested particle (e.g. surface functionalization, charge and specific surface area) as a 'vehicle-control' in experimental setups. Finally, it is recommended to track the abundance and (functional) composition of colonizing microbiota across the different experimental treatments over the exposure time to detect potential effects of the nanoparticle exposure on microbial colonization.

6.3 Effects of colonizing microbiota on nanoparticle toxicity

One of the key challenges in nanomaterial safety assessment, is to determine if the nanoform of a substance underlies its toxicity. If so, properties at the nanoscale, like the nanosized shapes, the high specific surface area and corresponding reactivity, or quantum effects of nanoparticles, contribute to nanomaterial toxicity (**chapter 1**, section 1.2). As part of this, it is important to differentiate between the effects of particles and shed ions of soluble nanomaterials. Since many of the nanomaterials that have been reported to interact with microbiota, can dissolve in aqueous media (see Fig. 1.1; Appendix Table S1), this also applies to investigations on the influence of microbiota on nanomaterial toxicity.

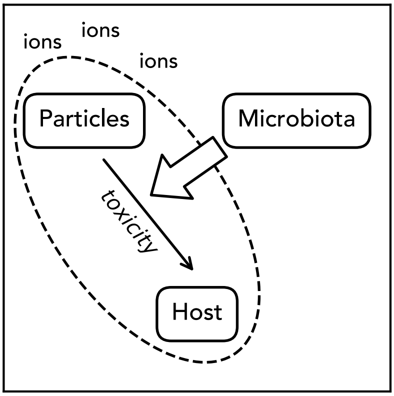

In **chapter 4**, we developed a protocol to quantify microbiota-dependent and particle-specific toxicity for soluble nanomaterials by means of the response-addition model (Bliss 1939). By testing the approach for the soluble nanomaterials nAg and nZnO, we could detect a marked protection of colonizing microbiota against the particle-specific toxicity of nAg in zebrafish larvae. Of note, the protocol can be adopted for any other test system or model organism that can be maintained under both germ-free and microbially-colonized conditions. Amongst others, these include intestinal *in vitro* and *ex vivo* models (Pearce et al. 2018), algae, daphnids (Sison-Mangus et al. 2015; Callens et al. 2016; Manakul et al. 2017), fruit flies (Kietz et al. 2018), jewel wasps (Shropshire et al. 2016; Wang and Brucker 2022), mice (Kennedy et al. 2018) and rats (Qv et al. 2020). This diversity in available test systems and model organisms allows for interesting comparisons of microbiota-dependent, particle-specific nanomaterial toxicity between different hosts and host tissues.

In recent years, considerable progress has been made in identifying particle-specific toxicity mechanisms of nanomaterials. Briefly, while nanoparticles, their shed ions, and their associated reactive oxygen species (ROS) can damage cells both externally and internally in a multitude of ways, their cytotoxicity generally results in oxidative stress and inflammatory responses (Garcés et al. 2021). Understanding these toxicity mechanisms supports strategies that are aimed to predict the effects of nanomaterials under environmentally realistic conditions. Knowledge on particle-specific toxicity mechanisms can moreover be employed to integrate human and environmental nanomaterial safety testing. Additionally, it can be implemented in the 'safe- and sustainable-by-design' process, promoted by the European Commission (2020) with the aim to support the development of new nanomaterials that provide functions or services with minimized harmful impacts to human health and the environment (Mech et al. 2022).

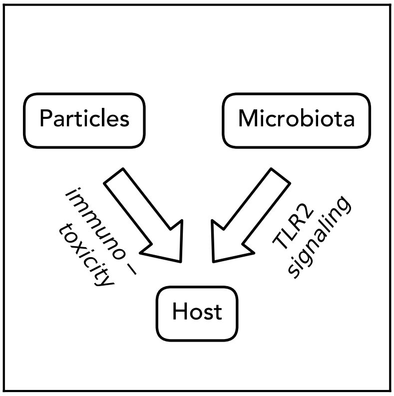

Focusing on the specific case of nAg toxicity in zebrafish larvae, the results of **chapter 5** demonstrate the importance to consider host-microbiota interactions in strategies that apply particle-specific toxicity mechanisms for the design and risk assessment of nanomaterials. These results reveal that, in addition to the effects of microbe-particle interactions on the fate, bioavailability and biodistribution of nanomaterials (section 6.2), interactions between microbiota and the host influence the sensitivity of the host to adverse effects of nanomaterials. In part, these host-microbiota interactions were mediated via toll-like receptors (TLRs), and concerned a pro-inflammatory cytokine response of the innate immune system against nanomaterials. The evolutionary conservation of these targets suggests that the results from this single case may apply to a wider range of organisms and nanomaterials. In the following paragraphs, we discuss this with regard to strategies that are aimed to 1) extrapolate findings from acute to chronic and repeated exposures (section 6.3.1); 2) employ grouping and read-across of nanomaterials for risk assessment (section 6.3.2); and 3) use conserved molecular targets to predict nanomaterial toxicity across a wider range of species (section 6.3.3). In support of this discussion, Fig. 6.1 to Fig. 6.3 provide several additional research findings which have not been presented in the previous chapters of this thesis.

6.3.1 Extrapolating microbiota-dependent nanoparticle toxicity from acute to chronic or repeated exposures

The loss of microbiota at sublethal exposure concentrations (Fig. 6.1) resembles the germ-free condition tested in **chapter 4** and **chapter 5**. We found that this microbiota-deficiency substantially increases the sensitivity of zebrafish larvae to nAg. This could imply that the loss of protective microbiota can sensitize the host to the immunotoxic effects of nanomaterials over longer term or repeated exposures. Similarly, co-exposure to (other) antimicrobial agents might intensify the immunotoxic effects of nanomaterials. This is a particularly relevant consideration in view of the widespread use and release of antibiotics in the environment (Larsson and Flach 2021; Wilkinson et

Considerations for acute to long-term exposure extrapolations: [a)]

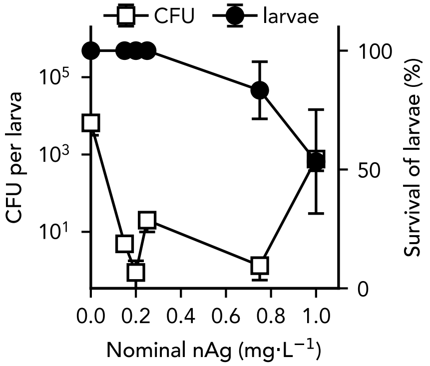

Figure 6.1: *Antimicrobial effects of nAg at sublethal exposure concentrations may sensitize zebrafish larvae over longer term exposures.* Colony-forming unit (CFU) count (white squares, left axis) and zebrafish larvae survival (black circles, right axis) are shown for two-day exposure (3-5 dpf) to nominal nAg concentrations ranging from 0.1 to 1.0 mg Ag·L^{-1}.

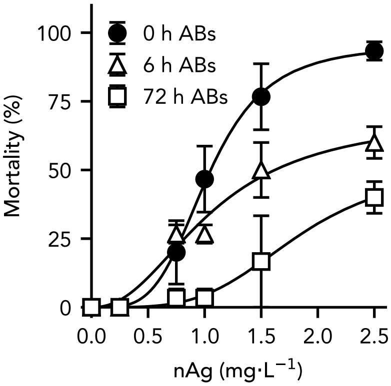

Figure 6.2: *In contrast to germ-free conditions, antibiotics reduce the sensitivity of zebrafish larvae to nAg.* The figure shows zebrafish larvae mortality for two-day exposure (3-5 dpf) to nAg following a pre-exposure of 0 h (black circles), 6 h (white triangles) and 72 h (white squares) to an antibiotic-antifungal cocktail comprising Ampicillin (100 µg·mL^{-1}), Kanamycin (5 µg·mL^{-1}) and Amphotericin B (250 ng·mL^{-1}). Nominal exposure concentrations of nAg are shown.

Considerations for read-across: [a)]

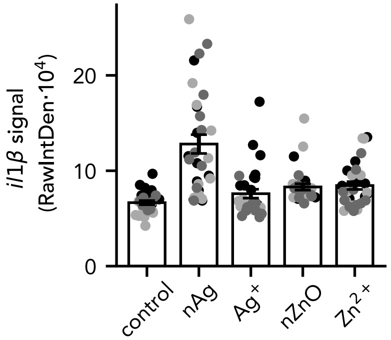

Figure 6.3: *Particle-specific il1β expression could serve as a potential biomarker for immunotoxic effects that are influenced by colonizing microbiota.* Bars present the *il1β* signal, as determined following the procedure described in chapter 5, following two-day exposure (3-5 dpf) to sublethal (nominal) exposure concentrations of nAg (0.25 mg Ag·L^{-1}) and nZnO (2.5 mg ZnO·L^{-1}), to corresponding shed-ion concentrations of Ag$^+$ (0.05 mg Ag·L^{-1}) and Zn^{2+} (1.1 mg Zn·L^{-1}), or to no particles or ions (control). Both the protective effect of microbiota (chapter 4) and enhanced *il1β* signal were only detected for nAg.

[a)] The corresponding data is available via Zenodo (DOI: 10.5281/zenodo.7066692).

al. 2022). However, predicting the effects of such mixed exposures is complicated by potential direct and microbiota-independent effects of antibiotics on host cells (Yang et al. 2017a). In agreement with the immuno-suppressive effects of broad-spectrum antibiotics (Oehlers et al. 2011), we found that pre-treatment to an antibiotic-antifungal cocktail, comprising Ampicillin, Kanamycin and Amphotericin B, reduced the sensitivity of zebrafish larvae to nAg toxicity (Fig. 6.2). This illustrates that common environmental pollutants, exerting microbiota-independent effects, should not be overlooked when assessing the consequences of the potential loss of protective microbiota on microbiota-dependent nanomaterial toxicity over longer-term and repeated exposures. These include, and are not limited to: endocrine-disrupting pollutants, carcinogenic, mutagenic and reprotoxic (CMR) pollutants and neurotoxic pollutants. Nevertheless, many of these pollutants, such as (nitrated) polyaromatic hydrocarbons (PAHs), nitrotoluenes, polychlorobiphenyls (PCBs), metals (like mercury), and azo dyes, can undergo microbiota-mediated transformations that affect their toxicity (Claus et al. 2016). Therefore, in many cases, both microbiota-dependent and microbiota-independent pathways should be taken into account when unravelling toxicity mechanisms for environmental pollutants.

6.3.2 Read-across for microbiota-dependent nanoparticle toxicity

Although we specifically dissect a microbiota-dependent toxicity mechanism for nAg (**chapter 5**), the observed protective effect of colonizing microbiota against nanomaterial toxicity could apply to other nanomaterials that elicit a comparable pro-inflammatory innate immune response. To date, a very diverse set of nanomaterials, including metal nanomaterials, carbon nanotubes and fullerenes, have been found to induce pro-inflammatory innate immune responses (Cronin et al. 2020). These materials interact with diverse cellular and non-cellular components of the innate immune system, responding to foreign structures, nanoparticle-induced oxidative stress and nanoparticle-induced cell damage (Engin and Hayes 2018). Whether a nanomaterial causes an innate immune response, and if so, what components of the innate immune system are involved in this response, depends on many factors, including the physicochemical properties of nanomaterials, such as core composition, surface modification, size, shape, and acquired biocorona, as well as on nanomaterial fate and biodistribution (Engin and Hayes 2018). This complicates the use of immunotoxic endpoints for read-across. In fact, in **chapter 4**, we show that colonizing microbiota protect zebrafish larvae against immunotoxic nAg, but do not offer protection against nano-zinc oxide (nZnO), while nZnO is also known to exert immunotoxic adverse effects. Nevertheless, in contrast to the results for nAg, presented in **chapter 5**, nZnO did not elicit a pro-inflammatory cytokine response as observed using an *il1β* reporter line (Fig. 6.3). Although we cannot differentiate between microbiota-dependent and microbiota-independent nanomaterial immunotoxicity based on a single comparison, this could be a first indication that enhanced *il1β* expression might serve as biomarker to detect microbiota-dependent nanomaterial immunotoxicity. Of note, in a review on the use of cytokines as biomarkers for nanoparticle immunotoxicity, Elsabahy and Wooley (2013) discuss that both nAg and double-walled carbon nanotubes have been found to trigger the release of IL1β in human monocytes. Ultimately, such comparisons, further linking material properties to toxicity pathways, may facilitate read-across once immunotoxicity mechanisms have been dissected for a larger set of nanomaterials, organisms and cell types.

6.3.3 Cross-host extrapolation for microbiota-dependent nanoparticle toxicity

Most of the experimental work in toxicology employs the benefits of a selection of test systems and model organisms that are easy to handle, have been well characterized in terms of their genomes and physiology, and ideally, reduce, refine and replace the use of (vertebrate) animal models. Based on these criteria, we adopted zebrafish larvae as an ideal model organism for the experimental work performed for **chapters 3-5**. When the results from these investigations are used to inform human and environmental effect assessment, this requires the extrapolation of results to different organisms, which is known as cross-species extrapolation. In view of the additional challenge in microbiota research, to account for differences in microbiota composition that exist between different host species, and even between different individuals of the same species, we refer this challenge as 'cross-host extrapolation' in the remainder. Fortunately, despite these differences in microbiota composition between hosts, the functions that are performed by microbiota of different hosts are generally well conserved (Rawls et al. 2006; Gaulke et al. 2020). This also applies to the protective effect of colonizing microbiota against nAg toxicity (**chapters 4-5**), which was consistently observed despite differences in the microbial taxa between larvae of different parental lines, as detected using 16S rRNA profiling (Table S2). Overall, this encourages the use of functional endpoints to assess microbiota-related toxicity outcomes across hosts.

Mechanistic insight into the pathobiological response of hosts to environmental stressors can facilitate cross-host extrapolation, using adverse outcome pathways (AOPs) as a framework in combination with toxicokinetic and toxicodynamic traits (Spurgeon et al. 2020). When responses are governed via specific receptors, the conservation of these targets across different species can be used as a first criterium to identify species for which similar responses can be expected. This rational has been incorporated in tools and databases that have been designed to support cross-species extrapolation, such as SeqAPASS (LaLone et al. 2016; https://seqapass.epa.gov/seqapass/) and ECOdrug (Verbruggen et al. 2017; http://www.ecodrug.org). For nanomaterials, which typically act via multiple molecular targets, such analyses are less straightforward. Nonetheless, we found that the influence of microbiota on nanoparticle toxicity is mediated via TLR2 (**chapter 5**). The recognition of commensal microbiota by receptors of the TLR family is highly conserved among vertebrate animals (Dierking and Pita 2020), and, despite of its absence in fruit flies, it has even been identified in basal metazoans like *Hydra* (Franzenburg et al. 2012). Clearly, there are many ‘candidate hosts’ which may benefit from the protective effect of microbiota against nanomaterial toxicity. Further research, comparing the different organs, tissues and cell types that are being exposed to nanomaterials, and investigating the conservancy of signaling pathways downstream of TLR2, such as those involved in innate immune responses and tissue regeneration, can help to elucidate the applicability of this cross-host extrapolation.

6.4 Conclusions and recommendations

Following up on the recent call for ‘microbiome-aware ecotoxicology’ (Duperron et al. 2020), this thesis illustrates, in a case-by-case manner, the specific relevance of host-associated microbiota in the field of nanotoxicology. In accord with basic principles of microbial ecotoxicology, which have been anchored in its definition (p. 31; Ghiglione et al. 2016), our investigations reveal that microbiota can also influence nanoparticle fate in realistic exposure scenarios for nanomaterials. In addition to the impacts of nanomaterials on the integrity of host-associated microbial communities, which have specifically been investigated by the time of writing, our work moreover demonstrates that interactions between microbiota and specific targets of the host can shape the host’s sensitivity to particle-specific nanomaterial toxicity. The evolutionary conservation of these targets supports the interesting hypothesis that these important interactions apply to a wider range of hosts and nanomaterials.

In a field that already faces great diversity in the intrinsic and extrinsic properties that influence nanomaterial toxicity, including host-microbiota and microbiota-particle interactions in models and test systems could add undesirable complexity to tools and methods for nanosafety testing. At the same time, current developments in nanosafety assessment strive for more realistic exposure characterization, and improved pathophysiological relevance of models and test systems. In view of this, I envision that the findings presented in this thesis could be used as a guideline to rationalize under what specific conditions, and for which kind of nanomaterials, host-microbiota and microbiota-particle interactions should be considered *a priori* in the selection, development and application of models and tools for nanosafety testing. These results could moreover be inquired to recognize the potential influence of microbiota on test outcomes and environmental monitoring results *a posteriori*. This merits including functional endpoints and biomarkers as (proxy) measures for microbiota integrity, thereby enabling the extrapolation of results from acute to chronic or repeated exposure regimes, between different kinds of nanomaterials, as well as between different hosts. Altogether, this could aid in the safe-and sustainable-design of nanomaterials, and could support more realistic, physiologically relevant nanosafety assessment, advancing towards 'microbiota-inclusive nanotoxicology'.

References

A

Abràmoff MD, Magelhae PJ, Ram SJ. 2004. Image processing with ImageJ. Biophotonics Int. 11: 36-42.

Adachi O, Kawai T, Takeda K, Matsumoto M, Tsutsui H, Sakagami M, Nakanishi K, Akira S. 1998. Targeted disruption of the MyD88 gene results in loss of IL-1- and IL-18-mediated function. Immunity. 9: 143-150. DOI: 10.1016/s1074-7613(00)80596-8

Adamovsky O, Buerger AN, Wormington AM, Ector N, Griffitt RJ, Bisesi Jr JH, Martyniuk CJ. 2018. The gut microbiome and aquatic toxicology: an emerging concept for environmental health. Environ Toxicol Chem. 37: 2758-2775. DOI: 10.1002/etc.4249

Agans RT, Gordon A, Hussain S, Paliy O. 2019. Titanium dioxide nanoparticles elicit lower direct inhibitory effect on human gut microbiota than silver nanoparticles. Toxicol Sci. 172: 411-416. DOI: 10.1093/toxsci/kfz183

Ahmed B, Ameen F, Rizvi A, Ali K, Sonbol H, Zaidi A, Khan MS, Musarrat J. 2020. Destruction of cell topography, morphology, membrane, inhibition of respiration, biofilm formation, and bioactive molecule production by nanoparticles of Ag, ZnO, CuO, TiO_2, and Al_2O_3 toward beneficial soil bacteria. ACS Omega. 5: 7861-7876. DOI: 10.1021/acsomega.9b04084

Akin D, Sturgis J, Ragheb K, Sherman D, Burkholder K, Robinson JP, Bhunia AK, Mohammed S, Bashir R. 2007. Bacteria-mediated delivery of nanoparticles and cargo into cells. Nat Nanotechnol. 2: 441-449. DOI: 10.1038/nnano.2007.149

Alder BJ, Wainwright TE. 1957. Phase transition for a hard sphere system. J Chem Phys. 27: 1208-1209. DOI: 10.1063/1.1743957

Al-Johani H, Abou-Hamad E, Jedidi A, Widdifield CM, Viger-Gravel J, Sangaru SS, Gajan D, Anjum DH, Ould-Chikh S, Hedhili MN, et al. 2017. The structure and binding mode of citrate in the stabilization of gold nanoparticles. Nat Chem. 9: 890-895. DOI: 10.1038/nchem.2752

Arias-Andres M, Kettner MT, Miki T, Grossart H-P. 2018. Microplastics: new substrates for heterotrophic activity contribute to altering organic matter cycles in aquatic ecosystems. Sci Total Environ. 635: 1152-1159. DOI: 10.1016/j.scitotenv.2018.04.199

Atkinson MJ, Bingman C. 1996. Elemental composition of commercial seasalts. J Aquaric Aquat Sci. 8: 39-43.

Avellan A, Simonin M, McGivney E, Bossa N, Spielman-Sun E, Rocca JD, Bernhardt ES, Geitner NK, Unrine JM, Wiesner, MR, et al. 2018. Gold nanoparticle biodissolution by a freshwater macrophyte and its associated microbiome. Nat Nanotechnol. 13: 1072-1077. DOI: 10.1038/s41565-018-0231-y

B

Bambino K, Chu J. 2017. Zebrafish in toxicology and environmental health. Curr Top Dev Biol. 124: 331-367. DOI: 10.1016/bs.ctdb.2016.10.007

Banjare P, Matore B, Singh J, Roy PP. 2021. In silico local QSAR modeling of bioconcentration factor of organophosphate pesticides. In Silico Pharmacol. [accessed 2022 Jan 26]:[13 p.]. DOI: 10.1007/s40203-021-00087-w

Barnoud J, Monticelli L. 2015. Coarse-grained force fields for molecular simulations. In: Kukol A, editor. Molecular modeling of proteins. New York: Springer Science+Business Media; p. 125-151. DOI: 10.1007/978-1-4939-1465-4

Barradas NP, Jeynes C. 2008. Advanced physics and algorithms in the IBA DataFurnace. Nucl Instr Meth Phys B. 266: 1875-1879.

Batel A, Borchert F, Reinwald H, Erdinger L, Braunbeck T. 2018. Microplastic accumulation patterns and transfer of benzo[a]pyrene to adult zebrafish (*Danio rerio*) gills and zebrafish embryos. Environm Pol. 235: 918-930. DOI: 10.1016/j.envpol.2018.01.028

Battimelli G, Ciccotti G. 2018. Berni Alder and the pioneering times of molecular simulation. Eur Phys J H. 43: 303-335. DOI: 10.1140/epjh/e2018-90027-5

Behler J. 2017. First principles neural network potentials for reactive simulations of large molecular and condensed systems. Angew Chem Int Ed. 56: 12828-12840. DOI: 10.1002/anie.201703114

Beiras R, Bellas J, Cachot J, Cormier B, Cousin X, Engwall M, Gambardella C, Garaventa F, Keiter S, Le Bihanic F, et al. 2018. Ingestion and contact with polyethylene microplastics does not cause acute toxicity on marine zooplankton. J Hazard Mater. 360: 452-460. DOI: 10.1016/j.jhazmat.2018.07.101

Bennett CM, Kanki JP, Rhodes J, Liu TX, Paw BH, Kieran MW, Langenau DM, Delahaye-Brown A, Zon LI, Fleming MD, et al. 2001. Myelopoiesis in the zebrafish, *Danio rerio*. Blood. 98: 643-651. DOI: 10.1182/blood.V98.3.643

Bernard NJ, O'Neill LA. 2013. Mal, more than a bridge to MyD88. IUBMB Life. 65: 777-786. DOI: 10.1002/iub.1201

Birchenough GMH, Nyström EEL, Johansson MEV, Hansson GC. 2016. A sentinel goblet cell guards the colonic crypt by triggering Nlrp6-dependent Muc2 secretion. Science. 352: 1535-1542. DOI: 10.1126/science.aaf7419

Birdsall CK, Langdon, AB. 2018. Plasma physics via computer simulation. 1st ed. Boca Raton: CRC Press. DOI: 10.1201/9781315275048

Bliss, CI. 1939. The toxicity of poisons applied jointly. Ann Appl Biol. 26: 585-615. DOI: 10.1111/j. 1744-7348.1939.tb06990.x

Böhme S. 2015. Development and application of quantification and visualization techniques to investigate the uptake of nanoparticles by cells and ecotoxicological test organisms [dissertation]. Helmholtz: Helmholtz Centre for Environmental Research (UFZ).

Böhme S, Stärk H-J, Kühnel D, Reemtsma T. 2015. Exploring LA-ICP-MS as a quantitative imaging technique to study nanoparticle uptake in *Daphnia magna* and zebrafish (*Danio rerio*) embryos. Anal Bioanal Chem. 407: 5477-5485. DOI: 10.1007/s00216-015-8720-4

Bondarenko O, Ivask A, Käkinen A, Kurvet I, Kahru A. 2013. Particle-cell contact enhances antibacterial activity of silver nanoparticles. PLoS One. [accessed 2019 Oct 30]:[12 p.]. DOI: 10.1371/journal.pone.0064060

Bonomi M, Branduardi D, Bussi G, Camilloni C, Provasi D, Raiteri P, Donadio D, Marinelli F, Pietrucci F, Broglia RA, et al. 2009. Plumed: a portable plugin for free-energy calculations with molecular dynamics. Comput Phys Commun. 180: 1961–1972. DOI: 10.1016/j.cpc.2009.05.011

Bove P, Malvindi MA, Kote SS, Bertorelli R, Summa M, Sabella S. 2017. Dissolution test for risk assessment of nanoparticles: a pilot study. Nanoscale. 9: 6315-6326. DOI: 10.1039/c6nr08131b

Bradley J-C, Acree WE, Lang ASID. 2014 Sep 22. Compounds with known Abraham descriptors [data set]. Figshare. [accessed 2020 June 13]. DOI: 10.6084/m9.figshare.1176994

Brandelli A, Ritter AC, Veras FF. 2017. Antimicrobial activities of metal nanoparticles. In: Cravo-Laureau C, Cagnon C, Lauga B, Duran R, editors. Microbial Ecotoxicology. New York City: Springer; p. 337-363. DOI: 10.1007/978-3-319-61795-4

Brinkmann BW, Koch BEV, Spaink HP, Peijnenburg WJGM, Vijver MG. 2020. Colonizing microbiota protect zebrafish larvae against silver nanoparticle toxicity. Nanotoxicology. 14: 725-739. DOI: 10.1080/17435390.2020.1755469

Brooke JS. 2012. *Stenotrophomonas maltophilia:* an emerging global opportunistic pathogen. Clin Microbiol Rev. 25: 2-41. DOI: 10.1128/CMR.00019-11

Browning LM, Lee KJ, Huang T, Nallathamby PD, Lowman JE, Xu X-HN. 2009. Random walk of single gold nanoparticles in zebrafish embryos leading to stochastic toxic effects on embryonic developments. Nanoscale. 1: 138-152. DOI: 10.1039/b9nr00053d

Brugman S, Ikeda-Ohtsubo W, Braber S, Folkerts G, Pieterse CMJ, Bakker PAHM. 2018. A comparative review on microbiota manipulation: lessons from fish, plants, livestock, and human research. Front Nutr. [accessed 2019 Oct 11]:[15 p.]. DOI: 10.3389/fnut.2018.00080

Brun NR, Koch BEV, Varela M, Peijnenburg WJGM, Spaink HP, Vijver MG. 2018. Nanoparticles induce dermal and intestinal innate immune system responses in zebrafish embryos. Environ Sci: Nano. 5: 904-916. DOI: 10.1039/c8en00002f

C

Callens M, Macke E, Muylaert K, Bossier P, Lievens B, Waud M, Decaestecker E. 2016. Food availability affects the strengths of mutualistic host-microbiota interactions in *Daphnia magna.* ISME J. 10: 911-920. DOI: 10.1038/ismej.2015.166

Campbell GA. 2014. Rare earth metals: A strategic concern. Miner Econ. 27: 21-31. DOI: 10.1007/s13563-014-0043-y

Chen L, Qi N, Wang X, Chen L,You H, Li J. 2014a. Ultrasensitive surface-enhanced Raman scattering nanosensor for mercury ion detection based on functionalized silver nanoparticles. RSC Adv. 4: 15055-15060. DOI: 10.1039/c3ra47492e

Chen Y, Qiao L, Song X, Ma L, Dou X, Xu C. 2021. Protective effects of selenium nanoparticle-enriched *Lactococcus lactis* NZ9000 against enterotoxigenic *Escherichia coli* K88-induced intestinal barrier damage in mice. Appl Environ Microbiol. [accessed 2022 May 8]:[15 p.]. DOI: 10.1128/AEM.01636-21

Chen R, Riviere, JE. 2017. Biological and environmental surface interactions of nanomaterials: characterization, modeling and prediction. WIREs. [accessed 2021 Jan 19]:[31 p.]. DOI: 10.1002/wnan.1440

Chen R, Zhang Y, Monteiro-Riviere NA, Riviere JE. 2016. Quantification of nanoparticle pesticide adsorption: computational approaches based on experimental data. Nanotoxicology. 10: 1118-1128. DOI: 10.1080/17435390.2016.1177745

Chen R, Zhang Y, Sahneh FD, Scoglio CM, Wohlleben W, Haase A, Monteiro-Riviere NA, Riviere JE. 2014b. Nanoparticle surface characterization and clustering through concentration-dependent surface adsorption modeling. ACS Nano. 8: 9446-9456. DOI: 10.1021/nn503573s

Chen H, Zhao R, Wang B, Cai C, Zheng L, Wang H, Wang M, Ouyang H, Zhou X, Chai Z, et al. 2017. The effects of orally administered Ag, TiO_2, and SiO_2 nanoparticles on gut microbiota composition and colitis induction in mice. NanoImpact. 8: 80-88. DOI: 10.1016/j.impact.2017.07.005

Cheng X, Ivanov I, 2012. Molecular dynamics. In: Reisfeld B, Mayeno AN, editors. Computational toxicology. Vol 1. New York: Springer Science + Business Media; p. 243-289. DOI: 10.1007/978-1-62703-050-2

Claus S, Guillou H, Ellero-Simatos S. 2016. The gut microbiota: a major player in the toxicity of environmental pollutants? NPJ Biofilms Microbiomes. [accessed 2017 Nov 14]:[12 p.]. DOI: 10.1038/npjbiofilms.2017.1

Comer J, Chen R, Poblete H, Vergara-Jaque A, Riviere JE. 2015. Predicting adsorption affinities of small molecules on carbon nanotubes using molecular dynamics simulation. ACS Nano. 9: 11761-11774. DOI: 10.1021/acsnano.5b03592

Coyte KZ, Rakoff-Nahoum S. 2019. Understanding competition and cooperation within the mammalian gut microbiome. Curr Biol: 29, R538-R544. DOI: 10.1016/j.cub.2019.04.017

Cronin JG, Jones N, Thornton CA, Jenkins GJS, Doak SH, Clift MJD. 2020. Nanomaterials and innate immunity: a perspective of the current status in nanosafety. Chem. Res. Toxicol. 33: 1061-1073. DOI: 10.1021/acs.chemrestox.0c00051

D

Dai Y, Chen F, Yue L, Li T, Jiang Z, Xu Z, Wang Z, Xing B. 2020. Uptake, transport, and transformation of CeO_2 nanoparticles by strawberry and their impact on the rhizosphere bacterial community. Sustainable Chem Eng. 8: 4792-4800. DOI: 10.1021/acssuschemeng.9b07422

Dawson K, Yan Y. 2021. Current understanding of biological identity at the nanoscale and future prospects. Nat Nanotechnol. 16: 229-242. DOI: 10.1038/s41565-021-00860-0.

Defaye M, Gervason S, Altier C, Berthon J-Y, Ardid D, Filaire E, Carvalho FA. 2020. Microbiota: a novel regulator of pain. J Neural Trans. 127: 445-465. DOI: 10.1007/s00702-019-02083-z

DeGruttola, AK, Low D, Mizoguchi A, Mizoguchi E. 2016. Current understanding of dysbiosis in disease in human and animal models. Inflamm Bowel Dis. 22: 1137-1150. DOI: 10.1097/MIB.0000000000000750

DeLoid GM, Cohen JM, Pyrgiotakis G, Demokritou P. 2016. Preparation, characterization, and *in vitro* dosimetry of dispersed, engineered nanomaterials. Nat Protoc. 12: 355-371. DOI: 10.1038/nprot.2016.172

Deng L, Zeng H, Hu X, Xiao M, He D, Zhang Y, Jin Y, Hu Y, Zhu Y, Gong L, et al. 2021. Se@Albumin nanoparticles ameliorate intestinal mucositis caused by cisplatin *via* gut microbiota-targeted regulation. Nanoscale. 13: 11250-11261. DOI: 10.1039/d0nr07981b

Desmau M, Carboni A, Le Bars M, Doelsch E, Benedetti MF, Auffan M, Levard C, Gelabert A. 2020. How microbial biofilms control the environmental fate of engineered nanoparticles? Front Environ Sci. [accessed 2021 Nov 7]:[20 p.]. DOI: 10.3389/fenvs.2020.00082

Dierking K, Pita L. 2020. Receptors mediating host-microbiota communication in the metaorganism: the invertebrate perspective. Front Immunol. [accessed 2021 Dec 7]:[17 p.]. DOI: 10.3389/fimmu.2020.01251

Dinarello CA. 2018. Overview of the IL-1 family in innate inflammation and acquired immunity. Immunol Rev. 281: 8-27. DOI: 10.111/imr.12621

Doak SH, Clift MJ, Costa A, Delmaar C, Gosens I, Halappanavar S, Kelly S, Peijnenburg WJGM, Rothen-Rutishauser B, Schins RPF, et al. 2022. The road to achieving the European Commission's chemical strategy for nanomaterial sustainability – a PATROLS perspective on new approach methodologies. Small. [accessed 2022 May 20]:[11 p.]. DOI: 10.1002/smll.202200231

Douglas AE. 2020. The microbial exometabolome: ecological resource and architect of microbial communities. Phil Trans R Soc B. [accessed 2021 May 17]:[9 p.]. DOI: 10.1098/rstb.2019.0250

Duan Z, Duan X, Zhao S, Wang X, Wang J, Liu Y, Peng Y, Gong Z, Wang L. 2020. Barrier function of zebrafish embryonic chorions against microplastics and nanoplastics and its impact on embryo development. J Hazard Mater. [accessed 2020 May 11]:[7 p.]. DOI: 10.1016/j.jhazmat.2020.122621

Duperron S, Halary S, Gallet A, Marie B. 2020. Microbiome-aware ecotoxicology of organisms: relevance, pitfalls and challenges. Front Public Health. [accessed 2017 Feb 6]:[8 p.]. DOI: 10.3389/fpubh.2020.00407

E

Eduok S, Coulon F. 2017. Engineered nanoparticles in the environments: Interactions with microbial systems and microbial activity. In: Cravo-Laureau C, Cagnon C, Lauga B, Duran R, editors. Microbial Ecotoxicology. New York City: Springer; p. 63-109. DOI: 10.1007/978-3-319-61795-4

EFSA Scientific Committee. 2018. Guidance on risk assessment of the application of nanoscience and nanotechnologies in the food and feed chain: Part 1, human and animal health. EFSA J. [accessed 2022 Aug 2]:[95 p.]. 16: DOI: 10.2903/j.efsa.2018.5327

Elsabahy M, Wooley KL. 2013. Cytokines as biomarkers of nanoparticle immunotoxicity. Chem Soc Rev. 42: 5552-5576. DOI: 10.1039/c3cs600064

Engin AB, Hayes AW. 2018. The impact of immunotoxicity in evaluation of the nanomaterials safety. Toxicol Res Appl. [accessed 2022 Apr 21]:[9 p.]. DOI: 10.1177/2397847318755579

Essmann U, Perera L, Berkowitz ML, Darden T, Lee H, Pedersen LG. 1995. A smooth particle mesh Ewald method. J Chem Phys. 103: 8577–8593. DOI: 10.1063/1.470117

European Commission. 2011. Commission recommendation of 18 October 2011 on the definition of nanomaterial. Off J EU. L275: 38-40. ELI: http://data.europa.eu/eli/reco/2011/696/oj

European Commission. 2020. Chemicals strategy for sustainability. Towards a toxic-free environment. Brussels: European Commission. Report No.: COM(2020) 667 final. Available from: https://ec.europa.eu/environment/strategy/chemicals-strategy_en

Evans DJ, Holian BL. 1985. The Nose–Hoover thermostat. J Chem Phys. 83: 4069–4074. DOI: 10.1063/1.449071

F

Fent K, Weisbrod CJ, Wirth-Heller A, Pieles U. 2010. Assessment of the uptake and toxicity of fluorescent silica nanoparticles in zebrafish (*Danio rerio*) early life stages. Aquat Toxicol. 100: 218-228. DOI: 10.1016/j.aquatox.2010.02.019

Fernández-Bravo A, Figueras MJ. 2020. An update on the genus *Aeromonas*: Taxonomy, epidemiology, and pathogenicity. Microorganisms. [accessed 2020 July 10]:[39 p.]. DOI: 10.3390/microorganisms8010129

Fiori J, Turroni S, Candela M, Gotti R. 2020. Assessment of gut microbiota fecal metabolites by chromatographic targeted approaches. J Pharm Biomed Anal. [accessed 2021 May 2020]:[23 p.]. DOI: 10.1016/j.jpba.2019.112867

Fliege J, Svaiter BF. 2000. Steepest descent methods for multicriteria optimization. Math Methods Oper Res. 51: 479–494. DOI: 10.1007/s001860000043

Franzenburg S, Fraune S, Künzel S, Baines JF, Domazet-Lošo T, Bosch TCG. 2012. MyD88-deficient *Hydra* reveal an ancient function of TLR signaling in sensing bacterial colonizers. Proc Natl Acad Sci USA. 109: 19374-19379. DOI: 10.1073/pnas.1213110109

Fulaz S, Vitale S, Quinn L, Casey E. 2019. Nanoparticle-biofilm interactions: the role of the EPS matrix. Trends Microbiol. 27: 915-926. DOI: 10.1016/j.tim.2019.07.004

G

Garcés M, Cáceres L, Chiappetta D, Magnani N, Evelson P. 2021. Current understanding of nanoparticle toxicity mechanisms and interactions with biological systems. New J Chem. 45: 14328-14344. DOI: 10.1039/d1nj01415c

Garland JL, Mills AL. 1991. Classification and characterization of heterotrophic microbial communities on the basis of patterns of community-level sole-carbon-source utilization. Appl Environ Microbiol. 57: 2351-2359

Gaulke CA, Beaver LM, Armour CR, Humphreys IR, Barton CL, Tanguay RL, Ho E, Sharpton T. 2020. An integrated gene catalog of the zebrafish gut microbiome reveals significant homology with mammalian microbiomes. BioRxiv. [accessed 2020 June 24]:[37 p.]. DOI: 10.1101/2020.06.15.153924

Gebauer JS, Malissek M, Simon S, Knauer SK, Maskos M, Stauber RH, Peukert W, Treuel, L. 2012. Impact of nanoparticle-protein corona on colloidal stability and protein structure. Langmuir. 28: 9673-9679. DOI: 10.1021/la301104a

Gellatly SL, Hancock, REW. 2013. *Pseudomonas aeruginosa*: new insights into pathogenesis and host defenses. Pathog Dis. 67: 159-173. DOI: 10. 1111/2049-632X.12033

Ghiglione J-F, Martin-Laurant F, Pesce S. 2016. Microbial ecotoxicology: an emerging discipline facing contemporary environmental threats. Environ Sci Pollut Res. 23: 3981-3983. DOI: 10.1007/s11356-015-5763-1

Gini G. 2018. QSAR: What else? In: Nicolotti O, editor. Computational toxicology. New York: Springer Science+Business Media; p. 79-107. DOI: 10.1007/978-1-4939-7899-1

Gliga AR, De Loma J, Di Bucchianico S, Skoglund S, Keshavan S., Wallinder IO, Karlsson HL, Fadeel B. 2020. Silver nanoparticles modulate lipopolysaccharide-triggered Toll-like receptor signaling in immune competent human cell lines. Nanoscale Adv. 2: 648-658. DOI: 10.1039/c9na00721k

Gramatica P. 2008. A short history of QSAR evolution. ResearchGate. [accessed 2022 Sept 7]:[9 p.]. https://www.researchgate.net/publication/252172555

Gramatica P, Cassani S, Roy PP, Kovarich S, Yap CW, Papa E. 2012. QSAR modeling is not 'Push a button and find a correlation': a case study of toxicity of (benzo-)triazoles on algae. Mol Inf. 31: 817-835. DOI: 10.1002/minf.201200075

Grisoni F, Ballabio D, Todeschini R, Consonni V. 2018. Molecular descriptors for structure-activity applications: a hands-on approach. In: Nicolotti O, editor. Computational toxicology. New York: Springer Science+Business Media; p. 3-55. DOI: 10.1007/978-1-4939-7899-1

Grossart H-P, Simon M. 1998. Bacterial colonization and microbial decomposition of limnetic organic aggregates (lake snow). Aquat Microb Ecol. 15: 127-140. DOI: 10.3354/ame015127

Guha, R. 2007. Chemical informatics functionality in R. J Stat Softw. [accessed 2021 May 22]:[16 p.]. DOI: 10.18637/jss.v018.i05

H

Hachicho N, Reithel S, Miltner A, Heipieper HJ, Küster E, Luckenbach T. 2015. Body mass parameters, lipid profiles and protein contents of zebrafish embryos and effects of 2,4-dinitrophenol exposure. PLoS One. [accessed 2020 May 18]:[19 p.]. DOI: 10.1371/journal.pone.0134755

Hacquard S, Garrido-Oter R, González A, Spaepen S, Ackermann G, Lebeis S, McHardy AC, Dangl JL, Knight R, Ley R, et al. 2015. Microbiota and host nutrition across plant and animal kingdoms. Cell Host Microbe. 17: 603-616. DOI: 10.1016/j.chom.2015.04.009

Hansch C, Fujita T. 1964. *σ-ρ-π* Analysis. A method for the correlation of biological activity and chemical structure. J Am Chem Soc. 86: 1616-1626. DOI: 10.1021/ja01078a623

Hasegawa T, Hall CJ, Crosier PS, Abe G, Kawakami K, Kudo A, Kawakami A. 2017. Transient inflammatory response mediated by interleukin-1ß is required for proper regeneration in zebrafish fin fold. eLIFE. [accessed 2020 March 22]:[22 p.]. DOI: 10.7554/eLife.22716

Heinz H, Lin T-J, Mishra RK, Emami FS. 2013. Thermodynamically consistent force fields for the assembly of inorganic, organic, and biological nanostructures: the interface force field. Langmuir. 29: 1754–1765. DOI: 10.1021/la3038846

Herbomel P, Thisse B, Thisse C. 1999. Ontogeny and behaviour of early macrophages in the zebrafish embryo. Development. 126: 3735-3745. DOI: 10.1242/dev.126.17.3735

Hess B, Bekker H, Berendsen HJC, Fraaije JGEM. 1997. Lincs: a linear constraint solver for molecular simulations. J Comput Chem. 18: 1463-1472.

Hill JH, Franzosa EA, Huttenhower C, Guillemin K. 2016. A conserved bacterial protein induces pancreatic beta cell expansion during zebrafish development. eLife. [accessed 2017 Nov 14]:[18 p.]. DOI: 10.7554/eLife.20145

Hinderliter PM, Minard KR, Orr G, Chrisler WB. Thrall BD, Pounds JG, Teeguarden JG. 2010. ISSD: A computational model of particle sedimentation, diffusion and target cell dosimetry for *in vitro* toxicity studies. Part Fibre Toxicol. [accessed 2022 March 15]:[20 p.]. DOI: 10.1186/1743-8977-7-36

Hoffmann T, Lowry GV, Ghoshal S, Tufenkji N, Brambilla D, Dutcher JR, Gilbertson LM, Giraldo, JP, Kinsella JM, Landry MK, et al. 2020. Technology readiness and overcoming barriers to sustainably implement nanotechnology-enabled plant agriculture. Nat Food. 1: 416-425. DOI: 10.1038/s43016-020-0110-1

Hörmann N, Brandão I, Jäckel S, Ens N. Lillich M, Walter U. Reinhardt C. 2014. Gut microbial colonization orchestrates TLR2 expression, signaling and epithelial proliferation in the small intestinal mucosa. PLoS One. [accessed 2022 March 24]:[11 p.]. DOI: 10.1371/journal.pone.0113080

Horng J-L, Lee C-Y, Liu S-T, Hung G-Y, Lin L-Y. 2022. Differential effects of silver nanoparticles on two types of mitochondrion-rich ionocytes in zebrafish embryos. Comp Biochem Physiol C. [accessed 2022 March 24]:[8 p.]. DOI: 10.1016/j.cbpc.2021.109244

Horzmann KA, Freeman JL. 2018. Making waves: new developments in toxicology with the zebrafish. Toxicol Sci. 163: 5-12. DOI:10.1093/toxic/kfy044

Howe K, Clark MD, Torroja CF, Torrance J, Bertehlost C, Muffato M, Collins JE, Humphray S, McLaren K, Matthews L, et al. 2013. The zebrafish reference genome sequence and its relationship to the human genome. Nature. 496: 498-503. DOI: 10.1038/nature12111

Hu W, Yang S, Shimada Y, Münch M, Marín-Juez R, Meijer AH, Spaink HP. 2019. Infection and RNA-seq analysis of a zebrafish *tlr2* mutant shows a broad function of this toll-like receptor in transcriptional and metabolic control and defense to *Mycobacterium marinum* infection. BMC Genomics. [accessed 2022 Feb 8]:[18 p.]. DOI: 10.1186/s12864-019-6265-1

Huang J, Lopes PEM, Roux B, MacKerell Jr AD. 2014. Recent advances in polarizable force fields for macromolecules: microsecond simulations of proteins using the classical drude oscillator model. J Phys Chem Lett. 5: 3144–3150. DOI: 10.1021/jz501315h

Huang H, Zhu J-J. 2019. The electrochemical applications of rare earth-based nanomaterials. Analyst. 144: 6789-6811. DOI: 10.1039/c9an01562k

Hughes ZE, Tomásio SM, Walsh TR. 2014. Efficient simulations of the aqueous bio-interface of graphitic nanostructures with a polarisable model. Nanoscale. 6: 5438-5448. DOI: 10.1039/c4nr00468j

Humphrey W, Dalke A, Schulten K. 1996. VMD: Visual Molecular Dynamics. J Mol Graph. 14: 33-38. DOI: 10.1016/0263-7855(96)00018-5

Hussain N, Florence AT. 1998. Utilizing bacterial mechanisms of epithelial cell entry: invasion-induced oral uptake of latex nanoparticles. Pharm Res. 15: 153-156. DOI: 10.1023/a:10119160840

I

Iqbal MI, Lin K, Sun F, Chen S, Pan A, Lee HH, Kan C-W, Lin CSK, Tso CY. 2022. Radiative cooling nanofabric for personal thermal management. Appl Mater Interfaces. 14: 23577-23587. DOI: 10.1021/acsami.2c05115

J

Jensen KA. 2018a. SOP for intra- and interlaboratory reproducible measurement of hydrodynamic size-distribution and dispersion stability of manufactured nanomaterials using dynamic light scattering (DLS). Version 1.1. Bilthoven: Dutch National Institute for Public Health and the Environment (RIVM).

Jensen KA. 2018b. The NANOGENOTOX standard operational procedure for preparing batch dispersions for in vitro and in vivo toxicological studies. Version 1.2. Paris: French Agency for Food, Environmental and Occupational Health & Safety (ANSES).

Jensen KA, Kembouche Y, Loeschner K., Correia M. 2018. SOP for probe-sonicator calibration of delivered acoustic power and de-agglomeration efficiency for *in vitro* an *in vivo* toxicological testing. Version 1.1. Bilthoven: Dutch National Institute for Public Health and the Environment (RIVM).

Jo S, Kim T, Iyer VG, Im W. 2008. CHARMM-GUI: a web-based graphical user interface for Charmm. J Comput Chem. 29: 1859–1865. DOI: 10.1002/jcc.20945

Jochum L, Stecher B. 2020. Label or concept – what is a pathobiont? Trends Microbiol. 28: 789-792. DOI: 10.1016/j.tim.2020.04.011

Johnston HJ, Verdon R, Gillies S, Brown DM, Fernandes TF, Henry TB, Rossi AG, Tran L, Tucker C, Tyler CR, Stone V. 2018. Adoption of *in vitro* systems and zebrafish embryos as alternative models for reducing rodent use in assessments of immunological and oxidative stress responses to nanomaterials. Crit Rev Toxicol. 48: 252-271. DOI: 10.1080/10408444.2017.1404965

Jovanović B. 2015. Review of titanium dioxide nanoparticle phototoxicity: developing a phototoxicity ratio to correct the endpoint values of toxicity tests. Environ Toxicol Chem. 34: 1070-1077. DOI: 10.1002/etc.2891

Ju Z, Ren G, Zhou M, Jing J, Xiang J, Liu X, Huang R, Zhou P-K. 2020. Exposure to a combination of silica nanoparticles and low-dose radiation aggravates lung fibrosis in mice via gut microbiota modulation. Environ Sci: Nano. 7: 3979-3998. DOI: 10.1039/d0en01021a

K

Kämpfer AAM, Busch M, Schins RPF. 2020. Advanced *in vitro* testing strategies and models of the intestine for nanosafety research. Chem Res Toxicol. 33: 1163-1178. DOI: 10.1021/acs.chemrestox.0c00079

Kang JS, Bong J, Choi J-S, Henry TB, Park JW. 2016. Differentially transcriptional regulation on cell cycle pathway by silver nanoparticles from ionic silver in larval zebrafish (*Danio rerio*). Biochem Biophys Res Commun. 479: 753-758. DOI: 10.1016/j.bbrc.2016.09.139

Karplus M, Porter RN, Sharma RD. 1965. Exchange reactions with activation energy. I. Simple barrier potential for (H,H_2). J Chem Phys. 43: 3259-3287. DOI: 10.1063/1.1697301

Kennedy EA, King KY, Baldridge MT. 2018. Mouse microbiota models: comparing germ-free mice and antibiotics treatment as tools for modifying gut bacteria. Front Physiol. 9: 1534. DOI: 10.3389/fphys.2018.01534

Kietz C, Pollari V, Meinander A. 2018. Generating germ-free *Drosophila* to study gut-microbe interactions: protocol to rear *Drosophila* under axenic conditions. Curr Protoc Toxicol. [accessed 2022 June 1]:[12 p.]. DOI: 10.1002/cptx.52

Kirstein IV, Kirmizi S, Wichels A, Garin-Fernandez A, Erler R, Löder M, Gerdts G. 2016. Dangerous hitchhikers? Evidence for potentially pathogenic *Vibrio* spp. on microplastic particles. Marine Environ Res. [accessed 2020 June 3]:[8 p.]. DOI: 10.1016/j.marenvres.2016.07.004

Klein CL, Comero S, Stahlmecke B, Romazanov J, Kuhlbusch TAJ, Van Doren E, De Temmerman P-J, Mast J, Wick P, Krug H, et al. 2011. NM-Series of representative manufactured nanomaterials: NM300 silver, characterization, stability, homogeneity. Luxembourg (Luxembourg): Publications Office of the European Union. Report No.: EUR 24693 EN. Available from: https://doi.org/10.2788/23079

Knight R, Vrbanac A, Taylor BC, Aksenov A, Callewaert C, Debelius J, Gonzalez A, Kosciolek T, McCall L-I, McDonald D, et al. 2018. Best practices for analysing microbiomes. Nat Rev Microbiol. 16: 410-422. DOI: 10.1038/s41579-018-0029-9

Knösel DH. 1984. Genus IV. *Phyllobacterium* (ex Knösel 1962) nom. rev. (*Phyllobacterium* Knösel 1962, 96). In: Krieg NR, Holt JG, editors. Bergey's manual of systematic bacteriology. Vol 1. Baltimore: Williams & Wilkins; p. 254-256.

Koch BEV, Yang S, Lamers G, Stougaard J, Spaink HP. 2018. Intestinal microbiome adjusts the innate immune setpoint during colonization through negative regulation of MyD88. Nat Commun. [accessed 2019 Oct 30]:[11 p.]. DOI: 10.1038/s41467-018-06658-4

Krautkramer KA, Fan J, Bäckhed F. 2021.Gut microbial metabolites as multi-kingdom intermediates. Nat Rev. 19: 77-94. DOI: 10.1038/s41579-020-0438-4

Kurtz CC, Mitchell S, Nielsen K, Crawford KD, Mueller-Spitz, SR. 2020. Acute high-dose titanium dioxide nanoparticle exposure alters gastrointestinal homeostasis in mice. J Appl Toxicol. 40: 1384-1395. DOI: 10.1002/jat.3991

L

Laio A, Gervasio FL. 2008. Metadynamics: a method to simulate rare events and reconstruct the free energy in biophysics, chemistry and material science. Rep Prog Phys. [accessed 2022 Feb 26]:[22 p.] DOI: 10.1088/0034-4885/71/12/126601

LaLone CA, Villeneuve DL, Lyons D, Helgen HW, Robinson SL, Swintek JA, Saari TW, Ankley GT. 2016. Sequence alignment to predict across species susceptibility (SeqAPASS): a web-based tool for addressing the challenges of cross-species extrapolation of chemical toxicity. Toxicol Sci. 153: 228-245. DOI: 10.1093/toxsci/kfw119

Lam SH, Chua HL, Gong Z, Lam TJ, Sin YM. 2004. Development and maturation of the immune system in zebrafish, *Danio rerio*: a gene expression profiling, in situ hybridization and immunological study. Dev Comp Immunol. 28: 9-28. DOI: 10.1016/S0145-305X(03)00103-4

Lane DJ. 1991. 16S/23S rRNA sequencing. In: Stackebrandt E, Goodfellow, M, editors. Nucleic acid techniques in bacterial systematics. New York City: John Wiley and Sons; p. 115-175.

Larsson DGJ, Flach C-F. 2021. Antibiotic resistance in the environment. Nat Rev. 20: 257-269. DOI: 10.1038/s41579-021-00649-x

Lee KJ, Browning LM, Nallathamby PD, Xu X-HN. 2013. Study of charge-dependent transport and toxicity of peptide-functionalized silver nanoparticles using zebrafish embryos and single nanoparticle plasmic spectroscopy. Chem Res Toxicol. 26: 904-917. DOI: 10.1021/tx400087d

Lee WS, Cho H-J, Kim E, Huh YH, Kim H-J, Kim B, Kang T, Lee J-S, Jeong J. 2019. Bioaccumulation of polystyrene nanoplastics and their effect on the toxicity of Au ions in zebrafish embryos. Nanoscale. 11: 3173-3185. DOI: 10.1039/c8nr09321k

Lee Y-L, Shih Y-S, Chen Z-Y, Cheng F-Y, Lu J-Y, Wu Y-H, Wang Y-J. 2022. Toxic effects and mechanisms of silver and zinc oxide nanoparticles on zebrafish embryos in aquatic ecosystems. Nanomaterials. [accessed 2022 Mar. 24]:[18 p.]. DOI: 10.3390/nano12040717

Li S-D, Huang L. 2010. Stealth nanoparticles: High density but sheddable PEG is a key for tumor targeting. J Control Release. 145: 178-181. DOI: 10.1016/j.jconrel.2010.03.016

Li Y, Li Y, Cao X, Jin X, Jin T. 2017. Pattern recognition receptors in zebrafish provide functional and evolutionary insight into innate immune signaling pathways. Cell Mol Immunol. 14: 80-89. DOI: 10.1038/cmi.2016.50

Li Y, Wang W-X, Liu H. 2022. Gut-microbial adaptation and transformation of silver nanoparticles mediated the detoxification of *Daphnia magna* and their offspring. Environ Sci: Nano. 9: 361-374. DOI: 10.1039/d1en00765c

Li Y, Yan N, Wong TY, Wang W-X, Liu H. 2019a. Interaction of antibacterial silver nanoparticles and microbiota-dependent holobionts revealed by metatranscriptomic analysis. Environ Sci: Nano. 6: 3242-3255. DOI: 10.1039/c9en00587k

Li X, Zhang Y, Li B, Cui J, Gao N, Sun H, Meng Q, Wu S, Bo J, Yan L, et al. 2019b. Prebiotic protects against anatase titanium dioxide nanoparticles-induced microbiota-mediated colonic barrier defects. NanoImpact. [accessed 2022 May 3]:[9 p.]. DOI: 10.1016/j.impact.2019.100164

Lietschke GJ, Oates AC, Crowhurst MO, Ward AC, Layton JE. 2001. Morphologic and functional characterization of granulocytes and macrophages in embryonic and adult zebrafish. Blood. 98: 3087-3096. DOI: 10.1182/blood.V98.10.3087

Lin S-C, Lo Y-C, Wu H. 2010. Helical assembly in the MyD88-IRAK4-IRAK2 complex in TLR/IL-1R signalling. Nature. 465: 885-890. DOI: 10.1038/nature09121

Lin IW-S, Lok C-N, Che C-M. 2014. Biosynthesis of silver nanoparticles from silver(I) reduction by periplasmic nitrate reductase c-type cytochrome subunit NapC in a silver-resistant E. coli. Chem Sci. 5: 3144-3150. DOI: 10.1039/C4SC00138A

Lin M, Tseng Y-H, Huang C-P. 2015. Interactions between nano-TiO_2 particles and algal cells at moderate particle concentration. Front Chem Sci Eng. 9: 242-257. DOI: 10.1007/s11705-015-1513-7

Lin S, Zhao Y, Xia T, Meng H, Ji Z, Liu R, George S, Xiong S, Wang X, Zhang H, et al. 2011. High content screening in zebrafish speeds up hazard ranking of transition metal oxide nanoparticles. ACS Nano. 5: 7284-7295. DOI: 10.1021/nn202116p.

Lindahl E. 2015. Molecular dynamics simulations. In: Kukol A, editor. Molecular modeling of proteins. New York: Springer Science+Business Media; p. 3-27. DOI: 10.1007/978-1-4939-1465-4

Llewellyn MS, Boutin S, Hoseinifar SH, Derome N. 2014. Teleost microbiomes: the state of the art in their characterization, manipulation and importance in aquaculture and fisheries. Front Microbiol. [accessed 30 Oct. 2019]:[17 p.]. DOI: 10.3389/fmic.2014.00207

Liu X, Dumitrescu E, Kumar A, Austin D, Goia D, Wallace KN, Andreescu S. 2019. Differential lethal and sublethal effects in embryonic zebrafish exposed to different sizes of silver nanoparticles. Environ Pollut. 248: 627-634. DOI: 10.1016/j.envpol.2019.02.085

Lowry GV, Gregory KB, Apte SC, Lead JR. 2012. Transformations of nanomaterials in the environment. Environ Sci Technol. 46: 63893-6899. DOI: 10.1021/es300839e

Lozano O, Mejia J, Masereel B, Toussain O, Lison D, Lucas S. 2012. Development of a PIXE analysis method for the determination of the biopersistence of SiC and TiC nanoparticles in rat lungs. Nanotoxicology. 6: 263-271. DOI: 10.3109/17435390.2011.572301

M

Madigan MT, Martinko JM, Stahl DA, Clark DP. 2011. Brock biology of microorganisms. 13th ed. San Francisco (CA): Pearson.

Makabenta JMV, Nabawy A, Li C-H, Schmidt-Malan S, Patel R, Rotello VM. 2021. Nanomaterial-based therapeutics for antibiotic-resistant bacterial infections. Nat Rev Microbiol. 19: 23-36. DOI: 10.1038/s41579-020-0420-1

Manakul P, Peerakietkhajorn S, Matsuura T, Kato Y, Watanabe H. 2017. Effects of symbiotic bacteria on chemical sensitivity of *Daphnia magna*. Mar Environ Res. 128: 70-75. DOI: 10.1016/j.marenvres.2017.03.001.

Mark P, Nilsson L. 2001. Structure and dynamics of the TIP3P, SPC, and SPC/E water models at 298 K. J Phys Chem A. 105: 9954–9960. DOI: 10.1021/jp003020w

Martin AM, Sun EW, Keatling DJ. 2020. Mechanisms controlling hormone secretion in human gut and its relevance to metabolism. J. Endocrinol. [accessed 2022 May 17]:[15 p.]. DOI: 10.1530/JOE-19-0399

Mazzini M, Callaini G, Mencarelli C. 1984. A comparative analysis of evolution of the egg envelopes and the origin of the yolk. Ital J Zool. 51: 35-101. DOI: 10.1080/1125000849439457

McCammon JA, Gelin BR, Karplus M. 1977. Dynamics of folded proteins. Nature. 267: 585-590. DOI: 10.1038/267585a0

McMillan DB. 2007. Ovulation. In: McMillan DB, editor. Fish histology, Female reproductive systems. Dordrecht: Springer; p. 209-284. DOI: 10.1007/978-1-4020-5715-1

Mech A, Gottardo S, Amenta V, Amodio A, Belz S, Bøwadt S, Drbohlavová J, Farcal L, Jantunen P, Małyska A, et al. 2022. Safe- and sustainable-by-design: the case of smart nanomaterials. A perspective based on a European workshop. Regul Toxicol Pharmacol [accessed 2022 April 28]:[14 p.]. DOI: 10.1016/j.yrtph.2021.105093

Meijer AH, Krens SFG. Rodriguez IAM, He S, Bitter W, Snaar-Jagalska BE, Spaink HP. 2004. Expression analysis of the Toll-like receptor and TIR domain adaptor families of zebrafish. Mol Immunol. 40: 773-783. DOI: 10.1016/j.molimm.2003.10.003

Meijer AH, Van der Vaart M, Spaink HP. 2014. Real-time imaging and genetic dissection of host-microbe interactions in zebrafish. Cell Microbiol. 16: 39-49. DOI: 10.1111/cmi.12236

Mergaert J, Cnockaert MC, Swings J. 2002. *Pyllobacterium myrsinacearum* (subjective synonym *Phyllobacterium rubiacearum*) emend. Int J Syst Evol Microbiol. 52: 1821-1823. DOI: 10.1099/00207713-52-5-1821

Monopoli MP, Åberg C, Salvati A, Dawson KA. 2012. Biomolecular coronas provide the biological identity of nanosized materials. Nat Nanotechnol. 7: 779-786. DOI: 10.1038/NNANO.2012.207

Monti S, Barcaro G, Sementa L, Carravetta V, Ågren H. 2017. Characterization of the adsorption dynamics of trisodium citrate on gold in water solution. RSC Adv. 7: 49655-49663. DOI: 10.1039/c7ra10759e

Mu W, Wang Y, Huang C, Fu Y, Li J, Wang H, Jia X, Ba Q. 2019. Effect of long-term intake of dietary titanium dioxide nanoparticles on intestine inflammation in mice. J Agric Food Chem. 67: 9382-9389. DOI: 10.1021/acs.jafc.9b02391

Muir DR, Kampa BM. 2015. FocusStack and StimServer: a new open source MATAB toolchain for visual stimulation and analysis of two-photon calcium neuronal imaging data. Front Neuroinform. [accessed 2016 Aug 22]:[13 p.]. DOI: 10.3389/fninf.2014.00085

N

Naha PC, Liu Y, Hwang G, Huang Y, Gubara S, Jonnakuti V, Simon-Soro A, Kim D, Gao L, Koo H, et al. 2019. Dextran-coated iron oxide nanoparticles as biomimetic catalysts for localized and pH-activated biofilm disruption. ACS Nano. 13: 4960-4971. DOI: 10.1021/acsnano.8b08702.

Nair S, Sasidharan A, Rani VVD, Menon D, Nair S, Manzoor K, Raina S. 2009. Role of size scale of ZnO nanoparticles and microparticles on toxicity toward bacteria and osteoblast cancer cells. J Mater Sci: Mater Med. 20: S235-S241. DOI: 10.1007/s10856-008-3548-5

Nasir A, Wang S, Friedman A. 2011. The emerging role of nanotechnology in sunscreens: an update. Expert Rev Dermatol. 6: 437-439. DOI: 10.1586/EDM.11.49

Nasser F, Constantinou J, Lynch I. 2019. Nanomaterials in the environment acquire an 'eco-corona' impacting their toxicity to *Daphnia magna* – a call for updating toxicity testing policies. Proteomics. [accessed 2020 April 1]:[15 p.]. DOI: 10.1002/pmic.201800412

Nel A, Mädler L, Velegol D, Xia T, Hoek EMV, Somasundaran P, Klaessig F, Castranova V, Thompson M. 2009. Understanding biophysicochemical interactions at the nano-bio interface. Nat Mater. 8: 543-557. DOI: 10.1038/NMAT2442

Nguyen-Chi M, Phan QT, Gonzalez C, Dubremetz JF, Levraud JP, Lutfalla G. 2014. Transient infection of the zebrafish notochord with *E. coli* induces chronic inflammation. Dis Model Mech. 7: 871-882. DOI: 10.1242/dmm.014498

Nielsen FH. 2014. Update on the possible nutritional importance of silicon. J Trace Elem Med Biol. 28: 379-382. DOI: 10.1016/j.jtemb.2014.06.024

Nilakantan R, Nunn DS, Greenblatt L, Walker G, Haraki K, Mobilio DA. 2006. Family of ring system-based structural fragments for use in structure-activity studies: database mining and recursive partitioning. J Chem Inf Model. 46: 1069-1077. DOI: 10.1021/ci050521b

Novoselov AA, Serrano P, Pacheco MLAF, Chaffin MS, O'Malley-James JT, Moreno SC, Ribeiro FB. 2013. From cytoplasm to environment: the inorganic ingredient for the origin of life. Astrobiology. 13: 294-302. DOI: 10.1089/ast.2012.0836

Novotný F, Wang H, Pumera M. 2020. Nanorobots: machines squeezed between molecular motors and micromotors. Chem. 6: 867-884. DOI: 10.1016/j.chempr.2019.12.028

O

OECD. 2013. Fish Embryo Acute Toxicity (FET) test. OECD guidelines for the testing of chemicals Paris: OECD. Test No.: 236. Available from: https://doi.org/10.1787/20745761

Odum EP. 1969. The strategy of ecosystem development. Science. 164: 262-270. DOI: 10.1126/science.164.3877. 262

Oehlers SH, Flores MV, Okuda KS, Hall CJ, Crosier KE, Crosier PS. 2011. A chemical enterocolitis model in zebrafish larvae that is dependent on microbiota and responsive to pharmacological agents. Dev Dyn. 240: 288-298. DOI: 10.1002/dvdy.22519

Ogle D, Wheeler P, Briand C. 2021. droglenc/FSA: Released v0.8.3.2 to CRAN [R package]. Version 0.8.32. Zenodo. [accessed 2021 Jan 16] DOI: 10.5281/zenodo.4443369

Osborne OJ, Johnston BD, Moger J, Balousha M., Lead JR, Kudoh T, Tyler CR. 2013. Effects of particle size and coating on nanoscale Ag and TiO_2 exposure in zebrafish (*Danio rerio*) embryos. Nanotoxicology. 7: 1315-1324. DOI: 10.3109/17435390.2012.737484

Osborne OJ, Mukaigasa K, Nakajima H, Stolpe B, Romer I, Philips U, Lynch I, Mourabit S, Hirose S, Lead JR, et al. 2016. Sensory systems and ionocytes are targets for silver nanoparticle effects in fish. Nanotoxicology. 10:1276-1286. DOI: 10.1080/17435390.2016.1206147

Ostadhossein F, Moitra P, Altun E, Dutta D, Sar D, Tripathi I, Hsiao S-H, Kravchuk V, Nie S, Pan D. 2021. Function-adaptive clustered nanoparticles reverse *Streptococcus mutans* dental biofilm and maintain microbiota balance. Commun Biol. 4: 846. DOI: 10.1038/s42003-021-02372-y

Otto M. 2009. "*Staphylococcus epidermis* – the 'Accidental' Pathogen." Nat Rev Microbiol. 7: 555–567. DOI: 10.1038/nrmicro2182

P

Panáček A, Kvítek L, Smékalová M, Večeřová R, Kolář M, Röderová M, Dyčka F, Šebela M, Prucek R, Tomanec O, et al. 2018. Bacterial resistance to silver nanoparticles and how to overcome it. Nat Nanotechnol. 13: 65-71. DOI: 10.1038/s41565-017-0013-y

Panigrahi P, Parida S, Nanda NC, Satpathy R, Pradhan L, Chandel DS, Baccaglini L, Mohapatra A, Mohapatra SS, Misra PR, et al. 2017. A randomized symbiotic trial to prevent sepsis among infants in rural India. Nature. 548: 407-412. DOI: 10.1038/nature23480

Paone P, Cani PD. 2020. Mucus barrier, mucins and gut microbiota: the expected slimy partners? Gut. 69: 2232-2243. DOI: 10.1136/gutjnl-2020-322260

Parrinello M, Rahman A. 1981. Polymorphic transitions in single crystals: a new molecular dynamics method. J Appl Phys. 52: 7182–7190. DOI: 10.1063/1.328693

Pastor RW, MacKerell Jr AD. 2011. Development of the CHARMM force field for lipids. J Phys Chem. 2: 1526–1532. DOI: 10.1021/jz200167q

Pearce SC, Coia HG, Karl JP, Pantoja-Feliciano IG, Zachos NC, Racicot K. 2018. Intestinal *in vitro* and *ex vivo* models to study host-microbiome interactions and acute stressors. Front Physiol. [accessed 2022 April 18]:[17 p.]. DOI: 10.3389/fphys.2018.01584

Pham LN, Kanther I, Semova I, Rawls JF. 2008. Methods for generating and colonizing gnotobiotic zebrafish. Nat Protoc. 3: 1862-1875. DOI: 10.1038/nprot.2008.186

Phelps D, Brinkman NE, Keely SP, Anneken EM, Catron TR, Betancourt D, Wood CE, Espenschied ST, Rawls JF, Tal T. 2017. Microbial colonization is required for normal neurobehavioral development in zebrafish. Sci Rep. [accessed 2017 Nov 27]:[13 p.]. DOI: 10.1038/s41598-017-10517-5

Philip AM, Wang Y, Mauro A, El-Rass S, Marshall JC, Lee WL, Slutsky AS, Dos Santos CC, Wen, X-Y. 2017. Development of a zebrafish sepsis model for high-throughput drug discovery. Mol Med. 23: 134-148. DOI: 10.2119/molmed.2016.00188

Poon W-L, Lee JC-Y, Leung KS, Alenius H, El-Nezami H, Karisola P. 2019. Nanosized silver, but not titanium dioxide or zinc oxide, enhances oxidative stress and inflammatory response by inducing 5-HETE activation in THP-1 cells. Nanotoxicology. 27: 453–467. DOI: 10.1080/17435390.2019.1687776

Preiswerk B, Ullrich S, Speich R, Bloemberg GV, Hombach M. 2011. Human infection with *Delftia tsuruhatensis* isolated from a central venous catheter. J Med Microbiol. 60: 246-248. DOI: 10.1099/jmm.0.021238-0

Q

Qin Y, Zhao R, Qin H, Chen L, Chen H, Zhao Y, Nie G. 2021. Colonic mucus accumulating tungsten oxide nanoparticles improve the colitis therapy by targeting Enterobacteriaceae. Nano Today. [accessed 2022 May 5]:[14 p.]. DOI: 10.1016/j.nantod.2021.101234

Qv L, Yang Z, Yao M, Mao S, Li Y, Zhang J, Li L. 2020. Methods for establishment and maintenance of germ-free rat models. Front Microbiol. [accessed 2022 April 8]:[13 p.]. DOI: 10.3389/fmicb.2020.01148

R

Rajpoot S, Wary KK, Ibbott R, Liu D, Saqib U, Thurnston TLM, Baig MS. 2021. TIRAP in the mechanism of inflammation. Front Immunol. [accessed 2021 Sept. 15]:[12 p.]. DOI: 10.3389/fimmu.2021.697588

Rakoff-Nahoum S, Paglino J, Eslami-Varzaneh F, Edberg S, Medzhitov R. 2004. Recognition of commensal microflora by Toll-like receptors is required for intestinal homeostasis. Cell. 118: 229-241. DOI: 10.1016/j.cell.2004.07.002

Rasmussen K, Mast J, De Temmerman P-J, Verleysen E, Waegeneers N, Van Steen F, Pizzolon JC, De Temmerman L, Van Doren E, Jensen KA, et al. 2014. Titanium dioxide, NM-100, NM-101, NM-102, NM-103, NM-104, NM-105: Characterisation and phyisco-chemical properties. Ispra: JRC Science and Policy Reports. Report No.: JRC 86291. DOI: 10.2788/79554

Rawls JF, Buck SS, Gordon JI. 2004. Gnotobiotic zebrafish reveal evolutionarily conserved responses to the gut microbiota. Proc Natl Acad Sci USA. 101: 4596-4601. DOI: 10.1073/pnas.0400706101

Rawls JF, Mahowald MA, Ley RE, Gordon JI. 2006. Reciprocal gut microbiota transplants from zebrafish and mice to germ-free recipients reveal host habitat selection. Cell. 127: 422-433. DOI: 10.1016/j.cell.2006.08.043

Reeßing F, Szymanski W. 2017. Beyond photodynamic therapy: light-activated cancer chemotherapy. Curr Med Chem. 24: 4905-4950. DOI: 10.2174/0929867323666160906103223

Ritz C, Baty F, Streibig JC, Gerhard D. 2015. Dose-response analysis using R. *PLoS One* [accessed 2019 Oct. 30]:[13 p.]. DOI: 10.1371/journal.pone.0146021

Roeselers G, Mittge EK, Stephens WZ, Parichy DM, Cavanaugh CM, Guillemin K, Rawls JF. 2011. Evidence for a core gut microbiota in the zebrafish. The ISME J. 5: 1595–1608. DOI: 10.1038/ismej.2011.38

Round JL, Lee SM, Li J, Tran G, Jabri B, Chatila TA, Mazmanian SK. 2011. The Toll-like receptor 2 pathway establishes colonization by a commensal of the human microbiota. Science. 332: 974-977. DOI: 10.1126/science.1206095

Roy J, Ghosh S, Ojha PB, Roy K. 2019. Predictive quantitative structure-property relationship (QSPR) modeling for adsorption of organic pollutants by carbon nanotubes (CNTs). Environ. Sci: Nano. 6: 224-247. DOI: 10.1039/c8en01059e

Ruan W, Engevik MA, Spinler JK, Versalovic J. 2020. Healthy human gastrointestinal microbiome: composition and function after a decade of exploration. Dig Dis Sci. 65: 695-705. DOI: 10.1007/s10620-020-06118-4

S

Sauma S, Casaccia P. 2020. Does the gut microbiota contribute to the oligodendrocyte progenitor niche? Neurosci Lett. [accessed 2021 May 17]:[6 p.]. DOI: 10.1016/j.neulet.2019.134574

Schmidt AF, Finan C. 2018. Linear regression and the normality assumption. J Clin Epidemiol. 98: 146-151. DOI: 10.1016/j.jclinepi.2017.12.006

Schür C, Rist S, Baun A, Mayer P, Hartmann NB, Wagner M. 2019. When fluorescence is not a particle: The tissue translocation of microplastics in *Daphnia magna* seems an artifact. Env Toxicol Chem. 38: 1495-1503. DOI: 10.1002/etc.4436

Science for Environmental Policy. 2017. Assessing the environmental safety of manufactured nanomaterials. Bristol: Science Communication Unit, UWE. Report No.: In-depth report 14. Available from https://doi.org/10.2779/690478

Seil JT, Webster TJ. 2012. Antimicrobial applications of nanotechnology: methods and literature. Int J Nanomed. 7: 2767-2781. DOI: 10.2147/IJN.S24805

Sender R., Fuchs S, Milo R. 2016. Revised estimates for the number of human and bacteria cells in the body. PloS Biol. [accessed 2021 June 17]:[14 p.]. DOI: 10.1371/journal.pbio.1002533

Senftle T, Hong S, Islam M Md, Kylasa SB, Zheng Y, Shin YK, Junkermeier C, Engel-Herbert R, Janik MJ, Aktulga HM, et al. 2016. The ReaxFF reactive force-field: development, applications and future directions. npj Comput Mater. [accessed 2022 Aug 24]:[14 p.]. DOI: 10.1038/npjcompumats.2015.11

Shah RM, McKenzie EJ, Rosin MT, Jadhav SR, Gondalia SV, Rosendale D, Beale DJ. 2020. An integrated multi-disciplinary perspective for addressing challenges of the human gut microbiome. Metabolites. [accessed 2020 Oct. 29]:[35 p.]. DOI: 10.3390/metabo10030094

Sharma VK, Prateeksha, Gupta SC, Singh BN, Rao CV, Barik SK. 2022. *Cinnamomum verum*-derived bioactives-functionalized gold nanoparticles for prevention of obesity through gut microbiota reshaping. Mater Today. [accessed 2020 May 6]:[15 p.]. DOI: 10.1016/j.mtbio.2022.100204

Shcherbakova EN, Scherbakov AV, Andronov EE, Gonchar LN, Kalenskaya SM, Chebotar VK. 2017. Combined pre-seed treatment with microbial inoculants and Mo nanoparticles changes composition of root exudates and rhizosphere microbiome structure of chickpea (*Cicer arietinum L.*) plants. Symbiosis. 73: 57-69. DOI: 10.1007/s13199-016-0472-1

Shih Y-J, Su C-C, Chen C-W, Dong C-D, Liu W, Huang CP. 2016. Adsorption characteristics of nano-TiO_2 onto zebrafish embryos and its impacts on egg hatching. Chemosphere. 154: 109-117. DOI: 10.1016/j.chemosphere.2016.03.061

Shin SY, Choi JY, Ko KS. 2012. Four cases of possible human infections with *Delftia lacustris.* Infection. 40: 709-712. DOI:10.1007/s1501-012-0339-1

Shropshire JD, Van Opstal EJ, Bordenstein SR. 2016. An optimized approach to germ-free rearing in the jewel wasp *Nasonia.* PeerJ. [accessed 2022 April 28]:[20 p.]. DOI: 10.771/peerj.2316

Sillen WMA, Thijs S, Abbamondi GR, Janssen J, Weyens N, White JC, Vangronsveld J. 2015. Effects of silver nanoparticles on soil microorganisms and maize biomass are linked in the rhizosphere. Soil Biol Biochem. 91: 14-22. DOI: 10.1016/j.soilbio.2015.08.2019

Silva YP, Bernardi A, Frozza RL. 2020. The role of short-chain fatty acids from gut microbiota in gut-brain communication. Front Endocrinol. [accessed 2021 May 17]:[14 p.]. DOI: 10.3389/fendo.2020.00025

Silver S. 2003. Bacterial silver resistance: molecular biology and use and misuses of silver compounds. FEMS Microbiol Rev. 27: 341-353. DOI: 10.1016/S0168-6445(03)00047-0

Singh C, Friedrichs S, Levin M, Birkedal R, Jensen KA, Pojana G, Wohlleben W, Schulte S, Wiench K, Turney T, et al. 2011. Zinc oxide NM-110, NM- 111, NM-112, NM-113: characterisation and test item preparation. Brussels: European Commission. Report No.: EUR 25066 EN. Available from https://doi.org/10.2787/55008

Sison-Mangus MP, Mushegian AA, Ebert D. 2015. Water fleas require microbiota for survival, growth and reproduction. ISME J. 9: 59-67. DOI: 10.1038/ismej.2014.116

Song M, Liu S, Yin J, Wang H. 2011. Interaction of human serum album and C_{60} aggregates in solution. Int J Mol Sci. 12: 4964-4974. DOI: 10.3390/ijms12084964

Spurgeon D, Lahive E, Robinson A, Short S, Kille P. 2020. Species sensitivity to toxic substances: evolution, ecology and applications. Front Environ Sci. [accessed 2022 May 1]:[25 p.]. DOI: 10.3389/fenvs.2020.588380

Stephens WZ, Burns AR, Stagaman K, Wong S, Rawls JF, Guillemin K, Bohannan BJM. 2016. The composition of the zebrafish intestinal microbial community varies across development. ISME J. 10: 644-654. DOI: 10.1038/ismej.2015.140

Stephens WZ, Wiles TJ, Martinez ES, Jemielita M, Burns AR, Parthasarathy R, Bohannan BJM, Guillemin K. 2015. Identification of population bottlenecks and colonization factors during assembly of bacterial communities within the zebrafish intestine. mBio. [accessed 2018 April 6]:[11 p.]. DOI: 10.1128/mBio.01163-15

Sukhanova A, Bozrova S, Sokolov P, Berestovoy M, Karaulov A, Nabiev I. 2018. Dependence of nanoparticle toxicity on their physical and chemical properties. Nanoscale Res Lett. [accessed 2019 Nov 17]:[21 p.]. DOI: 10.1186/s11671-018-2457-x

Sun D, Ding A. 2006. MyD88-mediated stabilization of interferon-γ-induced cytokine and chemokine mRNA. Nat Immunol. 7: 375-381. DOI: 10.1038/ni1308

Suzuki N, Kato K. 1953. Studies on suspended materials marine snow in the sea: Part I. Sources of marine snow. Bull Fac Fish Hokkaido Univ. 4: 132-137.

T

Teleki A, Wengeler R, Wengeler L, Nirschl H, Pratsinis SE. 2008. Distinguishing between aggregates and agglomerates of flame-made TiO_2 by high pressure dispersion. Powder Technol. 181: 292-300. DOI: 10.1016/j.powtec.2007.05.016

Thepphankulngarm N, Wonganan P, Sapcharoenkun C, Tuntulani T, Leeladee P. 2017. Combining vitamin B_{12} and cisplatin-loaded porous silica nanoparticles *via* coordination: a facile approach to prepare a targeted drug delivery system. New J Chem. 41: 13823-13829. DOI: 10.1039/c7nj02754k

Tian L, Wang X-W, Wu A-K, Fan Y, Friedman J, Dahlin A, Waldor MK, Weinstock GM, Weiss ST, Liu Y-Y. 2020. Deciphering functional redundancy in the human microbiome. Nat Commun. [2021 Oct. 20]:[11 p.]. DOI: 10.1038/s41467-020-19940-1

Tierney BT, Yang Z, Luber JM, Beaudin M, Wibowo MC, Baek C, Mehlenbacher E, Patel CJ, Kostic D. 2019. The landscape of genetic content in the gut and oral human microbiome. Cell Host Microbe. 26: 285-295. DOI: 10.1016/j.chom.2019.07.008

Trevelline BK, Fontaine SS, Hartup BK. 2019. Conservation biology needs a microbial renaissance: a call for the consideration of host-associated microbiota in wildlife management practices. Proc R Soc B. [accessed 2019 Oct. 30]:[9 p.]. DOI: 10.1098/rspb.2018.2448

V

Van den Broek B, Ashcroft B, Oosterkamp TH, Van Noort J. 2013. Parallel nanometric 3D tracking of intracellular gold nanorods using multifocal two-photon microscopy. Nano Lett. 13: 980-986. DOI: 10.1021/nl3040509

Van der Spoel D, Lindahl E, Hess B, Groenhof G, Mark AE, Berendsen HJC. 2005. GROMACS: Fast, Flexible, and Free. J Comput Chem. 26: 1701–1718. DOI: 10.1002/jcc.20291

Van Pomeren M, Brun NR, Peijnenburg WJGM, Vijver MG. 2017a. Exploring uptake and biodistribution of polystyrene (nano)particles in zebrafish embryos at different developmental stages. Aquat Toxicol. 190: 40-45. DOI: 10.1016/j.aquatox.2017.06.017

Van Pomeren M, Peijnenburg WJGM, Brun NR, Vijver MG. 2017b. A novel experimental and modeling strategy for nanoparticle toxicity testing enabling the use of small quantities. Int J Environ Res Public Health. [accessed 2017 Nov. 22]:[14 p.]. DOI: 10.3390/ijerph14111348

Van Pomeren M, Peijnenburg WJGM, Vlieg RC, Van Noort SJT, Vijver MG. 2019. The biodistribution and immuno-responses of differently shaped non-modified gold particles in zebrafish embryos. Nanotoxicology. 13: 558-571. DOI: 10.1080/17435390.2018.1564079

Vassaux M, Sinclair C, Richardson RA, Suter JL, Coveney PV. 2020. Toward high fidelity materials property prediction from multiscale modeling and simulation. Adv Theory Simul. [accessed 2022 Aug 22]:[12 p.]. DOI: 10.1002/adts.201900122

Venegas DP, De la Fuente MK, Landskron G, González MJ, Quera R, Dijkstra G, Harmsen HJM, Faber KN, Hermoso MA. 2019. Short chain fatty acids (SCFAs)-mediated gut epithelia and immune regulation and its relevance for inflammatory bowel diseases. Front Immunol. [accessed 2022 June 16]:[16 p.]. DOI: 10.3389/fimmu.2019.00277

Verbruggen B, Gunnarsson L, Kristiansson E, Österlund T, Owen SF, Snape JR, Tyler CR. 2017. ECOdrug: a database connecting drugs and conservation of their targets across species. Nucleic Acids Res. 46: D930-D936. DOI: 10.1093/nar/gkx1024

W

Walczyk D, Bombelli FB, Monopoli MP, Lynch I, Dawson K. 2010. What the cell ‘sees’ in bionanoscience. J Am Chem Soc. 132: 5761-5768. DOI: 10.1021/ja910675v

Wang G-H. Brucker RM. 2022. An optimized method for *Nasonia* germ-free rearing. Sci Rep. [accessed 2022 April 28]:[5 p.]. DOI: 10.1038/s41598-021-04363-9

Wang Y, Han R, Zhang H, Liu H, Li J, Liu H, Gramatica P. 2017. Combined ligand/structure-based virtual screening and molecular dynamics simulations of steroidal androgen receptor antagonists. BioMed Res Int. [accessed 2022 Jan. 23]:[18 p.]. DOI: 10.1155/2017/3572394

Wang C, Yue L, Cheng B, Chen F, Zhao X, Wang Z, Xing B. 2022. Mechanisms of growth-promotion and Se-enrichment in *Brassica chinensis* L. by selenium nanomaterials: beneficial rhizosphere microorganisms, nutrient availability, and photosynthesis. Environ Sci: Nano. 9, 302-312. DOI: 10.1039/d1en00740h

Westmeier D, Hahlbrock A, Reinhardt C, Fröhlich-Nowoisky J, Wessler S, Vallet C, Pöschl U, Knauer SK, Stauber RH. 2019. Nanomaterial-microbe cross-talk: physicochemical principles and (phatho)biological consequences. Chem Soc Rev. 47: 5312-5337. DOI: 10.1039/C6CS00691D

Wiles TJ, Jemielita M, Baker RP, Schlomann BH, Logan SL, Ganz J, Melancon E, Eisen JS, Guillemin K, Parthasarathy R. 2016. Host gut motility promotes competitive exclusion within a model intestinal microbiota. PLoS Biol. [accessed 2018 April 6]:[24 p.]. DOI: 10.1371/journal.pbio.1002517

Wilkins LJ, Monga M, Miller AW. 2019. Defining dysbiosis for a cluster of chronic diseases. Sci Rep. [accessed 2022 May 27]:[10 p.]. DOI: 10.1038/s41598-019-49452-y

Wilkinson JL, Boxall ABA, Kolpin DW, Leung KMY, Lai RWS, Galbán-Malagón C, Adell AD, Mondon J, Metian M, Marchant RA, et al. 2022. Pharmaceutical pollution of the world’s rivers. Proc Natl Acad Sci USA. [accessed 2022 April 27]:[10 p.]. DOI: 10.1073/pnas.2113947119

Willing BP, Russel SL, Finlay BB. 2011. Shifting the balance: antibiotic effects on host-microbiota mutualism. Nat Rev Microbiol. 9: 233-243. DOI: 10.1038/nrmicro2536

Willner MR, Vikesland PJ. 2018. Nanomaterial enabled sensors for environmental contaminants. J Nanobiotechnol. 16: 95. DOI: 10.1186/s12951-018-0419-1

Wu W-K, Hsu C-C, Sheen L-Y, Wu M-S. 2020**.** Measurement of gut microbial metabolites in cardiometabolic health and translational research. Rapid Commun Mass Spectrom. [accessed 2021 May 17]:[7 p.]. DOI: 10.1002/rcm.8537

Wu Z, Jiang Y, Kim T, Lee K. 2007. Effects of surface coating on the controlled release of vitamin B_1 from mesoporous silica tablets. J Control Release. 119: 215–221. DOI: 10.1016/j.jconrel.2007.03.001

X

Xia T, Lai W, Han M, Han M, Ma X, Zhang L. 2017. Dietary ZnO nanoparticles alters intestinal microbiota and inflammation response in weaned piglets. Oncotarget. 8: 64878-63891. DOI: 10.18632/oncotarget.17612

Xia X-R, Monteiro-Riviere NA, Riviere JE. 2010. An index for characterization of nanomaterials in biological systems. Nat Nanotechnol. 5: 671-675. DOI: 10.1038/NNANO.2010.164

Xing PY, Pettersson S, Kundu P. 2020. Microbial metabolites and intestinal stem cells tune intestinal homeostasis. Proteomics. [accessed 2022 May 17]:[16 p.]. DOI: 10.1002/pmic.201800419

Y

Yan W, Chen X, Li X, Feng X, Zhu J-J. 2008. Fabrication of a label-free electrochemical immunosensor of low-density lipoprotein. J Phys Chem B. 112: 1275-1281. DOI: 10.1021/jp0765594

Yang JH, Bhargava P, McCLoskey D, Mao N, Palsson BO, Collins JJ. 2017a. Antibiotic-induced changes to the host metabolic environment inhibit drug efficacy and alter immune function. Cell Host Microbe. 22: 757-765. DOI: 10.1016/j.chom.2017.10.020

Yang J, Cao W, Rui Y. 2017b. Interactions between nanoparticles and plants: phytotoxicity and defense mechanisms. J Plant Interact. 12: 158-169. DOI:10.1080/17429145.2017.1310944

Yin N, Gao R, Knowles B, Wang J, Wang P, Sun G, Cui Y. 2019. Formation of silver nanoparticles by human gut microbiota. Sci Total Environ. 651: 1489-1494. DOI: 10.1016/j.scitotenv.2018.09.312

Z

Zhai Y, Hunting ER, Liu G, Baas E, Peijnenburg WJGM, Vijver MG. 2019. Compositional alterations in soil bacterial communities exposed to TiO_2 nanoparticles are not reflected in functional impacts. Environ Res. [accessed 2020 June 22]:[9 p.]. DOI: 10.1016/j.envres.2019.108713

Zhai Y, Hunting ER, Wouters M, Peijnenburg WJGM, Vijver MG. 2016. Silver nanoparticles, ions, and shape governing soil microbial functional diversity: Nano shapes micro. Front Microbiol. [accessed 2019 Oct. 30]:[9 p.]. DOI: 10.3389/ fmicb.2016.01123

Zhang X, Chen L, Yuan L, Liu R, Li D, Liu X, Ge G. 2019. Conformation-dependent coordination of carboxylic acids with Fe_3O_4 nanoparticles Studied by ATR-FTIR spectral deconvolution. Langmuir. 35: 5770-5778. DOI: 10.1021/acs.langmuir.8b03303

Zhao Y, Liu S, Tang Y, You T, Xu H. 2021. *Lactobacillus rhamnosus* GG ameliorated long-term exposure to TiO_2 nanoparticles induced microbiota-mediated liver and colon inflammation and fructose-caused metabolic abnormality in metabolism syndrome mice. J Agric Food Chem. 69: 9788-9799. DOI: 10.1021/acs.jafc.1c03301

Zhao Y, Tang Y, Chen L, Lv S, Liu S, Nie P, Aguilar ZP, Xu H. 2020. Restraining the TiO_2 nanoparticles-induced intestinal inflammation mediated by gut microbiota in juvenile rats via ingestion of *Lactobacillus rhamnosus* GG. Ecotoxicol Environ Saf. [accessed 2022 May 4]:[11 p.]. DOI: 10.1016/j.ecoenv.2020.111393

Zheng H, Gu Z, Pan Y, Chen J, Xie Q, Xu S, Gao M, Cai X, Liu S, Wang W, et al. 2021. Biotransformation of rare earth oxide nanoparticles eliciting microbiota imbalance. Part Fibre Toxicol. [accessed 2022 May 5]:[14 p.]. DOI: 10.1186/s12989-021-00410-5

Zhu S, Zeng M, Feng G, Wu H. 2019. Platinum nanoparticles as a therapeutic agent against dextran sodium sulfate-induced colitis in mice. Int J Nanomed. 14: 8361-8378. DOI: 10.2147/IJN.S210655

Zhu X, Zhao L, Liu Z, Zhou Q, Zhu Y, Zhao Y, Yang X. 2021. Long-term exposure to titanium dioxide nanoparticles promotes diet-induced obesity through exacerbating intestinal mucus layer damage and microbiota dysbiosis. Nano Res. 14: 1512-1522. DOI: 10.1007/s12274-020-3210-1

Curriculum vitae

Bregje was born in 1993 in Haarlem, where she followed pre-university education (VWO) at Lyceum Sancta Maria (2006-2011). In September 2011, she started her academic training at Leiden University by following the BSc program in Biology. Here, she developed a particular interest in research investigating biological phenomena at different, interconnected scales in time and space. In February 2014, Bregje concluded her BSc degree at Naturalis Biodiversity Center with a research project 'looking for cryptic species in Pontoniine shrimps', under the supervision of dr. Charles H.J.M. Fransen. After graduating (*summa cum laude*) Bregje was awarded the 'Professor Kees Bakker prijs 2014' for her BSc degree, which, in combination with the ISME16 travel grant, supported her visit to the 16th International Symposium on Microbial Ecology in Montreal (Canada).

In September 2014, Bregje continued her academic training by following the MSc degree in Limnology & Oceanography (Biological Sciences) at the University of Amsterdam. In two research projects, she developed a growing interest in the effects of microbial activity on water quality and ecosystem functioning. In a first project, supervised by dr. J. Merijn Schuurmans and dr. Hans C.P. Matthijs, she studied the role of cyanotoxin microcystin in the sensitivity of cyanobacteria to strong oxidative stress. In a second project, supervised by dr. J. Arie Vonk and dr. Harm G. van der Geest, she studied algal survival in limnetic aggregates from the turbid water column of large and shallow delta lake Markermeer (the Netherlands). By way of a literature study, supervised by dr. Eva S. Deutekom, she also investigated the role of host-microbiota interactions in the adaptive potential of the coral holobiont to the negative impacts of ocean acidification on coral calcification. Bregje graduated (*cum laude*) for her MSc degree in November 2016.

In October 2017, Bregje returned to Leiden University as PhD candidate at the Institute of Environmental Sciences (CML). Here, she joined the Ecotox team led by prof. dr. Martina G. Vijver and prof. dr. Willie J.G.M. Peijnenburg, to study the effects of host-associated microbiota on particle-specific nanomaterial toxicity. Her research contributed to the Horizon 2020 project PATROLS (www.patrols-h2020.eu), awarded to Martina Vijver and fellow researchers. Bregje presented her work at the PATROLS General Assembly in Fribourg (Switzerland, 2019), at the PATROLS Early Career Researcher Webinar (online, 2020), at the Society of Environmental Toxicology and Chemistry Europe 30th Annual Meeting (SETAC SciCon, online, 2020), and at the 10th International Conference on Nanotoxicology (NanoTox, online, 2021). The results of her PhD research are presented in this thesis.

List of publications

Brinkmann BW, Singhal A, Sevink GJA, Neeft L, Vijver MG, Peijnenburg WJGM. 2022. Predicted adsorption affinity for enteric microbial metabolites to metal and carbon nanomaterials. J Chem Inf Model. 62: 3589-3603. DOI: 10.1021/acs.jcim.2c00492

Brinkmann BW, Koch BEV, Peijnenburg WJGM, Vijver MG. 2022. Microbiota-dependent TLR2 signaling reduces silver nanoparticle toxicity to zebrafish larvae. Ecotox Environ Saf. 237: 113522. DOI: 10.1016/j.ecoenv.2022.113522

Brinkmann BW, Beijk WF, Vlieg RC, Van Noort SJT, Mejia J, Colaux JL, Lucas S, Lamers G, Peijnenburg WJGM, Vijver MG. 2021. Adsorption of titanium dioxide nanoparticles onto zebrafish eggs affects colonizing microbiota. Aquat Toxicol. 232: 105744. DOI: 10.1016/j.aquatox.2021.105744

Brinkmann BW, Koch BEV, Spaink HP, Peijnenburg WJGM, Vijver MG. 2020. Colonizing microbiota protect zebrafish larvae against silver nanoparticle toxicity. Nanotoxicology. 14: 725-739. DOI: 10.1080/17435390.2020.1755469

Dovidat LC, Brinkmann BW, Vijver MG, Bosker T. 2020. Plastic particles adsorb to the roots of freshwater vascular plant *Spirodela polyrhiza* but do not impair growth. Limnol Oceanogr Lett. 5: 37-45. DOI: 10.1002/lol2.10118

Brinkmann BW, Vonk JA, Van Beusekom SAM, Ibanez M, De Lucas Pardo MA, Noordhuis R, Manders EMM, Verspagen JMH, Van der Geest HG. 2019. Benthic hotspots in the pelagic zone: Light and phosphate availability alter aggregates of microalgae and suspended particles in a shallow turbid lake. Limnol Oceanogr. 64: 585-596. DOI: 10.1002/lno.11062

Schuurmans JM, Brinkmann BW, Makower AK, Dittmann E, Huisman J, Matthijs HCP. 2018. Microcystin interferes with defense against high oxidative stress in harmful cyanobacteria. Harmful Algae. 78: 47-55. DOI: 10.1016/j.hal.2018.07.008

Brinkmann BW, Fransen CHJM. 2016. Identification of a new stony coral host for the anemone shrimp *Periclimenes rathbunae* Schmitt, 1924 with notes on the host-use pattern. Contrib Zool. 85: 437-456. DOI: 10.1163/18759866-08504004

Acknowledgements

This chapter is a celebration of all of the supportive, valuable, inspirational and fun interactions with colleagues and students that were part of my PhD research – and will hopefully be followed up in future.

First and foremost, I would like to thank my promotors Martina Vijver and Willie Peijnenburg. Thank you both for creating an open and inspirational research environment for me. Dear Martina, thank you for your encouraging and responsive supervision, always finding time to support me with complicated decisions. This has been very important to the success of the project, and above all, allowed me to further develop my skills in teaching and research. Dear Willie, thank you for contributing to the project with your positive mindset and broad scientific interest. This opened up many interesting research opportunities, and also ensured that there was always a surprising topic to chat about.

I would like to thank all members of the reading committee: prof. dr. A. Tukker, prof. dr. ir. P.M. van Bodegom, prof. dr. H.P. Spaink, dr. G.J.A. Sevink, prof. dr. I. Lynch and dr. L.M. Skjolding. Thank you for taking the time and effort to critically read and respond on my thesis

Many scientists and students have contributed to the research presented in this thesis. I am grateful to all co-authors: Bjørn Koch, Herman Spaink, Wouter Beijk, Gerda Lamers, Redmar Vlieg, John van Noort, Jorge Mejia, Julien Colaux, Stéphane Lucas, Lisette Neeft, Ankush Singahl, and Agur Sevink. Thank you for introducing me to your critical minds and interesting fields of expertise: this has made my PhD journey such a valuable experience. Special thanks go to Krijn Trimbos, for the interesting discussions we've had on some of the most challenging aspects of the project.

For experimental work, I was happy receive support from a great team of animal caretakers, technicians and students. Thank you Ulrike Nehrdich, Guus van der Velden, Ruth van Koppen and Natasha Montiadi for your professional care for the fish, and for the enjoyable chats we had in the early mornings. I am also grateful to Saskia Rueb, Emilie Didaskalou and Roel Heutink for managing the well-arranged labs of the Institute Biology Leiden (IBL) and the Institute of Environmental Sciences (CML). Thank you Rudo Verweij and Stefan Romeijn, for welcoming me at your labs for chemical and particle characterization. I am grateful to all students who joined me in the lab to work on my project: thank you Wouter Beijk, Lisette Neeft and Simon Pieksma. It was a pleasure to work with you, and without your input, commitment and hard work, I would probably still have been busy in the lab now.

Without doubt, I would not have smiled as much during my PhD project without my friendly and inspiring colleagues of CML. I am grateful to CML's supporting staff, and in particular to Susanna van den Oever, Joyce Glerum, Sammy Koning and Kimberley Graauw for their kind help and support in the office, and for their guidance with PhD formalities. I feel lucky to have shared office A3.02 with Marinda van Pomeren, Zhongxiao Sun, Henrik Barmentlo, Jianhong Zhou and Janneke van Oorschot: you can't have enough fruit, tea or coffee breaks with you guys. I enjoyed the lively discussions within the Ecotox group, during biweekly meetings, or whenever we could support or challenge each other in our research. Thank you Henrik, Marinda, Thijs Bosker, Yujia Zhai, Daniel Arenas-Lago, Tom Nederstigt, Pim Wassenaar, Qi Yu, Juan Wu, Olivier Burggraaff, Carlos Blanco Rocha, Nadja Brun, Ellard Hunting, Fazel Abdolahpur Monikh, Yuchao Song, Meiru Wang, Warisa Bunmahotama, Laura Zantis, Sofie Rasmussen, Martin van der Plas, Surendra Balraadjsing, and of course Willie and Martina, for making this possible. Thank you Weilin Huang for the time we've spent as co-chairs of the Environmental Biology department meeting: I really enjoyed teaming up with you. Tom, starting the PhD journey is definitely better together: you were a fantastic companion.

At office B1.20, close to the zebrafish lab, I enjoyed the company by my office neighbors: Sylvia Borgers, Peter Roemelé, Yvonne Kerkhof, Jeroen Haars, Marc Fluttert, André Kamp, Irma Bakker-Rijs, and Yvette Hochstenbach. Thank you all for the relaxing chats about sport, bikes, sailing, and gardening. I am grateful to all colleagues and friendly zebrafish experts from IBL for welcoming me to their department, and for sharing their expertise. I especially would like to thank Herman, Wanbin Hu, Annemarie Meijer, Mónica Varela, Marcel Schaaf, Erin Faught, and Jie Yin, for kindly sharing their fish lines. This opened up many interesting opportunities to investigate mechanisms and pathways that underly nanomaterial toxicity.

The deepest support has come from my friends, parents and brother. Thank you so much for your company, love and trust. This, of course, cannot be returned on paper: I can't wait to spend more time with all of you, sharing many more precious moments together.

Bregje

September 2022

APPENDIX

Supplementary tables for **Chapter 1** and **Chapter 6**.

Table S1: Experimental investigations on the effects of nanoparticles on host-associated microbiota.[a)] Experiments are sorted by the experimental context (‘environmental health’, or ‘human and animal health’), the presence or absence (‘N.D.’) of identified effects on microbiota composition, nanoparticle core material, and host species. Literature that has been published before or in March 2022 is presented.

ENVIRONMENTAL HEALTH: AQUEOUS EXPOSURE

Effect on microbiota	*Nanoparticle*				*Host*	*Microbiota*	*Concentration (µg·L^{-1})*	*Exposure time (d)*	*Reference (DOI)*
	Core[b)]	*Coating*[c)]	*Shape*[d)]	*Size*[e)]					
Yes	Ag	none	S	51	*Danio rerio*	Gut	10 - 100	45	Ma et al. 2018 (10.1039/c7en00740j)
Yes	Ag	none	S	15	*Danio rerio*	Body	250	2	Brinkmann et al. 2020 (10.1080/17435390.2020.1755469)
Yes	Ag	none	S	60	*Danio rerio*	Gut	100	15 -75	Chen et al. 2021 (10.1128/mSystems.00630-21)
Yes	Ag	citrate	S	20	*Daphnia magna*	Gut	0.43 - 4.3	1 - 21	Li et al. 2019 (10.1039/c9en00587k)
Yes	Ag	none	S	20	*Daphnia magna*	Gut	0.43	21 - 84	Li et al. 2022 (10.1039/d1en00765c)
Yes	Ag	none	A	20	*Drosophila melanogaster*	Gut	450·10^3	1.68	Han et al. 2014 (10.1016/j.scitotenv.2013.12.129)

Yes	Ag	carbon	A	25	*Populus nigra*	Phyllosphere	$1 \cdot 10^3$	70	Vitali et al. 2019 (10.1007/s00253-019-10071-2)
Yes	Ag	none	S	35	*Schmidtea mediterranea*	Body	$10 \cdot 10^3$	7	Bijnens et al. 2021 (10.1016/j.aquatox.2020.105672)
Yes	Ag	PVP	S	33	*Schmidtea mediterranea*	Body	$10 \cdot 10^3$	7	Bijnens et al. 2021 (10.1016/j.aquatox.2020.105672)
Yes	CeO_2	none	I	15	*Fragaria ananassa*	Rhizosphere	$0.3 \cdot 10^6$-$2 \cdot 10^6$	45	Dai et al. 2020 (10.1021/acssuschemeng.9b07422)
Yes	Mo	none	NA	60	*Cicer arientinum*	Rhizosphere	$10 \cdot 10^3$	40	Shcherbakova et al. 2017 (10.1007/s13199-016-0472-1)
Yes	Se	none	A	40	*Danio rerio*	Gut	100	90	Chen et al. 2022 (10.1016/j.scitotenv.2021.150963)
Yes	TiO_2	none	A	8	*Danio rerio*	Gut	100	90	Chen et al. 2022 (10.1016/j.scitotenv.2021.150963)
Yes	TiO_2	none	I	21	*Mytilus galloprovincialis*	Hemolymph	100	4	Auguste et al. 2019 (10.1016/j.scitotenv.2019.03.133)
Yes	ZnO	none	A	30	*Danio rerio*	Gut	100	90	Chen et al. 2022 (10.1016/j.scitotenv.2021.150963)

ENVIRONMENTAL HEALTH: FOOD EXPOSURE

Effect on microbiota	*Nanoparticle*				*Host*	*Microbiota*	*Concentration (mg·kg^{-1})*[f]	*Exposure time (d)*	*Reference (DOI)*
	Core[b]	*Coating*[c]	*Shape*[d]	*Size*[e]					
N.D.	TiO_2	none	A	31	*Oreochromis niloticus*	Gut	1 mg·kg bw^{-1}·d^{-1}	28	Sherif et al. 2021 (10.1111/are.15539)
N.D.	TiO_2	none	A	53	*Oreochromis niloticus*	Gut	1 mg·kg bw^{-1}·d^{-1}	28	Sherif et al. 2021 (10.1111/are.15539)
N.D.	ZnO	none	S	28	*Cyprinus carpio*	Gut	500	42	Chupani et al. 2019 (10.1007/s11356-019-05616-x)
Yes	Ag	none	S	20	*Cyprinus carpio*	Gut	50 to 150	60	Khorshidi et al. 2018 (10.1007/s40995-016-0130-8)
Yes	Ag	none	S	50	*Folsomia candida*	Gut	200	28	Zhu et al. 2018 (10.1021/acs.est.8b02825)
Yes	Ag	none	A	28	*Spodoptera litura*	Gut	6.4	1	Bharani and Namasivayam 2017 (10.1016/j.jece.2016.12.023)
Yes	CuO	none	S	40	*Bombyx mori*	Gut	10	5	Muhammad et al. 2022 (10.1016/j.scitotenv.2021.152608)

Yes	MoO_3	none	S	92	*Danio rerio*	Gut	0.2 to 0.4 (lyosol mass·kg water^{-1})	7	Aleshina et al. 2020 (10.1007/s13762-019-02509-x)
Yes	MoO_3	none	S	92	*Danio rerio*	Gill	0.2 to 0.4 (lyosol mass·kg water^{-1})	7	Aleshina et al. 2020 (10.1007/s13762-019-02509-x)
Yes	TiO_2	none	A	8	*Bombyx mori*	Gut	Leaves soaked in 5 mg·L^{-1}	4	Li et al. 2020 (10.1016/j.scitotenv.2019.135273)
Yes	TiO_2	none	A	13	*Oreochromis niloticus*	Gut	1 mg·kg bw^{-1}·d^{-1}	28	Sherif et al. 2021 (10.1111/are.15539)
Yes	ZnO	none	A	50	*Bombyx mori*	Gut	10	5	Muhammad et al. 2022 (10.1016/j.scitotenv.2021.152608)

ENVIRONMENTAL HEALTH: SOIL EXPOSURE

Effect on microbiota	*Nanoparticle*				*Host*	*Microbiota*	*Concentration (mg·kg^{-1})*[f]	*Exposure time (d)*	*Reference (DOI)*
	Core[b]	*Coating*[c]	*Shape*[d]	*Size*[e]					
Yes	Ag	none	S	50	*Eisenia fetida*	Gut	10 - 400	28	Swart et al. 2020 (10.1016/j.envpol.2020.115633)
Yes	Ag	none	S	15	*Lactuca sativa*	Rhizosphere	1 - 50	63	Wu et al. 2021 (10.1021/acssuschemeng.1c04987)
Yes	Ag	none	NA	16	*Linum usitatissimum*	Rhizosphere	0.125 (+ sprayed with 100 μg·L^{-1} after 7 d)	21	Gorczyca et al. 2018 (10.1007/s11356-018-3346-7)
Yes	Ag	carbon	A	25	*Populus nigra*	Rhizosphere	1 mg·L^{-1} pot water	70	Vitali et al. 2019 (10.1007/s00253-019-10071-2)
Yes	Ag	none	NA	16	*Triticum aestivum*	Rhizosphere	0.125 (+ sprayed with 100 μg·L^{-1} after 7 d)	21	Gorczyca et al. 2018 (10.1007/s11356-018-3346-7)
Yes	Ag	citrate	S	11	*Triticum aestivum*	Rhizosphere	3	14	Feng et al. 2021 (10.1016/j.scitotenv.2021.149200)
Yes	Ag	none	I	20	*Zea mays*	Rhizosphere	100	117	Sillen et al. 2020 (10.1186/s40168-020-00904-y)
Yes	Ag_2S	none	S	95	*Eisenia fetida*	Gut	114 - 34·10^{3}	60	Wu et al. 2020 (10.1021/acs.est.0c01241)
Yes	Ag_2S	none	S	95	Pontocolex corethrurus	Gut	114 - 34·103	60	Wu et al. 2020 (10.1021/acs.est.0c01241)
Yes	CuO	none	S	9	*Carya illinoinensis*	Rhizosphere	10 - 1·10^{3}	45	Salas-Leiva et al. 2021 (10.1016/j.apsoil.2020.103772)

Yes	CuO	none	CB	20	*Eisenia fetida*	Gut	160	28	Swart et al. 2020 (10.3390/nano10071337)
Yes	CuO	none	CB	20	*Eisenia fetida*	Gut	10 - 400	28	Swart et al. 2020 (10.1016/j.envpol.2020.115633)
Yes	CuO	none	I	23	*Enchytraeus crypticus*	Gut	100	21	Ma et al. 2020 (10.1016/j.envpol.2019.113463)
Yes	CuO	none	A	50	*Folsomia candida*	Gut	100	28	Ding et al. 2020 (10.1016/j.chemosphere.2020.127347)
Yes	CuO	none	NA	28	*Triticum aestivum*	Rhizosphere	50	28	Guan et al. 2020 (10.1021/acs.est.0c00036)
Yes	Se	none	S	62	*Brassica chinensis*	Rhizosphere	0.5	60	Wang et al. 2022 (10.1039/d1en00740h)
Yes	TiO_2	none	NA	68	*Linum usitatissimum*	Rhizosphere	0.125 (+ sprayed with 100 $\mu g\cdot L^{-1}$ after 7 d)	21	Gorczyca et al. 2018 (10.1007/s11356-018-3346-7)
Yes	TiO_2	none	NA	68	*Triticum aestivum*	Rhizosphere	0.125 (+ sprayed with 100 $\mu g\cdot L^{-1}$ after 7 d)	21	Gorczyca et al. 2018 (10.1007/s11356-018-3346-7)

HUMAN AND ANIMAL HEALTH: AIR EXPOSURE

	Nanoparticle								
Effect	*Core*[b)]	*Coating*[c)]	*Shape*[d)]	*Size*[e)]	*Host*	*Microbiota*	*Concentration* *(mg·kg bw*$^{-1}$*·d*$^{-1}$*)*[f)]	*Exposure time (d)*	*Reference (DOI)*
Yes	La_2O_3	none	S	23	Mus musculus	Lung	2	1	Zheng et al. 2021 (10.1186/s12989-021-00410-5)
Yes	NiO	none	NA	5	Rattus norvegicus	Lung	0.05-0.16 mg (one dose)	1-28	Jeong et al. 2022 (10.3390/ijerph19010522)
Yes	SiO_2	none	S	49	Mus musculus	Gut	2.5	45	Ju et al. 2020 (10.1039/d0en01021a)

HUMAN AND ANIMAL HEALTH: AQUEOUS EXPOSURE

	Nanoparticle								
Effect on microbiota	*Core*[b)]	*Coating*[c)]	*Shape*[d)]	*Size*[e)]	*Host*	*Microbiota*	*Concentration* *(*$\mu g\cdot L^{-1}$*)*[f)]	*Exposure time (d)*	*Reference (DOI)*
N.D.	Ag	glutathione	S	20	*Homo sapiens*	Gut	$7.6\cdot10^3$	2	Cueva et al. 2019 (10.1016/j.fct.2019.110657)

N.D.	Ag	PEG	S	4	*Homo sapiens*	Gut	$11\cdot10^3$	2	Cueva et al. 2019 (10.1016/j.fct.2019.110657)
N.D.	IO	carboxymethyl-dextran	A	7	*Rattus norvegicus*	Mouth	$1\cdot10^6$	21	Liu et al. 2018 (10.1038/s41467-018-05342-x)
N.D.	IO	dextran	S	35	*Rattus norvegicus*	Mouth	$1\cdot10^6$	21	Naha et al. 2019 (10.1021/acsnano.8b08702)
Yes	Ag	citrate	NA	14	*Homo sapiens*	Gut	$1\cdot10^3$	1	Catto et al. 2019 (10.1016/j.envpol.2018.11.019)
Yes	Ag	none	S	10	*Homo sapiens*	Mouth	$5.2\cdot10^3$	2	Espinosa-Cristoba et al. 2019 (10.1155/2019/3205971)
Yes	Ag	none	S	29	*Homo sapiens*	Mouth	$5.2\cdot10^3$	2	Espinosa-Cristoba et al. 2019 (10.1155/2019/3205971)
Yes	Ag	citrate	S	14	*Homo sapiens*	Gut	1-30	42	Li et al. 2021 (10.1016/j.scitotenv.2020.143983)
Yes	CHX PR_4^+	PS_{64}-*b*-$PDMA_{53}$	S	26	*Rattus norvegicus*	Mouth	$5\cdot10^5$ - $8\cdot10^5$	13	Ostadhossein et al. 2021 (10.1038/s42003-021-02372-y)
Yes	CeO_2	none	R	8	*Homo sapiens*	Gut	0.01	5	Taylor et al. 2015 (10.1089/ees.2014.0518)
Yes	CuO	none	A	40	*Homo sapiens*	Mouth	$10\cdot10^3$-$100\cdot10^3$	0.67	Kahn et al. 2013 (10.1016/j.matlet.2013.01.085)
Yes	Se	Polystyrene-4-sulfonate	S	46	*Gallus domesticus*	Gut	$9\cdot10^2$	2	Gangadoo et al. 2019 (10.1016/j.aninu.2019.06.004)
Yes	TiO_2	none	S	27	*Homo sapiens*	Gut	$3\cdot10^3$	5	Taylor et al. 2015 (10.1089/ees.2014.0518)
Yes	TiO_2	none	A	25	*Homo sapiens*	Gut	0.1 $\mu g\cdot d^{-1}$	7	Agans et al. 2019 (10.1093/toxsci/kfz183)
Yes	ZnO	none	A	35	*Homo sapiens*	Mouth	$10\cdot10^3$-$100\cdot10^3$	0.67	Kahn et al. 2013 (10.1016/j.matlet.2013.01.085)
Yes	ZnO	none	S	24	*Homo sapiens*	Gut	0.01	5	Taylor et al. 2015 (10.1089/ees.2014.0518)
Yes	ZnO	alcohol/ alkene	S	32	*Homo sapiens*	Gut	20	NA	Zhou et al. 2021 (10.3389/fmicb.2021.700707)

HUMAN AND ANIMAL HEALTH: FOOD EXPOSURE

	Nanoparticle								

Effect on microbiota	*Core*$^{b)}$	*Coating*$^{c)}$	*Shape*$^{d)}$	*Size*$^{e)}$	*Host*	*Microbiota*	*Concentration (mg·kg*$^{-1}$*)*$^{f)}$	*Exposure time (d)*	*Reference (DOI)*
N.D.	Ag	none	C	4	*Gallus domesticus*	Gut	50 (drinking water)*	30	Vadalasetty et al. 2018 (10.1186/s12917-017-1323-x)
N.D.	CeO_2	none	S	35	*Mus musculus*	Gut	$10 \cdot 10^{3}$	21	Bredeck et al. 2021 (10.1080/17435390.2021.1940339)
Yes	Ag	none	A	58	*Danio rerio*	Gut	500	14	Merrifield et al. 2013 (10.1016/j.envpol.2012.11.017)
Yes	Ag	PVP	A	55	*Mus musculus*	Gut	0.046-4.6	28	Van den Brule et al. 2016 (10.1186/s12989-016-0149-1)
Yes	Ag	PVP	S	40	*Mus musculus*	Gut	$2 \cdot 10^{3}$	28	Bredeck et al. 2021 (10.1080/17435390.2021.1940339)
Yes	Ag	PVP	A	55	*Mus musculus*	Gut	0.004-0.4	168	Perez et al. 2021 (10.1016/j.fct.2021.112352)
Yes	Au	*C. verum* bio-actives	S	15	*Mus musculus*	Gut	10 (drinking water) *	56	Sharma et al. 2022 (10.1016/j.mtbio.2022.100204)
Yes	Chitosan	none	A	50	*Sus domesticus*	Gut	100-400	28	Xu et al. 2020 (10.1111/jpn.13283)
Yes	Cu	none	A	87	*Danio rerio*	Gut	500	14	Merrifield et al. 2013 (10.1016/j.envpol.2012.11.017)
Yes	Cu	chitosan	NA	95	*Gallus domesticus*	Gut	50-150	42	Wang et al. 2011 (10.3382/ps.2011-01511)
Yes	Cu	none	NA	55	*Gallus domesticus*	Gut	1.7	28	Yausheva et al. 2018 (10.1007/s11356-018-1991-5)
Yes	Cu	none	S	50	*Rattus norvegicus*	Gut	3.25-6.5	28	Cholewinska et al. 2018 (10.1371/journal.pone.0197083)
Yes	CuZn	none	NA	65	*Gallus domesticus*	Gut	2.84	28	Yausheva et al. 2018 (10.1007/s11356-018-1991-5)
Yes	Fe	none	NA	50	*Gallus domesticus*	Gut	8	28	Yausheva et al. 2018 (10.1007/s11356-018-1991-5)
Yes	Pectin	none	NA	64	*Mus musculus*	Gut	$7.5 \cdot 10^{3}$ (drinking water)*	28	Chandrarathna et al. 2020 (10.3390/md18030175)
Yes	Spore coat	none	S	100	*Mus musculus*	Gut	$10 \cdot 10^{6}$ CFUs (drinking water)*	42	Song et al. 2021 (10.1002/adfm.202104994)
Yes	SiO_2	none	A	13	*Mus musculus*	Gut	$10 \cdot 10^{3}$	21	Bredeck et al. 2021 (10.1080/17435390.2021.1940339)
Yes	SiO_2	none	A	15.5	*Mus musculus*	Gut	0.8-80	168	Perez et al. 2021 (10.1016/j.fct.2021.112352)

Yes	Thyme	chitosan	S	90	*Gallus domesticus*	Gut	60	42	Hosseini et al. 2018 (10.1080/00071668.2018.1521511)
Yes	TiO_2	none	NA	10	*Mus musculus*	Gut	$1\cdot10^3$	91	Mu et al. 2019 (10.1021/acs.jafc.9b02391)
Yes	TiO_2	none	NA	50	*Mus musculus*	Gut	$1\cdot10^3$	91	Mu et al. 2019 (10.1021/acs.jafc.9b02391)
Yes	TiO_2	none	NA	100	*Mus musculus*	Gut	$1\cdot10^3$	91	Mu et al. 2019 (10.1021/acs.jafc.9b02391)
Yes	TiO_2	none	A	33	*Mus musculus*	Gut	1	56	Cao et al. 2020 (10.1002/smll.202001858)
Yes	TiO_2	none	A	26	*Mus musculus*	Gut	$10\cdot10^3$	28	Bredeck et al. 2021 (10.1080/17435390.2021.1940339)
Yes	TiO_2	none	S	25	*Mus musculus*	Gut	20	56	Zhao et al. 2021 (10.1021/acs.jafc.1c03301)
Yes	ZnO	none	NA	30	*Gallus domesticus*	Gut	25-100	63	Feng et al. 2017 (10.3389/fmicb.2017.00992)
Yes	ZnO	none	NA	90	*Gallus domesticus*	Gut	5	28	Yausheva et al. 2018 (10.1007/s11356-018-1991-5)
Yes	ZnO	none	NA	23	*Sus domesticus*	Gut	$600\text{-}2\cdot10^3$	14	Xia et al. 2017 (10.18632/oncotarget.17612)

HUMAN AND ANIMAL HEALTH: GAVAGE EXPOSURE

Effect on microbiota	*Nanoparticle*				*Host*	*Microbiota*	*Concentration (mg·kg bw^{-1}·d^{-1})*[f]	*Exposure time (d)*	*Reference (DOI)*
	Core[b]	*Coating*[c]	*Shape*[d]	*Size*[e]					
N.D.	Ag	PVP	20	A	*Mus musculus*	Gut	10	28	Wilding et al. 2016 (10.3109/17435390.2015.1078854)
N.D.	IO	dextran	50	NA	*Sus domesticus*	Gut	1.5^{**}	23	Mazgaj et al. 2021 (10.3390/ijms22189930)
N.D.	IO	phospholipid	100	NA	*Sus domesticus*	Gut	1.5^{**}	23	Mazgaj et al. 2021 (10.3390/ijms22189930)
N.D.	ZnO	none	40	A	*Mus musculus*	Gut	250	49	Wang et al. 2017 (10.1007/s12011-017-0934-1)
Yes	Ag	none	20	NA	*Mus musculus*	Gut	$2\cdot10^{-3}$	45	Wu et al. 2020 (10.1039/c9en01387c)

Yes	Ag	citrate	18	S	*Mus musculus*	Gut	3	7	Lyu et al. 2021 (10.1038/s41598-021-85919-7)
Yes	Ag	PVP	10	NA	*Mus musculus*	Gut	1-5	36	Meier et al. 2021 (10.1016/j.impact.2021.100343)
Yes	Ag	citrate	10	NA	*Rattus norvegicus*	Gut	9-36	91	Williams et al. 2014 (10.3109/17435390.2014.921346)
Yes	Ag	citrate	75	NA	*Rattus norvegicus*	Gut	9-36	91	Williams et al. 2014 (10.3109/17435390.2014.921346)
Yes	Ag	PVP	84	CB	*Rattus norvegicus*	Gut	3.6	14	Javurek et al. 2017 (10.1038/s41598-017-02880-0)
Yes	Ag	PVP	93	S	*Rattus norvegicus*	Gut	3.6	14	Javurek et al. 2017 (10.1038/s41598-017-02880-0)
Yes	Au	Tannic acid	5	S	*Mus musculus*	Gut	0.025	8	Zhu et al. 2018 (10.1186/s12951-018-0415-5)
Yes	Fullerenol	none	95	S	*Mus musculus*	Gut	20	28	Li et al. 2018 (10.1186/s12989-018-0241-9)
Yes	HAHp/ZnO	HAHp	50	H	*Mus musculus*	Gut	$1\cdot10^{3}$	14	Song et al. 2018 (10.3390/md16010023)
Yes	Hydrophobic segment (hydrocarbon)	PEG-catechol	100	S	*Rattus norvegicus*	Gut	$4\cdot10^{3}$	5	Zhao et al. 2021 (10.1038/s41467-021-27463-6)
Yes	IO	Ginsenoside-R3	8	I	*Mus musculus*	Gut	70	84	Ren et al. 2020 (10.1002/smll.201905233)
Yes	Polystyrene	none	47	S	*Mus musculus*	Gut	0.2-10	30	Xiao et al. 2022 (10.1016/j.envpol.2021.118184)
Yes	Pt	citrate	5	S	*Mus musculus*	Gut	0.025	8	Zhu et al. (201910.2147/IJN.S210655)
Yes	Se	none	40	S	*Mus musculus*	Gut	0.1	10	Deng et al. 2021 (10.1039/d0nr07981b)
Yes	Se	Albumin	96	S	*Mus musculus*	Gut	0.1	10	Deng et al. 2021 (10.1039/d0nr07981b)
Yes	Se	none	39	S	*Rattus norvegicus*	Gut	$3\cdot10^{-3}$	1	Lin et al. (202110.1016/j.nantod.2020.101010)
Yes	SiO_2	none	27	A	*Mus musculus*	Gut	$3\cdot10^{3}$	28	Diao et al. 2021 (10.1186/s12951-021-00916-2)
Yes	TiO_2	none	29	A	*Mus musculus*	Gut	100	28	Li et al. 2018 (10.1039/c8nr00386f)

Yes	TiO_2	none	25	A	*Mus musculus*	Gut	1	7	Li et al. 2019 (10.1016/j.impact.2019.100164)
Yes	TiO_2	none	85	I	*Mus musculus*	Gut	$1 \cdot 10^3$	1-14	Kurtz et al. 2020 (10.1002/jat.3991)
Yes	TiO_2	none	21	A	*Mus musculus*	Gut	150	30	Zhang et al. 2020 (10.1007/s00204-020-02698-2)
Yes	TiO_2	none	38	S	*Mus musculus*	Gut	100	10	Gao et al. 2021 (10.1039/d0nr08106j)
Yes	TiO_2	none	30	I	*Mus musculus*	Gut	40	56	Zhu et al. 2021 (10.1007/s12274-020-3210-1)
Yes	TiO_2	none	29	A	*Rattus norvegicus*	Gut	2-50	30	Chen et al. 2019 (10.1039/c9nr07580a)
Yes	TiO_2	none	29	A	*Rattus norvegicus*	Gut	2-50	90	Chen et al. 2019 (10.1186/s12989-019-0332-2)
Yes	TiO_2	none	21	A	*Rattus norvegicus*	Gut	5	13	Mao et al. 2019 (10.1186/s11671-018-2834-5)
Yes	TiO_2	none	25	A	*Rattus norvegicus*	Gut	1-100	14	Zhao et al. 2020 (10.1016/j.ecoenv.2020.111393)
Yes	WO_3	none	48	S	*Mus musculus*	Gut	0.3 mmol·kg bw^{-1}	7	Qin et al. (202110.1016/j.nantod.2021.101234)
Yes	ZnO	none	50	S	*Mus musculus*	Gut	26	30	Chen et al. 2020 (10.1039/d0nr04563b)

HUMAN AND ANIMAL HEALTH: OTHER EXPOSURES

Effect on microbiota	*Nanoparticle*				*Host*	*Microbiota*	*Concentration*	*Exposure time (d)*	*Reference (DOI)*
	Core[b]	*Coating*[c]	*Shape*[d]	*Size*[e]					
Yes	Ag	protein	sphere	49	*Homo sapiens*	Gut	396 mg (capsule)	8.5	Vamanu et al. 2018 (10.3390/nu10050607)
Yes	$AgVO_3$	Ag nano-particle	wire	10	*Homo sapiens*	Mouth	10-50 mg·L resin^{-1}	7	De Castro et al. 2021 (10.1007/s10266-020-00582-0)

---

[a] Literature was retrieved from the Web of Science Core Collection database, accessed on 27 March 2022 through Leiden University's library, using the search string '(nanomaterial* OR nanoparticle*)' for the title, and the search string '(microbiome OR microbiota)' for the abstract of articles.

b) Nanoparticle core abbreviations: Ag, silver; Ag_2S, silver sulfide; Au, gold; $AgVO_3$, silver vanadate; CeO_2, cerium dioxide; CHX PR_4^+, cationic phenyl-bis biguanide chlorhexidine tributylhexadecylphosphonium bromide; Cu, copper; CuO, copper oxide; Fe, iron; HAHp, half-fin anchovy hydrolysates; La_2O_3, lanthanum oxide; Mo, molybdenum; MoO_3, molybdenum trioxide; NiO, nickel oxide; IO, iron oxide;; Pt, platinum; Se, selenium; SiO_2, silicium dioxide; TiO_2, titanium dioxide; WO_3, tungsten trioxide ;ZnO, zinc oxide.

c) Nanoparticle coating abbreviations: HAHp, half-fin anchovy hydrolysates; PEG, polyethylene glycol; PS-PDMA, polystyrene-poly(*N*,*N*-dimethylacrylamide); PVP, polyvinylpyrrolidone.

d) Nanoparticle shape abbreviations: A, amorphous; C, crystal; CB, cuboid; H, hexagonal; I, irregular; R, rods; S, (semi)-spherical.

e) For cuboids and wires, the smallest external dimension is presented.

f) In case different concentration units were reported, this is specified at the concerning rows.

* For drinking water exposures, 1 L water is expressed as 1 kg ‘food’.

** The concentration was based on the average weight of exposed piglets over the exposure time.

Supplementary table S2 starts at the next page.

Table S2: Relative abundances of bacterial taxa in zebrafish larvae microbiota as determined based on 16S rRNA sequencing. Replicates 1, 2 and 3 correspond to the pooled DNA of 30 larvae at 3 days post-fertilization. Mean and standard error of the mean (SEM) are given in the final column. Sequence data can be retrieved from the Sequence Read Archive under BioProject PRJNA860062 (BioSamples SAMN29820940, SAMN29820941 and SAMN29820942). Genus and species level identification was based on the SILVA 138 small subunit (16S/18S) rRNA database Ref NR 99, and family to phylum level classifications were retrieved from NCBI Taxonomy Browser. The total number of amplicon sequence variants upon filtering of sequences from a negative control (BioSample SAMN29820946), chloroplasts and mitochondria for replicate 1, 2 and 3 were 2950, 1948, and 3874, respectively. The corresponding QIIME2 pipeline is available via Zenodo (DOI: 10.5281/zenodo.6891712).

					Relative abundance (%)			
Phylum	*Class*	*Order*	*Family*	*Species*	*1*	*2*	*3*	*Mean ± SEM*
Actinobacteriota	Actinobacteria	Bifidobacteriales	Bifidobacteriaceae	*Bifidobacterium* sp.	1.9	0	0	0.6 ± 0.6
		Propionibacteriales	Propionibacteriaceae	*Cutibacterium* sp.	0	0.6	0	0.2 ± 0.2
	Coriobacteriia	Coriobacteriales	Coriobacteriaceae	*Collinsella* sp.	0.6	0	0	0.2 ± 0.2
Bacteroidota	Bacteroidia	Bacteroidales	Barnesiellaceae	*Barnesiella* sp.	0.2	0	0	0.1 ± 0.1
		Cytophagales	Prevotellaceae	*Prevotella* sp.	0.6	0	0	0.2 ± 0.2
				Prevotella nigrescens	0.3	0	0	0.1 ± 0.1
				Flectobacillus sp.	0	0	3.1	1.0 ± 1.0
		Flavobacteriales	Weeksellaceae	*Chryseobacterium* sp.	0.2	0	0	0.1 ± 0.1
				Candidatus *Chryseobacterium* sp.	0	1.4	0	0.5 ± 0.5
Firmicutes	Bacilli	RF39	RF39	RF39 bacterium	0.1	0	0	0.1 ± 0.03
	Clostridia	Eubacteriales	Eubacteriaceae	*Eubacterium coprostanoligenes*	0.8	0	0	0.3 ± 0.3
			Lachnospiraceae	*Agathobacter rectale*	0.7	0	0	0.2 ± 0.2
				Blautia sp.	0.6	0	0	0.2 ± 0.2
				Coprococcus sp.	0.9	0	0	0.3 ± 0.3
				Dorea sp.	0.4	0	0	0.2 ± 0.1
				Fusicatenibacter sp.	0.9	0	0	0.3 ± 0.3
			Oscillospiraceae	*Ruminococcus* sp.	0.6	0	0	0.2 ± 0.2
				Subdoligranulum sp.	0.6	0	0	0.2 ± 0.2
				UCG-002 bacterium	1.1	0	0	0.4 ± 0.4
				UCG-005 bacterium	0.2	0	0	0.1 ± 0.1
			Peptostreptococcaceae	*Romboutsia* sp.	0.8	0	0	0.3 ± 0.3

		Tissierellales	Peptoniphilaceae	*Anaerococcus* sp.	0.2	0	0	0.1 ± 0.1
				Parvimonas sp.	0	0	0.7	0.2 ± 0.2
	Negativicutes	Veillonellales	Veillonellaceae	*Dialister invisus*	1.3	0	0	0.4 ± 0.4
Proteobacteria	Alpha-proteobacteria	Caulobacterales	Caulobacteraceae	*Caulobacter* sp.	0	2.3	0	0.8 ± 0.8
				Unassigned	1.3	0	0	0.4 ± 0.4
		Hyphomicrobiales	Boseaceae	*Bosea* sp.	0	0	1.1	0.4 ± 0.4
			Bradyrhizobiaceae	*Bradyrhizobium* sp.	1.4	0	0	0.5 ± 0.5
			Methylobacteriaceae	*Methylobacterium jeotgali*	0	1.3	0	0.4 ± 0.4
			Pleomorphomonadaceae	Unassigned	0.9	0	0	0.3 ± 0.3
			Rhizobiaceae Bradyrhizobiaceae	*Allorhizobium-Neorhizobium-Pararhizobium-Rhizobium* sp.	2.3	6.0	0.9	3.1 ± 1.5
		Rhodospirillales	Rhodospirallaceae	*Taonella* sp.	0.2	3.0	0	1.1 ± 1.0
		Sphingomonadales	Sphingomonadaceae	*Sphingomonas* sp.	0.5	4.2	0	1.6 ± 1.3
	Beta-proteobacteria	Burkholderiales	Burkholderiaceae	*Limnobacter humi*	0	0.3	0	0.1 ± 0.1
				Ralstonia sp.	5.0	5.4	0	3.5 ± 1.7
				Unassigned	0.2	2.0	3.2	1.8 ± 0.9
			Chromatiaceae	*Rheinheimera* sp.	0.5	0	0	0.2 ± 0.2
			Comamonadaceae	*Delftia* sp.	0	1.5	1.4	1.0 ± 0.5
				Pelomonas sp.	1.8	6	0.4	2.7 ± 1.7
				Pelomonas puraquae	0.6	0	0	0.2 ± 0.2
			Oxalobacteraceae	*Massilia* sp.	0	0.8	0	0.3 ± 0.3
				Pseudoduganella sp.	0	1.4	0	0.5 ± 0.5
				Unassigned	0.7	2.6	4.4	2.5 ± 1.1
				Undibacterium sp.	0.4	0	0	0.1 ± 0.1
		Neisseriales	Chromobacteriaceae	*Vogesella* sp.	58.4	53.6	69.9	60.6 ± 4.8
		Rhodocyclales	Azonexaceae	*Dechloromonas* sp.	1.8	0.9	0	0.9 ± 0.5
	Gamma-proteobacteria	Aeromonadales	Aeromonadaceae	*Aeromonas* sp.	0.4	0	0.7	0.4 ± 0.2
			Unassigned	Unassigned	0.4	0	0	0.1 ± 0.1
		Cardiobacteriales	Cardiobacteriaceae	*Cardiobacterium hominis*	0.5	0	0	0.2 ± 0.2
		Enterobacteriales	Enterobacteriaceae	*Escherichia/Shigella* sp.	0	0	0.6	0.2 ± 0.2
		Nevskiales	Solimonadaceae	Unassigned	1.1	0	0	0.4 ± 0.4
		Pseudomodales	Pseudomonadaceae	*Pseudomonas* sp.	0.6	0	4.5	1.7 ± 1.4

				Pseudomonas luteola	0	0	0.9	0.3 ± 0.3
		Xanthomonadales	Xanthomonadaceae	*Stenotrophomonas* sp.	4.3	0	3.1	2.5 ± 1.3
Verrucomicrobiota	Verrucomicrobiae	Puniceicoccales	Puniceicoccaceae	Unassigned	0.4	0	0	0.1 ± 0.1
Unassigned bacteria	Unassigned	Unassigned	Unassigned	Unassigned	2.1	3.6	2.3	2.7 ± 0.5
Unassigned	Unassigned	Unassigned	Unassigned	Unassigned	0.9	3.2	2.8	2.3 ± 0.7

Bregje W. Brinkmann **2022**